Spectroscopy and imaging of spin waves and valley excitons in two dimensions

Carmiggelt, J.J.

DOI
10.4233/uuid:8b974567-3db2-48e1-a54c-19ad6f615449

Publication date
2023

Document Version
Final published version

Citation (APA)
Carmiggelt, J. J. (2023). *Spectroscopy and imaging of spin waves and valley excitons in two dimensions*. [Dissertation (TU Delft), Delft University of Technology]. https://doi.org/10.4233/uuid:8b974567-3db2-48e1-a54c-19ad6f615449

SPECTROSCOPY AND IMAGING OF SPIN WAVES AND VALLEY EXCITONS IN TWO DIMENSIONS

SPECTROSCOPY AND IMAGING OF SPIN WAVES AND VALLEY EXCITONS IN TWO DIMENSIONS

Proefschrift

ter verkrijging van de graad van doctor
aan de Technische Universiteit Delft,
op gezag van de Rector Magnificus Prof.dr.ir. T.H.J.J. van der Hagen,
voorzitter van het College voor Promoties,
in het openbaar te verdedigen op donderdag 26 januari 2023 om 12:30 uur

door

Joris Jip CARMIGGELT

Master of Science in Physics,
Universiteit Leiden, Nederland,
geboren te Den Haag, Nederland.

Dit proefschrift is goedgekeurd door de promotoren.

Samenstelling promotiecommissie bestaat uit:

Rector Magnificus	voorzitter
Prof. dr. G. A. Steele	Technische Universiteit Delft, promotor
Dr. T. van der Sar	Technische Universiteit Delft, promotor

Onafhankelijke leden:

Prof. dr. A. F. Otte	Technische Universiteit Delft
Prof. dr. R. A. Duine	Universiteit Utrecht
Prof. dr. P. Maletinsky	Universiteit van Bazel, Zwitserland
Dr. H. Schultheiß	Helmholtz-Zentrum Dresden-Rossendorf, Duitsland
Prof. dr. ir. H. S. J. van der Zant	Technische Universiteit Delft, reservelid

Keywords: Spin waves, NV centers, magnetism, nonlinear magnonics, excitons, valleytronics

Printed by: Gildeprint, Enschede

Front & Back: Artist's impression of a diamond sensor that images spin waves excited by microwave striplines. Image by Enrique Sahagún, SCIXEL. Design by Iacopo Bertelli and Toeno van der Sar.

Casimir PhD Series, Delft-Leiden 2023-03

ISBN 978-90-8593-551-3

An electronic version of this dissertation is available at
http://repository.tudelft.nl/.

Voor pa, ma, Roen en Laar

CONTENTS

SUMMARY

Knowledge about the magnetic and electronic properties of materials does not only expand our fundamental understanding of nature, but is also crucial for the development of new technologies. Today's electronic devices rely on electrical currents to transport and process information, which generate a lot of heat waste via Joule heating. These devices could become much more energy efficient by using the electron's spin or valley degree of freedom to encode information, rather than its charge. In this dissertation we study the elementary excitations of magnetic and semiconducting materials, called spin waves and excitons, which have been proposed as respectively spin and valley information carriers in future electronic devices.

In the first part of this thesis we detect spin waves via their microwave magnetic field using both electrical spectroscopy and nitrogen-vacancy (NV) centers in diamond. Spin waves are collective, wave-like precessions of electron spins that can propagate through magnetic insulators free of Joule heating. To harness spin waves for data transport, it is essential to develop spin-wave detection techniques that can give insight in their microscopic behaviour and dynamics. NV centers are defects in the diamond crystal lattice of which the photoluminescence depends on the NV spin state. Since the spin state is sensitive to spin-wave magnetic fields, we can locally study spin waves via the NV photoluminescence.

In the second part of this thesis we study excitons in semiconducting transition metal dichalcogenide (TMD) monolayers. These electron-hole bound states can be selectively excited in one of the two TMD bandstructure valleys using circularly polarized light. Information stored in the excitonic valley index is typically quickly lost due to rapid scattering between the valleys. We use chemical doping to realize a large steady-state valley polarization of excitons at room temperature.

Chapter 1 introduces NV centers as magnetic-field sensors and describes how they could be harnessed for characterization of future *valleytronic* and *magnonic* devices (a magnon is an elementary spin-wave excitation). Next, we review the theory behind NV centers, spin waves and excitons in chapter 2 and discuss the experimental setups used to study them. Chapters 3-6 describe the research results obtained in this thesis.

A key advantage of magnetic microscopy with NV centers is that it can provide a direct view on spin waves, even when they are hidden underneath optically-opaque materials. In chapter 3 we demonstrate NV-based magnetic imaging of coherent spin waves excited by microstrips in an yttrium iron garnet (YIG) film (see the cover of this thesis for an artist's impression). We determine the spin-wave dispersion and magnetic damping from the measured spin-wave images, and explain the observed autofocussing of spin

waves by considering the anisotropy of the dispersion.

An important limitation of NV magnetometry is that it is only sensitive to a narrow frequency band in the microwave regime. We greatly extend the microwave detection bandwidth of NV centers by converting target microwave frequencies on-chip to the NV detection frequency using two nonlinear spin-wave mixing protocols in YIG. The first protocol described in chapter 4 relies on four-spin-wave mixing and allows microwave detection over a gigahertz range at a constant external magnetic field. In addition, it enables coherent control of NV spins using off-resonant microwaves. The second detection scheme relies on difference frequency generation and enables the detection of microwave signals at multi-gigahertz detuning from the NV detection frequency. This protocol paves the way for detecting high-frequency magnetization dynamics in atomically-thin van-der-Waals magnets with NV centers.

In addition to its ultralow spin-wave damping, YIG is a prime magnonic material due to the tunability of its magnetic properties via doping. For instance, the introduction of gallium dopants strongly reduces the magnetization such that the spin-wave dispersion becomes isotropic, making gallium-doped YIG (Ga:YIG) a promising material for spin-wave optics. Chapter 5 focuses on the electrical detection of spin waves in Ga:YIG by measuring the spin-wave-mediated microwave transmission between two microstrips. We reconstruct the spin-wave dispersion from the propagating spin wave spectroscopy measurements, while considering the out-of-plane magnetic anisotropy. In addition, we characterize the foldover of the spin-wave modes at increased microwave drive powers.

Chapter 6 presents polarization-resolved optical measurements of valley excitons in WS_2 monolayers. We demonstrate that chemical doping with anisole induces a significant steady-state valley polarization of the TMD excitons. The doping stimulates the conversion of neutral excitons into charged trions, which decreases the exciton lifetime compared to the intervalley scattering time. We use a rate equation model to explain the observed valley polarization in terms of the doping-controlled trion-exciton equilibrium.

In chapter 7 we summarize our findings and suggest potential directions for future research.

SAMENVATTING

Kennis over magnetische en elektronische eigenschappen van materialen verruimt niet alleen ons inzicht in de natuur, maar is ook cruciaal voor de ontwikkeling van nieuwe technologieën. Hedendaagse elektronische apparaten maken gebruik van elektrische stroompjes om informatie te transporteren en verwerken, waarbij veel restwarmte vrijkomt als gevolg van het Joule effect. Codering van informatie in elektronische apparaten kan veel energie-efficiënter worden door gebruik te maken van de spin- of valleivrijheidsgraad van het elektron. In dit proefschrift bestuderen we de elementaire excitaties van magnetische en halfgeleidende materialen, genaamd spingolven en excitonen. Beiden zijn aangedragen als respectievelijk spin- en vallei-informatiedragers in toekomstige elektronica.

In het eerste deel van dit proefschrift bestuderen we spingolven door hun microgolfmagneetveld te detecteren met behulp van zowel elektrische spectroscopie als stikstof-gat (nitrogen-vacancy, NV) centra in diamant. Spingolven zijn collectieve, golvende precessies van elektronenspins in magnetische materialen. Zij kunnen zich door magnetische isolatoren voortbewegen, vrij van de warmteproductie die gepaard gaat met elektrische stroom. Om spingolven voor datatransport te gebruiken, is het essentieel spingolfdetectietechnieken te ontwikkelen die inzicht kunnen geven in hun microscopische gedrag en dynamica. Zo zijn NV centra defecten in het diamanten kristalrooster, waarvan de fotoluminescentie afhangt van de NV spintoestand. We kunnen spingolven lokaal bestuderen via de NV fotoluminescentie, aangezien de NV spin gevoelig is voor spingolfmagneetvelden.

In het tweede deel van dit proefschrift bestuderen we excitonen in halfgeleidende transitiemetaal dichalcogenide (TMD) monolagen. Deze gebonden toestanden van een elektron en een elektronengat kunnen in één van de twee TMD bandstructuurvalleien aangeslagen worden door gebruik te maken van circulair gepolariseerd licht. Informatie opgeslagen in de excitonische vallei-index gaat doorgaans snel verloren door verstrooiing tussen de valleien. Wij gebruiken chemische dotering om een grote valleipolarisatie van excitonen bij kamertemperatuur te realiseren.

Hoofdstuk 1 introduceert NV centra als magneetveldsensoren en beschrijft hoe deze gebruikt kunnen worden om toekomstige *valleitronische* en *magnonische* apparaten te karakteriseren (een magnon is een elementaire spingolfexcitatie). Vervolgens komt de theorie achter NV centra, spingolven en excitonen in hoofdstuk 2 aan bod, alsmede de experimentele opstellingen waarmee ze bestudeerd worden. Hoofdstukken 3-6 beschrijven de resultaten van dit promotieonderzoek.

Een cruciaal voordeel van magnetische microscopie met NV centra is dat het zicht op spingolven geeft, zelfs wanneer deze verborgen zijn onder ondoorzichtige materialen. In hoofdstuk 3 demonstreren we magnetische beeldvorming van coherente spingolven, die door microdraden in een dunne laag yttrium-ijzer-granaat (YIG) worden aangeslagen (zie de omslag van dit proefschrift voor een artistieke impressie). Vervolgens bepalen we de spingolfdispersie en magnetische demping met behulp van gemeten spingolfafbeeldingen. Tot slot verklaren we het geobserveerde autofocussen van de spingolven aan de hand van de anisotropie van de spingolfdispersie.

Het feit dat NV magneetvelddetectie alleen gevoelig is voor een smalle frequentieband in het microgolfregime vormt een belangrijke beperking. In hoofdstuk 4 vergroten we de microgolfdetectie brandbreedte van NV centra door microgolffrequenties lokaal naar de NV detectiefrequentie om te zetten via twee niet-lineaire spingolfmengprotocolen in YIG. Het eerste protocol maakt gebruik van vier-spingolfmenging en laat microgolfdetectie over een gigahertzbereik toe bij een constant extern magneetveld. Bovendien maakt het coherente controle van NV spins mogelijk met niet-resonante microgolven. Het tweede detectieschema berust op verschilfrequentiegeneratie en maakt het mogelijk microgolfsignalen te detecteren die meerdere gigahertz verwijderd zijn van NV detectiefrequentie. Dit protocol maakt de weg vrij voor detectie van hoogfrequente magnetisatie dynamica in atomair-dunne van-der-Waals magneten met behulp van NV centers.

YIG is een uitermate geschikt materiaal voor magnonica aangezien het, naast een ultralage spingolfdemping, magnetische eigenschappen heeft die via dotering te veranderen zijn. De introductie van galliumdotering zorgt bijvoorbeeld voor een sterke reductie van de magnetisatie, zodat de spingolfdispersie isotroop wordt. Hiermee is galliumgedoteerde YIG (Ga:YIG) een veelbelovend materiaal voor spingolfoptica. Hoofdstuk 5 concentreert zich op de elektrische detectie van spingolven in Ga:YIG, door de spingolfgemedieerde microgolftransmissie tussen twee microdraden te meten. We reconstrueren de spingolfdispersie op basis van de spingolfspectroscopiemetingen, waarbij we de magnetische anisotropie uit het vlak in acht nemen. Daarnaast karakteriseren we de omslag van de spingolfmodi bij hoge microgolfaandrijfkrachten.

Hoofdstuk 6 presenteert polarisatie-afhankelijke, optische metingen van vallei-excitonen in WS_2 monolagen. We laten zien dat chemische dotering met anisol tot een significante, stabiele valleipolarisatie van de TMD excitonen leidt. De dotering stimuleert de omzetting van neutrale excitonen in geladen trionen, wat de exciton levensduur verkleint ten opzichte van de vallei-verstrooiingstijd. We gebruiken een snelheidsvergelijkingmodel om de geobserveerde valleipolarisatie te verklaren aan de hand van het doteringgecontroleerde trion-exciton evenwicht.

In hoofdstuk 7 vatten we onze bevindingen samen en suggereren we potentiële richtingen voor toekomstig onderzoek.

1

INTRODUCTION

Sensors are omnipresent in daily life. They enable *measurements* of our surroundings by converting a physical quantity to a detectable signal. For example, mercury-in-glass thermometers convert the outdoor temperature to a certain mercury level in a glass tube. The sensor's sensitivity indicates how fast tiny signals can be detected. It is determined by how much the output (in this case, the mercury level) changes upon small variations of the measured input (the outdoor temperature) compared to the intrinsic noise of the sensor (fluctuations of the mercury level that are not related to temperature changes, e.g., due to mechanical vibrations). In many day-to-day situations relatively coarse measurements of physical quantities are satisfactory (for instance, often it is sufficient to know the outside temperature with the precision of a degree). However, when studying the microscopic world large sensor sensitivities are required as the signals to be detected are tiny.

Quantum systems are famously sensitive to external disturbances. These systems have discrete energy levels, which can be occupied in a quantum superposition. The system's energy state can be initialized and manipulated, but evolves inevitably over time to a random state due to uncontrolled interactions with the environment. This process is known as *decoherence* and poses a central challenge to the development of quantum computing and communication technologies, where sufficient control over the quantum state is required. Vice versa, the fragility of quantum states is an opportunity for the field of quantum sensing, which harnesses the sensitivity of quantum systems to infer information about the environment [1]. Examples of quantum sensors include gravity gradient sensors based on interferometry of free-falling cold atoms [2], and nanoscale magnetic-field sensors based on superconducting quantum interference devices (SQUIDs) [3] or solid-state spins [4].

1.1. MAGNETIC-FIELD SENSING WITH NV CENTERS

Nitrogen-vacancy (NV) centers are lattice defects in diamond where two neighbouring carbon atoms are replaced by a nitrogen atom and a lattice vacancy (Fig. 1.1a). The

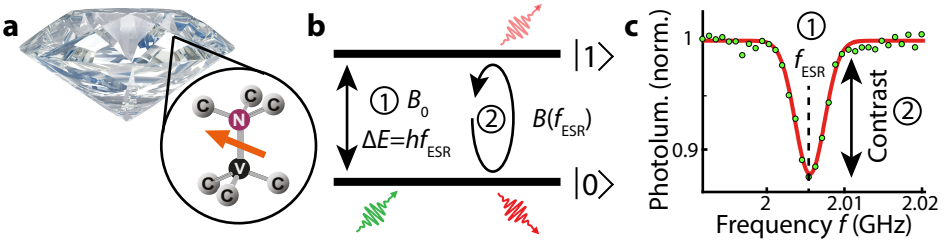

Figure 1.1: The nitrogen-vacancy center as quantum magnetometer. (**a**) Nitrogen-vacancy (NV) centers are defects in the carbon (C, gray) lattice of diamond comprising a nitrogen atom (N, purple) and an adjacent lattice vacancy (V, black). The electron spin of the NV center (orange arrow) is effectively modeled as a two-level quantum system that can detect magnetic fields in two ways (**b**). (1) The static (DC) magnetic field B_0 determines the energy difference ΔE between the $|0\rangle$ and $|1\rangle$ spin levels and is extracted by measuring the ESR frequency f_{ESR}. (2) Microwave (AC) magnetic fields oscillating at the ESR frequency $B(f_{\mathrm{ESR}})$ drive transitions between the two energy levels and are measured by detecting changes of the spin state via the spin-dependent NV photoluminescence (red wiggly arrows). (**c**) Sketch of the NV photoluminescence dip measured in an optically detected magnetic resonance (ODMR) experiment. A continuous-wave green laser excites the NV centers and pumps the NV spin into $|0\rangle$ [green wiggly arrow in (b)], while the NV photoluminescence is monitored. The $|1\rangle$ state becomes occupied when the microwave frequency f is at the ESR frequency, leading to more dark decay of the NV and therefore a decrease of the NV photoluminescence. The static magnetic field is determined from the measured ESR frequency (1), while the microwave magnetic-field strength scales with the ESR contrast (2).

electron spin of the NV center is a highly coherent quantum system and has become a workhorse in quantum computing and entangling experiments [5–7]. As such, when harnessed as a sensor NV centers are being called "quantum sensors", even though most sensing experiments do not rely on quantum coherent coupling between the NV and the sample under study [1]. NV spins have been used to study temperature [8], stress [9], and electric [10] and magnetic fields [11–13] in a wide variety of microscopic biological [14], geological [15] and condensed-matter systems [16]. Due to their point-like nature, NV centers can provide *local* measurements with a spatial resolution that is only limited by their stand-off distance to the sample of interest.

In this thesis we harness NV spins for detecting magnetic fields [4]. Previously, NV magnetometry was used to study nuclear magnetic resonance [17, 18], electric currents [19, 20] and magnetism [16] at the nanoscale. We can detect both static magnetic fields and fields oscillating in the gigahertz range (GHz, also known as *microwaves*, ~ billion cycles per second) by monitoring the spin-dependent photoluminescence of NV centers.

In a simplified picture the NV spin corresponds to a qubit [1] with two quantized spin energy levels, labeled $|0\rangle$ and $|1\rangle$. A green laser pulse brings the NV center to its electronic excited state without changing its spins state, from which it falls back to the electronic ground state either by emitting a photon (bright decay) or by decaying via a metastable state without emitting a photon (dark decay) [21]. Dark decay is more likely when the NV is in the $|1\rangle$ spin-state, causing spin-dependent NV photoluminescence that enables *readout* of the NV spin (Fig. 1.1b). Furthermore, the metastable state decays preferentially towards $|0\rangle$, enabling *initialization* of the spin in $|0\rangle$ by repeatedly cycling between

the electronic ground and excited states.

Importantly, both the *energy gap* between the spin levels and the *quantum state* of NV centers are sensitive to magnetic fields. Microwave magnetic fields drive transitions between $|0\rangle$ and $|1\rangle$ when they are resonant with the energy gap, which is determined by the static magnetic field B_0 at the position of the NV (Fig. 1.1b). Therefore, static and microwave magnetic fields can be locally measured from the NV photoluminescence during an optically detected magnetic resonance (ODMR) experiment [22].

In an ODMR experiment a continuous-wave green laser continuously pumps the NV center into $|0\rangle$, while the frequency f of a microwave field B is swept and the NV photoluminescence is monitored. A dip in the photoluminescence due to an increased occupation in $|1\rangle$ is recorded when the microwave frequency is resonant with the energy difference ΔE between the NV spin states depicted in Fig. 1.1b, such that

$$f = f_{\mathrm{ESR}} = \Delta E / h, \tag{1.1}$$

where h is the Planck constant and f_{ESR} is the electron spin resonance (ESR) frequency.

The static magnetic field is determined from the measured ESR frequency (Fig. 1.1c, labeled 1), which depends linearly on the field strength according to the Zeeman effect (see section 2.1). The depth of the measured photoluminescence dip (also known as the *ESR contrast*, Fig. 1.1c, labeled 2) is a probe for the amplitude of the microwave magnetic fields at the ESR frequency $B(f_{\mathrm{ESR}})$ [23], where a deeper dip indicates a larger field. Throughout this thesis we mostly focus on measuring the ESR contrast of NV centers, as it allows us to study the microwave magnetic fields of spin waves in magnetic materials.

1.2. SPIN WAVES AND THEIR APPLICATIONS IN MAGNONICS

Spin waves are emergent phenomena in which many electron spins in a magnetically-ordered material precess in a collective, wave-like manner [24, 25] (Fig. 1.2a). In this thesis we locally detect the microwave magnetic fields generated by spin waves with NV centers, from which we obtain a direct view on the interactions and dynamics of spin waves. Besides improving our fundamental understanding of magnetism, these insights are valuable when harnessing spin waves in next-generation electronic devices.

Currently electronic devices rely on electrical currents in thin metal electrodes to process and transport information. However, the moving electrons dissipate a lot of energy, resulting in Ohmic heating of the electrodes. This constrains further miniaturization of devices, puts high demands on the energy supply of electronics and causes a huge energy consumption by the global ICT sector [26].

Spin waves can propagate through magnetic materials even when the carrier electrons remain at fixed positions. As such, spin-wave transport is free of Ohmic heat dissipation in magnetic insulators, making spin waves an attractive alternative information carrier in spin-wave electronics [27–29] (also refered to as *magnonics*, since the quanta of spin

waves are called magnons). Spin waves have a few other technologically-appealing properties, which we summarize below.

1. Spin waves have frequencies in the gigahertz/terahertz range, such that they can be manipulated at ultrashort timescales.

2. They can have nanoscale wavelengths, allowing their integration in miniature integrated circuits.

3. They propagate quickly through materials (group velocities up to 650 km/s have been reported [30]), enabling rapid data transfer.

4. Spin waves stably exist over a wide temperature range, allowing their integration in room-temperature devices.

5. Spin waves can propagate over millimeter distances without significant decay in magnetic materials with low spin-wave damping [27].

6. The wave-like nature of spin waves allows encoding information in their amplitude *and* phase, making them suitable for non-boolean logic [31].

7. Multiple data streams can be processed at the same time using spin waves with different frequencies [32]. This is called "multiplexing".

8. Spin waves exhibit a rich variety of nonlinear effects that could be used in devices [29].

9. Devices could potentially harness processes associated to the quantum nature of magnons, such as magnon condensation [33].

Prototype magnonic devices that have been realized in the past include majority gates [34], directional couplers [35] and transistors [36].

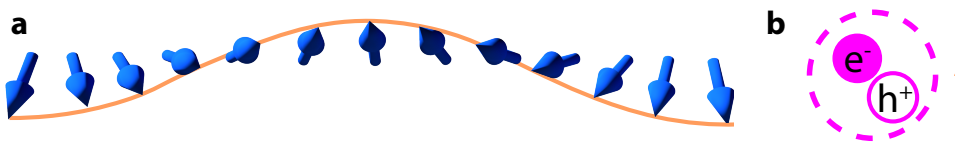

Figure 1.2: Solid-state excitations as measurement target. (**a**) Spin waves are collective excitations of magnetic materials in which neighbouring spins (blue arrows) precess with a slight phase difference with respect to their neighbours. As a result a wavelike excitation (the spin wave, highlighted in orange) propagates through the spin ensemble. (**b**) Excitons are the excitations of semiconducting materials and consist of bound states of negatively charged electrons (e^-) and positively charged holes (h^+). Spin waves and excitons both generate magnetic fields that can be detected using NV centers in diamond. (a) is adapted from [37].

1.2.1. HYBRID MAGNON-QUANTUM SYSTEMS

An intense and rapidly growing research field is the realization of hybrid magnon-quantum systems, which are a special class of magnonic devices [38]. In these devices new functionalities are added to quantum systems, such as NV centers, by coupling them to spin waves.

In this thesis we greatly extend the microwave frequency sensitivity of NV sensors by interfacing them with spin waves in a hybrid magnet-diamond system. Generally, NV centers are only sensitive to microwave frequencies near the ESR frequency, where the functional bandwidth is limited to the linewidth of the photoluminescence dip measured in an ODMR experiment (typically around 0.01 GHz, c.f. Fig. 1.1c). We circumvent this limitation by converting microwave frequencies on-chip to the ESR using spin-wave mixing in a nearby magnet. This enables NV-based microwave sensing over an 1-GHz bandwidth and allows coherent quantum control of NV spins using broadband microwaves.

1.3. VALLEYTRONICS WITH EXCITONS IN TMD MONOLAYERS

Besides measurements on spin-wave excitations in magnetic materials, this thesis also presents measurements on excitons, the elementary excitations of semiconducting materials. Just like spin waves, excitons have been proposed as information carrier in future electronic devices, which store and process information using the *valley* degree of freedom of the excitons [39].

Excitons are bound states of electrons and holes that can stably exist at room temperature [25] (Fig. 1.2b). We study excitons in transition metal dichalcogenide (TMD) monolayers of which the bandstructure is characterized by two valleys, labeled K and K'. Circularly polarized light selectively excites excitons in one of the valleys (e.g., left (right) circularly polarized light excites excitons in the $K^{(\prime)}$ valley), which induces a *valley polarization* of the excitons [40–42].

The valley index is viewed as a "pseudospin", as it resembles a binary quantum degree of freedom analogous to a spin-1/2 system [43]. As such, excitons can be excited in a valley superposition using linearly polarized light, a phenomenon known as *valley coherence* [44]. After initialization, the valley state can be manipulated using ultrashort light pulses [45]. Valleytronic devices could naturally be integrated into photonic circuits, since excitons emit photons upon electron-hole recombination with a polarization depending on the valley state (e.g., excitons in $K^{(\prime)}$ valley emit photons that are left (right) circularly polarized).

In the final part of this thesis we present measurements aimed towards detecting TMD excitons with NV magnetometry. Each exciton has a magnetic dipole moment with a sign depending on its valley index [46]. Strongly valley-polarized excitons are thus expected to generate a magnetic field that could in principle be detected with NV centers. This would allow nanoscale characterization of the valley dynamics while the excitons are excited. However, at room temperature it is challenging to maintain a large steady-state valley polarization [47] due to strong intervalley scattering of excitons via phonons [48]

and Coulomb interactions [49]. We show via optical measurements that a large room-temperature excitonic valley polarization in TMD monolayers can be realized using electron doping.

Although our results resemble a first step towards NV-based detection of valley polarization, many other challenges remain to be solved. For instance, it is difficult to separate the NV photoluminescence from the excitonic photoluminescence, making it challenging to readout NV centers that are in close proximity to TMD excitons. In addition, the optically-induced exciton density is typically small, such that the magnetic fields generated by the valley magnetization are expected to be weak and therefore hard to detect.

1.4. THESIS OUTLINE

This thesis consists of two parts. The first three research chapters focus on the detection of spin waves, while the final research chapter focusses on the optical characterization of TMD excitons. We start by covering the relevant theory behind NV center magnetometry, spin waves and excitons in TMD monolayers in chapter 2.

In chapters 3 and 4 we place a diamond with an NV sensing layer on top of a magnet (as depicted in the artist's impression on the cover of this thesis). In chapter 3 we use the NV centers to detect the microwave magnetic fields of spin waves resonant with the NV ESR frequency. This allows imaging the spin-wave wavefronts and characterization of the spin-wave dispersion. We explain the observed autofocussing of spin waves using an analytical model of the spin-wave dynamics.

In chapter 4 we demonstrate NV-based detection of spin waves with frequencies *detuned* from the NV ESR frequency. By harnessing nonlinear magnetization dynamics we convert off-resonant target frequencies to the ESR, facilitating their detection. Excitingly, this enables broadband microwave sensing with NV centers and coherent control of the NV spin state using off-resonant microwaves. It also opens the door for detecting high-frequency spin waves in atomically-thin magnets.

In chapter 5 we detect spin waves in an unconventional magnet by measuring the microwave transmission between two micro-antennae fabricated directly on the magnet's surface. We show that we can reconstruct the spin-wave dispersion from our measurements and observe strongly nonlinear spin-wave behaviour. As such, electrical spectroscopy is a useful tool for characterizing spin waves in unknown magnetic materials prior to NV measurements.

In chapter 6 we realize a large valley polarization in monolayer WS_2 at room temperature. Using chemical doping we stimulate the conversion of excitons into trions (charged excitons), which quenches the exciton lifetime. We explain the observed quenching-induced valley polarization using a rate equation model that describes the valley dynamics of the exciton-trion equilibrium. The realized valley polarization could potentially facilitate the detection of excitons with NV centers in future experiments.

BIBLIOGRAPHY

[1] C. L. Degen, F. Reinhard, and P. Cappellaro, "Quantum sensing", Reviews of Modern Physics **89**, 035002 (2017).

[2] B. Stray et al., "Quantum sensing for gravity cartography", Nature **602**, 590 (2022).

[3] D. Vasyukov et al., "A scanning superconducting quantum interference device with single electron spin sensitivity", Nature Nanotechnology **8**, 639 (2013).

[4] L. Rondin et al., "Magnetometry with nitrogen-vacancy defects in diamond", Reports on Progress in Physics **77**, 056503 (2014).

[5] L. Childress et al., "Coherent Dynamics of Coupled Electron and Nuclear Spin Qubits in Diamond", Science **314**, 281 (2006).

[6] B. Hensen et al., "Loophole-free Bell inequality violation using electron spins separated by 1.3 kilometres", Nature **526**, 682 (2015).

[7] S. L. N. Hermans et al., "Qubit teleportation between non-neighbouring nodes in a quantum network", Nature **605**, 663 (2022).

[8] G. Kucsko et al., "Nanometre-scale thermometry in a living cell", Nature **500**, 54 (2013).

[9] S. Hsieh et al., "Imaging stress and magnetism at high pressures using a nanoscale quantum sensor", Science **366**, 1349 (2019).

[10] F. Dolde et al., "Electric-field sensing using single diamond spins", Nature Physics **7**, 459 (2011).

[11] J. M. Taylor et al., "High-sensitivity diamond magnetometer with nanoscale resolution", Nature Physics **4**, 810 (2008).

[12] J. R. Maze et al., "Nanoscale magnetic sensing with an individual electronic spin in diamond", Nature **455**, 644 (2008).

[13] G. Balasubramanian et al., "Nanoscale imaging magnetometry with diamond spins under ambient conditions", Nature **455**, 648 (2008).

[14] R. Schirhagl, K. Chang, M. Loretz, and C. L. Degen, "Nitrogen-Vacancy Centers in Diamond: Nanoscale Sensors for Physics and Biology", Annual Review of Physical Chemistry **65**, 83 (2014).

[15] D. R. Glenn et al., "Micrometer-scale magnetic imaging of geological samples using a quantum diamond microscope", Geochemistry, Geophysics, Geosystems **18**, 3254 (2017).

[16] F. Casola, T. van der Sar, and A. Yacoby, "Probing condensed matter physics with magnetometry based on nitrogen-vacancy centres in diamond", Nature Reviews Materials **3**, 17088 (2018).

[17] N. Aslam et al., "Nanoscale nuclear magnetic resonance with chemical resolution", Science **357**, 67 (2017).

[18] I. Lovchinsky et al., "Magnetic resonance spectroscopy of an atomically thin material using a single-spin qubit", Science **355**, 503 (2017).

[19] J. P. Tetienne et al., "Quantum imaging of current flow in graphene", Science Advances **3**, e1602429 (2017).

[20] M. J. H. Ku et al., "Imaging viscous flow of the Dirac fluid in graphene", Nature **583**, 537 (2020).

[21] M. W. Doherty et al., "The nitrogen-vacancy colour centre in diamond", Physics Reports **528**, 1 (2013).

[22] A. Gruber et al., "Scanning Confocal Optical Microscopy and Magnetic Resonance on Single Defect Centers", Science **276**, 2012 (1997).

[23] P. Appel, M. Ganzhorn, E. Neu, and P. Maletinsky, "Nanoscale microwave imaging with a single electron spin in diamond", New Journal of Physics **17** (2015).

[24] D. D. Stancil and A. Prabhakar, *Spin waves* (Springer, 2009).

[25] T. Mueller and E. Malic, "Exciton physics and device application of two-dimensional transition metal dichalcogenide semiconductors", npj 2D Materials and Applications **2**, 29 (2018).

[26] N. Jones, "The information factories", Nature (2018).

[27] A. A. Serga, A. V. Chumak, and B. Hillebrands, "YIG magnonics", Journal of Physics D: Applied Physics **43**, 264002 (2010).

[28] A. V. Chumak, V. I. Vasyuchka, A. A. Serga, and B. Hillebrands, "Magnon spintronics", Nature Physics **11**, 453 (2015).

[29] P. Pirro, V. I. Vasyuchka, A. A. Serga, and B. Hillebrands, "Advances in coherent magnonics", Nature Reviews Materials (2021).

[30] K. Lee et al., "Superluminal-like magnon propagation in antiferromagnetic NiO at nanoscale distances", Nature Nanotechnology **16**, 1337 (2021).

[31] G. Csaba, A. Papp, and W. Porod, "Spin-wave based realization of optical computing primitives", Journal of Applied Physics **115**, 17C741 (2014).

[32] K. Vogt et al., "Realization of a spin-wave multiplexer", Nature Communications **5**, 3727 (2014).

[33] S. O. Demokritov et al., "Bose–Einstein condensation of quasi-equilibrium magnons at room temperature under pumping", Nature **443**, 430 (2006).

[34] G. Talmelli et al., "Reconfigurable submicrometer spin-wave majority gate with electrical transducers", Science Advances **6**, eabb4042 (2020).

[35] Q. Wang et al., "A nonlinear magnonic nano-ring resonator", npj Computational Materials **6**, 192 (2020).

[36] A. V. Chumak, A. A. Serga, and B. Hillebrands, "Magnon transistor for all-magnon data processing", Nature Communications **5**, 4700 (2014).

[37] J. J. Carmiggelt, B. G. Simon, I. Bertelli, and T. van der Sar, "Spinsensoren in diamant onthullen golvende spinzee", Nederlands Tijdschrift voor Natuurkunde (2021).

[38] D. D. Awschalom et al., "Quantum Engineering With Hybrid Magnonic Systems and Materials (Invited Paper)", IEEE Transactions on Quantum Engineering **2**, 1 (2021).

[39] J. R. Schaibley et al., "Valleytronics in 2D materials", Nature Reviews Materials **1**, 16055 (2016).

[40] K. F. Mak, K. He, J. Shan, and T. F. Heinz, "Control of valley polarization in monolayer MoS_2 by optical helicity", Nature Nanotechnology **7**, 494 (2012).

[41] T. Cao et al., "Valley-selective circular dichroism of monolayer molybdenum disulphide", Nature Communications **3**, 887 (2012).

[42] H. Zeng, J. Dai, W. Yao, D. Xiao, and X. Cui, "Valley polarization in MoS_2 monolayers by optical pumping", Nature Nanotechnology **7**, 490 (2012).

[43] X. Xu, W. Yao, D. Xiao, and T. F. Heinz, "Spin and pseudospins in layered transition metal dichalcogenides", Nature Physics **10**, 343 (2014).

[44] A. M. Jones et al., "Optical generation of excitonic valley coherence in monolayer WSe_2", Nature Nanotechnology **8**, 634 (2013).

[45] Z. Ye, D. Sun, and T. F. Heinz, "Optical manipulation of valley pseudospin", Nature Physics **13**, 26 (2017).

[46] D. Xiao, W. Yao, and Q. Niu, "Valley-contrasting physics in graphene: magnetic moment and topological transport", Phys. Rev. Lett. **99**, 236809 (2007).

[47] K. M. McCreary, M. Currie, A. T. Hanbicki, H.-J. Chuang, and B. T. Jonker, "Understanding Variations in Circularly Polarized Photoluminescence in Monolayer Transition Metal Dichalcogenides", ACS Nano **11**, 7988 (2017).

[48] G. Kioseoglou, A. T. Hanbicki, M. Currie, A. L. Friedman, and B. T. Jonker, "Optical polarization and intervalley scattering in single layers of MoS_2 and $MoSe_2$", Scientific Reports **6**, 25041 (2016).

[49] C. R. Zhu et al., "Exciton valley dynamics probed by Kerr rotation in WSe_2 monolayers", Phys. Rev. B **90**, 161302 (2014).

2

THEORETICAL AND EXPERIMENTAL FRAMEWORK

In this chapter we provide an overview of the theory and experimental techniques relevant for this thesis. We first describe the physics of nitrogen-vacancy (NV) centers in section 2.1 and discuss how we use them to detect microwave magnetic fields. Next we cover the basic theory behind spin waves in section 2.2. We derive the spin-wave dispersion from the Landau-Lifshitz-Gilbert equation, discuss how spin waves can be inductively excited using microwave antennae and describe the nonlinear effects that arise when spin waves are driven to large amplitudes. In section 2.3 we calculate the magnetic fields generated by spin waves and discuss how these fields can be experimentally detected using NV magnetometry and electrical spectroscopy measurements. Finally, we cover the theory behind valley polarization of excitons in section 2.4 and discuss how valley-polarized excitons could potentially be detected with NV centers.

2.1. NV MAGNETOMETRY OF MICROWAVES

Nitrogen-vacancy (NV) centers [1] are lattice defects in the carbon lattice of diamond, where two adjacent carbon atoms are substituted for a lattice vacancy and a nitrogen atom (Fig. 2.1a). NV centers can exist in two charge states: A charge neutral state (NV^0) and a negatively-charged state (NV^-), in which an electron is trapped by the vacancy. In this thesis we only consider NV^- centers, which we will denote as "NV centers" for conciseness.

The NV electronic structure can be described as a spin-triplet ground and excited state and intermediate spin-singlet states [2] (Fig. 2.1b). The electronic ground and excited states are connected by an optical transition with a zero-phonon line at 637 nm, which is accompanied by a phonon sideband both in the emission and absorption [3]. The phonon sideband allows spin-preserving excitation of the NV to its electronic excited state by absorbing a high-energy green photon (515 nm in our experiments) and emitting a phonon to compensate the excess energy. Vice versa, the NV can relax back to its electronic ground state by emitting a low-energy red photon (typically 650-800 nm), while emitting a second phonon.

In the electronic ground state, the electrons associated with the NV defect form an effective spin-1 system [1] ($S = 1$). NV-based microwave sensing relies on detecting microwave-driven transitions of the NV spin between $m_s = 0$ ($|0\rangle$) and $m_s = \pm 1$ ($|\pm 1\rangle$), where m_s indicates the spin projection along the NV quantization axis. The spin eigenstates are described by the Hamiltonian

$$H = DS_z^2 + \gamma \mathbf{B} \cdot \mathbf{S}, \tag{2.1}$$

with $\gamma = 28$ GHz/T the electronic gyromagnetic ratio, $\mathbf{B}$ a static magnetic bias field and S_i the ith spin-1 Pauli matrix (where $i \in \{x, y, z\}$). The Hamiltonian is given in the reference frame with z along the "NV axis" defined by the nitrogen atom and the vacancy, which can be oriented along one of the four diamond <111>-crystallographic axes (Fig. 2.1a). The first term describes the "zero-field splitting" due to spin-spin interactions, which split the $|0\rangle$ and $|\pm 1\rangle$ spin states in the electronic ground (excited) state by $D \approx 2.87$ GHz ($D_{\mathrm{ES}} \approx 1.42$ GHz). The second term describes the Zeeman interaction, which allows tuning the spin levels using a magnetic bias field.

When the bias field B_{NV} is applied along the NV axis, the energy difference between the $|0\rangle$ and $|\pm 1\rangle$ eigenstates is

$$f_{\mathrm{ESR}} = D \pm \gamma B_{\mathrm{NV}}. \tag{2.2}$$

Microwave magnetic fields at the electron spin resonance (ESR) frequencies f_{ESR} can drive transitions between between the $|0\rangle$ and $|\pm 1\rangle$ eigenstates. Transitions between $|-1\rangle$ and $|+1\rangle$ are magnetic dipole forbidden, but can be driven via mechanical strain [4] or electric fields [5].

NV centers occur in four different orientations in the diamond lattice, which each make a 71° angle with respect to the other three axes due to crystal symmetry. Therefore, when the bias field is applied along the axis of one NV family, the other families experience the

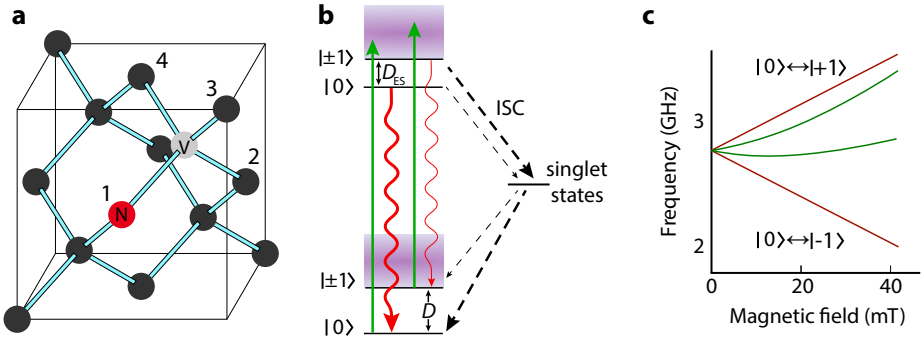

Figure 2.1: Structural, electronic and spin properties of NV centers in diamond. (**a**) Atomic structure of an nitrogen-vacancy (NV) center in the diamond carbon lattice (black spheres). NV centers exist in four lattice orientations (also called "families"), as indicated by the numbered lattice sites that the nitrogen atom can occupy with respect to the vacancy. (**b**) Electronic structure of an NV center, indicating the intermediate singlet states and the triplet ground and excited states with corresponding phonon side bands (purple shading). The green and wiggly red arrows indicate optical excitation and photoluminescence, respectively. (**c**) Ground state electron spin resonance (ESR) frequencies as a function of magnetic bias field applied along the NV axis (red lines). The other three NV families experience the same misaligned field such that they have degenerate ESR frequencies (green lines). Figures are adapted from [6].

same off-axis field, such that they have mixed eigenstates with the same ESR frequencies (Fig. 2.1c). The key property of NV centers is that resonantly-driven ESR transitions can be recorded optically via the spin-dependent NV photoluminescence, which enables the detection of microwave fields at the ESR frequencies, as described in the next section.

2.1.1. OPTICALLY DETECTED MAGNETIC RESONANCE

Instead of emitting a photon, an NV can also relax from the electronic excited state to the ground state via the optically-dark singlet states (Fig. 2.1b). This alternative decay channel has two crucial properties. First, it is spin-dependent. The NV has a larger chance to decay via the singlet states when it is in the $|\pm1\rangle$-state than in the $|0\rangle$-state [2, 7]. The NV spin state can thus be inferred by monitoring the NV photoluminescence, which is less bright in the $|\pm1\rangle$-state. Second, the singlet states decay preferentially towards $|0\rangle$, allowing initialization of the NV spin into $|0\rangle$ by repeatedly cycling between the ground- and excited state [8].

In an optically detected magnetic resonance (ODMR) measurement [9] both these properties are harnessed simultaneously to detect microwave magnetic fields at the ESR frequency. A continuous-wave green laser excites the NV centers, while the frequency of a microwave field is swept and the NV photoluminescence is recorded using a confocal microscope (Fig. 2.2a). Since the NV centers are continuously pumped into $|0\rangle$ by the optical excitation, the $|\pm1\rangle$-state only becomes significantly occupied when the microwave field $\mathbf{B}_{AC}$ is resonant with the corresponding $|0\rangle \leftrightarrow |\pm1\rangle$ ESR frequency. Therefore, dips in the NV photoluminesence are observed when the microwave frequency matches the ESR frequencies (Fig. 2.2b).

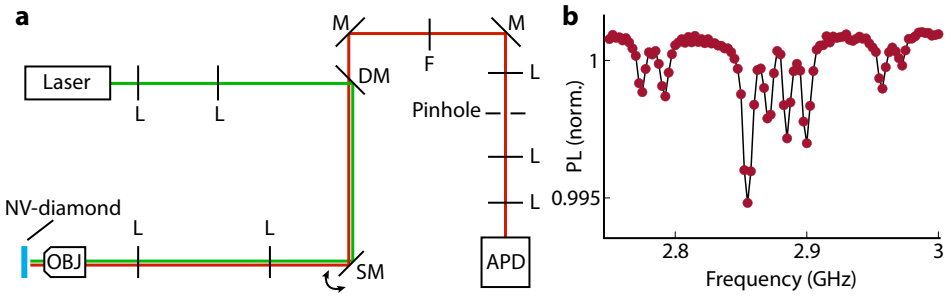

Figure 2.2: Optically detected magnetic resonance with NV centers in diamond. (**a**) Schematic overview of a confocal microscope used to readout the NV photoluminescence. A green laser (*Cobolt, 06-MLD*, $\lambda = 515$ nm) is focused to a diffraction-limited spot by an objective (OBJ, *Olympus, MPlanApo 50X*, NA= 0.95) after passing through a beam expander (two positive lenses (L)). A scanning mirror (SM, *Thorlabs, GVS212/M*) and another two lenses move the laserspot over the sample. The same objective collects the red NV photoluminescence, which is separated from the excitation by a dichroic mirror (DM, cutoff at 607 nm). The photoluminescence is long-pass filtered (F) and spatially filtered by a pinhole (diameter 50 µm) before it is collected by a avalange photodiode (APD, *Laser Components, COUNT-NIR-100*). (**b**) Example of an ESR photoluminescence (PL) spectrum for a small, misaligned bias field, such that eight photoluminescence dips corresponding to the two ESR transitions of the four NV families are visible. Figures are adapted from [6].

The depth of a photoluminescence dip ("the ESR contrast") is a measure for the magnitude of the microwave field at the ESR frequency. In the NV coordinate frame (with z along the NV axis) the ESR contrast $C^{\pm}$ for the $|0\rangle \leftrightarrow |\pm 1\rangle$ transition is expressed as [6, 10]

$$C^{\pm} = C_0 \frac{|B_{\mathrm{AC},\,x} \pm i B_{\mathrm{AC},\,y}|^2}{|B_{\mathrm{AC},\,x} \pm i B_{\mathrm{AC},\,y}|^2 + \Phi}, \tag{2.3}$$

where C_0 is the maximum ESR contrast in the limit of strong driving, $B_{\mathrm{AC},\,x(y)}$ are complex phasor components of the Jones vector describing the amplitude and polarization of $\mathbf{B}_{\mathrm{AC}}$ in the xy-plane and Φ is a parameter that depends on the optical excitation power and the NV spin coherence time. $|B_{\mathrm{AC},\,x} \pm i B_{\mathrm{AC},\,y}|$ corresponds to the right and left circular-polarized components of $\mathbf{B}_{\mathrm{AC}}$, indicating that the $|0\rangle \leftrightarrow |+1\rangle$ and $|0\rangle \leftrightarrow |-1\rangle$ ESR transitions are most efficiently driven by circularly-polarized microwave fields with opposite handedness in the plane perpendicular to the NV axis [11]. Linearly-polarized microwave fields drive both transitions equally, since they can be decomposed into two counter-rotating circularly-polarized fields.

Although the ESR contrast gives a qualitative estimate for the strength of the microwave drive field, it does not provide a quantitative measurement as often the value of Φ is not precisely known. In addition, it is of limited use when the drive fields are strong, since the contrast saturates towards C_0 when $|B_{\mathrm{AC},\,x} \pm i B_{\mathrm{AC},\,y}|^2 \gg \Phi$. Rabi oscillation measurements do not suffer from these limitations and enable quantitative, non-saturating measurements of the microwave magnetic field strength.

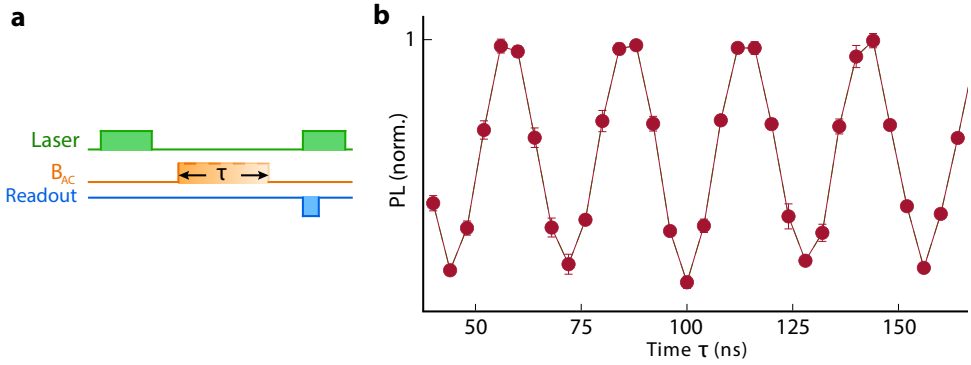

Figure 2.3: Rabi oscillations. (**a**) Pulse sequence used to measure Rabi oscillations. We first initialize the NV spin in the $|0\rangle$-state via a $\sim$ 1-µs green laser pulse, then we drive the spin using a microwave pulse of variable duration τ that is resonant with the $|0\rangle \leftrightarrow |\pm 1\rangle$ ESR frequency and finally we read out the NV photons in the first 300-400 ns of a second laser pulse. (**b**) Optically detected Rabi oscillations measured using the pulse sequence in (a), corresponding to a Rabi frequency of approximately 40 MHz. Figures are adapted from [6].

2.1.2. RABI OSCILLATIONS

In a Rabi measurement [12], we harness laser and microwave pulses to measure coherent NV spin rotations (Fig. 2.3a). When sweeping the duration of the microwave pulse (τ), we observe oscillations in the NV photoluminescence (Fig. 2.3b). These "Rabi oscillations" result from coherent rotations of the NV spin in the Bloch sphere between the $|0\rangle$ and $|\pm 1\rangle$ states.

Since the microwave amplitude determines the spin rotation speed, the Rabi oscillation frequency Ω_R is a quantitative measure for the microwave field strength, according to [6]

$$\Omega_R^{\pm} = \frac{\gamma}{\sqrt{2}} |B_{\mathrm{AC},\,x} \pm i B_{\mathrm{AC},\,y}|. \tag{2.4}$$

Here it is assumed that the microwave frequency is resonant with the ESR transition and the $\pm$-sign depends on the transition that is driven, similar as in Eq. 2.3. As the electronic gyromagnetic ratio is precisely known ($\gamma/2\pi$ = 28 GHz/T), the amplitude of the circular-polarized microwave component corresponding to the driven ESR transition can be quantitatively determined. Unlike the ESR contrast, the Rabi frequency does not saturate when strongly driven but continues increasing linearly with microwave amplitude.

2.1.3. STARK SHIFT

Both the ODMR and Rabi measurement schemes only allow detection of microwave frequencies that are within the linewidth of the ESR photoluminescence dip (typically ~10 MHz, c.f. Fig. 2.2b). Often a magnetic bias field B_{NV} is used to tune the ESR frequency into resonance with the frequency of interest. However, such a bias field can change the properties of e.g. magnetic or superconducting samples under study [13, 14], limiting its application in materials science and technology.

The dynamic (A.C.) Stark effect [15–17] can be used to detect microwave signals that are frequency detuned from the ESR by Δ. Such an off-resonant drive causes a "Stark shift" δf of the ESR frequency that increases the frequency difference between the ESR and the drive by

$$\delta f = \frac{\Omega_R^2}{4\Delta}, \tag{2.5}$$

with Ω_R the Rabi frequency at zero detuning. In contrast to the ODMR and Rabi measurement schemes, the Stark shift only provides insight in the ratio between amplitude of the drive and its frequency detuning. In addition, the Stark shift δf decreases rapidly for increasing frequency detunings Δ, requiring strong drive fields to probe far off-resonant frequencies.

In chapter 5 of this thesis we present a new measurement scheme for detecting off-resonant microwave frequencies, in which we use the nonlinear magnetization dynamics of a nearby magnetic film to convert detuned microwave frequencies to the ESR frequency. Very recently, two alternative off-resonant microwave detection protocols were reported that rely on frequency conversion by a magnetic microdisk [18] and quantum frequency mixing induced by nonlinear Floquet effects [19].

2.2. SPIN-WAVE THEORY

In this thesis we use NV centers and electrical spectroscopy to detect the microwave magnetic fields emitted by spin waves in magnetic materials. In this section we discuss the spin-wave theory required for interpreting the measurements in chapters 3-5.

In magnetic materials unpaired electron spins have a preferred orientation with respect to their neighbours as a result of the exchange interaction [20, 21]. Neighbouring spins are oriented parallel in a *ferromagnet* and antiparallel in an *antiferromagnet*. Spin waves are the collective, wave-like excitations of this magnetically ordered spin texture [20–23]. Magnons are the quasiparticle excitations of the spin-wave modes and correspond to spin flips in the magnetically ordered electronic spin lattice. Since electrons have spin 1/2, each spin flip changes the spin of the entire system by $S = 1/2 - (-1/2) = 1$, indicating that magnons are bosonic excitations. As such, they obey Bose-Einstein statistics in equilibrium and can form Bose-Einstein condensates [24–26], in which a large fraction of magnons occupies the magnon mode with the lowest energy.

Since a small magnetic dipole moment is associated to each spin and spin-wave excitations involve many spins, a macroscopic oscillating magnetic field is generated by spin waves in ferromagnets. In this work we detect this gigahertz field using NV magnetometry and electrical measurements, which provides important insights in the spin waves themselves. Magnetometry of antiferromagnetic spin waves remains beyond the scope of this thesis. Their magnetic field largely cancels due to the antiparallel spin alignment and their frequencies are typically in the terahertz range (THz, 1000 GHz), making them challenging to detect with electrical microwave devices or NV centers [27].

2.2.1. YTTRIUM IRON GARNET

One of the main challenges of working with spin waves is that they typically damp out quickly over short (micron) length scales. The spin-wave damping is parametrized by the phenomenological "Gilbert damping" parameter α_G [28]. Multiple spin-wave decay mechanism contribute to the total Gilbert damping. For instance, in metallic ferromagnets spin waves rapidly dissipate energy because their oscillating magnetic fields inductively drive Eddy currents in the film [29]. Furthermore, spin waves can lose energy by scattering into other spin-wave modes [29–31], phonons [32–34] or (magnetic) defects [29, 35, 36].

We detect spin waves in the model-magnet yttrium iron garnet [37] (YIG, $Y_3Fe_5O_{12}$). Of all known magnets, YIG has the lowest Gilbert damping (α_G can be as low as 10^{-4} for 10-nanometer thick films [38]), such that spin waves can propagate over millimeter distances. YIG is electrically insulating (so no Eddy currents!) and it can be grown in high-quality monocrystalline films using liquid phase epitaxy on lattice-matched gadolinium gallium garnet (GGG, $Gd_3Ga_5O_{12}$) substrates [38, 39]. Furthermore, YIG is ferrimagnetic, meaning that the iron spins inside its rather complicated, cubic unit cell are antiparallel aligned, but exhibit different magnetic moments. Therefore, each unit cell has an uncompensated magnetic moment, making the material effectively behave as a ferromagnet on length scales that are large compared to the inter-spin distance. The magnetic properties of YIG can be tuned by doping the material with other elements [40, 41]. This is the focus of study in chapter 5, where we study spin waves in gallium-doped YIG [42, 43].

2.2.2. SPIN WAVES IN THE MAGNETIC PLANE

We study spin waves in YIG thin films with in-plane wavelengths much larger than the film thickness. These spin waves have quantized mode profiles in the thickness direction resulting from the out-of-plane confinement [44, 45] (Fig. 2.4a). Typically we detect spin waves in the lowest ("zeroth") order mode, for which the magnetization amplitude is homogeneous along the thickness. Like all wave-like excitations, a key property of these (quasi) two-dimensional spin waves is the dispersion, which relates the spin-wave frequency to the spin-wave wavelength.

In general, the spin-wave frequency is determined by the coupling between spins on the scale of the spin-wave wavelength, where a stronger coupling leads to a higher frequency. In ferromagnets there exist two coupling mechanisms that operate on different length scales. First, the magnetic exchange interaction couples directly neighbouring spins (Fig. 2.4b). This interaction is isotropic in YIG, meaning that each spin couples equally strong to its neighbours in all directions. Second, spins are coupled over much longer length scales via their magnetic fields. This dipolar coupling is anisotropic, since every spin generates a strongly anisotropic magnetic field (see Fig. 2.4c, the field lines are non-spherical symmetric). Therefore, spins couple differently to spins located parallel to its orientation than perpendicular to it.

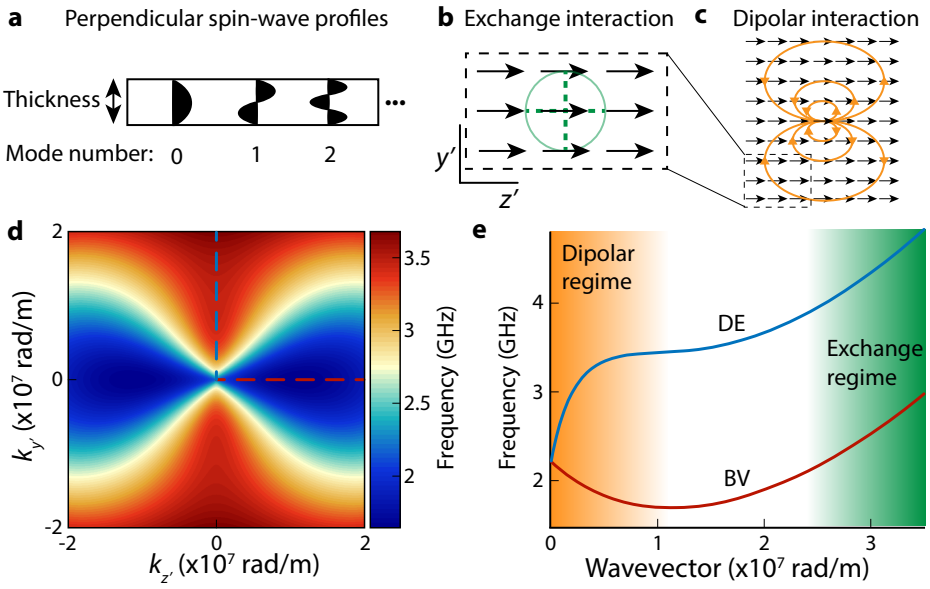

Figure 2.4: Spin-wave dispersion. (**a**) Sketch of the magnetization amplitude along the thickness of the magnetic film (black shading) for different perpendicular spin-wave modes. In this thesis we focus on spin waves in the zeroth mode. (**b, c**) Top-view sketches of the exchange and dipolar interactions between in-plane magnetized spins (black arrows). (**d**) Spin-wave dispersion in YIG at B_B = 30 mT calculated using Eq. 2.17. Due to the anisotropic dipolar interaction, the dispersion is anisotropic for long wavelengths, but becomes more isotropic for smaller wavelengths. (**e**) Linecuts indicated by the dashed lines with corresponding color in (d), showing the Damon-Eshbach (DE) and backward-volume (BV) dispersion. (d, e) are adapted from [6].

As a result of these interactions the spin-wave dispersion can be split up in two regimes depending on the spin-wave wavelength. The "dipolar regime" contains long-wavelength spin waves with frequencies set by the saturation magnetization M_s, which corresponds to the magnetic moment density in the sample. The "exchange regime" contains short-wavelength spin waves with frequencies determined by the exchange interaction, which is parametrized by the exchange constant α_{ex}.

The dispersion is anisotropic in the dipolar regime when the magnetization points in-plane due to the anisotropic dipolar coupling (Fig. 2.4d). Therefore, spin waves with a fixed, long wavelength have a different frequency when they propagate parallel to the magnetization (*backward volume spin waves*) than perpendicular to it (*Damon-Eshbach spin waves*). At shorter wavelengths the dispersion becomes increasingly more isotropic as the exchange interaction starts to dominate (Fig. 2.4e). The dipolar interaction is isotropic when the magnetization points out of the plane, such that the dispersion of *forward volume spin waves* is isotropic both in the dipolar and exchange regimes [46].

The spin-wave dispersion is given by the poles of the transverse magnetic susceptibility $\overleftrightarrow{\chi}$ [47], which relates the transverse magnetization amplitude $\mathbf{m}_T$ to a drive field

$\mathbf{B}_{\mathrm{AC}}$, according to

$$\mathbf{m}_{\mathrm{T}} = \overleftrightarrow{\chi}\mathbf{B}_{\mathrm{AC}}. \tag{2.6}$$

In the next section, we derive the magnetic susceptibility from the Landau-Lifshitz-Gilbert equation for a magnetic film in the xy-plane with perpendicular magnetic anisotropy (PMA) and a magnetic bias field $\mathbf{B}_B$ in an arbitrary direction. We neglect cubic magnetic anisotropy as it is relatively small in YIG films [38].

2.2.3. LANDAU-LIFSHITZ-GILBERT EQUATION

The Landau-Lifshitz-Gilbert (LLG) equation describes the dynamics of the unit magnetization vector $\mathbf{m}$ [28] (Fig. 2.5a)

$$\dot{\mathbf{m}} = -\gamma\mathbf{m}\times\mathbf{B} - \alpha_{\mathrm{G}}\dot{\mathbf{m}}\times\mathbf{m}, \tag{2.7}$$

where the "overdot" denotes the time derivative. We solve this equation in the (x',y',z') magnet frame that is tilted with respect to the (x,y,z) lab frame by an angle θ_0, such that the equilibrium magnetization points in the $\hat{\mathbf{z}}'$ direction and the $\hat{\mathbf{y}}^{(\prime)}$ axes overlap (Fig. 2.5b). $\mathbf{B} = \mathbf{B}_{\mathrm{eff}} + \mathbf{B}_{\mathrm{AC}}$, with $\mathbf{B}_{\mathrm{eff}}$ the effective magnetic field as derivative of the magnetic free energy density F

$$B_{\mathrm{eff},\alpha'} = -\frac{1}{M_{\mathrm{s}}}\frac{\partial F}{\partial m_{\alpha'}}, \tag{2.8}$$

where $\alpha' \in \{x',y',z'\}$ indicates the vector components in the magnet frame. The free energy density includes the Zeeman energy, the demagnetizing field $\mathbf{B}_{\mathrm{d}}$, the PMA energy F_{A}, and the exchange interaction

$$F = -M_{\mathrm{s}}\mathbf{m}\cdot(\mathbf{B}_B + \frac{\mathbf{B}_{\mathrm{d}}}{2}) + F_{\mathrm{A}} + \frac{D}{2}\sum_{\alpha,\beta=x,y,z}\left(\frac{\partial m_{\alpha'}}{\partial\beta}\right)^2. \tag{2.9}$$

In the magnet frame

$$F_{\mathrm{A}} = \frac{K}{2}m_z^2 = \frac{K}{2}(\sin\theta_0 m_{x'} + \cos\theta_0 m_{z'})^2, \tag{2.10}$$

such that the x' and z' components of the anisotropy effective field are

$$\begin{aligned} B_{\mathrm{A},x'} &= -\frac{1}{M_{\mathrm{s}}}\frac{\partial F}{\partial m_{x'}} = -\frac{K}{M_{\mathrm{s}}}(\sin^2\theta_0 m_{x'} + \cos\theta_0\sin\theta_0 m_{z'}),\\ B_{\mathrm{A},z'} &= -\frac{1}{M_{\mathrm{s}}}\frac{\partial F}{\partial m_{z'}} = -\frac{K}{M_{\mathrm{s}}}(\cos\theta_0\sin\theta_0 m_{x'} + \cos^2\theta_0 m_{z'}). \end{aligned} \tag{2.11}$$

The contributions of the Zeeman-, demagnetizing- and exchange energy to $\mathbf{B}_{\mathrm{eff}}$ have been derived in Refs. [29, 47].
In linear response with $m_{z'} \approx 1$, the LLG equation describes the transverse magnetization dynamics. In the frequency domain it reads

$$\begin{aligned} -i\omega m_{x'} &= -\gamma(m_{y'}B_{z'} - B_{y'}) + i\alpha_{\mathrm{G}}\omega m_{y'},\\ -i\omega m_{y'} &= \gamma(m_{x'}B_{z'} - B_{x'}) - i\alpha_{\mathrm{G}}\omega m_{x'}, \end{aligned} \tag{2.12}$$

where ω is the angular frequency. Substituting the components of the effective magnetic field and rewriting the equations in matrix form,

$$\begin{pmatrix} \omega_2 - i\alpha_G\omega & -\omega_1 + i\omega \\ -\omega_1 - i\omega & \omega_3 - i\alpha_G\omega \end{pmatrix} \begin{pmatrix} m_{x'} \\ m_{y'} \end{pmatrix} = \gamma \begin{pmatrix} B_{AC,x'} \\ B_{AC,y'} \end{pmatrix}, \tag{2.13}$$

where

$$\begin{aligned} \omega_0 &= -(\omega_M - \omega_K)\cos^2\theta_0 + \omega_B \cos(\theta_B - \theta_0) + \omega_D k^2, \\ \omega_1 &= \frac{1}{2}\omega_M f \sin(2\phi)\cos\theta_0, \\ \omega_2 &= \omega_0 + \omega_M f(\cos^2\phi\cos^2\theta_0 - \sin^2\theta_0) + (\omega_M - \omega_K)\sin^2\theta_0, \\ \omega_3 &= \omega_0 + \omega_M f \sin^2\phi, \end{aligned} \tag{2.14}$$

and $\omega_B = \gamma B_B$, $\omega_M = \gamma\mu_0 M_s$, $\omega_D = \frac{\gamma D}{M_s}$ and $\omega_K = \frac{\gamma K}{M_s}$. μ_0 is the vacuum permeability, $k = |\mathbf{k}| = \frac{2\pi}{\lambda}$ is the modulus of the wavevector along an angle ϕ with respect to the in-plane projection of the magnetization (with λ the spin-wave wavelength), θ_B is the angle of the magnetic bias field with respect to the plane normal (z axis), and $f = 1 - \frac{1-e^{-kt}}{kt}$ depends on the film thickness t. By inverting the matrix in Eq. 2.13, we obtain the transverse magnetic susceptibility tensor $\overleftrightarrow{\chi}$ (cf. Eq. 2.6)

$$\overleftrightarrow{\chi} = \frac{\gamma}{(\omega_2 - i\alpha_G\omega)(\omega_3 - i\alpha_G\omega) - \omega_1^2 - \omega^2} \begin{pmatrix} \omega_3 - i\alpha_G\omega & \omega_1 - i\omega \\ \omega_1 + i\omega & \omega_2 - i\alpha_G\omega \end{pmatrix}. \tag{2.15}$$

From the magnetic susceptibility we can derive a couple of important spin-wave properties, which we summarized below.

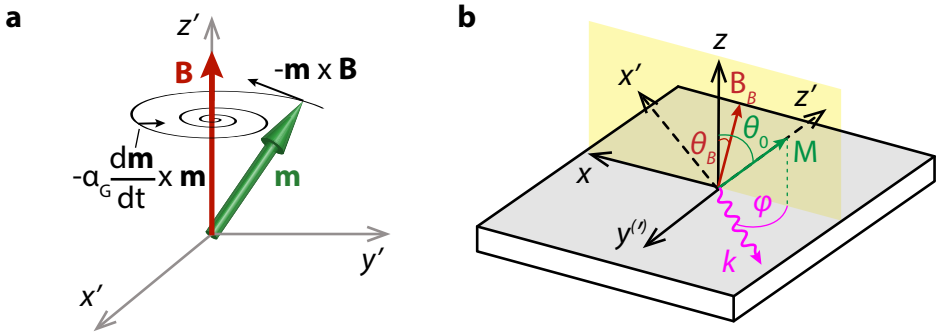

Figure 2.5: Magnetization precession described by the Landau-Lifshitz-Gilbert equation. (**a**) The magnetization rotates around **B** due to the first term in Eq. 2.7 and the precession is damped by the second term. In this sketch **B** is static, but in our experiments it is dynamic due to the drive field $\mathbf{B}_{AC}$, such that a steady-state spin-wave precession is maintained. (**b**) Sketch of the (x',y',z') magnet frame (black dashed arrows), which is rotated with respect to the (x,y,z) lab frame (black solid arrows) by an angle θ_0 along y, such that z' is parallel to the equilibrium magnetization (M, green arrow). θ_B is the angle of the bias field B_B with respect to the film normal and ϕ is the angle between spin-wave wavevector k and the in-plane projection of the magnetization. (a) is adapted from [6].

1. **The spin-wave dispersion.**
The susceptibility diverges when

$$\Lambda = (\omega_2 - i\alpha_G\omega)(\omega_3 - i\alpha_G\omega) - \omega_1^2 - \omega^2 = 0. \tag{2.16}$$

Assuming $\alpha_G \ll 1$, the real part of the solutions of this quadratic equation gives the spin-wave dispersion as the angular frequency ω versus k [44, 48]

$$\omega = \sqrt{\omega_2\omega_3 - \omega_1^2}. \tag{2.17}$$

2. **The FMR frequency.**
The spin-wave mode with infinite wavelength is called the ferromagnetic resonance (FMR) and corresponds to the uniform precession of the magnetization [49]. In measurements it often gives the largest signal as it can be driven to large amplitudes by spatially homogeneous (cavity or antenna) drive fields. By setting $k = 0$ in Eq. 2.17, we obtain the FMR frequency for an arbitrary field and magnetization orientation

$$f_{FMR} = \frac{\gamma}{2\pi} \sqrt{\left(B_B\cos(\theta_B - \theta_0) - (\mu_0 M_s - \frac{K}{M_s})\cos(2\theta_0)\right)\left(B_B\cos(\theta_B - \theta_0) - (\mu_0 M_s - \frac{K}{M_s})\cos^2(\theta_0)\right)}. \tag{2.18}$$

When both the magnetization and bias field point in-plane ($\theta_B = \theta_0 = \pi/2$)

$$f_{FMR(||)} = \frac{\gamma}{2\pi}\sqrt{B_B\left(B_B + \mu_0 M_s - \frac{K}{M_s}\right)}, \tag{2.19}$$

which is also known as Kittel's formula [21]. When both the magnetization and bias field point out-of-plane ($\theta_B = \theta_0 = 0$), we obtain

$$f_{FMR(\perp)} = \frac{\gamma}{2\pi}\left(B_B - \mu_0 M_s + \frac{K}{M_s}\right). \tag{2.20}$$

This equation only gives positive values when $B_B > \mu_0 M_s - \frac{K}{M_s}$, which corresponds to the requirement to overcome the demagnetizing field and lift the magnetization out-of-plane. As demonstrated in chapter 5, the saturation magnetization and magnetic anisotropy fields can be determined by measuring the FMR frequency with an in-plane and out-of-plane bias field. We also show how the Gilbert damping α_G can be extracted from the frequency dependence of the FMR magnetic-field linewidth ΔB_{FWHM} via [39, 50]

$$\Delta B_{FWHM} = \Delta B_0 + \frac{2\alpha_G}{\gamma_{||}}\omega_{FMR(||)}. \tag{2.21}$$

Here, ΔB_0 is the inhomogeneous broadening and the magnetic field is applied in the plane.

In general the FMR frequency increases with magnetic field when the magnetization points parallel to the field. The FMR is the spin-wave mode with the lowest frequency in the Damon-Eshbach configuration, but in the backward volume configuration also spin waves below the FMR exist (Fig. 2.4e). The backward volume mode with the lowest frequency is referred to as "the bottom of the spin-wave band" and its frequency increases with field, similar to the FMR. The frequency range below the bottom of the band is called "the spin-wave gap", since no spin-wave modes exist at these frequencies.

3. **The spin-wave decay length.**
The spin-wave decay length y_{decay} is given by the inverse of the imaginary part of the spin-wave wavevector k, according to

$$k = \frac{2\pi}{\lambda} + i\frac{1}{y_{\text{decay}}}, \tag{2.22}$$

with λ the spin-wave wavelength. This can be understood by substituting k into the spatial profile of the transverse magnetization

$$\mathbf{m}_{\text{T}} \propto e^{ikx} = e^{i2\pi\frac{x}{\lambda}} e^{-\frac{x}{y_{\text{decay}}}}. \tag{2.23}$$

We derive the decay length from the susceptibilty in k-space, which we find by Taylor expanding

$$\omega(k) \approx \omega(k_0) + \frac{\partial\omega}{\partial k}(k-k_0) = \sqrt{\omega_2\omega_3 - \omega_1^2} + v_{\text{g}}(k-k_0). \tag{2.24}$$

Here v_{g} is the group velocity of spin wave with wavevector k_0 and $\omega(k_0)$ is its angular frequency according to Eq. 2.17. Substituting Eq. 2.24 into Eq. 2.16 gives

$$\Lambda = 2\omega(k_0)\big(v_{\text{g}}(k-k_0) - i\alpha_{\text{G}}\frac{\omega_1+\omega_2}{2}\big) = 0, \tag{2.25}$$

where we only kept the first-order terms in α_{G} and $\delta k = k - k_0$. Solving this equation gives

$$k = k_0 + i\alpha_{\text{G}}\frac{\omega_1+\omega_2}{2v_{\text{g}}}, \tag{2.26}$$

such that decay length is given by

$$y_{\text{decay}} = \frac{2v_{\text{g}}}{\alpha_{\text{G}}(\omega_1+\omega_2)}. \tag{2.27}$$

We use this equation in chapter 5 to estimate the decay length of spin waves in gallium-doped YIG.

4. **The handedness of the magnetization precession.**
When electron spins are aligned to the externally applied bias magnetic field, the Larmor precession is counter-clockwise around the direction of the magnetic field.

For small wavelengths the magnetization in a magnet precesses circularly with the same handedness as can be deduced from Eq. 2.15 in the limit of large k, giving

$$\frac{m_{x'}}{m_{y'}} = \frac{B_{\mathrm{AC},x'}\omega_D k^2 - iB_{\mathrm{AC},y'}\omega_D k^2}{iB_{\mathrm{AC},x'}\omega_D k^2 + B_{\mathrm{AC},y'}\omega_D k^2}, \tag{2.28}$$

where we again used $\alpha_G \ll 1$. We obtain $m_{y'} = im_{x'}$, indicating that spin precession is always right-circularly polarized, independent from orientation of the spin-wave wavevector. When $B_{\mathrm{AC},x'} = iB_{\mathrm{AC},y'}$ the amplitudes of $m_{x'}$ and $m_{y'}$ become zero, indicating that only right-circular polarized magnetic fields can excite circularly-polarized, short-wavelength spin waves. This becomes important in section 2.2.4, where we discuss the excitation of spin waves using a microwave stripline. The spin precession of long-wavelength spin waves is influenced by the dipolar demagnetizing field generated by the other spins in the magnetic film, resulting in right-elliptically polarized spin precession.

5. **The spin-wave ellipticity.**
For in-plane magnetization ($\omega_1 = 0$), the ellipticity η of the long-wavelength spin-wave modes is given by the ratio of the elements in $\overleftrightarrow{\chi}$

$$\eta = \frac{|m_{x'}|}{|m_{y'}|} = \frac{|\chi_{x'x'}|}{|\chi_{y'x'}|} = \frac{|\chi_{x'y'}|}{|\chi_{y'y'}|} = \sqrt{\frac{\omega_3}{\omega_2}}, \tag{2.29}$$

where we have set $\alpha_G = 0$. The ellipticity is important, as it has a large influence on the magnetic field that is generated by the spin waves (see section 2.3.1).

The orientation of the equilibrium magnetization minimizes the free energy F (Eq. 2.9) and is found by numerically solving $\frac{\partial F}{\partial \theta_0}(\theta_B) = 0$ (in absence of any in-plane anisotropy, the in-plane angle of $\mathbf{B}_B$ and $\mathbf{m}$ overlap). For a magnetic film the magnetization is pushed in the plane by the demagnetizing field, which is given by M_s [51] (~ 175 mT in YIG). Only when a magnetic bias field or a PMA field overcomes the demagnetizing field, the magnetization points fully out-of-plane, as is the case in chapter 5.

2.2.4. SPIN-WAVE EXCITATION

At finite temperature, spin waves are always present in a magnet as a result of thermal excitation. At room temperature the spin-wave band is occupied according to the Rayleigh-Jeans distribution [52], which is the high-temperature limit of the Bose-Einstein distribution. These thermal spin waves are referred to as "spin-wave noise", as they span a continuum of frequencies and are incoherent, meaning that their phase fluctuates rapidly over time. Driving the FMR raises the spin chemical potential and thus increases the thermal spin-wave occupation. Incoherent, broadband spin waves can also be injected via the spin Hall effect by running a DC current through a metal with a large spin-orbit coupling, such as platinum [53].

In this thesis we use a microwave drive field to excite propagating, coherent spin waves with a well-defined frequency and phase that are locked to the drive [54]. This microwave magnetic field is generated by an oscillating microwave current in a narrow microstrip fabricated on top of the magnet. Monochromatic spin-waves can also be excited

using other techniques, e.g. via surface acoustic waves [55] or light pulses [56].

The spin-wave excitation efficiency is determined by the wavevector overlap between the target spin-wave mode and the drive field [57–62]. This can be understood intuitively by realizing that a spatially homogeneous drive field is very inefficient in exciting spin waves with a very small wavelength as their spatial profiles do not overlap. Since the width of the stripline sets the spatial confinement of the drive field, generally only spin-wave wavelengths larger than the width are efficiently excited. In chapter 5 we experimentally verify this by using striplines with different widths for spin-wave excitation.

For a stripline along x and with z out-of-plane (from now on called "the lab coordinate frame") the magnetic-field vector components generated by a straight microstrip of width w, thickness δ and length l have an oscillating profile in k-space [6, 13]

$$B_{\mathrm{AC},z(y)}(z;k_y,k_x) = 2i\mu_0 J(\omega)\frac{e^{-ik_z z}}{k_z}\frac{e^{ik_z\delta}-1}{k_{z(y)}}\sin\left(k_y\frac{w}{2}\right)\frac{\sin(k_x l/2)}{k_x}, \tag{2.30}$$

where $J(\omega)$ is the current density at an angular frequency ω. At gigahertz frequencies $k = \sqrt{k_x^2+k_y^2+k_z^2} = \omega/c \ll 100\,\mathrm{rad/m}$, whereas in our experiments the spin-wave wavenumbers are in the range of 10^5-10^7 rad/m. Therefore, we may approximate $k_z = \sqrt{k^2-k_y^2-k_x^2} \approx i\sqrt{k_y^2+k_x^2} = i\kappa$, with κ the norm of the spin-wave wavevector, such that

$$\begin{aligned} B_{\mathrm{AC},z}(z;k_y,k_x) &= -2i\mu_0 J(\omega)e^{\kappa z}\frac{e^{-\kappa\delta}-1}{\kappa^2}\sin\left(k_y\frac{w}{2}\right)\frac{\sin(k_x l/2)}{k_x}, \\ B_{\mathrm{AC},y}(z;k_y,k_x) &= 2\mu_0 J(\omega)e^{\kappa z}\frac{e^{-\kappa\delta}-1}{\kappa k_y}\sin\left(k_y\frac{w}{2}\right)\frac{\sin(k_x l/2)}{k_x}. \end{aligned} \tag{2.31}$$

The drive field is inefficient in exciting short wavelengths parallel to the stripline as in this direction its amplitude falls off rapidly in k-space (Fig. 2.6a, green line). For wavevectors perpendicular to the stripline, it is inefficient in exciting wavelengths that fit an integer times in its width, as represented by the nodes in the spectrum (red line). In practice spin-waves in the second maximum of the spectrum are still excited with a significant amplitude (see chapter 5). By using magnetic coplanar waveguides [63] or magnetic nanowire gratings [64] spin-wave wavelengths much smaller than the antenna width can be excited efficiently.

Importantly, the Fourier components of the drive field corresponding to wavevectors perpendicular to the striplines ($k = k_y$) are circularly-polarized with a chirality locked to the sign of the momentum (Fig. 2.6b). This reflected by the relation

$$B_{\mathrm{AC},z} = -iB_{\mathrm{AC},y}k_y/\kappa = -i\,\mathrm{sgn}(k_y)B_{\mathrm{AC},y}. \tag{2.32}$$

For clarity we note that, even though drive field curves circularly around the stripline, it is *linearly* polarized at every point in space. However, as discussed before, any linear

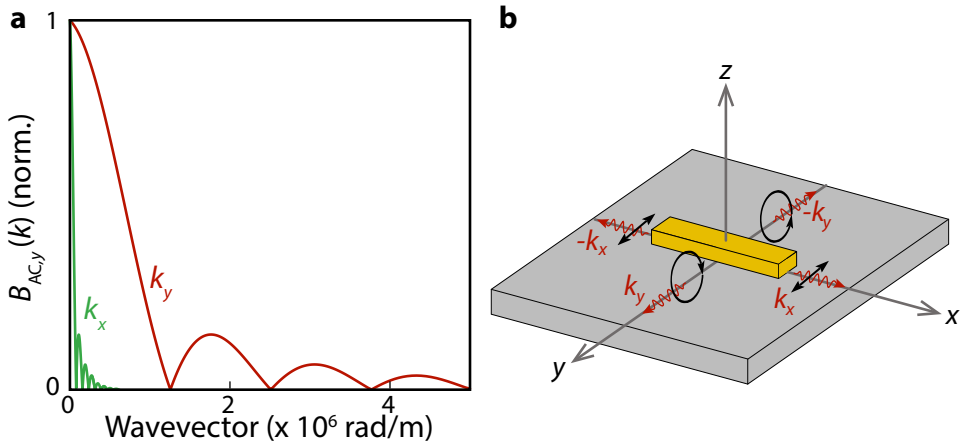

Figure 2.6: Amplitude and polarization of the stripline-field in Fourier space. (**a**) Normalized Fourier amplitude of the drive field calculated for a stripline with length $l = 100$ µm (along x) and width $w = 5$ µm (along y). (**b**) Sketch of the stripline-field polarization (black arrows) that couple to the different spin-wave wavevectors. Figures are adapted from [6].

polarized field can be decomposed in two *circularly*-polarized fields with opposite handedness. Since spin-wave modes only couple to the Fourier component of the drive field corresponding to their wavevector, Eq. 2.32 shows that opposite spin-wave wavevectors perpendicular to the stripline are driven by circular-polarized drive field components of opposite handedness. Wavevectors parallel to the stripline ($k = k_x$) are driven by the linear drive in the y direction, since then $B_{AC,z} = 0$.

According to the magnetic susceptibility (Eq. 2.15), spin waves are excited by the stripline-field components perpendicular to the equilibrium magnetization. We now review the spin-wave excitation for in-plane magnetization parallel and perpendicular to the stripline.

1. **Damon-Eshbach configuration.**
   In this configuration the bias field and magnetization are parallel to the stripline (along x), such that Damon-Eshbach spin waves ($k = k_y$) are excited by circularly-polarized drive fields with opposite handedness for $\pm k_y$. By combining Eqs. 2.32 and 2.15, we find a scaling of the magnetization amplitude

$$m_y(\pm k_y) \propto i\omega B_{AC,z}(\pm k_y) + \omega_2 B_{AC,y}(\pm k_y) = B_{AC,y}(\omega_2 \pm \omega) = B_{AC,y}\omega_2(1 \pm \eta), \quad (2.33)$$

   where we used in the last step the expressions for the ellipticity $\eta = \sqrt{\frac{\omega_3}{\omega_2}}$ (Eq. 2.29) and the spin-wave frequency $\omega = \sqrt{\omega_2\omega_3} = \omega_2\eta$ (Eq. 2.17, $\omega_1 = 0$ for $\phi = \pi/2$). Clearly, the momentum-locking of the drive field's chirality leads to highly anisotropic spin-wave excitation. Circularly-polarized spin-waves ($\eta = 1$) with negative wavevector are not excited by the stripline field, whereas positive wavevectors are efficiently excited. For elliptically-polarized spin waves the excitation efficiency becomes more symmetric. In contrast, the excitation of (long-wavelength) backward-

volume spin waves ($k = k_x$) is symmetric, since they are driven by a linear field

$$m_y(\pm k_x) \propto \omega_2 B_{\mathrm{AC},y}. \tag{2.34}$$

2. **Backward-volume configuration.**
In this configuration the bias field and magnetization are in-plane perpendicular to the stripline (along y), such that only the out-of-plane component of the circular-polarized drive field couples to backward volume spin waves ($k = k_y$), resulting in a symmetric spin-wave amplitude

$$m_x(\pm k_y) \propto i\omega B_{\mathrm{AC},z}. \tag{2.35}$$

Long-wavelength Damon-Eshbach spin waves are not excited by the stripline, since the linear drive field $B_{\mathrm{AC},y}$ is parallel to the magnetization and thus does not couple to it,

$$m_x(\pm k_x) = 0. \tag{2.36}$$

2.2.5. NONLINEAR SPIN WAVES

When driven to large amplitudes, spin waves exhibit nonlinear behaviour [54]. In this thesis we study several nonlinear spin-wave processes, which we briefly introduce below.

MAGNON-MAGNON SCATTERING

Spin waves scatter with each other at large densities. These scattering processes conserve energy and momentum, and are described by the magnon-magnon interaction (mmi) terms in the spin-wave Hamiltonian [65]

$$\begin{aligned} H_{\mathrm{mmi}} = & \\ & \sum_{k_1,k_2,k_3} T_{k_1,k_2,k_3} c_{k_1} c^\dagger_{k_2} c^\dagger_{k_3} \delta(k_1 - k_2 - k_3) \\ & + \sum_{k_1,k_2,k_3,k_4} W_{k_1,k_2,k_3,k_4} c_{k_1} c_{k_2} c^\dagger_{k_3} c^\dagger_{k_4} \delta(k_1 + k_2 - k_3 - k_4). \end{aligned} \tag{2.37}$$

Here $c^{(\dagger)}$ is the magnonic annihilation (creation) operator and the Kronecker delta ensures conservation of momentum. As observed in the electrical spectroscopy measurements of chapter 3, three-magnon scattering (represented by the first term in the Hamiltonian) is very efficient [29], leading to a rapid decay of magnons with frequency ω_1 into two other magnon with frequency $\omega_2 + \omega_3 = \omega_1$. However, no magnon modes are available when ω_2 and ω_3 are below the minimum of the spin-wave band ω_{BM}, such that the process only occurs when $\omega_1 > 2 \cdot \omega_{\mathrm{BM}}$. When $\omega_1 < 2 \cdot \omega_{\mathrm{BM}}$ four-magnon scattering is the dominant scattering process [30, 31], which we harness in chapter 4 to realize broadband microwave sensing with NV centers. Spin waves can also scatter efficiently to the first perpendicular spin-wave mode when the bands of the zeroth and first perpendicular modes cross, as observed in chapters 3 and 4.

FMR FOLDOVER

The magnetization precession associated to spin waves reduces the static, longitudinal component of the magnetization. Therefore, the effective saturation magnetization M_s decreases with the spin-wave amplitude, according to

$$M_s = M_s^0 \sqrt{1 - |m_T|^2}, \tag{2.38}$$

where M_s^0 is the saturation magnetization without spin waves in the sample and m_T is the transverse component of the unit magnetization. Since the spin-wave frequency depends on M_s via the dispersion (Eq. 2.17), it changes with increasing spin-wave amplitude. The FMR typically experiences the largest frequency shifts, since it can be driven to large amplitudes most efficiently.

At large amplitudes the frequency shift results in the foldover of the FMR [66–68], similar to a Duffing oscillator. In this case the FMR amplitude is bistable in a certain frequency window, where it follows a low- or high-amplitude branch depending on the excitation frequency sweep direction. In practice the FMR amplitude is limited by decay into other spin-wave modes via Suhl instabilities [69–72]. As such, the strongest hysteresis of the FMR amplitude has been observed in nanomagnets [68], where the confined geometry strongly reduces the spin-wave density of states, limiting the available decay channels. In the Hamiltonian formalism the frequency shift of the FMR is caused by the four-magnon self-interaction term, as discussed in Ref. [65] and chapter 5.

2.3. SPIN-WAVE DETECTION

There are various experimental methods to detect spin waves. Optical techniques such as Brillouin light scattering (BLS) [73] and magneto-optical Kerr microscopy [74, 75] allow table-top imaging of broadband spin waves at picosecond timescales with a diffraction-limited spatial resolution set by the wavelength of the photons. X-ray scattering at synchrotron facilities uses radiation with nanometer wavelengths, providing a view on spin waves with nanoscale wavelengths [76]. In this thesis, we detect spin waves using electrical spectroscopy measurements and NV magnetometry.

2.3.1. NV MAGNETOMETRY OF SPIN WAVES

NV magnetometry could in principle provide nanoscale resolution in a table-top setup over a wide temperature range [8, 77, 78]. To this end, a single NV center is integrated in an atomic force microscope (AFM) and scanned over a sample of interest, while reading out its photoluminescence [79]. We use a different measurement geometry, in which we place a diamond membrane containing a near-surface NV layer directly on top of a sample (see the cover of this thesis) and readout the photoluminescence by scanning the excitation laser over the diamond surface. This enables diffraction-limited imaging of spin waves using a confocal microscope setup (Fig. 2.1d).

Compared to optical techniques, NV magnetometry has the advantage that it enables quantitative imaging of DC and gigahertz magnetic-field profiles by monitoring the spatial dependence of the ESR and Rabi frequency. It also allows imaging of magnetization

patterns that are hidden underneath optically opaque materials [29].

In the lab frame with the equilibrium magnetization pointing in the plane along x, the stray magnetic field above a magnetic film with thickness t generated by a spin wave is given by [6, 13]

$$\begin{aligned}
B_{\mathrm{SW},z}(z;\mathbf{k}) &= \frac{\mu_0 M_s}{2} e^{-kz}(1-e^{-kt})\left(-m_z(\mathbf{k}) + i\sin\phi m_y(\mathbf{k})\right) \\
&= B^0_{\mathrm{SW}} m_y(\mathbf{k}) i\left(\eta + \sin\phi\right), \\
B_{\mathrm{SW},y}(z;\mathbf{k}) &= \frac{\mu_0 M_s}{2} e^{-kz}(1-e^{-kt})\left(i\sin\phi m_z(\mathbf{k}) + \sin^2\phi m_y(\mathbf{k})\right) \\
&= B^0_{\mathrm{SW}} m_y(\mathbf{k})\left(\eta\sin\phi + \sin^2\phi\right), \\
B_{\mathrm{SW},x}(z;\mathbf{k}) &= \frac{\mu_0 M_s}{2} e^{-kz}(1-e^{-kt})\left(i\cos\phi m_z(\mathbf{k}) + \frac{1}{2}\sin(2\phi) m_y(\mathbf{k})\right) \\
&= B^0_{\mathrm{SW}} m_y(\mathbf{k})\left(\eta\cos\phi + \frac{1}{2}\sin(2\phi)\right).
\end{aligned} \tag{2.39}$$

Below the film the spin-wave field is given by the complex conjugate of the first expression. In the second expression we substituted $m_z = -i\eta m_y$ and $B^0_{\mathrm{SW}} = \frac{\mu_0 M_s}{2} e^{-kz}(1-e^{-kt})$. Using $\sin\phi = k_y/k$ and $\cos\phi = k_x/k$, we find

$$\begin{aligned}
B_{\mathrm{SW},y} &= -i(k_y/k) B_{\mathrm{SW},z}, \\
B_{\mathrm{SW},x} &= -i(k_x/k) B_{\mathrm{SW},z}.
\end{aligned} \tag{2.40}$$

Clearly, the field is circularly polarized in the yz plane for Damon-Eshbach spin waves ($k = k_y$) and in the xz plane for backward volume spin waves ($k = k_x$), with opposite handedness for opposite wavevectors.

The spin waves generate an evanescent field with a transverse spin angular momentum, since the axis around which the polarization rotates is perpendicular to the propagation direction [80, 81]. In contrast, free-space photons only have a longitudinal spin component with an electromagnetic field oriented *perpendicular* to the propagation direction [82]. Electromagnetic fields with transverse spin can exist (i.e., obey Maxwell's equations) when light is spatially confined, for instance in plasmonic systems [83] or photonic crystal waveguides [84, 85]. A similar confinement is established by spin waves, as the spin-wave wavelength (~micrometers) is much smaller than the wavelength of free-space microwave radiation (~millimeters).

The ESR transitions of NV centers are driven by circularly-polarized fields in the plane perpendicular to the NV axis (Eq. 2.4). Compared to the lab frame, the NV coordinate frame is rotated around y by $\theta_{\mathrm{NV}} = 35.3°$, such that the NV axis is parallel the x' axis. Even though a static bias field is applied along the NV axis in our experiments, the magnetization points approximately along x as it is pushed in the plane by the demagnetizing field

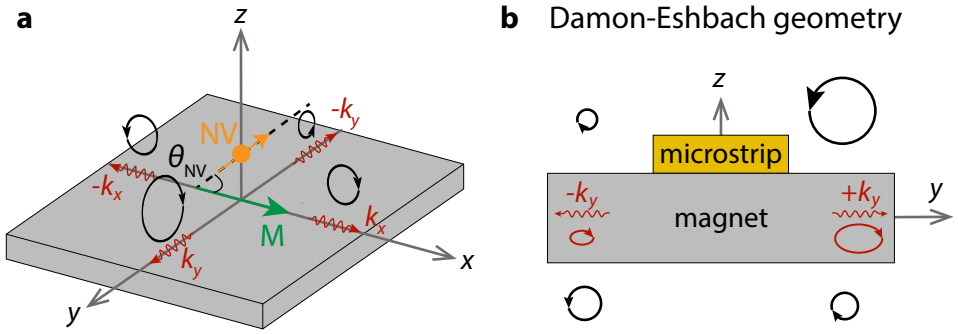

Figure 2.7: Momentum-locked handedness of the spin-wave field. (**a**) Sketch of the spin-wave magnetic field polarization for different wavevectors. The magnetization M (green arrow) points along x and the NV is sensitive to circularly-polarized fields perpendicular to its axis (orange arrow), which tilted out of plane with respect to the magnetization by an angle θ_{NV}. (**b**) Side-view sketch of magnetization (red) and magnetic-field (black) polarization in the Damon-Eshbach geometry with the magnetization parallel to the excitation stripline (yellow rectangle). Due to the momentum-locked chirality of the drive field elliptically-polarized Damon-Eshbach spin waves are more efficiently excited in the positive y direction. For opposite wavevectors the field has an opposite handedness and is larger at opposite sides of the magnetic film.

(Fig. 2.7a). In the NV frame, the spin-wave magnetic fields are thus given by

$$\begin{aligned} B_{SW,z'} &= B_{SW,z}\cos\theta_{NV} - B_{SW,x}\sin\theta_{NV}, \\ B_{SW,y'} &= B_{SW,y}, \\ B_{SW,x'} &= B_{SW,x}\cos\theta_{NV} + B_{SW,z}\sin\theta_{NV}, \end{aligned} \tag{2.41}$$

where the expressions for the spin-wave field in the lab frame are given by Eqs. 2.39. Therefore, when driving the $|0\rangle \leftrightarrow |\pm 1\rangle$ ESR transition, the Rabi frequency caused by the spin-wave magnetic field is given by

$$\Omega_R^{\mp} = \frac{\gamma}{\sqrt{2}}|B_{AC,\,z'} \pm i B_{AC,\,y'}| = \frac{\gamma}{\sqrt{2}}|B_{SW,z}\cos\theta_{NV} - B_{SW,x}\sin\theta_{NV} \pm i B_{AC,\,y}|. \tag{2.42}$$

By substituting the expressions for the spin-wave fields into Eq. 2.42, we obtain a few interesting cases (Fig. 2.7a).

1. **Backward volume spin waves.**
   For $\phi = 0$ and $\phi = \pi$ the spin-wave wavevector is parallel to the magnetization and the spin-wave driven Rabi frequency is given by

   $$\Omega_R^{\mp} = |\frac{\gamma}{\sqrt{2}} B_{SW}^0 m_y(\mathbf{k})\eta|. \tag{2.43}$$

   Clearly, both $|0\rangle \leftrightarrow |\pm 1\rangle$ ESR transitions are driven equally. This is expected, since the projection of the circularly-polarized field generated by backward volume spin waves is a linearly-polarized field in the plane perpendicular to the NV axis, which can be decomposed in two counter-rotating fields that each drive an ESR transition.

2. **Damon-Eshbach spin waves.**
Damon-Eshbach spin waves are called "surface spin waves" [86, 87], as their amplitude decays exponentially with depth, such that in thick magnetic films they are confined to either the upper or lower surface depending on their propagation direction. Even though in practice the surface confinement can be neglected when the spin-wave wavelength is much larger than the film thickness, Damon-Eshbach spin waves are said to be "chiral", meaning that their chirality index Z is fixed and always equal to 1 [81]

$$Z = \hat{n} \cdot (\hat{M} \times \hat{k}) = 1. \tag{2.44}$$

Here, $\hat{M}$ indicates the unit static magnetization direction, $\hat{k}$ the unit spin-wave wavevector and $\hat{n}$ is the unit normal of the surface that the spin wave is confined to. As a result of the chirality, circularly-polarized Damon-Eshbach spin waves generate only a magnetic field at one side of the film depending on the spin-wave momentum and magnetization direction (the transverse magnetization corresponds to a Halbach array [88]). Therefore, the Rabi frequency induced by Damon-Eshbach spin waves ($\phi = \pm\pi/2$) strongly depends on the sign of its wavevector. We consider both cases separately below.

- $\phi = \pi/2$ **(positive k_y)**
The Rabi frequency is given by

$$\Omega_R^{\mp} = |\frac{\gamma}{\sqrt{2}} B_{\mathrm{SW}}^0 m_y(\mathbf{k})(\eta + 1)(\cos\theta_{\mathrm{NV}} \pm 1)|. \tag{2.45}$$

If the NV would be only sensitive to fields in the zy-plane ($\theta_{\mathrm{NV}} = 0$), only the $|0\rangle \leftrightarrow |-1\rangle$ transition is driven. The field does not couple to the $|0\rangle \leftrightarrow |+1\rangle$ due to its chirality. The Rabi frequency decreases when the spin precession becomes more elliptical.

- $\phi = -\pi/2$ **(negative k_y)**
The Rabi frequency is given by

$$\Omega_R^{\mp} = |\frac{\gamma}{\sqrt{2}} B_{\mathrm{SW}}^0 m_y(\mathbf{k})(\eta - 1)(\cos\theta_{\mathrm{NV}} \mp 1)|. \tag{2.46}$$

In this case only the $|0\rangle \leftrightarrow |+1\rangle$ transition is driven for $\theta_{\mathrm{NV}} = 0$, since the chirality of the field has reversed. Also the field entirely disappears for circularly-polarized spin waves ($\eta = 1$). These spin waves only produce a magnetic field *below* the film. The missing mode overlap of the magnetic fields generated by counterpropagating Damon-Eshbach spin waves is expected to give rise to backscattering immunity [36, 89]. Elliptically-polarized spin waves also contain a clockwise precessing spin component (in addition to the usual counterclockwise component), which generates a field with opposite handedness *above* the film that drives the $|0\rangle \leftrightarrow |+1\rangle$ transition (Fig. 2.7b).

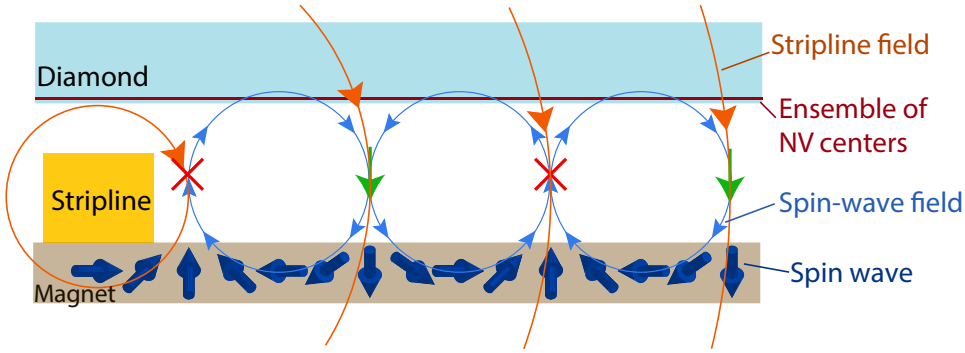

Figure 2.8: Phase contrast via interference of the spin-wave field and a reference field. We achieve phase-sensitive imaging by letting the spin-wave field interfere with a spatially-homogeneous reference field (in this sketch, the field of the excitation stripline). The interference results in a standing-wave in the magnitude of microwave field above the film, which is imaged by NV sensors. Figure is adapted from [90].

Summarizing, Damon-Eshbach spin waves drive the NV $|0\rangle \leftrightarrow |-1\rangle$ ESR transition only efficiently at the one side of a stripline [91], as a combined result of

(a) the asymmetric spin-wave excitation efficiency of the stripline drive field,

(b) the momentum-locked handedness of the spin-wave field,

(c) the confinement of the spin-wave field above and below the magnetic film.

Although the phase of the spin-wave field $\mathbf{B}_{\mathrm{SW}}$ changes in space with the spin-wave wavelength (according to Eqs. 2.39, $\mathbf{B}_{\mathrm{SW}} \propto m_y(\mathbf{k}) \propto e^{i\mathbf{k}\cdot\mathbf{r}}$, with $\mathbf{r}$ the real-space vector), the Rabi frequency does not allow imaging the spin-wave wavefronts since it is only sensitive to the *magnitude* of the drive field. In our experiments we obtain a finite phase contrast by letting the spin-wave field interfere with a reference field $\mathbf{B}_{\mathrm{REF}}$ that has a constant phase in space [13, 36]. The stripline drive field can serve as a reference field (Fig. 2.8), but it decays inversely on the scale of the stripline width, preventing phase-imaging over large areas. By sending microwaves through a bonding wire spanned over the sample a large-area reference field can be created, as is done in chapter 3.

2.3.2. PROPAGATING SPIN WAVE SPECTROSCOPY

Measurements of the spin-wave-mediated microwave transmission between two striplines can provide insight in the spin-wave dispersion without requiring an optical setup [57–62]. Such electrical spectroscopy measurements can complement NV magnetometry measurements by providing an estimate for the expected spin-wave wavelength at the ESR frequencies. For these measurements two parallel striplines are fabricated on top of a magnet and connected to the ports of a vector network analyzer (VNA, Fig. 2.9a). This device performs a lock-in measurement of the microwave transmission between the striplines by sweeping the frequency of a microwave voltage V_1 at port 1 and measuring the phase and amplitude of the retrieved signal V_2 at port 2.

Even when the microstrips are not physically connected, a finite microwave voltage $V_2 = \Sigma$ is detected due to the parasitic inductive and capacitive coupling between the striplines.

The detected voltage changes when the microwave frequency becomes resonant with spin-wave modes in the magnet. The magnetic field generated by the microwaves in the first stripline excites spin waves that propagate towards the second stripline, where their oscillating magnetic fields inductively induces a voltage σ. Spin waves with wavevectors perpendicular to the striplines generate the largest voltages, since the efficiency of both the inductive excitation *and* detection are proportional to the Fourier amplitude of the stripline magnetic field at the spin-wave wavevector (Eq. 2.30, Fig. 2.6a). Typically the largest signal is obtained in the Damon-Eshbach configuration with the bias field oriented such that the direction of efficient spin-wave excitation is towards the second stripline [62]. The spin-wave-induced microwave voltage σ interferes with the voltage generated by the direct parasitic coupling Σ, resulting in oscillations in the frequency-dependent microwave transmission.

The interference can best be understood using a phasor representation of the parasitic and spin-wave microwave voltages (Fig. 2.9b). Each voltage $\{\Sigma,\sigma\}$ is represented by a vector in the complex plane, where the length $\{\Sigma_0,\sigma_0\}$ and angle $\{\Theta,\theta\}$ of the vector corresponds to the amplitude and phase of the voltage, respectively. The length of the vector sum of both components gives the normalized microwave transmission $|S_{21}|$ measured by the VNA

$$|S_{21}| = |\frac{V_2}{V_1}| = |\frac{\Sigma+\sigma}{V_1}| = \frac{1}{V_1}|\Sigma_0 e^{i\Theta} + \sigma_0 e^{i\theta}|, \tag{2.47}$$

in which we defined V_1 to be real and positive in the last step. As the parasitic coupling is typically large compared to the spin-wave signal, we represent it as a long vector along the positive real axis. The spin-wave signal is a small vector pointing in an arbitrary direction, since its phase is generally different than that of the parasitic signal.

When the microwave frequency ω is swept by the VNA, the phase of the parasitic signals changes due to the changing microwave wavelength λ_{MW} in the cables connecting the striplines, according to

$$\Theta \propto 2\pi\frac{L}{\lambda_{MW}} \propto \frac{\omega}{c}L, \tag{2.48}$$

where c is the speed of light and L is the electric length between the VNA ports. The spin-wave-mediated microwave signal experiences the same phase shift, such that the changing microwave wavelength does not influence the *relative* phase between both signals and therefore it does not change the interference. In contrast, the changing spin-wave wavelength λ_{SW} with frequency (Eq. 2.17) leads to a different spin-wave phase at the position of the second stripline without changing the phase of the parasitic signal. Therefore, the phase of the spin-wave signal has two contributions

$$\theta \propto 2\pi\frac{L}{\lambda_{MW}} + 2\pi\frac{s}{\lambda_{SW}(\omega)} \tag{2.49}$$

where s is the separation distance between the striplines. The measured microwave transmission is thus proportional to

$$|S_{21}| \propto |\Sigma_0 e^{i\left(2\pi\frac{L}{\lambda_{MW}}\right)} + \sigma_0 e^{i\left(2\pi\frac{L}{\lambda_{MW}}+2\pi\frac{s}{\lambda_{SW}}\right)}| = |\Sigma_0 + \sigma_0 e^{i2\pi\frac{s}{\lambda_{SW}(\omega)}}|. \tag{2.50}$$

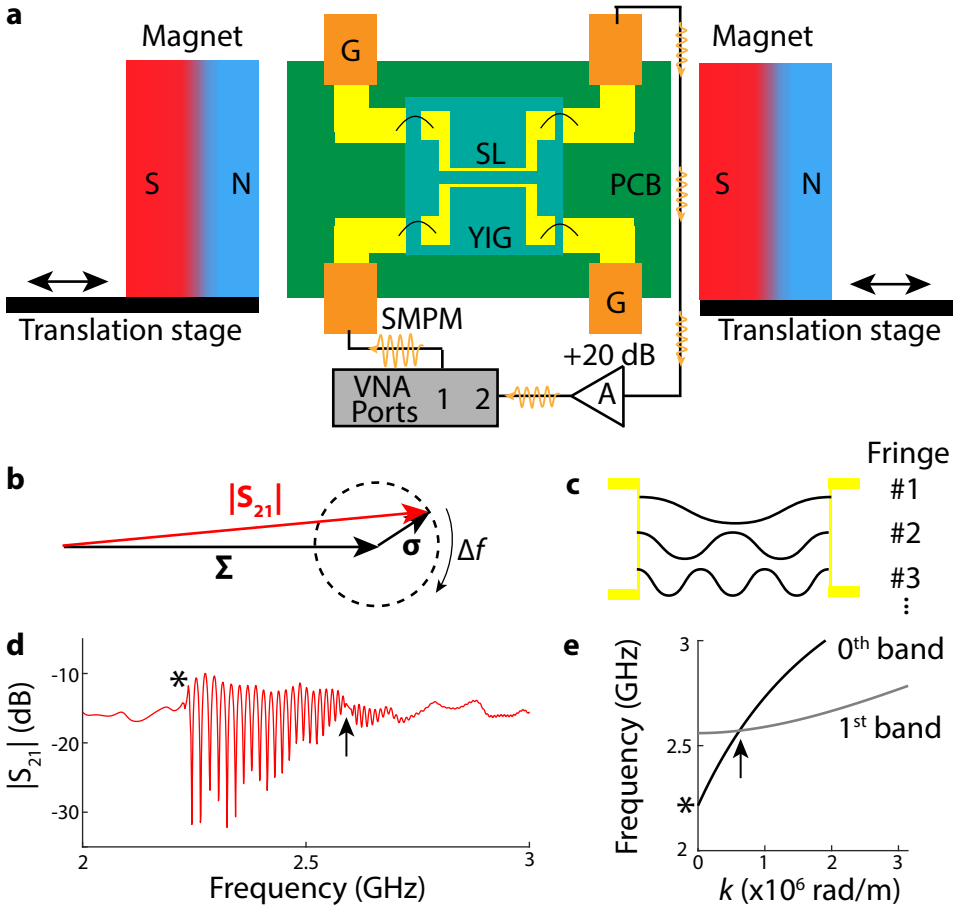

Figure 2.9: Propagating spin wave spectroscopy (**a**) Sketch of the experimental setup (not to scale). Gold striplines (SL) are e-beam patterned and evaporated onto a magnet (in this figure, YIG) and wirebonded to a printed circuit board (PCB). The striplines are U-shaped to minimize the parasitic coupling. Each stripline is connected at one side to a port of a vector network analyser (VNA, *Keysight, P9372A*) using non-magnetic SMPM connectors (*Amphenol RF, 925-169J-51PT*), while the other side is 50 Ohm terminated (G). The microwave transmission is amplified (A, +20 dB, *Minicircuits, ZX60-83LN-S+*) and detected by VNA port 2. The static in-plane bias field is swept using two cylindrical magnets (*Supermagnete, S35-20-N*) on computer-controlled translation stages (range: 25 mm, *Thorlabs, MTS25-Z8*). (**b**) Phasor diagram of the microwave transmission. The measured $|S_{21}|$ is the norm of the vector sum of the parasitic coupling (Σ) and the spin-wave-mediated transmission (σ). Due to the changing spin-wave wavelength, the phase of the spin-wave signal changes with respect to parasitic signal when sweeping frequency by Δf, resulting in fringes in the microwave transmission every time another wavelength fits between the striplines (**c**). (**d**) Example of the microwave transmission spectrum measured at 30 mT bias field in the Damon-Eshbach configuration on YIG using striplines with length 300 µm, width 5 µm, height 200 nm, and center-to-center distance s = 200 µm. The spin-wave fringes start at the bottom of the zeroth-order perpendicular mode Damon-Eshbach band (indicated by the star), which is analytically calculated in (**e**). At the crossing between the zeroth and first perpendicular band (indicated by the arrow), the spin-wave signal disappears as a result of efficient scattering into the first perpendicular mode.

Effectively, the spin-wave vector rotates as a function of frequency, while the parasitic coupling vector remains the same (Fig. 2.9b). A full rotation is made every time an extra wavelength fits in between the two microstrips (Fig. 2.9c), corresponding to a change of the spin-wave wavevector by

$$\Delta k = \frac{2\pi}{s}. \tag{2.51}$$

The phasor rotations are detected as frequency-dependent fringes in the absolute value of the microwave transmission (Fig. 2.9d) and give insight in the spin-wave dispersion (Fig. 2.9e). Since each fringe corresponds to a wavevector change Δk, the spin-wave group velocity v_g can be determined from the frequency spacing $\Delta f = \frac{\Delta\omega}{2\pi}$ between consecutive fringes

$$v_g = \frac{\partial\omega}{\partial k} \approx \frac{\Delta\omega}{\Delta k} = \Delta f s. \tag{2.52}$$

The spin-wave dispersion can be reconstructed from the frequency-dependence of the measured group velocity, as we demonstrate in chapter 5. In practice, the spin-wave fringes are best visualized by substracting the absolute microwave transmission without spin-wave-mediated transmission, for instance by applying a large enough bias field such that the microwave frequencies of interest lie inside the spin-wave gap.

2.4. EXCITON THEORY

In addition to spin waves, we study a second kind of excitations called excitons, which are bound states of electrons and holes in semiconducting materials. As discussed in section 1.3, excitons have recently been proposed as information carriers in valleytronic devices, where information is stored in the valley index of the excitons. In 2012 it was predicted that excitons in two-dimensional semiconductors give rise to a valley-dependent magnetic moment that should be measurable with NV magnetometry [92]. The idea is that circularly polarized light induces a magnetization by exciting excitons in one valley, which generates a magnetic field that can be detected with NV centers. Imaging of the excitonic magnetic field could give insight in the spatial distribution and dynamics of excitons at the nanoscale. In this thesis we focus on excitons in atomically-thin tungsten disulfide (WS_2) layers and take the first steps towards detecting the magnetic moment of excitons with NV sensors.

2.4.1. VALLEY POLARIZATION IN TMD MONOLAYERS

Transition metal dichalcogenides (TMD) are semiconducting materials of the type MX_2, with M a transition metal atom (e.g., Mo, W) and X a chalogen atom (e.g, S, Se) [93, 94]. They are van-der-Waals materials that can be thinned down to the monolayer limit using scotch-tape exfoliation. The crystal lattice of TMD monolayers has a honeycomb structure similar to graphene with a broken inversion symmetry (Fig. 2.10a). Graphene is a semi-metal with a bandstructure that is characterized by two Dirac cones near the Fermi level [95]. In contrast, the broken inversion symmetry opens a direct bandgap in TMD monolayers [96, 97], allowing efficient excitation of electrons using light. Furthermore, the electrons acquire a finite effective mass [92], such that the dispersion becomes

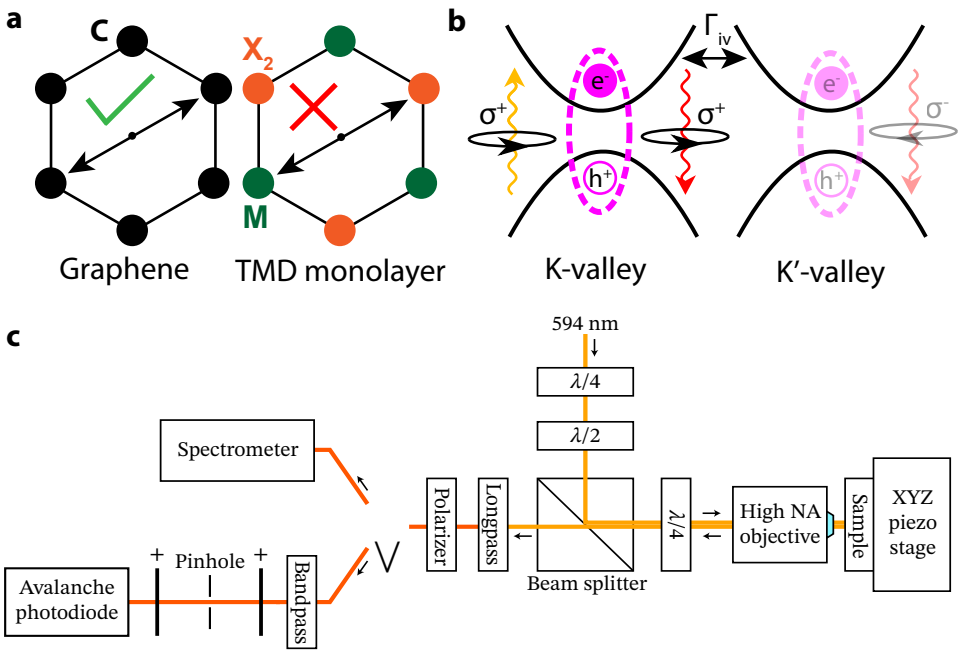

Figure 2.10: Detecting valley polarization in TMD monolayers. (**a**) TMD monolayers have a hexagonal unit cell similar to graphene. However, parity symmetry is broken in these materials, since atoms of type M are mapped onto atoms of type X_2 upon inversion. (**b**) Sketch of the TMD monolayer bandstructure, which consists of two valleys with a bandgap near the Fermi level. Electrons (e^-) are near-resonantly excited to the conduction band in the K valley by σ^+ circularly-polarized photons (λ = 594 nm), leaving a hole (h^+) in the conduction band. The electrons and holes form excitonic bound state, which scatter between the valleys at a rate Γ_{iv}. Upon recombination excitons in the $K^{(\prime)}$ valley emit photons with polarization $\sigma^{+(-)}$, which provide insight in the steady-state valley polarization and are detected using a home-built microscope sketched in (**c**). The first quarter-lambda plate ($\lambda/4$) corrects for imperfections in the laser polarization (*Coherent, OBIS 594 nm*) and makes it perfectly linear, such that the excitation polarization can be controlled by turning the half-lambda plate ($\lambda/2$). A 10:90 beam splitter (R:T, *Thorlabs*) separates the excitation from the detection. The polarization of the detection is controlled by the orientation of the second quarter-lambda plate relative to the transmission axis of the polarizer. The objective (*Olympus, 50X NA=0.95*) focuses the laser and collects the photoluminescence of the sample, which is positioned using an XYZ piezo stage (*Mad City Labs, Nano-3D200FT*). Two longpass filters (*Semrock, BLP01-594R-25*) eliminate the laser reflection. Depending on the orientation of a mirror on a computer-controlled flipmount (indicated by the V) the photoluminescence is detected by an avalanche photodiode (APD, *Laser Components*) or spectrometer (*Andor, Kymera 193 spectrograph* with an air-cooled, front illuminated *Andor, iVac 324 CCD detector*). Before the emission is detected by the APD, it is filtered with a pinhole and bandpass filter (*Semrock, FF01-623/32-25*).

parabolic near the Fermi level and thus the bandstructure is characterized by two "valleys", labelled K and K' (Fig. 2.10b).

The broken lattice symmetry also allows electrons to have a finite valley-dependent Berry curvature [92, 94] and enables valley-selective excitation of electrons using circularly polarized light, such that left (right) polarized photons excite electrons to the conduction band of the the $K^{(\prime)}$ valley [98–100]. The hole left behind in the valence band attracts the

excited electron via the Coulomb interaction [93], resulting in the formation of bound electron-hole states (excitons) that can stably exist even at room temperature.

Excitons in TMD monolayers have been proposed as next-generation information carriers [101, 102], in which a $|0\rangle$ or $|1\rangle$ corresponds to an excitons being either in the K or K' valley. A crucial requirement for realizing valley-electronic ("*valleytronic*") devices are long-lived, valley-polarized excitons. This is challenging, since valley-polarized excitons are typically rapidly redistributed over both valleys by intervalley scattering [98, 103].

In chapter 6 we develop a new technique to maintain a large steady-state valley polarization in WS_2 monolayers at room temperature after exciting electrons in one valley with circularly polarized light. Physisorption of anisole molecules increases the electron density in the monolayer, such that valley-polarized excitons rapidly capture an additional electron after being created. As such, a new exciton complex is created comprising two electrons and one hole [104, 105]. These negatively-charged trions have a strongly reduced lifetime compared to charge-neutral excitons [106]. This is the result of enhanced recombination via charged lattice defects [107] and Auger recombination [108–110], in which the energy associated to electron-hole pair is released non-radiatively by converting it into kinetic energy of the excess electron. We show that electron doping can reduce the exciton lifetime below the intervalley scattering time, such that a finite valley polarization is obtained.

The steady-state valley polarization is measured through optical circular dichroism measurements [103] (Fig. 2.10c). In these experiments excitons are excited by circular polarized laser light, while the polarization of their photoluminescence is analyzed. Upon recombination excitons emit circularly polarized photons with a handedness depending on the exciton valley, such that a finite valley polarization ρ results in polarized exciton photoluminescence, according to

$$\rho = \frac{I_{\sigma^+} - I_{\sigma^-}}{I_{\sigma^+} + I_{\sigma^-}}, \tag{2.53}$$

with the $I_{\sigma^\pm}$ the left/right circularly-polarized emission under σ^+ excitation.

2.4.2. TOWARDS NV MAGNETOMETRY OF EXCITONS

Excitonic valley polarization could potentially also be detected using NV magnetometry. The valley-dependent Berry curvature induces a self-rotation of electrons in the unit cell, which effectively acts as a magnetic moment with a sign depending on the valley-index [92, 111]. Previously the valley magnetic moment was detected optically via the valley Zeeman effect [112, 113], electrically via the valley Hall effect [114] (which can also be induced by applying uniaxial stress [115]), and optomechanically using suspended TMD monolayers [116]. By detecting the magnetic stray fields generated by valley-polarized excitons using NV centers, the valley polarization can be probed with nanoscale resolution while the excitons are excited.

In an experiment aimed to detect valley-polarized excitons it is crucial to maximize the

magnetic-field sensitivity of the NV centers, since the optically-excited valley magnetization is expected to be small. By turning the target field into a megahertz signal, for instance by repeatedly switching the polarization handedness of the excitation laser, the valley magnetic field could be detected using highly-sensitive pulsed AC magnetometry sequences [77]. Such sensing sequences have already allowed NV-based detection of chiral Nernst photocurrents in TMD monolayers [117]. To detect the valley magnetic moment it is crucial to realize a large steady-state valley polarization, which we achieve in chapter 6. The induced valley magnetization is expected to be uniform over the area excited by the laserspot, such that the largest magnetic fields are expected near sharp boundaries, like the edges of the flake.

BIBLIOGRAPHY

[1] M. W. Doherty et al., "The nitrogen-vacancy colour centre in diamond", Physics Reports **528**, 1 (2013).

[2] L. Robledo, H. Bernien, T. van der Sar, and R. Hanson, "Spin dynamics in the optical cycle of single nitrogen-vacancy centres in diamond", New Journal of Physics **13**, 025013 (2011).

[3] J. Jeske et al., "Stimulated emission from nitrogen-vacancy centres in diamond", Nature Communications **8**, 14000 (2017).

[4] E. R. MacQuarrie et al., "Coherent control of a nitrogen-vacancy center spin ensemble with a diamond mechanical resonator", Optica **2**, 233 (2015).

[5] P. V. Klimov, A. L. Falk, B. B. Buckley, and D. D. Awschalom, "Electrically Driven Spin Resonance in Silicon Carbide Color Centers", Physical Review Letters **112**, 087601 (2014).

[6] I. Bertelli, "Magnetic imaging of spin waves and magnetic phase transitions with nitrogen-vacancy centers in diamond", PhD thesis (Leiden University, 2021).

[7] J.-P. Tetienne et al., "Magnetic-field-dependent photodynamics of single NV defects in diamond: an application to qualitative all-optical magnetic imaging", New Journal of Physics **14**, 103033 (2012).

[8] L. Rondin et al., "Magnetometry with nitrogen-vacancy defects in diamond", Reports on Progress in Physics **77**, 056503 (2014).

[9] A. Gruber et al., "Scanning Confocal Optical Microscopy and Magnetic Resonance on Single Defect Centers", Science **276**, 2012 (1997).

[10] A. Dréau et al., "Avoiding power broadening in optically detected magnetic resonance of single nv defects for enhanced dc magnetic field sensitivity", Phys. Rev. B **84**, 195204 (2011).

[11] T. P. M. Alegre, C. Santori, G. Medeiros-Ribeiro, and R. G. Beausoleil, "Polarization-selective excitation of nitrogen vacancy centers in diamond", Physical Review B **76**, 165205 (2007).

[12] F. Jelezko, T. Gaebel, I. Popa, A. Gruber, and J. Wrachtrup, "Observation of coherent oscillations in a single electron spin", Phys. Rev. Lett. **92**, 076401 (2004).

[13] I. Bertelli et al., "Magnetic resonance imaging of spin-wave transport and interference in a magnetic insulator", Science Advances **6**, eabd3556 (2020).

[14] L. Thiel et al., "Quantitative nanoscale vortex imaging using a cryogenic quantum magnetometer", Nature Nanotechnology **11**, 677 (2016).

[15] C. Wei, A. S. Windsor, and N. B. Manson, "A strongly driven two-level atom revisited: Bloch-Siegert shift versus dynamic Stark splitting", Journal of Physics B: Atomic, Molecular and Optical Physics **30**, 21 (1997).

[16] T. van der Sar, F. Casola, R. Walsworth, and A. Yacoby, "Nanometre-scale probing of spin waves using single-electron spins.", Nature communications **6**, 7886 (2015).

[17] R. Li et al., "Wideband microwave magnetometry using a nitrogen-vacancy center in diamond", Phys. Rev. A **99**, 062328 (2019).

[18] M. Bejarano et al., "Nonlinear magnon control of atomic spin defects in scalable quantum devices", (2022).

[19] G. Wang et al., "Sensing of arbitrary-frequency fields using a quantum mixer", Phys. Rev. X **12**, 021061 (2022).

[20] S. Blundell, *Magnetism in Condensed Matter* (Oxford University Press, 2001).

[21] C. Kittel, P. McEuen, and P. McEuen, *Introduction to solid state physics*, Vol. 8 (Wiley New York, 1996).

[22] A. G. Gurevich and G. A. Melkov, *Magnetization Oscillations and Waves* (CRC Press, 1996).

[23] D. D. Stancil and A. Prabhakar, *Spin waves* (Springer, 2009).

[24] M. Schneider et al., "Bose–Einstein condensation of quasiparticles by rapid cooling", Nature Nanotechnology **15**, 457 (2020).

[25] S. O. Demokritov et al., "Bose–Einstein condensation of quasi-equilibrium magnons at room temperature under pumping", Nature **443**, 430 (2006).

[26] A. A. Serga et al., "Bose–Einstein condensation in an ultra-hot gas of pumped magnons", Nature Communications **5**, 3452 (2014).

[27] A. Finco et al., "Imaging non-collinear antiferromagnetic textures via single spin relaxometry", Nature Communications **12**, 767 (2021).

[28] T. Gilbert, "A phenomenological theory of damping in ferromagnetic materials", IEEE Transactions on Magnetics **40**, 3443 (2004).

[29] I. Bertelli et al., "Imaging Spin-Wave Damping Underneath Metals Using Electron Spins in Diamond", Advanced Quantum Technologies **4**, 2100094 (2021).

[30] T. Hula et al., "Nonlinear losses in magnon transport due to four-magnon scattering", Applied Physics Letters **117**, 042404 (2020).

[31] H. Schultheiss, K. Vogt, and B. Hillebrands, "Direct observation of nonlinear four-magnon scattering in spin-wave microconduits", Phys. Rev. B **86**, 054414 (2012).

[32] D. A. Bozhko, V. I. Vasyuchka, A. V. Chumak, and A. A. Serga, "Magnon-phonon interactions in magnon spintronics (Review article)", Low Temperature Physics **46**, 383 (2020).

[33] K. An et al., "Coherent long-range transfer of angular momentum between magnon Kittel modes by phonons", Phys. Rev. B **101**, 060407 (2020).

[34] T. Hioki, Y. Hashimoto, and E. Saitoh, "Coherent oscillation between phonons and magnons", Communications Physics **5**, 115 (2022).

[35] S. J. Hämäläinen, M. Madami, H. Qin, G. Gubbiotti, and S. van Dijken, "Control of spin-wave transmission by a programmable domain wall", Nature Communications **9**, 4853 (2018).

[36] T. X. Zhou et al., "A magnon scattering platform", Proceedings of the National Academy of Sciences of the United States of America **118**, 2019473118 (2021).

[37] A. A. Serga, A. V. Chumak, and B. Hillebrands, "YIG magnonics", Journal of Physics D: Applied Physics **43**, 264002 (2010).

[38] C. Dubs et al., "Low damping and microstructural perfection of sub-40nm-thin yttrium iron garnet films grown by liquid phase epitaxy", Physical Review Materials **4**, 024416 (2020).

[39] C. Dubs et al., "Sub-micrometer yttrium iron garnet LPE films with low ferromagnetic resonance losses", Journal of Physics D: Applied Physics **50**, 204005 (2017).

[40] M. Evelt et al., "Emission of Coherent Propagating Magnons by Insulator-Based Spin-Orbit-Torque Oscillators", Physical Review Applied **10**, 041002 (2018).

[41] L. Soumah et al., "Ultra-low damping insulating magnetic thin films get perpendicular", Nature Communications **9**, 3355 (2018).

[42] J. J. Carmiggelt, O. C. Dreijer, C. Dubs, O. Surzhenko, and T. van der Sar, "Electrical spectroscopy of the spin-wave dispersion and bistability in gallium-doped yttrium iron garnet", Applied Physics Letters **119**, 202403 (2021).

[43] T. Böttcher et al., "Fast long-wavelength exchange spin waves in partially compensated Ga:YIG", Applied Physics Letters **120**, 102401 (2022).

[44] B. A. Kalinikos and A. N. Slavin, "Theory of dipole-exchange spin wave spectrum for ferromagnetic films with mixed exchange boundary conditions", Journal of Physics C: Solid State Physics **19**, 7013 (1986).

[45] S. Klingler et al., "Measurements of the exchange stiffness of YIG films using broadband ferromagnetic resonance techniques", Journal of Physics D: Applied Physics **48**, 015001 (2015).

[46] A. Haldar, C. Tian, and A. O. Adeyeye, "Isotropic transmission of magnon spin information without a magnetic field", Science Advances **3**, e1700638 (2017).

[47] A. Rustagi, I. Bertelli, T. van der Sar, and P. Upadhyaya, "Sensing chiral magnetic noise via quantum impurity relaxometry", Phys. Rev. B **102**, 220403 (2020).

[48] B. A. Kalinikos, M. P. Kostylev, N. V. Kozhus, and A. N. Slavin, "The dipole-exchange spin wave spectrum for anisotropic ferromagnetic films with mixed exchange boundary conditions", Journal of Physics: Condensed Matter **2**, 9861 (1990).

[49] M. Farle, "Ferromagnetic resonance of ultrathin metallic layers", Reports on Progress in Physics **61**, 755 (1998).

[50] Y.-Y. Song, S. Kalarickal, and C. E. Patton, "Optimized pulsed laser deposited barium ferrite thin films with narrow ferromagnetic resonance linewidths", Journal of Applied Physics **94**, 5103 (2003).

[51] K. Y. Guslienko and A. N. Slavin, "Magnetostatic Green's functions for the description of spin waves in finite rectangular magnetic dots and stripes", Journal of Magnetism and Magnetic Materials **323**, 2418 (2011).

[52] C. Du et al., "Control and local measurement of the spin chemical potential in a magnetic insulator", Science **357**, 195 (2017).

[53] L. J. Cornelissen, J. Liu, R. A. Duine, J. B. Youssef, and B. J. van Wees, "Long-distance transport of magnon spin information in a magnetic insulator at room temperature", Nature Physics **11**, 1022 (2015).

[54] P. Pirro, V. I. Vasyuchka, A. A. Serga, and B. Hillebrands, "Advances in coherent magnonics", Nature Reviews Materials (2021).

[55] M. Geilen et al., "Fully resonant magneto-elastic spin-wave excitation by surface acoustic waves under conservation of energy and linear momentum", Applied Physics Letters **120**, 242404 (2022).

[56] J. R. Hortensius et al., "Coherent spin-wave transport in an antiferromagnet", Nature Physics **17**, 1001 (2021).

[57] V. Vlaminck and M. Bailleul, "Current-Induced Spin-Wave Doppler Shift", Science **322**, 410 (2008).

[58] H. Yu et al., "Magnetic thin-film insulator with ultra-low spin wave damping for coherent nanomagnonics", Scientific Reports **4**, 6848 (2014).

[59] V. Vlaminck and M. Bailleul, "Spin-wave transduction at the submicrometer scale: experiment and modeling", Phys. Rev. B **81**, 014425 (2010).

[60] H. Qin, S. J. Hämäläinen, K. Arjas, J. Witteveen, and S. van Dijken, "Propagating spin waves in nanometer-thick yttrium iron garnet films: Dependence on wave vector, magnetic field strength, and angle", Physical Review B **98**, 224422 (2018).

[61] J. Lucassen et al., "Optimizing propagating spin wave spectroscopy", Applied Physics Letters **115**, 12403 (2019).

[62] U. K. Bhaskar, G. Talmelli, F. Ciubotaru, C. Adelmann, and T. Devolder, "Backward volume vs Damon–Eshbach: A traveling spin wave spectroscopy comparison", Journal of Applied Physics **127**, 33902 (2020).

[63] P. Che, K. Baumgaertl, A. Kúkol'ová, C. Dubs, and D. Grundler, "Efficient wavelength conversion of exchange magnons below 100 nm by magnetic coplanar waveguides", Nature Communications **11**, 1445 (2020).

[64] J. Chen et al., "Excitation of unidirectional exchange spin waves by a nanoscale magnetic grating", Phys. Rev. B **100**, 104427 (2019).

[65] P. Krivosik and C. E. Patton, "Hamiltonian formulation of nonlinear spin-wave dynamics: Theory and applications", Physical Review B **82**, 184428 (2010).

[66] Y. Fetisov, C. Patton, and V. Synogach, "Nonlinear ferromagnetic resonance and foldover in yttrium iron garnet thin films-inadequacy of the classical model", IEEE Transactions on Magnetics **35**, 4511 (1999).

[67] Y. S. Gui, A. Wirthmann, and C.-M. Hu, "Foldover ferromagnetic resonance and damping in permalloy microstrips", Physical Review B **80**, 184422 (2009).

[68] Y. Li et al., "Nutation Spectroscopy of a Nanomagnet Driven into Deeply Nonlinear Ferromagnetic Resonance", Physical Review X **9**, 041036 (2019).

[69] H. Suhl, "Ferromagnetic Resonance in Nickel Ferrite Between One and Two Kilomegacycles", Physical Review **97**, 555 (1955).

[70] H. M. Olson, P. Krivosik, K. Srinivasan, and C. E. Patton, "Ferromagnetic resonance saturation and second order Suhl spin wave instability processes in thin Permalloy films", Journal of Applied Physics **102**, 23904 (2007).

[71] S. Y. An et al., "High power ferromagnetic resonance and spin wave instability processes in Permalloy thin films", Journal of Applied Physics **96**, 1572 (2004).

[72] B. A. McCullian et al., "Broadband multi-magnon relaxometry using a quantum spin sensor for high frequency ferromagnetic dynamics sensing", Nature Communications **11**, 5229 (2020).

[73] T. Sebastian, K. Schultheiss, B. Obry, B. Hillebrands, and H. Schultheiss, "Micro-focused Brillouin light scattering: imaging spin waves at the nanoscale", Frontiers in Physics **3**, 35 (2015).

[74] Y. Acremann et al., "Imaging precessional motion of the magnetization vector", Science **290**, 492 (2000).

[75] P. Wessels et al., "Direct observation of isolated Damon-Eshbach and backward volume spin-wave packets in ferromagnetic microstripes", Scientific Reports **6**, 22117 (2016).

[76] G. Dieterle et al., "Coherent excitation of heterosymmetric spin waves with ultrashort wavelengths", Phys. Rev. Lett. **122**, 117202 (2019).

[77] C. L. Degen, F. Reinhard, and P. Cappellaro, "Quantum sensing", Reviews of Modern Physics **89**, 035002 (2017).

[78] F. Casola, T. van der Sar, and A. Yacoby, "Probing condensed matter physics with magnetometry based on nitrogen-vacancy centres in diamond", Nature Reviews Materials **3**, 17088 (2018).

[79] P. Maletinsky et al., "A robust scanning diamond sensor for nanoscale imaging with single nitrogen-vacancy centres", Nature Nanotechnology **7**, 320 (2012).

[80] A. Aiello, P. Banzer, M. Neugebauer, and G. Leuchs, "From transverse angular momentum to photonic wheels", Nature Photonics **9**, 789 (2015).

[81] T. Yu, Z. Luo, and G. E. W. Bauer, "Chirality as Generalized Spin-Orbit Interaction in Spintronics", (2022).

[82] D. J. Griffiths, *Introduction to Electrodynamics* (Cambridge University Press, 2017).

[83] K. Y. Bliokh and F. Nori, "Transverse spin of a surface polariton", Phys. Rev. A **85**, 061801 (2012).

[84] J. Petersen, J. Volz, and A. Rauschenbeutel, "Chiral nanophotonic waveguide interface based on spin-orbit interaction of light", Science **346**, 67 (2014).

[85] B. le Feber, N. Rotenberg, and L. Kuipers, "Nanophotonic control of circular dipole emission", Nature Communications **6**, 6695 (2015).

[86] J. R. Eshbach and R. W. Damon, "Surface magnetostatic modes and surface spin waves", Phys. Rev. **118**, 1208 (1960).

[87] R. W. Damon and J. R. Eshbach, "Magnetostatic modes of a ferromagnet slab", Journal of Physics and Chemistry of Solids **19**, 308 (1961).

[88] K. Halbach, "Application of permanent magnets in accelerators and electron storage rings (invited)", Journal of Applied Physics **57**, 3605 (1985).

[89] M. Mohseni et al., "Backscattering immunity of dipole-exchange magnetostatic surface spin waves", Phys. Rev. Lett. **122**, 197201 (2019).

[90] J. J. Carmiggelt, B. G. Simon, I. Bertelli, and T. van der Sar, "Spinsensoren in diamant onthullen golvende spinzee", Nederlands Tijdschrift voor Natuurkunde (2021).

[91] B. G. Simon et al., "Directional Excitation of a High-Density Magnon Gas Using Coherently Driven Spin Waves", Nano Letters **21**, 8213 (2021).

[92] D. Xiao, G.-B. Liu, W. Feng, X. Xu, and W. Yao, "Coupled spin and valley physics in monolayers of MoS_2 and other group-vi dichalcogenides", Phys. Rev. Lett. **108**, 196802 (2012).

[93] T. Mueller and E. Malic, "Exciton physics and device application of two-dimensional transition metal dichalcogenide semiconductors", npj 2D Materials and Applications **2**, 29 (2018).

[94] X. Xu, W. Yao, D. Xiao, and T. F. Heinz, "Spin and pseudospins in layered transition metal dichalcogenides", Nature Physics **10**, 343 (2014).

[95] A. H. Castro Neto, F. Guinea, N. M. R. Peres, K. S. Novoselov, and A. K. Geim, "The electronic properties of graphene", Rev. Mod. Phys. **81**, 109 (2009).

[96] K. F. Mak, C. Lee, J. Hone, J. Shan, and T. F. Heinz, "Atomically Thin MoS_2: A New Direct-Gap Semiconductor", Phys. Rev. Lett. **105**, 136805 (2010).

[97] A. Splendiani et al., "Emerging Photoluminescence in Monolayer MoS_2", Nano Letters **10**, 1271 (2010).

[98] K. F. Mak, K. He, J. Shan, and T. F. Heinz, "Control of valley polarization in monolayer MoS_2 by optical helicity", Nature Nanotechnology **7**, 494 (2012).

[99] T. Cao et al., "Valley-selective circular dichroism of monolayer molybdenum disulphide", Nature Communications **3**, 887 (2012).

[100] H. Zeng, J. Dai, W. Yao, D. Xiao, and X. Cui, "Valley polarization in MoS_2 monolayers by optical pumping", Nature Nanotechnology **7**, 490 (2012).

[101] K. F. Mak, D. Xiao, and J. Shan, "Light–valley interactions in 2D semiconductors", Nature Photonics **12**, 451 (2018).

[102] J. R. Schaibley et al., "Valleytronics in 2D materials", Nature Reviews Materials **1**, 16055 (2016).

[103] K. M. McCreary, M. Currie, A. T. Hanbicki, H.-J. Chuang, and B. T. Jonker, "Understanding Variations in Circularly Polarized Photoluminescence in Monolayer Transition Metal Dichalcogenides", ACS Nano **11**, 7988 (2017).

[104] K. F. Mak et al., "Tightly bound trions in monolayer MoS_2", Nature Materials **12**, 207 (2013).

[105] J. S. Ross et al., "Electrical control of neutral and charged excitons in a monolayer semiconductor", Nature Communications **4**, 1474 (2013).

[106] P. H L, P. Mondal, A. Bid, and J. K. Basu, "Electrical and Chemical Tuning of Exciton Lifetime in Monolayer MoS_2 for Field-Effect Transistors", ACS Applied Nano Materials **3**, 641 (2020).

[107] D.-H. Lien et al., "Electrical suppression of all nonradiative recombination pathways in monolayer semiconductors", Science **364**, 468 (2019).

[108] C. M. E. Chow et al., "Monolayer Semiconductor Auger Detector", Nano Letters **20**, 5538 (2020).

[109] A. T. Hanbicki et al., "Anomalous temperature-dependent spin-valley polarization in monolayer WS_2", Scientific Reports **6**, 18885 (2016).

[110] A. Kurzmann, A. Ludwig, A. D. Wieck, A. Lorke, and M. Geller, "Auger Recombination in Self-Assembled Quantum Dots: Quenching and Broadening of the Charged Exciton Transition", Nano Letters **16**, 3367 (2016).

[111] D. Xiao, W. Yao, and Q. Niu, "Valley-contrasting physics in graphene: magnetic moment and topological transport", Phys. Rev. Lett. **99**, 236809 (2007).

[112] A. Srivastava et al., "Valley Zeeman effect in elementary optical excitations of monolayer WSe_2", Nature Physics **11**, 141 (2015).

[113] G. Aivazian et al., "Magnetic control of valley pseudospin in monolayer WSe_2", Nature Physics **11**, 148 (2015).

[114] K. F. Mak, K. L. McGill, J. Park, and P. L. McEuen, "The valley Hall effect in MoS_2 transistors", Science **344**, 1489 (2014).

[115] J. Lee, Z. Wang, H. Xie, K. F. Mak, and J. Shan, "Valley magnetoelectricity in single-layer MoS_2", Nature Materials **16**, 887 (2017).

[116] H.-K. Li et al., "Valley optomechanics in a monolayer semiconductor", Nature Photonics **13**, 397 (2019).

[117] B. B. Zhou et al., "Spatiotemporal mapping of a photocurrent vortex in monolayer MoS_2 using diamond quantum sensors", Phys. Rev. X **10**, 011003 (2020).

3

MAGNETIC RESONANCE IMAGING OF SPIN-WAVE TRANSPORT AND INTERFERENCE IN A MAGNETIC INSULATOR

Spin waves — the elementary excitations of magnetic materials — are prime candidate signal carriers for low-dissipation information processing. Being able to image coherent spin-wave transport is crucial for developing interference-based spin-wave devices. We introduce magnetic resonance imaging of the microwave magnetic stray fields that are generated by spin waves as a new approach for imaging coherent spin-wave transport. We realize this approach using a dense layer of electronic sensor spins in a diamond chip, which combines the ability to detect small magnetic fields with a sensitivity to their polarization. Focusing on a thin-film magnetic insulator, we quantify spin-wave amplitudes, visualize spin-wave dispersion and interference, and demonstrate time-domain measurements of spin-wave packets. We theoretically explain the observed anisotropic spin-wave patterns in terms of chiral spin-wave excitation and stray-field coupling to the sensor spins. Our results pave the way for probing spin waves in atomically thin magnets, even when embedded between opaque materials.

This chapter has been published in *Science Advances* **6**, eabd3556 (2020) by I. Bertelli, **J. J. Carmiggelt**, T. Yu, B. G. Simon, C. C. Pothoven, G. E. W. Bauer, Y. M. Blanter, J. Aarts, and T. van der Sar.

Related work has been published in *Proceedings of the National Academy of Sciences* **118**, e2019473118 (2021) by T. X. Zhou*, **J. J. Carmiggelt***, L. M. Gächter*, I. Esterlis, D. Sels, R. J. Stöhr, C. Du, D. Fernandez, J. F. Rodriguez-Nieva, F. Büttner, E. Demler, and A. Yacoby.
* indicates equal contribution.

A popular scientific discussion about the work (in Dutch) has been published in *Nederlands Tijdschrift voor Natuurkunde* (2021) by **J. J. Carmiggelt**, B. G. Simon, I. Bertelli, and T. van der Sar.

3.1. INTRODUCTION

Over the last few decades, the desire to understand and control spin transport, and to use it in information technology, has invigorated the field of spintronics. A central goal of the field is to provide information processing based on the spin of the electron instead of its charge and thereby avoid the heating associated with charge currents. As heating is currently the main obstacle for increasing computational speed, spin-based information processing may provide the next transformative change in information technology.

Promising signal carriers for low-dissipation information transport are spin waves [1, 2] — the collective spin excitations of magnetic materials. Spin waves exist even in electrically insulating magnets, where they are able to propagate inherently free of the dissipative motion of charge. They can have nanometer wavelengths and gigahertz frequencies well suited for chip-scale device technologies and interference-based spin-wave logic circuits [2]. Consequently, a growing research field focuses on spin-wave devices such as interconnects, interferometers, transistors, amplifiers, and spin-torque oscillators [3–7].

Being able to image coherent spin waves in thin-film magnets is crucial for developing spin-wave device technology. Leading techniques for imaging coherent spin waves, such as transmission x-ray microscopy [8, 9], Brillouin light scattering [10], and Kerr microscopy [11], rely on a spin-dependent optical response of a magnetic material. Here, we introduce a new approach: phase-sensitive magnetic resonance imaging of the microwave magnetic stray fields generated by coherent spin waves. We realize this approach using a layer of electronic sensor spins in a diamond chip as imaging platform (Fig. 3.1A). These spins enable quantitative measurements of microwave magnetic fields including their polarization, making the approach well suited for spin-wave imaging in magnetic thin films.

Focusing on a ~200-nm-thick magnetic insulator, we quantify spin-wave amplitudes, visualize the spin-wave dispersion, and demonstrate time-domain measurements of spin-wave packets. We observe unidirectional emission of spin waves that autofocus, interfere, and produce chiral magnetic stray fields with a handedness that matches that of the natural precession of the sensor spins. We present a theoretical analysis of the chiral spin-wave excitation and stray-field coupling to the sensor spins and show that it accurately describes the observed spatial spin-wave maps.

We detect the magnetic fields generated by spin waves using electron spins associated with nitrogen-vacancy (NV) lattice defects in diamond [12]. These spins can be initialized and read out optically and manipulated with high fidelity by microwaves. Over the last decade, NV magnetometry has emerged as a powerful platform for probing static and dynamic magnetic phenomena in condensed matter systems [13]. Key is an NV-sample distance tunable between 10 and 1000 nm that is well matched with the length scales of spin textures such as magnetic domain walls, cycloids, vortices, and skyrmions [14–16] as well as those of dynamic phenomena such as spin waves [17–21]. Recent experiments demonstrated that NV magnetometry has the sensitivity required for imaging the static magnetization of monolayer van der Waals magnets [22]. Here, we develop

NV-based magnetic resonance imaging into a platform for studying coherent spin waves via the gigahertz magnetic fields that they generate.

3.2. RESULTS

Our imaging platform consists of a diamond chip hosting a dense layer of shallowly implanted NV spins. We position this chip onto a thin film of yttrium iron garnet (YIG) — a ferrimagnetic insulator with record-high magnetic quality (Fig. 3.1A-B) [23]. The typical distance between the diamond and the magnetic film is ~ 1 µm (section 3.5.1). We excite spin waves using microwave striplines microfabricated onto the YIG. When the spin-wave frequency matches an NV electron spin resonance (ESR) frequency, the oscillating magnetic stray field B_{SW} drives NV spin transitions [17, 19] that we detect through the NV's spin-dependent photoluminescence (Methods). By tuning the external static magnetic field B_0, we sweep the NV ESR frequencies through the spin-wave band, thereby probing spin waves with different wavelength (Fig. 3.1C).

We start by characterizing the NV photoluminescence as a function of B_0 and the frequency ω_{MW} of a microwave drive current sent through the stripline, at a distance of ~ 5 µm from the stripline edge (Fig. 3.1D). This microwave current not only generates an oscillating magnetic field that drives ESR transitions of the NV spins directly but also excites spin waves in the YIG film that can drive NV ESR transitions via their magnetic stray field (Fig. 3.1A). The dips in the observed NV photoluminescence correspond to the ESR frequencies of the NV spins in the diamond (Fig. 3.1D; Methods). We observe an enhanced contrast for the ω_- transition when $B < B_0^{(2)}$. In this region, the excited spin waves efficiently drive the ω_- ESR transition.

We image the spin waves excited by the stripline in the YIG film by characterizing the contrast of the ω_- ESR transition as a function of the distance to the stripline (Fig. 3.2A). We do so by tuning the magnetic field such that the ω_- frequency is 2.17 GHz, i.e., 160 MHz above the bottom of the spin-wave band, thereby exciting spin waves in the film. To gain the phase sensitivity required for detecting the individual wavefronts of these propagating spin waves, we let their stray field interfere with an additional, externally applied microwave magnetic field B_{REF} that is spatially homogeneous and has the same frequency (Methods). As formulated mathematically below, this interference leads to a spatial standing-wave pattern in the total magnetic field that drives the NV ESR transition with a spatial periodicity equal to the spin-wave wavelength. We can thus rapidly visualize the spin waves by measuring the ratio between the NV photoluminescence with and without applied microwaves (Fig. 3.2A).

Quantifying the amplitude of a spin wave is a challenging task for any technique because the coupling between spin wave and probe is often not well known. With NV magnetometry, however, we accurately measure the microwave magnetic field generated by a spin wave as described by Maxwell's equations. We can therefore determine the amplitude of a spin wave of known direction and ellipticity with high confidence by solving a well-defined inverse problem.

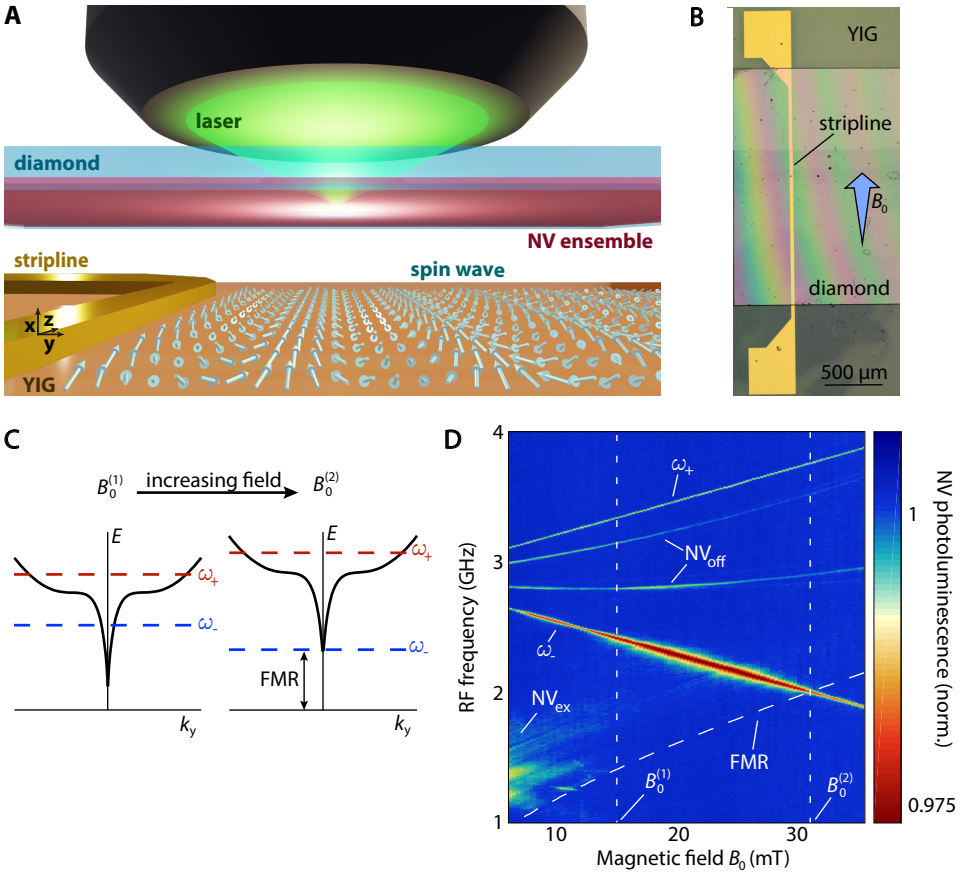

Figure 3.1: Imaging spin waves using NV spins in diamond. (**A**) A diamond hosting a layer of NV spins implanted at 20 nm below its surface is placed onto a film of YIG (thickness of 245 nm) grown on gadolinium gallium garnet (GGG). The NVs detect the magnetic fields of stripline-excited spin waves. (**B**) NV-containing diamond (thickness of ~ 40 µm) on YIG with gold stripline. B_0 is applied along the stripline at $\phi = 35°$ relative to the sample plane, aligning it with one of the four possible NV orientations. (**C**) The NV ESR frequencies $\omega_\pm$ are swept over the Damon-Eshbach spin-wave dispersion (black line) by tuning B_0. For any $B_0^{(1)} < B_0^{(2)}$, ω_- is resonant with spin waves of finite wavelength. At $B_0 < B_0^{(2)}$, ω_- is resonant with the ferromagnetic resonance (FMR). (**D**) Normalized NV photoluminescence versus B_0 and microwave drive frequency, measured at ~ 5 µm from a 2.5 µm-wide stripline. Indicated are the electronic ground-state ESR transitions $\omega_\pm$ (NV_{off}) of the NVs aligned (not aligned) with B_0. An electronic excited-state ESR transition (NV_{ex}) is visible because of the continuous optical and microwave excitation and identified through its location at $\omega_+/2$ [12]. The FMR is calculated from the independently determined saturation magnetization (section 3.5.2).

To illustrate the concept, we formulate the magnetic stray field of a spin wave traveling perpendicularly to the static magnetization (such as the one in Fig. 3.2B) in the reference frame depicted in Fig. 3.1A with transverse magnetization

$$\mathbf{m}_\perp(y) = m_\perp^0 \mathrm{Re}\left\{e^{i(k_y y-\omega t)}(\hat{\mathbf{y}} - i\eta\hat{\mathbf{x}})\right\} \tag{3.1}$$

where k_y, ω, and η are the wave number, angular frequency, and ellipticity of the spin wave, respectively; t is the time; and hats denote unit vectors. This spin wave produces a magnetic stray field above the film that rotates in the xy plane (see section 3.5.3 and [24]).

$$\mathbf{B}_{\mathrm{SW}}(y) = -B_{\mathrm{SW}}^0 \mathrm{Re}\left\{e^{i(k_y y-\omega t)}(\hat{\mathbf{y}} + i\,\mathrm{sgn}(k_y)\hat{\mathbf{x}})\right\} \tag{3.2}$$

where $B_{\mathrm{SW}}^0 = \mu_0 m_\perp^0 \left[1+\mathrm{sgn}(k_y)\eta\right]|\mathbf{k}|d e^{-|k_y|x_0}/2$, x_0 is the NV-YIG distance, and d is the thickness of the YIG film.

The handedness of $\mathbf{B}_{\mathrm{SW}}$ is opposite to that of $\mathbf{m}_\perp$ for a spin wave traveling to the right (i.e., with $k_y > 0$; as in Fig. 3.2B), which drives the ω_- (rather than the ω_+) NV spin transition (section 3.5.3). Moreover, the amplitude B_{SW}^0 depends on the propagation direction and degree of ellipticity η of the spin wave: Those traveling to the right (left) generate a stronger field above (below) the magnetic film. Therefore, only the ω_- transition of NV centers to the right of the stripline in Fig. 3.2B is excited (section 3.5.3). The resulting NV spin rotation rate (Rabi frequency) ω_{Rabi} is determined by the interference between the spin-wave field and the reference field B_{REF}

$$\omega_{\mathrm{Rabi}} = \sqrt{2}\gamma|B_{\mathrm{SW}}^0 \cos^2\left(\frac{\phi}{2}\right)e^{ik_y y} - B_{\mathrm{REF}}| \tag{3.3}$$

where $\phi = 35°$ is the angle with respect to (w.r.t.) the film of the NV centers used in Fig. 3.2 and $\gamma/2\pi = 28$ GHz/T is the (modulus of the) electron gyromagnetic ratio. Fitting the data in Fig. 3.2B by Eq. 3.3 (including a spatial decay; see section 3.5.3), we extract a spin-wave amplitude $m_\perp^0 = 0.033(1)\,M_s$ at the location of the stripline and a decay length of 1.2(1) mm, corresponding to a Gilbert damping parameter $1.2(1)\cdot 10^{-4}$, which is similar to the typically reported $1\cdot 10^{-4}$ for films of similar thickness [25].

By tuning the externally applied magnetic field, we sweep the NV ESR frequency through the spin-wave band and access spin waves with different wavelengths (Fig. 3.3A), as schematically described in Fig. 3.1C. In Fig. 3.3A-B, we visualize the individual spin-wave fronts using the interference between the direct stripline field and the stray field of the propagating spin wave. We extract the spin-wave dispersion from the frequency dependence of the wavelength (Fig. 3.3C). This dispersion matches the one calculated using values of the saturation magnetization M_s and film thickness d determined by independent measurements (section 3.5.2).

Travelling spin-wave packets can be used for pulsed quantum control of distant spins such as those of the NV centers [19, 20]. Understanding the distance-dependent response of the spins to an applied control sequence requires knowledge of the spin-wave

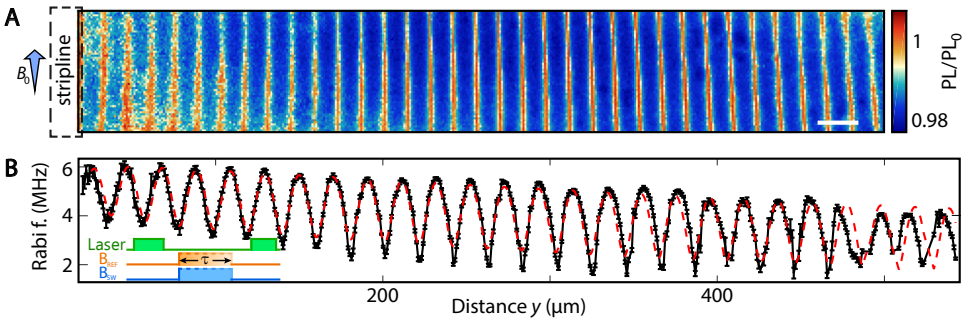

Figure 3.2: Imaging coherent spin waves. (**A**) Spatial ESR contrast at $B_0 = 25$ mT when a spin wave of frequency $\omega_{SW} = \omega_- = 2\pi\times$ 2.17 GHz is excited by a microwave current in the stripline (length of 2 mm, width of 30 μm, and thickness of 200 nm) at the left image edge. The NV photoluminescence with applied microwaves (PL) is normalized to that without applied microwaves (PL$_0$). The NV-YIG distance at the stripline was 1.8(2) μm, determined by measuring the field of a DC stripline current (section 3.5.1). Scale bar, 20 μm. (**B**) Rabi frequency $\omega_{Rabi}/2\pi$ versus distance from the stripline. $\omega_{SW} = \omega_- = 2\pi\times$ 2.11 GHz, $B_0 = 27$ mT. In (A) and (B), the microwaves were split between the stripline and a bonding wire, located ≈100 μm above the YIG and oriented along y to generate a spatially homogeneous field B_{REF}, creating an interference pattern (see text). Red line: Fit to a model including the field of the stripline, the bonding wire, and the spin waves (section 3.5.3). Inset: Measurement sequence. Laser pulses (1 μs) are used to initialize and read out the NV spins. Microwave pulses (duration τ) drive Rabi oscillations. ω_{Rabi} was calculated from the measured $\omega_{Rabi,0}$ using $\omega_{Rabi} = \sqrt{\omega_{Rabi,0}^2 - \Delta^2}$ to account for a $\Delta = 2\pi\times$ 1.5 MHz detuning between the drive frequency and the two hyperfine-split ESR resonances caused by the ^{15}N nuclear spin.

group velocity. We demonstrate a time-domain characterization of the spin-wave propagation using pulsed control of the NV spins (Fig. 3.3D-E). In our measurement scheme (Fig. 3.3D), the NV spins at a target distance from the stripline are prepared in $m_s = 0$ using a green laser pulse. A spin-wave pulse (excited by the stripline) flips the NV spins into the dark $m_s = -1$ state only if it arrives either before or after a set of two reference pulses acting on the $0 \leftrightarrow +1$ transition (generated by a wire above the sample), resulting in low photoluminescence upon spin readout. In contrast, if the spin-wave pulse reaches the NVs between the two reference pulses, then it does not affect the NV spins because they are in $m_s = +1$ due to the first reference pulse. The second reference pulse subsequently flips the spin back to the bright $m_s = 0$ state, resulting in high photoluminescence upon spin readout. Measurements as a function of time between spin-wave and reference pulses and distance from the stripline reveal the spin-wave packet in the time domain and allow the extraction of the group velocity (Fig. 3.3E). We find a velocity of 3.6(2) km/s at a frequency of 2.169 GHz and a wavelength of 12 μm, consistent with the YIG spin-wave dispersion.

The 2-mm-long stripline used in Figs. 3.2 and 3.3 corresponds to an effectively one-dimensional situation. We now turn to spin waves injected by a shorter stripline with a length comparable to the scanned area (Fig. 3.4A). We observe a focused emission

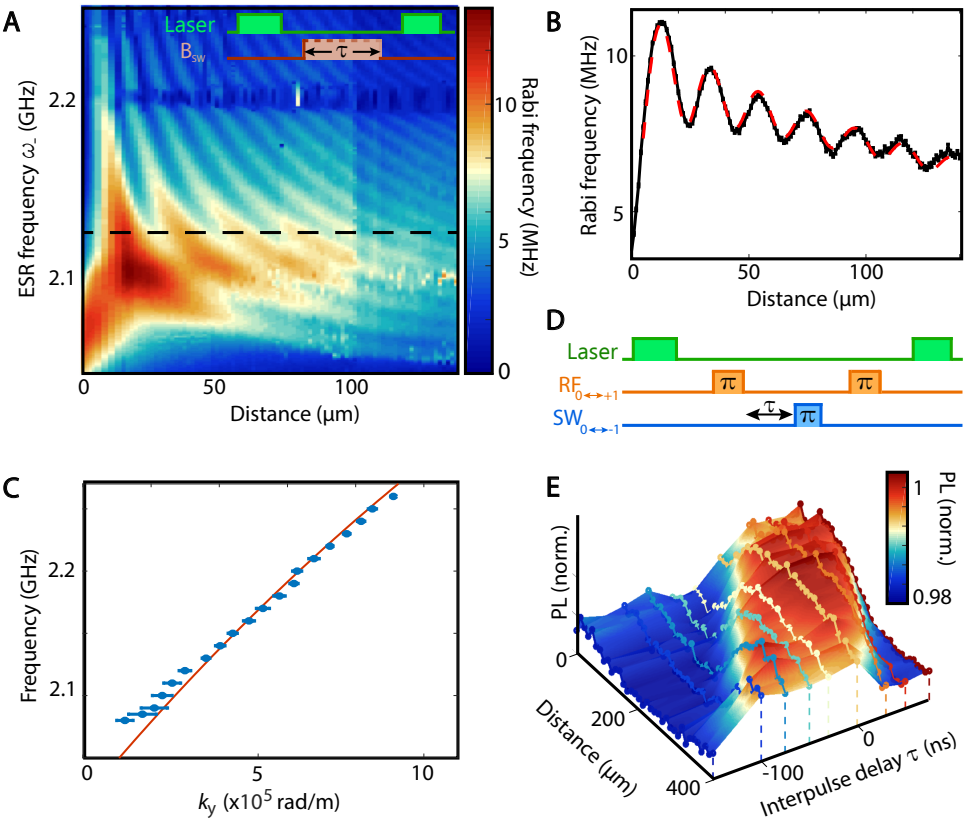

Figure 3.3: Spin-wave dispersion in the space and time domains. (**A**) NV Rabi frequency versus microwave drive frequency and distance from the stripline. The feature at 2.2 GHz matches the first perpendicular spin-wave mode (section 3.5.2). Inset: Measurement sequence. (**B**) Linecut of (A) with fit (red line) at 2.119 GHz. (**C**) Blue dots: Spin-wave frequency versus wave number extracted from (A). Red line: Calculated spin-wave dispersion. (**D**) Pulse sequence for studying spin-wave packets in the time domain [see text for details; data in (E)]: Laser pulses (1 μs) are used for NV spin initialization and readout. Two reference (RF) π pulses separated by 100 ns are applied at the $0 \leftrightarrow +1$ ESR frequency via a wire above the sample. After a time τ from the end of the first RF pulse, a spin wave–mediated π-pulse (SW) is generated at the $0 \leftrightarrow -1$ ESR frequency. (**E**) Normalized NV photoluminescence (PL) during the first 400 ns of the laser readout pulse [see (D)] versus distance from the stripline and delay time π. Negative τ indicates a spin-wave packet generated before the first RF pulse. For example, for $\tau = -100$ ns (i.e., the spin-wave pulse is generated 100 ns before the first RF pulse), the signal rises at 360 μm, indicating a spin-wave group velocity of 3.6 km/s. Circles, data; colored surface, interpolation.

pattern that is dominated by spin-wave beams traveling at specific angles (Fig. 3.4B-C). Such "caustics" occur when the dispersion is strongly anisotropic [26, 27]. They can be understood in terms of stationary points in the isofrequency curves in reciprocal space (Fig. 3.4D). In optics, such an isofrequency curve $k_z = k_z(k_y)$ is called "slowness" curve, because it is perpendicular to the group velocity $\mathbf{v}_g = \nabla_{\mathbf{k}}\omega(\mathbf{k})$. The states for which the angle of the group velocity $\theta = -\arctan(dk_z(k_y)/dk_y)$ is stationary along the curve, i.e., when $d\theta/dk_y \propto d^2k_z(k_y)/dk_y^2 = 0$, dominate emission, generating high-intensity spin-wave beams. The external magnetic field and the drive frequency can tune the beam direction and intensity [26, 27], providing opportunities to optimize the efficiency of spin wave–mediated magnetic field driving of distant spins at target locations.

Last, we image the interference between spin waves excited by two adjacent striplines on the YIG chip (Fig. 3.4, E and F), which shows rich interference patterns radiating from the three crossing points of the main caustics (i.e., ~ 80 μm from the striplines edge). The strongly anisotropic spin-wave dispersion causes a triangular "dark" region between the striplines in which no spin waves are detected, because spin waves traveling at small angles with respect to the equilibrium magnetization direction or having large wave numbers are neither efficiently excited (when the wavelength is shorter than the half-width of the stripline) nor efficiently detected due to the ~ 1 μm NV-sample distance. The downward directionality of the observed spin-wave patterns has two causes: The chiral spin-wave field has the correct handedness to drive the ω_- NV transition, and the handedness of the stripline field excites downward-propagating spin waves more efficiently (section 3.5.3). We note that these waves are not intrinsically directional because their wavelength far exceeds the film thickness [28], in contrast with Damon-Eshbach surface waves in thick films [29]. The observed directionality and interference patterns agree well with linear response calculations of the nonlocal dynamic susceptibility and the spatial profile of the microwave drive field, as described in section 3.5.3. These quantitative measurements of the spin wave–generated rotating magnetic stray fields illustrate the power of NV-based magnetic resonance imaging in magnonics.

3.3. DISCUSSION

Our results demonstrate that ensembles of NV spins in diamonds enable quantitative, phase-sensitive magnetic imaging of coherent spin waves in thin-film magnets. A theoretical analysis explains the NV sensor signals in terms of the rotating stray fields generated by spin waves that are excited unidirectionally by the stripline magnetic field. In contrast to other spin-wave imaging techniques, our technique images spin waves by their microwave magnetic stray fields. This does not require a specific spin-photon or spin-electron interaction and enables imaging spin waves through optically opaque materials. These capabilities provide new opportunities, e.g., for studying top-gated materials and the interaction of spin waves with magnetic and nonmagnetic materials placed on top of a magnetic film, which play an important role for spin-wave excitation and damping and form the basis for nonreciprocal devices [30]. NV magnetometry also allows high-resolution imaging of electric currents [31], enabling spatial studies of the interaction between spin waves and charge transport.

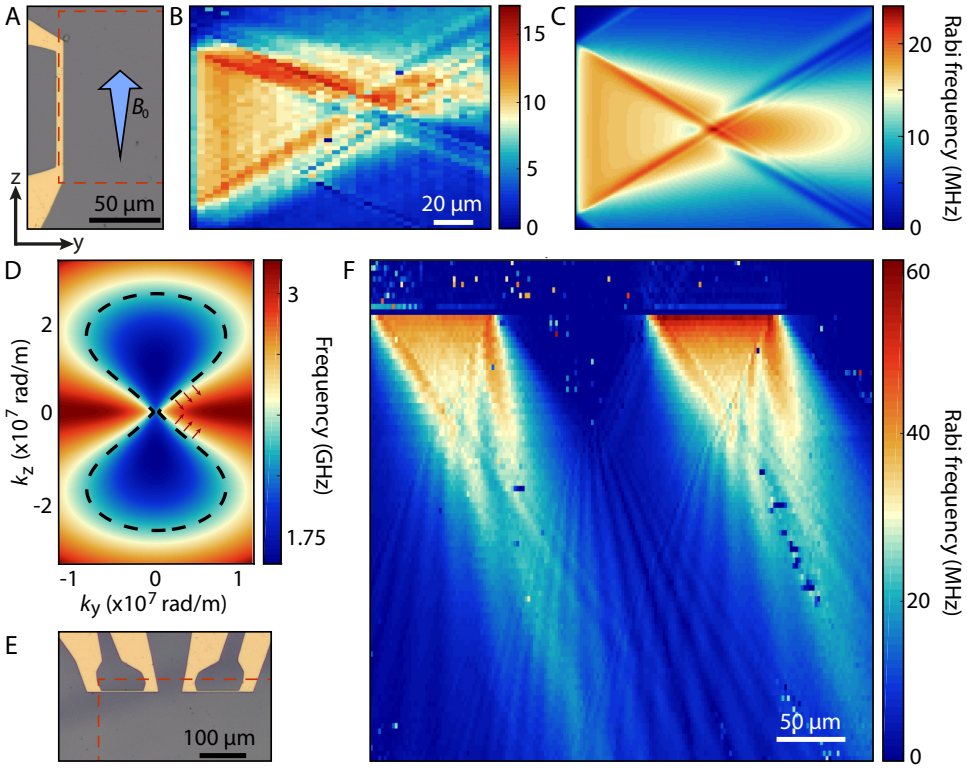

Figure 3.4: Imaging interference and caustics of spin waves excited by one and two short striplines. (**A**) Optical micrograph of the stripline (width of 5 µm) used to excite spin waves. The dashed red lines indicate the region where (B) is acquired. (**B**) Rabi frequency map corresponding to the dashed region of (A) for $B_0 = 27.1$ mT and $\omega/2\pi = 2.11$ GHz. The small asymmetry is attributed to a small misalignment of B_0 with respect to the striplines. (**C**) Simulation of the emission pattern observed in (B). (**D**) Calculated two-dimensional spin-wave dispersion relation $\omega(k_y, k_z)/2\pi$ at $B_0 = 20.5$ mT. The dashed line is an isofrequency contour at 2.292 GHz, indicating which wave vectors can be excited at this frequency and field. Red arrows indicate the direction of the spin-wave caustics. (**E**) Optical micrographs of the two injector striplines of width 2.5 µm. The dashed lines indicates the region where (F) is acquired. (**F**) Rabi frequency map under simultaneous driving of the two striplines, showing unidirectional excitation of autofocused spin-wave patterns that interfere and drive NV Rabi oscillations via their chiral magnetic stray fields.

Both the NV-sample distance and the optical resolution of our microscope limit the resolution of our technique. The typical NV-magnet distances are here 0.5 to 2 μm (limited by, e.g., dust particles), comparable to our diffraction-limited optical resolution. Shallow NV centers in diamond chips that are wafer-bonded to (i.e., in direct contact with) a magnetic sample should allow the detection of spin waves with wavelengths comparable to the implantation depth of the NV centers of a few nanometers [32]—albeit without phase sensitivity. This requires resonance between the spin waves and the NV sensors, e.g., by tuning a magnetic field and/or magnetic anisotropies. This may be difficult for magnetically hard materials. We can probe nonresonant spin waves by detecting the Stark shift that they impart on the sensor spins [33] or by detecting intraband spin-wave transitions using NV spin relaxometry [34]. Phase-sensitive imaging of spin waves with wavelengths below the diffraction limit could be enabled using specialized NV control sequences such as phase encoding schemes [35]. Furthermore, the techniques presented here are directly transferrable to single-NV scanning probe microscopes with real-space resolution on the 10-nm scale [36].

Our results pave the way for studying spin waves in other magnetic material systems such as magnetic nanodevices and atomically thin magnets. NV magnetometry works at cryogenic temperatures [37–39], allowing studies of magnets with low Curie temperatures such as complex oxide or van der Waals magnets. Because the dipole density per unit area $M_s d = 3.6 \cdot 10^3$ μ_B/nm^2 of the YIG film studied here is only about two orders of magnitude above the 16 μ_B/nm^2 of the monolayer van der Waals magnet CrI_3 [22], the magnetic stray fields generated by spin waves in such monolayer magnets are within the sensitivity range of NV-based magnetic imaging. The sensitivity of our technique is rooted in measuring the sum of a reference field and the spin-wave field. A good strategy for measuring weak spin-wave fields is to apply a strong reference field and measure the variations in the Rabi frequency caused by the spin-wave field, because Rabi frequency variations of ~ 100 kHz can easily be detected (the average error bar in Fig. 3.4 is 75 kHz). We can further increase the sensitivity by applying a stronger reference field, which decouples the NV spin from noise sources [40]. Increasing the microwave drive current and reducing the NV-sample distance (for instance, by depositing a van der Waals material directly onto the diamond [41]) would further increase the detection capability.

3.4. MATERIALS AND METHODS

3.4.1. SAMPLE FABRICATION

The diamond samples used in this work are chemical vapor deposition (CVD)–grown, electronic-grade type IIa diamonds (Element 6), laser-cut, and polished down to 2 mm × 2 mm × 0.05 mm chips (Almax easyLab). These chips were cleaned with nitric acid, and the top ~ 5 μm were removed using inductively-coupled plasma (ICP) reactive ion etching (30 min Ar/Cl, 20 min O_2) to mitigate polishing damage. The chips were subsequently implanted with ^{15}N ions at 6 keV with a dose of 1×10^{13} ions/cm^2 (INNOViON), tri-acid cleaned (mixture of nitric, sulfuric, and perchloric acid, 1:1:1), annealed at 800°C for 4 hours at 10^{-6} mbar, and tri-acid cleaned again to remove possibly graphitized lay-

ers on the surface, resulting in an estimated density of NV centers of $\sim 1 \times 10^{11}$ NV/cm^2 at a depth of ~10 to 20 nm.

The YIG films were 245 nm thick, grown on gadolinium gallium garnet (GGG) substrates by liquid-phase epitaxy (Matesy GmbH). Before stripline fabrication, the YIG/GGG chips were sonicated in acetone and cleaned for a few seconds in an O_2 descum plasma to remove contaminants. Striplines for spin-wave excitation were fabricated directly onto the YIG films by e-beam lithography using a PMMA(A8 495)/PMMA(A3 950) double-layer resist and subsequent e-beam evaporation of Cr/Au (5 nm/200 nm). To attach an NV-containing diamond to the YIG film, a small droplet of isopropanol was deposited onto the YIG, on top of which a diamond chip was placed, with the NV surface facing down. The diamond chip was gently pressed down until the isopropyl alcohol had evaporated [42]. The resulting NV-YIG distance was measured to be 1.8(2) μm (see Fig. 3.5).

3.4.2. MEASUREMENT SETUP

The optical setup used for all the measurements was a homebuilt confocal microscope. A 515-nm laser (Cobolt 06-MLD) was used for optical excitation of the NV centers, focused to a diffraction-limited spot by an Olympus 50×, numerical aperture = 0.95 objective. The NV luminescence was collected by the same objective, separated from the excitation light by a Semrock dichroic mirror and long-pass filter (617 nm cutoff), spatially filtered by a pinhole, and detected using a single-photon counting module (Laser Components). The microwaves signals used for driving NVs and spin waves were generated using Rohde & Schwarz microwave generators (SGS100A). The reference field B_{REF} used to produce the interference pattern in Fig. 3.2 was generated by a wire located ~ 200 μm above the diamond and oriented perpendicularly to the stripline. To simultaneously drive the pair of striplines in Fig. 3.4, the microwave excitation was split using a Mini-Circuits power combiner (ZFRSC-123-S+). A National Instruments data acquisition card was used for triggering the data acquisition, while a SpinCore programmable pulse generator (PulseBlaster ESR-PRO 500) was used to control the timing sequences of the laser excitation, microwaves, and detection window. The photons were collected during the first 300 to 400 ns of the laser readout pulse, which was kept fixed to 1 μs. All measurements were performed at room temperature.

3.4.3. NV MAGNETOMETRY

The NV spins are initialized and read out using nonresonant optical excitation at 515 nm. To measure NV spin rotations (Rabi oscillations), we first apply a ~ 1 μs green laser pulse to polarize the NV spin into the $m_s = 0$ state. A subsequently applied microwave magnetic field resonant with an NV ESR frequency drives Rabi oscillations between the corresponding NV spin states ($m_s = 0$ and -1 in Fig. 3.2B). The NV spin state is read out by applying a laser pulse and measuring the spin-dependent photoluminescence that results from spin-selective nonradiative decay via a metastable singlet state. The ESR frequencies of the four NV families (Fig. 3.1D) in a magnetic field B_0 are determined by the NV spin Hamiltonian $H = DS_z^2 + \gamma \mathbf{B}_0 \cdot \mathbf{S}$, where γ is the electron gyromagnetic ratio, D is the zero-field splitting (2.87 GHz), and $S_{(i=x,y,z)}$ is the Pauli spin matrices for a spin 1. We apply the magnetic field B_0 using a small permanent magnet (diameter, 1 cm; height,

2 cm).

3.4.4. WAVELENGTH OF THE SPIN WAVES DRIVING NV RABI OSCILLATIONS

We excite spin waves at a frequency that matches the ω_- ESR transition of the NV spins, allowing us to detect the spin waves via the resulting NV Rabi oscillations. Hence, for a given field B_0 applied along the NV axis, the wave number of the spin waves driving Rabi oscillations is determined by equating the NV frequency $\omega_-/2\pi = D - \gamma B_0$ to the spin-wave frequency given by the spin-wave dispersion (eq. 3.14)

$$\frac{\omega(B_0,k)}{\gamma\mu_0 M_s} = \sqrt{\left(\frac{B_0\cos\theta}{\mu_0 M_s} + \alpha_{ex}k^2 + \frac{1-e^{-|k_y|d}}{|k_y|d}\right)\left(\frac{B_0\cos\theta}{\mu_0 M_s} + \alpha_{ex}k^2 + \frac{k_y^2}{k^2}\left(1-\frac{1-e^{-|k_y|d}}{|k_y|d}\right)\right)} \tag{3.4}$$

where k is the SW wave number; k_y is its in-plane component perpendicular to the static magnetization; μ_0 is the magnetic permeability of vacuum; and M_s, $\alpha_{ex} = 3.0\cdot10^{-16}$ m^2, and d are the YIG saturation magnetization, exchange constant [23], and thickness, respectively.

ACKNOWLEDGEMENTS

Funding: This work was supported by the Dutch Research Council (NWO) as part of the Frontiers of Nanoscience (NanoFront) program through NWO Projectruimte grant 680.91.115, JSPS KAKENHI grant no. 19H006450, and Kavli Institute of Nanoscience Delft.

Author contributions: I.B., J.J.C., and T.v.d.S. designed the experiment. I.B. fabricated the diamond-YIG samples, realized the imaging setup, performed the NV measurements, and analyzed the data. B.G.S. prepared the diamonds. C.C.P. performed the vector network analyzer (VNA) measurements, for which J.J.C. fabricated the samples. T.Y., Y.M.B., and G.E.W.B. developed the theoretical model describing spin-wave caustics and interference. I.B. and T.v.d.S. wrote the manuscript with help from all coauthors. J.A. contributed to the discussions of the results and the manuscript.

Competing interests: The authors declare that they have no competing interests.

Data and materials availability: All data contained in the figures are available at Zenodo.org with the identifier 10.5281/zenodo.4005488. Additional data related to this paper may be requested from the authors.

3.5. SUPPLEMENTARY MATERIAL

3.5.1. DETERMINATION OF THE NV-YIG DISTANCE

The distance x_0 between the YIG surface and the NV sensing layer is an important parameter for the reconstruction of spin-wave amplitude from the detected field (Fig. 3.2). We determined x_0 by sending a DC current I_{DC} through the stripline and characterizing the resulting magnetic field $\mathbf{B}_{DC}(x_0, y)$ using the NV sensing layer. This field causes spatially dependent shifts in the NV ESR frequencies (Fig. 3.5A-B) from which we can extract x_0 as described next. Considering an infinitely thin stripline of width w with its center at

$x = y = 0$, the stripline field is given by

$$\mathbf{B}_{\mathrm{DC}}(x_0, y) = \frac{\mu_0 I_{DC}}{2\pi w}\left(\frac{1}{2}\ln\left(\frac{x_0^2 + (y + w/2)^2}{x_0^2 + (y - w/2)^2}\right)\hat{x} + \arctan\left(\frac{w x_0}{x_0^2 + y^2 - (w/2)^2}\right)\hat{y}\right) \tag{3.5}$$

To facilitate the analysis of the ESR spectra, we also applied a small bias field $\mathbf{B_0}$ to increase the splitting of the 8 ESR transitions of the 4 NV families. From the total field $\mathbf{B} = \mathbf{B_0} + \mathbf{B}_{\mathrm{DC}}$, we calculate the ESR frequencies for the 4 NV families by diagonalizing the NV spin Hamiltonian $H = DS_z^2 + \gamma(B_\parallel S_z + B_\perp S_x)$, where $B_\parallel$ is the projection of $\mathbf{B}$ onto the NV axis and $B_\perp = \sqrt{B^2 - B_\parallel^2}$. From the fit to this model (Fig. 3.5C), we extract $\mathbf{B_0}$ = (0.461(3), 3.568(3), 0.626(3)) mT, D = 2.872(1) GHz and x_0 = 1.8(2) µm. For the sample in Fig. 3.4 we used an alternative, optical method to determine the distance, focusing the excitation laser first on the YIG surface and then on the NV layer, reading off the change in the position of the microscope objective from its closed-loop piezo-controller, measuring $x_{0,\mathrm{Sample\,2}}$ = 1.0(3) µm.

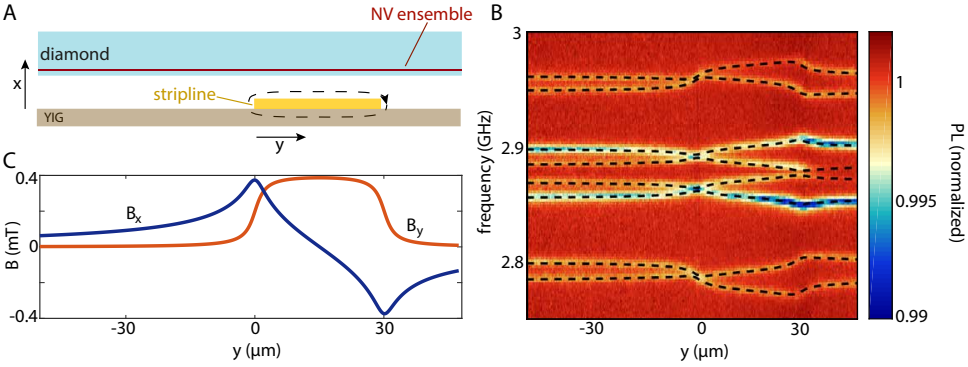

Figure 3.5: Determination of the YIG-NV distance. (**A**) Idea of the measurement. The diamond is located at a height x above the current-carrying stripline fabricated on the YIG. ESR spectra are measured along a line perpendicular to the stripline. The current in the stripline generates a magnetic field (dashed black line), causing a shift of the NV ESR frequencies. (**B**) NV ESR spectra measured along a line oriented perpendicularly to the stripline (which is located between $y = 0$ and $y = 30$ µm). The eight dips in the photoluminescence (PL) are caused by the ESR transitions of the four NV families having different orientations in the diamond crystal lattice. (**C**) Stripline magnetic field in the NV layer corresponding to the values extracted from the fit.

3.5.2. DETERMINATION OF M_s AND THICKNESS OF YIG WITH VNA MEASUREMENTS

The YIG saturation magnetization M_s and thickness d are important parameters for analyzing the spin-wave dispersion. Here we describe the extraction of these parameters using vector network analyzer (VNA) measurements.

We flip-chip a YIG chip on the central conductor of a coplanar waveguide (CPW) and use a VNA to measure the microwave transmission S_{21} through the CPW as a function of a magnetic field B_0 applied in-plane and parallel to the central conductor of the CPW

(Fig. 3.6 A). When the frequency matches the YIG FMR, energy is absorbed and S_{21} decreases. We extract $M_s = 1.42(1) \cdot 10^5$ A/m by fitting the data with the Kittel equation $\omega = \gamma\sqrt{B_0(B_0 + \mu_0 M_s)}$.

We determine the thickness of the YIG chip from the frequency of the first perpendicular standing spin-wave mode (PSSW) [43].To extract the frequency of the first PSSW, we measure the spin-wave mediated transmission of microwaves between two striplines using the VNA (Fig. 3.6B-C). The PSSW manifests as a small dip in the transmission (indicated by the dashed black line in Fig. 3.6B and the black arrow in Fig. 3.6D). To extract the thickness d, we calculate the PSSW frequency at each field for fixed M_s and different values of the thickness using [44]. The best match is reached for $d = 245(5)$ nm.

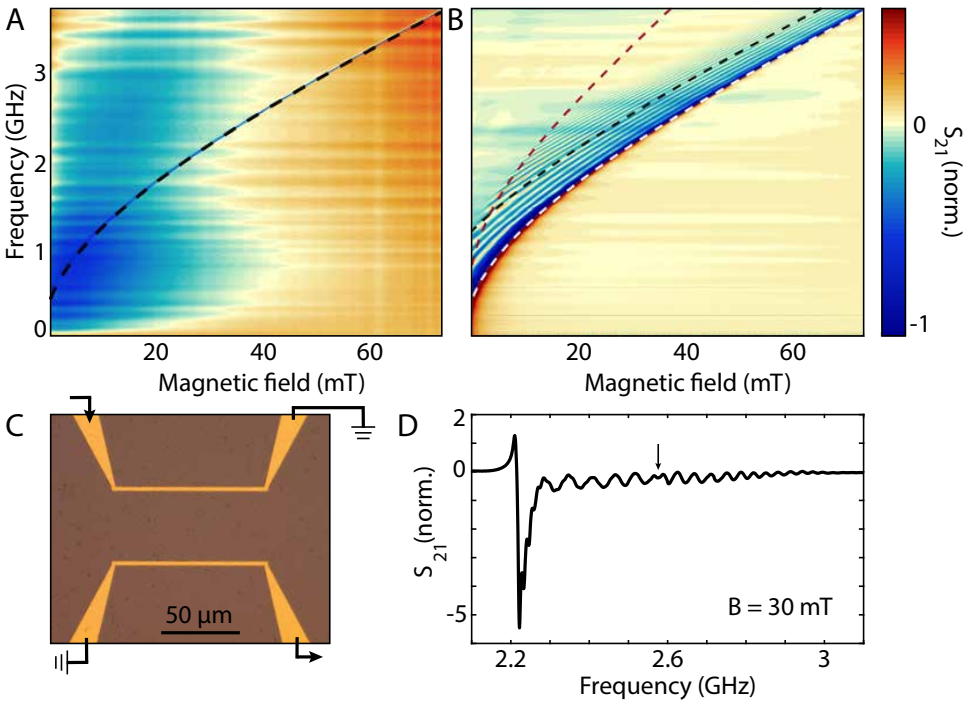

Figure 3.6: VNA-FMR detection of spin waves to determine M_s and thickness of the YIG chip. (**A**) Transmission $S_{21}(B,\omega)$ through the central conductor of a CPW on top of which a YIG chip is placed. The absorption of YIG at the FMR (dark blue line in the data) is extremely sharp (FWHM<10 MHz). The dashed black line is calculated using the extracted value of $M_s = 1.42 \cdot 10^5$ A/m. (**B**) $S_{21}(B,\omega)$ mediated by spin waves across the device shown in (C). The white and black dashed lines are the calculated frequencies of the FMR and 1st-order PSSW, respectively. The red dashed line indicates a frequency that is twice that of the calculated band minimum. Above this frequency, three-magnon scattering becomes allowed, which may contribute to the observed vanishing of the spin-wave mediated transmission above this frequency. (**C**) Device used to obtain the measurement in (B). The two gold striplines fabricated on YIG and connected to the input and output of the VNA as indicated by the arrows. Stripline width = 2.5 µm, thickness = 200 nm. (**D**) Vertical linecut of (B) at 30 mT, showing the FMR absorption dip followed by several oscillations and the PSSW, indicated by the black arrow.

3.5.3. EFFECT OF THE SPIN WAVE STRAY FIELD ON THE NV SPINS

In this section we derive the NV Rabi frequency due to the stray fields from spin waves excited in the YIG by a stripline carrying an oscillating current. In section 3.5.3 we present the magnetization profile excited by the stripline magnetic field, based on the spin susceptibility of the YIG. In section 3.5.3 we provide the dipolar field generated by the magnetization oscillations at the NV centers and determine their Rabi frequency by evaluating the efficiency of the field in driving the NV spins, including the chirality of the spin-wave field. In section 3.5.3, we extend the results obtained to the case of two adjacent striplines and calculate the interference pattern. Our theoretical framework captures and explains several effects visible in the data, such as the spin wave focussing and caustics beams, as well as the interference fringes.

MODEL AND PARAMETERS

We use the reference frame depicted in Fig. 3.1. Additionally, the length, width and thickness of the stripline are referred to as l, w and δ, respectively, the thickness of the yttrium iron garnet (YIG) film is d, and the NV-YIG distance is x_0. The static magnetic field B_0 is always applied at a $\phi = 35°$ angle with respect to the sample plane and parallel to the striplines. Because B_0 in the experiments of Figs. 3.2-3.4 does not exceed 27 mT, which is much smaller than the YIG saturation magnetization $\mu_0 M_s \approx 178$ mT, the static magnetization of the film only tilts out of plane by a small angle $B_0 \sin\phi/(\mu_0 M_s) \lessapprox 5°$. We therefore disregard the out-of-plane component of the static magnetizaton and magnetic field B_0 in the calculations. We use the parameters $w = 2.5$ µm, $\delta = 200$ nm, $l = 88$ µm, $d = 245$ nm and $x_0 = 1$ µm. The striplines in Fig. 3.4E-F are 110 µm apart and driven with a phase difference of π.

MAGNETIZATION EXCITED BY A MICROWAVE STRIPLINE OF FINITE LENGTH

Stripline magnetic field Two striplines $i = \{1,2\}$ carrying a current density $\mathbf{J}_i(\mathbf{r},\omega)$ with frequency ω generate the vector potentials [45]

$$\mathbf{A}_i(\mathbf{r},\omega) = \frac{\mu_0}{4\pi}\int d\mathbf{r}'\mathbf{J}_i(\mathbf{r}',\omega)\frac{e^{ik|\mathbf{r}-\mathbf{r}'|}}{|\mathbf{r}-\mathbf{r}'|}, \tag{3.6}$$

parallel to the direction of the current (the z-direction). μ_0 is the vacuum permeability and $k = \omega/c$. Substituting the Weyl identity [46],

$$\frac{e^{ik\sqrt{(x-x')^2+(y-y')^2+(z-z')^2}}}{\sqrt{(x-x')^2+(y-y')^2+(z-z')^2}} = \frac{i}{2\pi}\int dk_y dk_z \frac{e^{ik_x|x-x'|+ik_y(y-y')+ik_z(z-z')}}{k_x}, \tag{3.7}$$

where $k = \sqrt{k_x^2+k_y^2+k_z^2}$ (and hence $k_x = \sqrt{k^2-k_y^2-k_z^2}$), the Fourier components of the magnetic field $\mu_0(H_x,H_y)^{(i)} = (\partial A_z/\partial y, -\partial A_z/\partial x)^{(i)}$ in reciprocal space are

$$H_x^{(i)}(x;k_y,k_z) = 2iJ_i(\omega)\frac{e^{-ik_x x}}{k_x}\frac{e^{ik_x\delta}-1}{k_x}\sin\left(k_y\frac{w}{2}\right)\frac{\sin(k_z l_i/2)}{k_z}e^{-ik_z z_i}, \tag{3.8}$$

$$H_y^{(i)}(x;k_y,k_z) = 2iJ_i(\omega)\frac{e^{-ik_x x}}{k_x}\frac{e^{ik_x\delta}-1}{k_y}\sin\left(k_y\frac{w}{2}\right)\frac{\sin(k_z l_i/2)}{k_z}e^{-ik_z z_i}, \tag{3.9}$$

where $k_x = \sqrt{(\omega/c)^2 - k_y^2 - k_z^2}$, z_i are the z-coordinates of the centers of the striplines and the total current is given by $J_i w\delta$. The generated magnetic field is perpendicular to the stripline axis, i.e. $H_z = 0$, and $k_x H_x(x;k_y,k_z) = k_y H_y(x;k_y,k_z)$. Since $l \gg w$, the magnetic field oscillates as function of k_z with a short period of $4\pi/l$, while it oscillates with k_y with a much longer period of $4\pi/w$ (Fig. 3.7A). For a frequency $\omega/(2\pi) \sim 2$ GHz, $k_0 \equiv \omega/c = 4.19$ rad/m with characteristic wavelength $\lambda_0 = 2\pi/k_0 = 0.15$ m. The wavelength of the excited spin waves is much smaller than this scale, indicating that $\sqrt{k_y^2 + k_z^2} \gg \omega/c$. Thus, $k_x \to i\sqrt{k_y^2 + k_z^2} = i\kappa$. With $\kappa\delta \ll 1$:

$$H_x^{(i)}(x;k_y,k_z) = -2iJ_i(\omega)e^{\kappa x}\frac{e^{-\kappa\delta}-1}{\kappa^2}\sin\left(k_y\frac{w}{2}\right)\frac{\sin(k_z l_i/2)}{k_z}e^{-ik_z z_i},$$
$$H_y^{(i)}(x;k_y,k_z) = 2J_i(\omega)e^{\kappa x}\frac{e^{-\kappa\delta}-1}{\kappa k_y}\sin\left(k_y\frac{w}{2}\right)\frac{\sin(k_z l_i/2)}{k_z}e^{-ik_z z_i}. \tag{3.10}$$

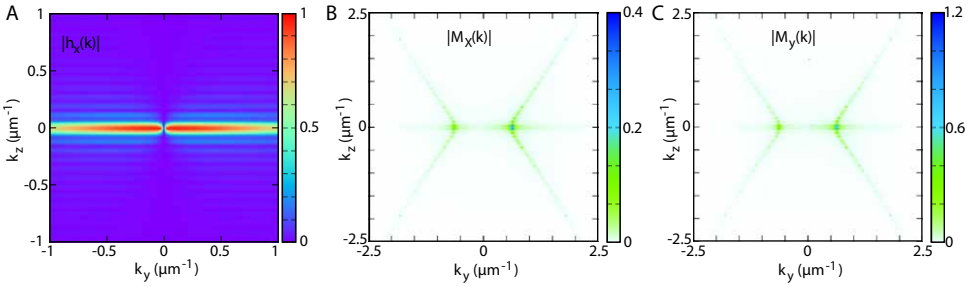

Figure 3.7: Drive field and excited magnetization in reciprocal space. **(A)** $x-$component of the magnetic field generated by the stripline in momentum space. **(B)-(C)** Resulting transverse magnetization amplitude, for $\alpha_G = 1\times10^{-4}$, $\omega = 2.29$ GHz, $\mu_0 M_s = 0.178$ T, and applied magnetic field $B_0 = 20$ mT. Note the different scales used for plotting $|M_x|$ and $|M_y|$.

The magnetic field distribution in $\mathbf{k}$-space is plotted in Fig. 3.7A for the sample dimensions specified above, emphasizing the fast k_z oscillations. A microwave excitation with field components $h_x = \pm i h_y$ is circularly polarized. The relation

$$H_x(x;k_y,k_z) = -i(k_y/\kappa)H_y(x;k_y,k_z). \tag{3.11}$$

implies that when $|k_y| \ll |k_z|$, $|H_x| \ll |H_y|$, so the radiation is nearly linearly-polarized along the $\hat{\mathbf{y}}$-direction (in momentum space). On the other hand, when $|k_y| \gg |k_z|$, $H_x(x;k_y,k_z) \to -i\,\mathrm{sgn}(k_y)H_y(x;k_y,k_z)$ is nearly right- (left-) circularly polarized for positive (negative) k_y. The polarization-momentum locking of the stripline magnetic field is responsible for the chiral pumping of circularly-polarized spin waves [24, 30, 47].

Excited magnetization The stripline magnetic field excites spin waves in the YIG film. In the mixed position and momentum space, the dynamic magnetization $\mathbf{M}(x,\mathbf{k},\omega)$

reads in linear response [24, 30, 47]

$$M_\alpha(x,\mathbf{k},\omega) = \frac{1}{d}\int_{-d}^{0} dx' \chi_{\alpha\beta}(x,x',\mathbf{k},\omega) H_\beta(x',\mathbf{k},\omega) \tag{3.12}$$

where we sum over repeated Cartesian indices $\alpha,\beta = \{x,y,z\}$. γ is the electron gyromagnetic ratio and the spin susceptibility reads [24]

$$\chi_{\alpha\beta}(x,x',\mathbf{k},\omega) = -\gamma\mu_0 M_s m_\alpha^{\mathbf{k}}(x) m_\beta^{\mathbf{k}*}(x') \frac{1}{\omega-\omega_{\mathbf{k}}+i\Gamma_{\mathbf{k}}}. \tag{3.13}$$

Here, $m_\alpha^{\mathbf{k}}(x)$ characterize the ellipticity of the magnetization precession associated with the spin waves (see Eqs. 3.15 and 3.17), and $\Gamma_{\mathbf{k}} = 2\alpha_G\omega_{\mathbf{k}}$ is the Gilbert damping of the spin waves with frequency $\omega_{\mathbf{k}}$.

For the parameters of our experiments, the spin waves are in the dipolar-exchange regime with strongly anisotropic dispersion. For the long wavelengths considered here, the magnetization is homogeneous across the film thickness, which allows for an analytical treatment. The spin-wave dispersion for free magnetization boundary conditions reads [24, 30, 47]

$$\omega_{\mathbf{k}} = \gamma\mu_0 M_s \sqrt{\left[\Omega_H + \alpha_{ex}k^2 + 1 - f(|k_y|)\right]\left[\Omega_H + \alpha_{ex}k^2 + (k_y^2/k^2) f(|k_y|)\right]}, \tag{3.14}$$

where α_{ex} is the exchange stiffness, $\Omega_H \equiv B_0\cos(\phi)/\mu_0 M_s$, and

$$f(|k_y|) = 1 - \frac{1}{|k_y|d} + \frac{1}{|k_y|d}\exp(-|k_y|d).$$

At long wavelengths, m_x and m_y are homogeneous across the film thickness and given by

$$m_x = \sqrt{\frac{\mathscr{D}+1}{(\mathscr{D}-1)}}, \quad m_y = i\sqrt{\frac{\mathscr{D}-1}{(\mathscr{D}+1)}}, \tag{3.15}$$

with

$$\mathscr{D} = \frac{1/2 - (1/2)\left(1+k_y^2/k^2\right) f(|k_y|)}{\omega_{\mathbf{k}}/(\mu_0\gamma M_s) - \left(\Omega_H + \alpha_{ex}k_y^2 + 1/2\right) + (1/2)\left(1-k_y^2/k^2\right) f(|k_y|)}. \tag{3.16}$$

We define the ellipticity parameter

$$\eta = \frac{|m_x|}{|m_y|} = \frac{\mathscr{D}+1}{\mathscr{D}-1}. \tag{3.17}$$

In the dipolar regime, the spin waves precess elliptically. When $\mathbf{k}\to 0$, $f(|k_y|)\to 0$, $\omega_{\mathbf{k}} \to \mu_0\gamma M_s\sqrt{\Omega_H(\Omega_H+1)}$ (corresponding to the FMR frequency), $\mathscr{D}\to -1-2\Omega_H-2\sqrt{\Omega_H(\Omega_H+1)}$. When $\Omega_H\to 0$ with a small static magnetic field, $\mathscr{D}\to -1-2\sqrt{\Omega_H}$, $|m_y| \gg |m_x|$, leading to a (nearly) linearly-polarized Kittel mode. When k is large, the exchange interaction dominates and the spin waves are right-circularly polarized.

We plot the calculated excited transverse magnetization amplitude in momentum space in Fig. 3.7B-C with parameters similar to those in Fig. 3.4F, i.e. $M_s = 1.42 \cdot 10^5$ A/m, $\alpha_G = 1 \times 10^{-4}$, $\omega/2\pi = 2.29$ GHz. The momentum distribution of the resonantly excited spin waves reflects the hyperboles formed by the cut through the anisotropic spin wave dispersion at the given frequency. The excitation becomes unidirectional when the spin waves are circularly-polarized [24, 47], in which case only those with positive values of k_y are excited. Due to the YIG thickness much smaller than the wavelengths considered, this chirality is not the intrinsic one of Damon-Eshbach surface modes, which exist only in much thicker films

The real part of the inverse Fourier transform of Eq. 3.12 gives the observable spatiotemporal magnetization

$$\mathbf{M}_\alpha(\boldsymbol{\rho}, t) = \frac{1}{4\pi^2} \iint d\mathbf{k} e^{i\boldsymbol{\rho}\cdot\mathbf{k} - i\omega t} \mathbf{M}_\alpha(x, \mathbf{k}) \tag{3.18}$$

with $\boldsymbol{\rho} = (y, z)$. Using this equation, we calculate a snapshot of the dynamic magnetization when spin waves are driven by a stripline as in Fig. 3.4 (Fig. 3.8). We observe interference of spin waves with frequency ω. Triangular areas of weak and strong excitation exist at the sides and in front of the stripline, respectively, with a spin-wave focus point at the vertex of the latter triangle. These features can be understood from the anisotropy of the spin-wave dispersion that leads to a critical opening angle of available spin-wave momenta at a given frequency.

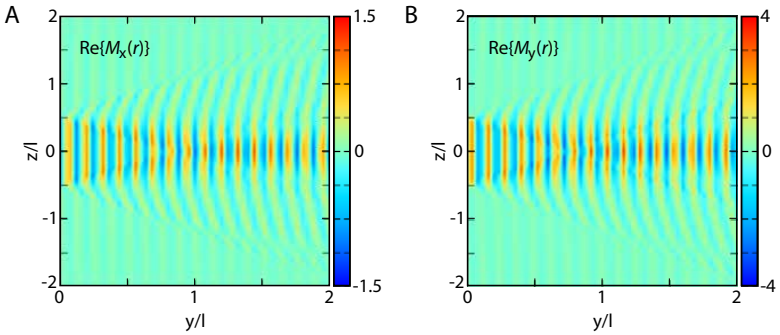

Figure 3.8: Spatial profile of the excited magnetization. Spatial profile of the out-of-plane **(A)** and in-plane **(B)** of the transverse magnetization oscillations excited by a single stripline, located at $y = 0$ between $z/l = -0.5$ and $z/l = +0.5$.

DIPOLAR FIELD AND RABI FREQUENCY

When the frequency of the magnetic stray field generated by a spin wave matches an NV ESR frequency, it can drive Rabi rotations of the NV spin if it has a circularly polarized component of the correct handedness. Here we describe the spin-wave induced Rabi driving of the NV spins.

Dipolar field generated by an oscillating magnetization The magnetic field generated by a magnetization pattern can be calculated using Coulomb's law [45]

$$\mathbf{B}_\beta(\mathbf{r},t) = \frac{\mu_0}{4\pi}\partial_\beta\partial_\alpha \int d\mathbf{r}' \frac{\mathbf{M}_\alpha(\mathbf{r}',t)}{|\mathbf{r}-\mathbf{r}'|}. \tag{3.19}$$

By substituting the magnetization from Eq. (3.18) and using the Coulomb integral

$$\int d\mathbf{r}' \frac{e^{i\mathbf{k}\cdot\boldsymbol{\rho}'} f(x')}{|\mathbf{r}-\mathbf{r}'|} = \frac{2\pi}{k} e^{i\mathbf{k}\cdot\boldsymbol{\rho}} \int dx' e^{-|x-x'|k} f(x'), \tag{3.20}$$

where $k = |\mathbf{k}|$, we obtain the magnetic field above the film ($x > 0$) [24, 30, 47]

$$B_{\mathrm{SW},x}(x,\mathbf{k},t) = \frac{\mu_0}{2} e^{-kx-i\omega t}(1-e^{-kd})\left(M_x(\mathbf{k}) - i\frac{k_y}{k}M_y(\mathbf{k})\right), \tag{3.21}$$

with $B_{\mathrm{SW},y}(\mathbf{k}) = -i(k_y/k)B_{\mathrm{SW},x}(\mathbf{k})$, and $B_{\mathrm{SW},z}(\mathbf{k}) = -i(k_z/k)B_{\mathrm{SW},x}(\mathbf{k})$. Thus, when $|k_z| \ll |k_y|$, $B_{\mathrm{SW},y}(\mathbf{k}) = -i\,\mathrm{sign}(k_y)B_{\mathrm{SW},x}(\mathbf{k})$, i.e. the polarization and momentum are locked. $B_{\mathrm{SW},(x,y)}$ vanishes for negative k_y when the spin waves are right circularly-polarized since $M_x(\mathbf{k}) - iM_y(\mathbf{k})k_y/k \to 0$ [24, 47]. The right-forward dipolar field is left-circularly polarized.

In real space, the stray field generated by the spin wave is given by the real part of the inverse Fourier transform

$$\mathbf{B}_{\mathrm{SW}}(x,\boldsymbol{\rho},t) = \frac{1}{4\pi^2}\iint e^{i\boldsymbol{\rho}\cdot\mathbf{k}}\mathbf{B}_{\mathrm{SW}}(x,\mathbf{k},t)d\mathbf{k}. \tag{3.22}$$

A snapshot of the spin-wave stray field at a distance x_0 above the film is plotted in Fig. 3.9. Since the distance to the film is much smaller than the relevant wavelengths, the interference pattern of the spin waves is well resolved. We note that $|B_{\mathrm{SW},z}| \ll |B_{\mathrm{SW},x}|, |B_{\mathrm{SW},y}|$ because the excited spin waves propagate almost perpendicular to the stripline. The strong chirality (unidirectionality) is caused by both the stripline magnetic field (see in Fig. 3.7) and the stray field from the spin waves [24, 30, 47]. All Cartesian vector components exert a torque on the NV center spin, which is oriented at an angle to the film. The dipolar field shows a focal point with large amplitude, which can be controlled by tuning the magnetic field and stripline frequency, which could be interesting for spintronic applications.

The field of a spin wave that is characterized by $|k_z| \ll |k_y|$ (therefore $\mathbf{k} \perp \mathbf{M}$, corresponding to a Damon-Eshbach geometry and an effectively one-dimensional configuration) is given by ($x > 0$)

$$\mathbf{B}_{\mathrm{SW}}(x,\mathbf{k},t) = -\frac{\mu_0}{2} e^{-kx-i\omega t}(1-e^{-kd})M_y(\mathbf{k})\left(1+\mathrm{sign}(k_y)\eta\right)\left(\hat{y}+i\,\mathrm{sign}(k_y)\hat{x}\right), \tag{3.23}$$

where we used $M_x = -i\eta M_y$. To arrive at the Eqns. 3.2 and 3.3, we calculate the field of a traveling spin wave given by the real part of $\mathbf{m}_\perp = m_\perp^0 e^{i(k_0 y-\omega t)}(\hat{y} - i\eta\hat{x})$. The Fourier transform of the y-component is

$$M_y(k_y) = m_\perp^0 2\pi\delta(k_y - k_0). \tag{3.24}$$

Substituting into Eq. 3.23 and taking the inverse Fourier transform, we get Eq. 3.2

$$\mathbf{B}_{\mathrm{SW}}(y) = -\mathrm{Re}[\frac{\mu_0 m_\perp^0}{2} e^{-|k_0|x_0} e^{i(k_0 y-\omega t)}(1-e^{-|k_0|d})(1+\mathrm{sign}(k_0)\eta)(\hat{y}+i\,\mathrm{sign}(k_0)\hat{x})] \quad (3.25)$$

$$= -\mathrm{Re}[B_{\mathrm{SW}}^0 e^{i(k_0 y-\omega t)}(\hat{y}+i\,\mathrm{sign}(k_0)\hat{x})] \quad (3.26)$$

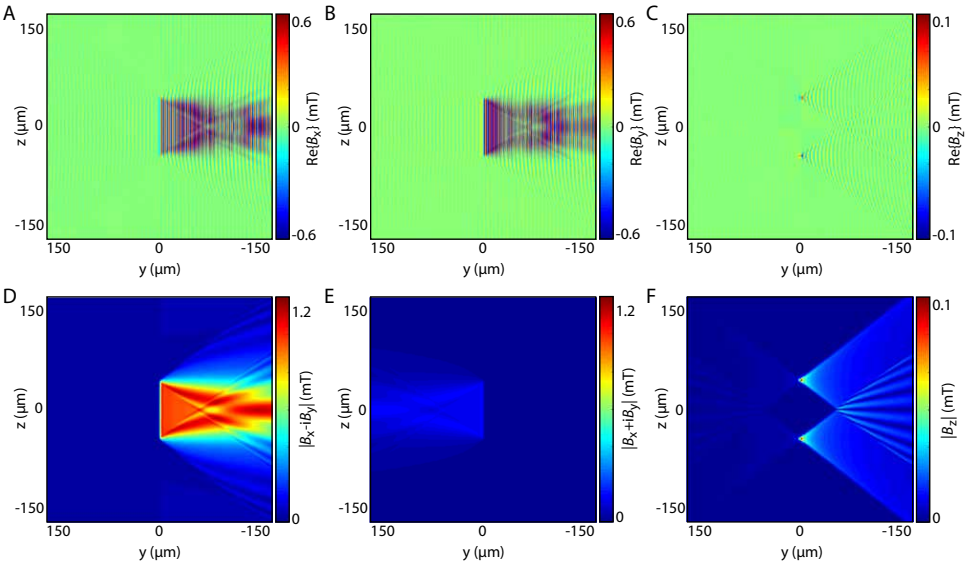

Figure 3.9: Spatial profile of the dipolar field generated by spin waves. Snapshot of the stray field in real space at $t = 0$ for a microwave driving with a frequency $\omega = 2.29$ GHz and a stripline current of 0.7 mA at a distance x_0 above the film. The stripline is located at $y = 0$, $z \in [-40, 40]$ μm. The damping coefficient is $\alpha_{\mathrm{G}} = 10^{-4}$.

Calculation of the Rabi frequency The dynamic magnetic field generated by the spin waves can induce transitions between the spin states of the NV center when its frequency matches an NV ESR frequency as described by the NV spin Hamiltonian. We write the dynamic part of the magnetic field as

$$\mathbf{B}_{\mathrm{SW}}(y) = \mathrm{Re}[(B_x\hat{x} + B_y\hat{y} + B_z\hat{z})e^{-i\omega t}] \quad (3.27)$$

In the local coordinates of the NV center, with the z'-direction along the applied static magnetic field (therefore along the NV axis), the field amplitudes becomes

$$B_{x'} = B_x\cos\phi - B_z\sin\phi, \quad (3.28)$$

$$B_{y'} = B_y, \quad (3.29)$$

$$B_{z'} = B_z\cos\phi + B_x\sin\phi. \quad (3.30)$$

The Hamiltonian describing the NV spin dynamics is given by

$$H_{\mathrm{NV}} = DS_z^2 + \gamma \mathbf{B}' \cdot \mathbf{S} \tag{3.31}$$

where $\mathbf{S} = (S_x, S_y, S_z)$ are the Pauli matrices for a spin 1 and $D/2\pi = 2.87$ GHz is the zero-field frequency. The two magnetic-dipole allowed transitions between the $m_s = 0$ and the $m_s = \pm 1$ states are driven by magnetic fields of opposite handedness. When the magnetic-field frequency ω matches one of the NV ESR frequencies $D \pm \gamma B_0$, the NV spin will Rabi oscillate between the corresponding $m_s = 0$ and $m_s = \pm 1$ states with a Rabi frequency given by

$$\omega_{\mathrm{Rabi}}^{\pm} = \frac{\gamma}{\sqrt{2}} \left| B_{x'} \pm i B_{y'} \right|. \tag{3.32}$$

We use Eq. 3.32 to calculate the spin-wave induced Rabi frequency caused by the spatial magnetization profile shown in Fig. 3.8. The Rabi frequency closely resembles the spatial magnetization profile, including the presence of caustic beams and a focal point (Fig. 3.10).

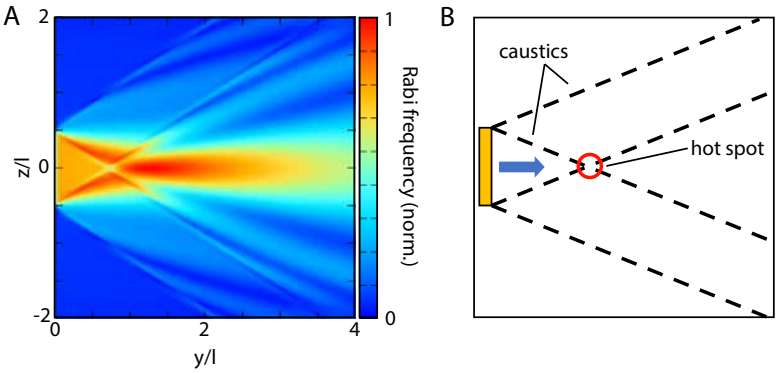

Figure 3.10: Calculated spatial map of the Rabi frequency for a single stripline. **(A)** Rabi frequency calculated from the dipolar field without the (small) direct contribution from the stripline at $y = 0$ and $z/l \in [-0.5, 0.5]$. **(B)** Schematics indicating the emergence of caustic spin-wave beams and the "hot spot" where energy gets focussed.

When the NV ω_- transition is driven by a resonant Damon-Eshbach spin wave with $k_0 > 0$, we get

$$\omega_{\mathrm{Rabi}}^{-} = \sqrt{2}\gamma B_{\mathrm{SW}}^0 \cos^2 \frac{\phi}{2}. \tag{3.33}$$

If the NV spin is also driven by a magnetic field that is given by $\mathrm{Re}[\mathbf{B}_{\mathrm{REF}} e^{-i\omega t}]$, we get

$$\omega_{\mathrm{Rabi}}^{-} = \frac{\gamma}{\sqrt{2}} \left| 2B_{\mathrm{SW}}^0 e^{ik_0 y} \cos^2 \frac{\phi}{2} + B_{\mathrm{REF,x'}} - i B_{\mathrm{REF,y'}} \right|. \tag{3.34}$$

from which follows Eq. 3.3. Including a damping parameter into Eq. 3.34, we fit the data of Fig. 3.2B, from which we extract the spin-wave amplitude $m_\perp^0$ (using the ellipticity

parameter calculated with Eq. 3.17) and the spin-wave damping:

$$\omega_{\text{Rabi}}^{-} = \frac{\gamma}{\sqrt{2}} \left| 2B_{\text{SW}}^{0} e^{ik_0 y - y/y_0} \cos^2 \frac{\phi}{2} + e^{i\theta} B_{\text{REF}} \right|. \tag{3.35}$$

Here, y_0 is the spin-wave decay length from which the Gilbert damping parameter is extracted using $y_0 = v_g/(2\omega\alpha_G)$, with v_g the group velocity, leading to $\alpha_G = 1.2(1) \cdot 10^{-4}$. The main contribution to the uncertainty is caused by the uncertainty in the NV-YIG distance, which we measured to be 1.8(2) µm (see section 3.5.1) at the location of the stripline and which increases by about 0.4 µm/mm as estimated from the optical interference fringes visible in Fig. 3.1B (the distance change between two fringes is given by $\lambda_0/2$, with λ_0 the wavelength of the light in air). Using Eq. 3.35, we also fitted the data shown in Fig. 3.3B, with B_{REF} given by Eq. 3.5.

EFFECT OF MAGNETIC FIELD MISALIGNMENT ON THE OBSERVED SPIN-WAVE PATTERNS

To explain the asymmetry along $\hat{\mathbf{z}}$ of the observed spin-wave patterns in Fig. 3.4, we repeat the calculation of Fig. 3.4C with the introduction of a 5° misalignment between the static field and the stripline (Fig. 3.11). The tilt is from the $\hat{\mathbf{z}}$ toward the $-\hat{\mathbf{y}}$ axis.

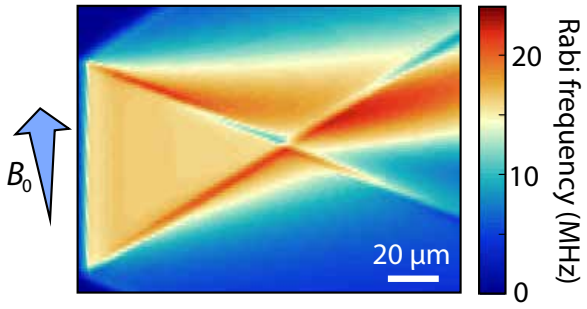

Figure 3.11: Effect of a small angle between the stripline and the in-plane component of the static field $\mathbf{B_0}$. Calculated spatial map of the Rabi frequency when the in-plane projection of the static field (B_0) is oriented at a 5° angle from the stripline.

INFLUENCE OF THE SPIN-WAVE PROPAGATION DIRECTION ON THE FIELD PROFILE

As previously explained (Eq. 3.32), right(left)-propagating spin waves generate a circularly-polarized field with handedness that drives the ω_- (ω_+) transition. Moreover, for perfectly circular polarization, the right(left)-propagating waves only generate a field above (below) the film, which can be simply explained by cancellation of the field contributions of neighbouring spins (Fig. 3.12). For elliptical polarization, the field suppression is not complete.

INTERFERENCE BETWEEN SPIN WAVES GENERATED BY TWO ADJACENT STRIPLINES

Finally, we calculate the interference pattern generated by two striplines on the YIG film, with centers separated by 200 µm. With $l_1 = 100$ µm and $l_2 = -100$ µm in Eq. 3.10 and

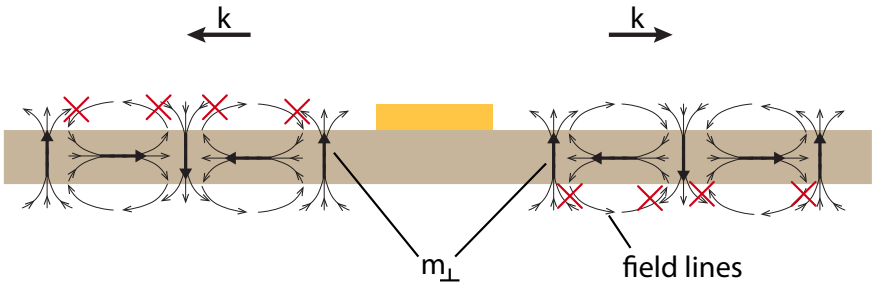

Figure 3.12: Magnetic field generated by spin waves propagating to the left and right. The magnetic stray field generated by a spin wave is the sum of the fields generated by the individual precessing spins in the magnet. The phases of the spin waves traveling to the right interfere constructively/destructively above/below the film, and vice versa for spin waves traveling to the left.

considering the π phase difference between the two striplines

$$H_x(x;k_y,k_z) = -2iJ(\omega)e^{\kappa x}\frac{e^{-\kappa\delta}-1}{\kappa^2}\sin\left(k_y\frac{w}{2}\right)\frac{\sin(k_z l/2)}{k_z}(e^{-ik_z z_1}-e^{-ik_z z_2}), \tag{3.36}$$

$$H_y(x;k_y,k_z) = 2J(\omega)e^{\kappa x}\frac{e^{-\kappa\delta}-1}{\kappa k_y}\sin\left(k_y\frac{w}{2}\right)\frac{\sin(k_z l/2)}{k_z}(e^{-ik_z z_1}-e^{-ik_z z_2}). \tag{3.37}$$

By substitution into Eqs. 3.12 and 3.21, we obtain the Rabi frequencies of the NV center in Fig. 3.13. The spin-wave interference is clearly reflected in the Rabi frequency.

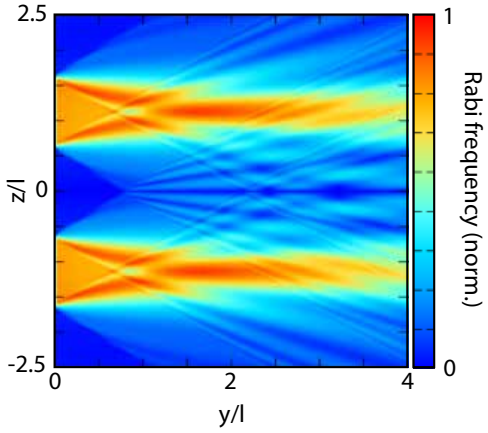

Figure 3.13: Calculated spatial map of the Rabi frequency induced by two adjacent striplines. We observe interference of spin waves generated by two striplines located at $y = 0$ for $z \in \pm[0.5, 1.5]$.

BIBLIOGRAPHY

[1] V. V. Kruglyak, S. O. Demokritov, and D. Grundler, "Magnonics", Journal of Physics D: Applied Physics **43**, 264001 (2010).

[2] A. V. Chumak, V. I. Vasyuchka, A. A. Serga, and B. Hillebrands, "Magnon spintronics", Nature Physics **11**, 453 (2015).

[3] K. Vogt et al., "Realization of a spin-wave multiplexer", Nature Communications **5**, 3727 (2014).

[4] A. V. Chumak, A. A. Serga, and B. Hillebrands, "Magnon transistor for all-magnon data processing", Nature Communications **5**, 4700 (2014).

[5] L. J. Cornelissen, J. Liu, B. J. van Wees, and R. A. Duine, "Spin-Current-Controlled Modulation of the Magnon Spin Conductance in a Three-Terminal Magnon Transistor", Physical Review Letters **120**, 097702 (2018).

[6] V. E. Demidov et al., "Synchronization of spin Hall nano-oscillators to external microwave signals.", Nature communications **5**, 3179 (2014).

[7] Q. Wang et al., "Reconfigurable nanoscale spin-wave directional coupler", Science Advances **4**, e1701517 (2018).

[8] T. Warwick et al., "A scanning transmission x-ray microscope for materials science spectromicroscopy at the advanced light source", Review of Scientific Instruments **69**, 2964 (1998).

[9] V. Sluka et al., "Emission and propagation of 1D and 2D spin waves with nanoscale wavelengths in anisotropic spin textures", Nature Nanotechnology **14**, 328 (2019).

[10] T. Sebastian, K. Schultheiss, B. Obry, B. Hillebrands, and H. Schultheiss, "Micro-focused Brillouin light scattering: imaging spin waves at the nanoscale", Frontiers in Physics **3**, 35 (2015).

[11] Y. Acremann et al., "Imaging precessional motion of the magnetization vector", Science **290**, 492 (2000).

[12] L. Rondin et al., "Magnetometry with nitrogen-vacancy defects in diamond", Reports on Progress in Physics **77**, 056503 (2014).

[13] F. Casola, T. van der Sar, and A. Yacoby, "Probing condensed matter physics with magnetometry based on nitrogen-vacancy centres in diamond", Nature Reviews Materials **3**, 17088 (2018).

[14] I. Gross et al., "Real-space imaging of non-collinear antiferromagnetic order with a single-spin magnetometer", Nature **549**, 252 (2017).

[15] L. Rondin et al., "Stray-field imaging of magnetic vortices with a single diamond spin.", Nature communications **4**, 2279 (2013).

[16] Y. Dovzhenko et al., "Magnetostatic twists in room-temperature skyrmions explored by nitrogen-vacancy center spin texture reconstruction", Nature Communications **9**, 2712 (2018).

[17] T. van der Sar, F. Casola, R. Walsworth, and A. Yacoby, "Nanometre-scale probing of spin waves using single-electron spins.", Nature communications **6**, 7886 (2015).

[18] C. Du et al., "Control and local measurement of the spin chemical potential in a magnetic insulator", Science **357**, 195 (2017).

[19] P. Andrich et al., "Long-range spin wave mediated control of defect qubits in nanodiamonds", npj Quantum Information **3**, 28 (2017).

[20] D. Kikuchi et al., "Long-distance excitation of nitrogen-vacancy centers in diamond via surface spin waves", Applied Physics Express **10**, 103004 (2017).

[21] C. S. Wolfe et al., "Off-resonant manipulation of spins in diamond via precessing magnetization of a proximal ferromagnet", Physical Review B **89**, 180406 (2014).

[22] L. Thiel et al., "Probing magnetism in 2D materials at the nanoscale with single-spin microscopy", Science **364**, 973 (2019).

[23] A. A. Serga, A. V. Chumak, and B. Hillebrands, "YIG magnonics", Journal of Physics D: Applied Physics **43**, 264002 (2010).

[24] T. Yu, Y. M. Blanter, and G. E. W. Bauer, "Chiral Pumping of Spin Waves", Physical Review Letters **123**, 247202 (2019).

[25] C. Dubs et al., "Sub-micrometer yttrium iron garnet LPE films with low ferromagnetic resonance losses", Journal of Physics D: Applied Physics **50**, 204005 (2017).

[26] T. Schneider et al., "Nondiffractive subwavelength wave beams in a medium with externally controlled anisotropy", Physical Review Letters **104**, 197203 (2010).

[27] R. Gieniusz et al., "Single antidot as a passive way to create caustic spin-wave beams in yttrium iron garnet films", Applied Physics Letters **102**, 102409 (2013).

[28] M. Mohseni et al., "Backscattering Immunity of Dipole-Exchange Magnetostatic Surface Spin Waves", Physical Review Letters **122**, 197201 (2019).

[29] J. R. Eshbach and R. W. Damon, "Surface magnetostatic modes and surface spin waves", Physical Review **118**, 1208 (1960).

[30] J. Chen et al., "Spin wave propagation in ultrathin magnetic insulators with perpendicular magnetic anisotropy", Applied Physics Letters **114**, 212401 (2019).

[31] J. P. Tetienne et al., "Quantum imaging of current flow in graphene", Science Advances **3**, e1602429 (2017).

[32] T. Rosskopf et al., "Investigation of surface magnetic noise by shallow spins in diamond", Physical Review Letters **112**, 147602 (2014).

[33] C. Wei, A. S. Windsor, and N. B. Manson, "A strongly driven two-level atom revisited: Bloch-Siegert shift versus dynamic Stark splitting", Journal of Physics B: Atomic, Molecular and Optical Physics **30**, 21 (1997).

[34] B. Flebus and Y. Tserkovnyak, "Quantum-Impurity Relaxometry of Magnetization Dynamics", Physical Review Letters **121**, 187204 (2018).

[35] K. Arai et al., "Fourier magnetic imaging with nanoscale resolution and compressed sensing speed-up using electronic spins in diamond", Nature Nanotechnology **10**, 859 (2015).

[36] G. Balasubramanian et al., "Nanoscale imaging magnetometry with diamond spins under ambient conditions", Nature **455**, 648 (2008).

[37] L. Thiel et al., "Quantitative nanoscale vortex imaging using a cryogenic quantum magnetometer", Nature Nanotechnology **11**, 677 (2016).

[38] M. Pelliccione et al., "Scanned probe imaging of nanoscale magnetism at cryogenic temperatures with a single-spin quantum sensor", Nature Nanotechnology **11**, 700 (2016).

[39] E. Schaefer-Nolte, F. Reinhard, M. Ternes, J. Wrachtrup, and K. Kern, "A diamond-based scanning probe spin sensor operating at low temperature in ultra-high vacuum", Review of Scientific Instruments **85**, 013701 (2014).

[40] J. M. Cai et al., "Robust dynamical decoupling with concatenated continuous driving", New Journal of Physics **14**, 113023 (2012).

[41] S. E. Lillie et al., "Imaging Graphene Field-Effect Transistors on Diamond Using Nitrogen-Vacancy Microscopy", Physical Review Applied **12**, 024018 (2019).

[42] S. Bogdanović et al., "Robust nano-fabrication of an integrated platform for spin control in a tunable microcavity", APL Photonics **2**, 126101 (2017).

[43] M. A. Schoen, J. M. Shaw, H. T. Nembach, M. Weiler, and T. J. Silva, "Radiative damping in waveguide-based ferromagnetic resonance measured via analysis of perpendicular standing spin waves in sputtered permalloy films", Physical Review B **92**, 184417 (2015).

[44] B. A. Kalinikos and A. N. Slavin, "Theory of dipole-exchange spin wave spectrum for ferromagnetic films with mixed exchange boundary conditions", Journal of Physics C: Solid State Physics **19**, 7013 (1986).

[45] J. D. Jackson, *Classical Electrodynamics* (Wiley, New York, 1998).

[46] L. Novotny and B. Hecht, *Principles of nano-optics* (Cambridge University Press, Cambridge, 2006).

[47] T. Yu, Y. M. Blanter, and G. E. W. Bauer, "Chiral Pumping of Spin Waves", Physical Review Letters **123**, 247202 (2019).

4

BROADBAND MICROWAVE DETECTION USING ELECTRON SPINS IN A HYBRID DIAMOND-MAGNET SENSOR CHIP

Quantum sensing has developed into a main branch of quantum science and technology. It aims at measuring physical quantities with high resolution, sensitivity, and dynamic range. Electron spins in diamond are powerful magnetic field sensors, but their sensitivity in the microwave regime is limited to a narrow band around their resonance frequency. Here, we realize broadband microwave detection using spins in diamond interfaced with a thin-film magnet. A pump field locally converts target microwave signals to the sensor-spin frequency via the nonlinear spin-wave dynamics of the magnet. Two complementary conversion protocols enable sensing and high-fidelity spin control over a gigahertz bandwidth, allowing characterization of the spin-wave band at multiple gigahertz above the sensor-spin frequency. The pump-tunable, hybrid diamond-magnet sensor chip opens the way for spin-based sensing in the 100-gigahertz regime at small magnetic bias fields.

This chapter has been submitted for publication by **J. J. Carmiggelt**, I. Bertelli, R. W. Mulder, A. Teepe, M. Elyasi, B. G. Simon, G. E. W. Bauer, Y. M. Blanter, and T. van der Sar.

4.1. INTRODUCTION

Electron spins associated with nitrogen-vacancy (NV) defects in diamond are magnetic field sensors that provide high spatial resolution and sensitivity at room temperature [1, 2]. They have been used to study nuclear magnetic resonance at the nanoscale [3, 4], bio- [5], paleo- [6], and solid-state magnetism [7], and electric currents in quantum materials [8, 9]. Most of these applications focus on detecting magnetic fields in the 0-100 megahertz (MHz) frequency range, in which a toolbox of spin-control techniques enables high sensitivity and a tunable detection frequency without requiring a specific electron spin resonance (ESR) frequency [1]. In contrast, NV-based sensing in the microwave regime [1-100 gigahertz (GHz)] currently relies on tuning the ESR to the frequency of interest using a magnetic bias field [10]. This bias field changes the properties of e.g. magnetic or superconducting samples under study [11, 12], for instance by altering their excitation spectrum, which limits its application in materials science. Furthermore, the field must be on the Tesla scale for operation in the 10-100 GHz range [13], making the required magnets large and slow to adjust, precluding the small sensor packaging desired for technological applications.

Here, we enable broadband spin-based microwave sensing by interfacing a diamond chip containing a layer of NV sensor spins with a thin-film magnet. The central concept is that the nonlinear dynamics of spin waves - the collective spin excitations of the magnetic film [14] - locally convert a target signal to the NV ESR frequency under the application of a pump field (Fig. 4.1A-B). We realize a ~1-GHz detection bandwidth at fixed magnetic bias field via four-spin-wave mixing, and microwave detection at multiple GHz above the ESR frequency via difference-frequency generation. The pump-tunable detection frequency enables characterizing the spin-wave band structure despite a multi-GHz detuning and provides insight into the nonlinear spin-wave dynamics limiting the conversion process. Furthermore, the converted microwaves are highly coherent, enabling high-fidelity control of the sensor spins via off-resonant drive fields.

Our hybrid diamond-magnet sensor platform consists of an ensemble of near-surface NV spins in a diamond membrane positioned onto a thin film of yttrium iron garnet (YIG) - a magnetic insulator with low spin-wave damping [14] (Fig. 4.1B). A stripline delivers the "two-color" signal and pump microwave fields to the YIG film, in which they excite spin waves at the signal and pump frequencies, f_s and f_p, respectively. The frequency-converted microwaves at the ESR frequency f_{NV} are detected by measuring the spin-dependent NV photoluminescence under green laser excitation (Methods and Fig. 4.1C). The ESR frequency is fixed by an external magnetic bias field B_{NV} (Fig. 4.1D).

4.2. RESULTS

Our first detection protocol harnesses degenerate four-spin-wave mixing [15–20] - the magnetic analogue of optical four-wave mixing (Fig. 4.2A). In the quasiparticle picture, this process corresponds to the scattering of two "pump" magnons into a "signal" magnon and an "idler" magnon at frequency $f_i = 2f_p - f_s$. This conversion enables the detection

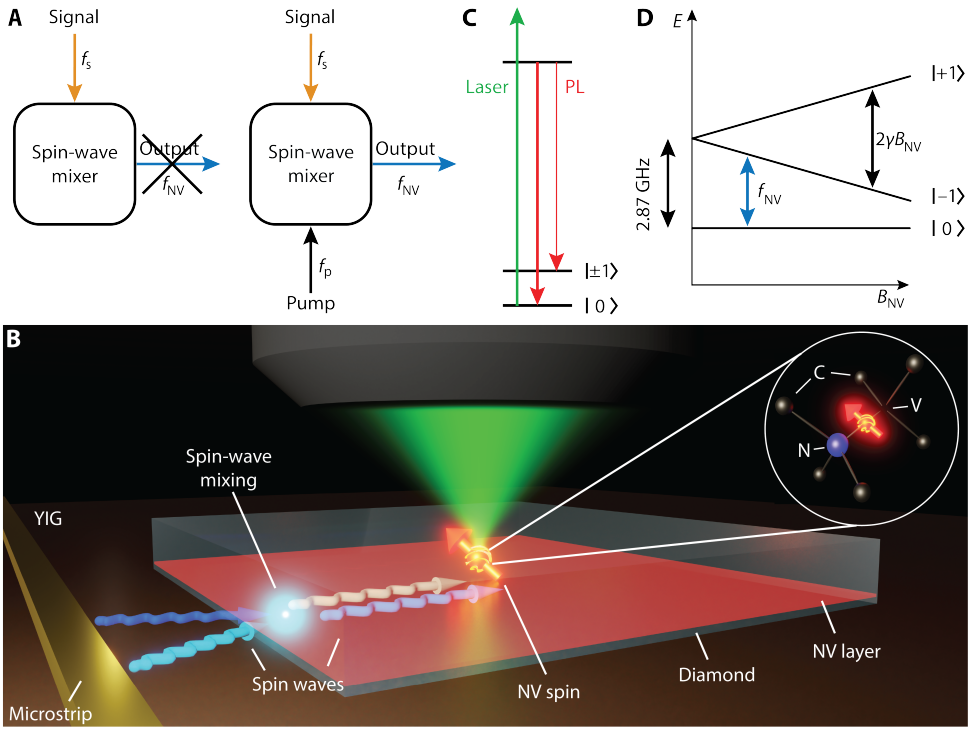

Figure 4.1: Detecting microwave magnetic fields using spins in diamond via on-chip spin-wave-mediated frequency conversion. (**A**) Idea of the experiment. A "spin-wave mixer" uses a pump to convert a microwave signal at frequency f_s to an output frequency f_{NV} that is detectable by nitrogen-vacancy (NV) sensor spins in diamond. (**B**) Sketch of the setup. A diamond with NV centers implanted ~ 10-20 nm below its surface is placed onto a film of yttrium iron garnet (YIG, thickness: 235 nm). A microstrip delivers the signal and pump microwaves, which excite spin waves in the YIG. Spin-wave mixing enables detection of the signal field by converting its frequency to the NV electron spin resonance (ESR) frequency. Inset: Atomic structure of an NV center in the diamond carbon (C) lattice. (**C**) Initialization and readout of the NV spins is achieved through excitation by a green laser and detection of the red photoluminescence (PL). The PL is stronger in the $m_s = |0\rangle$ state than in the $m_s = |\pm 1\rangle$ states. (**D**) NV spin energy levels in the electronic ground state. A magnetic field B_{NV} along the NV axis splits the $m_s = |\pm 1\rangle$ states via the Zeeman interaction. From the four possible configurations in the diamond lattice, we use the NV orientation with in-plane projection parallel to the stripline. f_{NV} denotes the $|0\rangle \leftrightarrow |-1\rangle$ ESR transition frequency.

of a microwave signal that is detuned from the ESR frequency, which would be otherwise invisible in the optical response of the NV centers (Fig. 4.2B). By tuning the frequency of the pump, we enable the detection of signals of specific microwave frequencies (Fig. 4.2C).

We characterize the bandwidth of the four-wave-mixing detection scheme by measuring the NV photoluminescence contrast as a function of the microwave signal frequency and magnetic bias field. As in Fig. 4.2B, when the pump field is switched off, we only detect signals resonant with f_{NV} (Fig. 4.2D). In contrast, when the pump is switched on, a broad band of frequencies becomes detectable (Fig. 4.2E). The bandwidth Δf of ~ 1

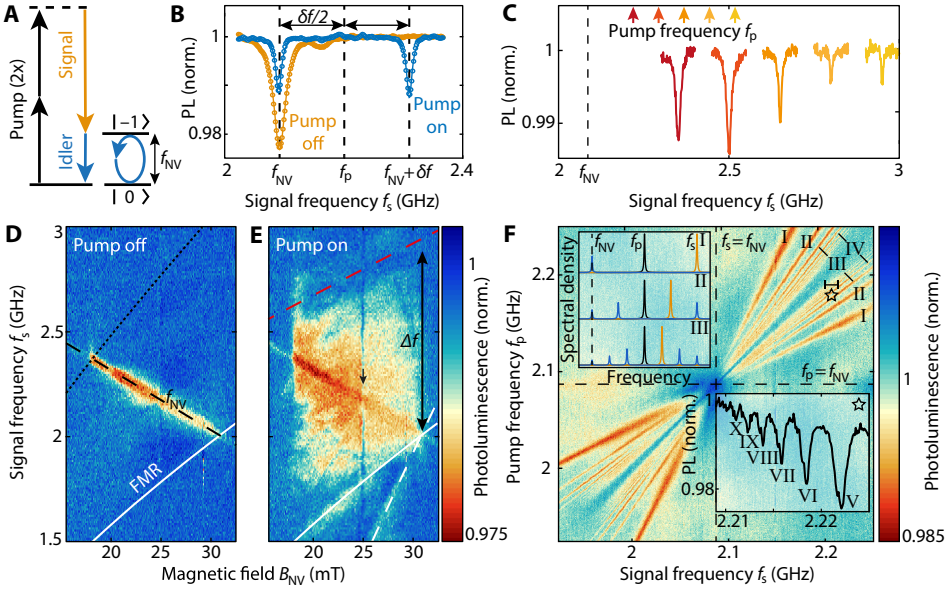

Figure 4.2: Microwave detection via four-spin-wave mixing and frequency combs. (**A**) Energy diagram of four-spin-wave mixing. The signal at frequency f_s stimulates the conversion of the pump to the idler at f_{NV}. (**B**) Normalized NV photoluminescence (PL) versus f_s . Without pump (orange data), an ESR dip is only observed when $f_s = f_{NV}$. With pump at $f_p = f_{NV} + \delta f/2$ (blue data), a signal at $f_s = f_{NV} + \delta f$ becomes detectable. (**C**) Tuning the pump (colored arrows) shifts the detectable signal frequency, observed through the shifting ESR dips (matching colors). (**D**) Normalized NV PL vs f_s and magnetic field in the absence of a pump. Only signals at f_{NV} (dashed black line) can be detected. Dotted black line: Frequency above which three-magnon scattering limits the spin-wave amplitude [21]. White line: Ferromagnetic resonance (FMR) frequency. (**E**) Applying a pump at $f_p = (f_s + f_{NV})/2$ opens a detection window from the FMR up to the second node (dashed red line) in the Fourier spectrum of the stripline field (Fig. 4.7). (Dashed) white line: Signal (Pump) drives FMR. Black arrow: Line of reduced contrast caused by scattering into the first perpendicular standing spin-wave mode [11]. (**F**) Spin-wave comb observed in the PL versus f_s and f_p. Data is normalized (Fig. 4.5). Upper inset: Spectrum (sketch) illustrating the detection of idlers I-III (black: pump, orange: signal, blue: idlers). Lower inset: Linecut along the small black line at the star in the main panel, showing idlers up to the tenth order.

GHz is limited from below by the ferromagnetic resonance (FMR), the spatially homogenous spin-wave mode below which spin waves cannot be excited in our measurement geometry, and from above by the limited efficiency of our 5-micron-wide stripline to excite high-momentum spin waves. As such, the bandwidth can be extended by using narrower striplines or magnetic coplanar waveguides [22].

At 14 dBm signal and pump power, consecutive mixing processes generate higher-order idler modes at discrete and equally spaced frequencies (Fig. 4.2F). Motivated by the success of their optical counterparts in high-precision spectrometry [23], such “spin-wave frequency combs” are of great interest because of potential applications in microwave metrology [20, 24, 25]. We use the spin-wave comb to realize sensitivity to multiple mi-

crowave frequencies by detecting the n-th order idler frequency,

$$f_{\mathrm{i}}^{n} = (n+1) f_{\mathrm{p}} - n f_{\mathrm{s}} \tag{4.1}$$

when it is resonant with the ESR frequency (Fig. 4.2F, upper inset). An increasing number of idler modes appears with increasing drive power (Fig. 4.6), such that at large powers we resolve up to the $n = 10$th idler order (Fig. 4.2F, bottom inset). The shift of the idler frequency is amplified by the integer n over the shift of the signal frequency (Eq. 4.1), leading to a $1/n$ decrease in the linewidth of the NV ESR response [25] (Fig. 4.2F) and a correspondingly enhanced ability to resolve closely spaced signal frequencies.

In addition to enabling off-resonant quantum sensing, the idlers also provide a resource for off-resonant control of spin- or other quantum systems. The resolving of the NV's 3-MHz hyperfine splitting in the idler-driven ESR spectrum (Fig. 4.3A) evidences the high coherence of the microwave field emitted by the idler spin wave, implying that the linewidth is determined by the drive rather than the spin-wave damping [25]. This allows driving coherent NV spin rotations (Rabi oscillations) by pulsing the pump with varying duration τ (Fig. 4.3B).

Remarkably, these Rabi oscillations respond to externally applied microwaves that are detuned by hundreds of MHz from the ESR frequency (Fig. 4.3C). Such magnon-mediated, off-resonant Rabi control is a new instrument in the toolbox of spin-manipulation techniques, providing universal off-resonant quantum control with potential applications in quantum information processing. The idler-driven Rabi frequency exceeds the signal-induced AC Stark shift [26] by about an order of magnitude for the same off-resonant signal power (Fig. 4.8). The decrease of the Rabi frequency with increasing detuning δf (Fig. 4.3C) is the combined result of a reduced spin-wave excitation efficiency at higher frequency, because the stripline is less efficient in exciting spin waves with short wavelengths (Supplementary Information), and a reduced spin-wave scattering strength due to the increasing momentum mismatch between signal and pump spin waves [17–19].

Since the Rabi frequency depends linearly on the idler amplitude [11], it provides insight into the magnetization dynamics in the film. As expected, the idler amplitude initially grows with increasing signal and pump power [15, 20], but then reaches a maximum and starts to decrease (Fig. 4.3D). We attribute the decrease to Suhl instabilities of the second type [16]: Both signal and pump modes decay into a pair of high-momentum magnons beyond a certain threshold amplitude, which drains energy from the idler mode. This interpretation is supported by a model of the four-wave interactions between the dominant two idler modes, the signal and pump modes, and the two pairs of high-momentum "Suhl" magnons (Figs. 4.9 and 4.10). The intermode coupling is induced by exchange and dipolar interactions, as well as crystalline anisotropy, and follows from the leading-order terms in the Holstein-Primakoff expansion [17]. Based on the interacting eight-mode Hamiltonian we compute the steady-state dynamics of the idler mode as a function of pump and signal power (Fig. 4.3E, Supplementary Information), which qualitatively reproduces the observed power dependence in Fig. 4.3D.

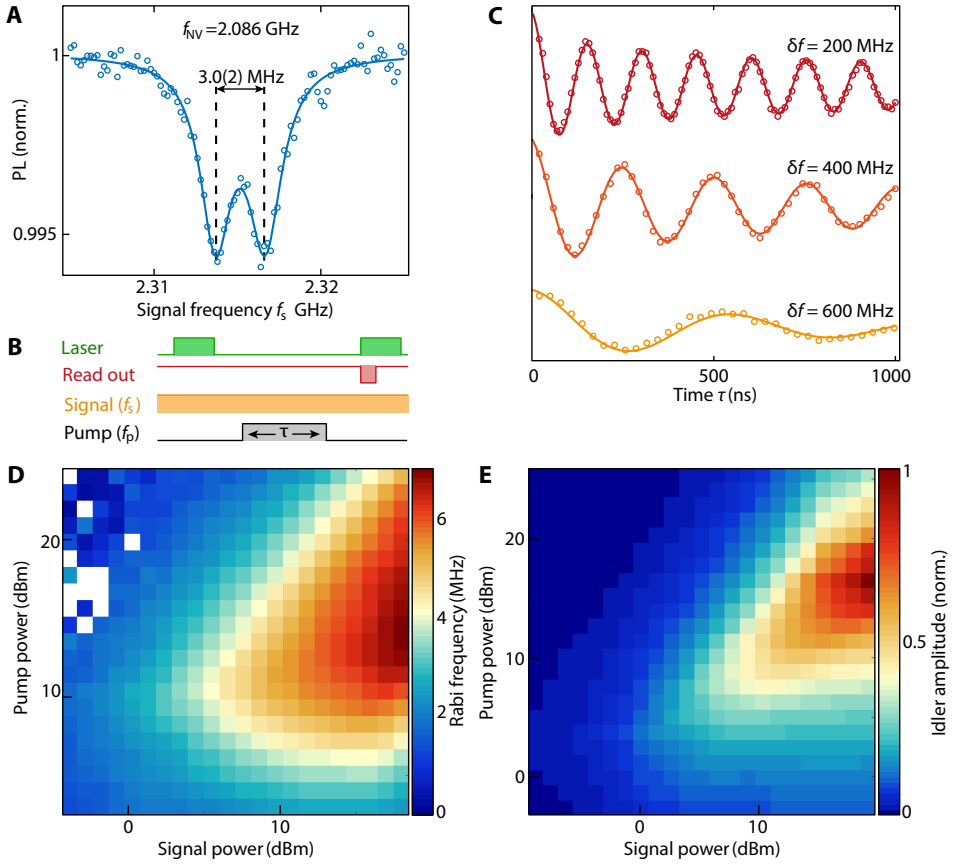

Figure 4.3: Off-resonant quantum control of NV spins via frequency conversion based on four-spin-wave mixing. (**A**) Idler-driven NV ESR spectrum with the ESR frequency at f_{NV} = 2.086 GHz and the pump at f_p = 2.2 GHz. The narrow linewidth of the idler allows resolving the 3-MHz hyperfine splitting associated with the ^{15}N nucleus. (**B**) Pulse sequence for driving coherent NV spin rotations (Rabi oscillations) with an off-resonant signal field. The pulsed pump and continuous-wave signal generate a pulsed idler at f_{NV} that drives Rabi oscillations. (**C**) Optically-detected Rabi oscillations driven by the first-order idler mode for different detuning $\delta f = f_s - f_{NV}$. (**D**) Frequency of the idler-driven Rabi oscillations versus power of the pump (f_p = 2.2 GHz) and signal (f_s = 2.314 GHz). The Rabi frequency initially increases with both signal and pump power, but then decreases because of spin-wave instabilities. This non-monotonic behavior is reproduced by numerical calculations of the normalized idler amplitude in (**E**) (details in the Supplementary Information).

Our second detection protocol relies on difference-frequency generation, which enables down-conversion of GHz signals to MHz frequencies accessible to established quantum sensing techniques [1]. The difference frequency is generated by the longitudinal component of the magnetization under the driving of two spin waves of different frequencies [27] (Fig. 4.4A). In contrast to the four-wave mixing protocol, the converted frequency does not have to lie within the spin-wave band. By tuning the ESR frequency into resonance with the difference frequency (Fig. 4.4B), we detect microwave signals that are

detuned by several gigahertz when $f_p - f_s = \pm f_{NV}$ (Fig. 4.4C). Alternatively, AC magnetometry protocols can provide difference-frequency detection with enhanced sensitivity at arbitrary bias [1]. We only observe ESR contrast when both f_s and f_p are above the FMR (Fig. 4.4D), confirming that the conversion is mediated by spin waves in the YIG. We anticipate the conversion process can also be applied in other magnetic materials to characterize high-frequency magnetic band structures that would otherwise be out of reach for NV magnetometry. Similar to Fig. 4.2E, the conversion is limited by the spin-wave excitation efficiency, which explains the observation of the largest ESR contrast for long-wavelength spin waves (i.e. just above the FMR).

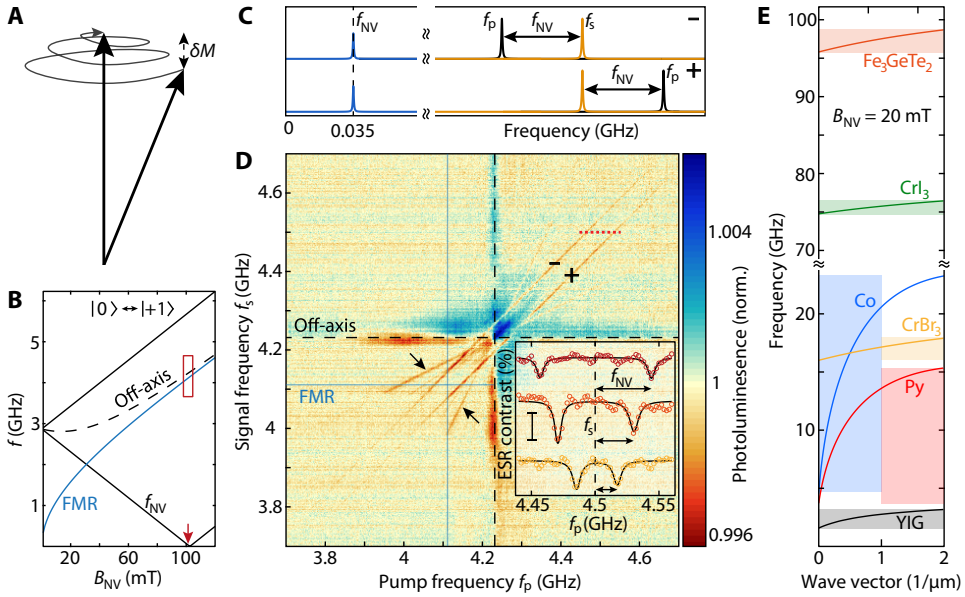

Figure 4.4: Microwave detection via difference-frequency generation. (**A**) Sketch of the spiraling precession of the magnetization M when driven by microwave frequencies f_s and f_p. The longitudinal component of the magnetization oscillates with amplitude δM at the difference frequency ($|f_s - f_p|$), which is detected when resonant with f_{NV}. (**B**) Field dependence of the FMR (solid blue line) and the NV ESR frequencies, with the solid (dashed) black line corresponding to the on-axis (off-axis) NV families. f_{NV} of the on-axis family enters the MHz regime near B_{NV} = 100 mT (red arrow). (**C**) Sketch of the frequency spectrum. Difference-frequency generation creates a detectable signal at f_{NV} when the pump frequency is at $f_p = f_s \pm f_{NV}$. (**D**) Photoluminescence versus f_s and f_p at B_{NV} = 101.3 mT, such that f_{NV} = 35 MHz [red box in (B)]. The parallel, diagonal lines [labeled + and – as in (C)] indicate the difference-frequency detection. Also visible are idler spin waves (indicated by the arrows) generated by four-wave mixing at the off-axis ESR frequency (dashed black lines). The data is normalized, leaving artefacts at the off-axis frequency (Methods). Inset: Line traces at f_s = 4.5 GHz (dotted red line in main panel) for different B_{NV}, showing the shift of the frequency difference resonant with f_{NV}. Scale-bar: 0.1% ESR contrast. (**E**) Sketched spin-wave dispersion of various 100 nm-thick magnets for B_{NV} = 20 mT. Matched color shading highlights the accessible detection bandwidth using a 500-nm-wide stripline.

4.3. CONCLUSIONS

We demonstrate magnon-mediated, spin-based sensing of microwave magnetic fields over a gigahertz bandwidth at fixed magnetic bias field. The frequency of the pump determines the detection frequency, with a detection range that is limited only by the frequencies at which spin waves can be excited efficiently. This range could be extended to the 10-100 GHz scale using materials with a larger magnetization that increases the spin-wave group velocity or crystal anisotropies that increase the spin-wave gap (Fig. 4.4E). The four-spin-wave mixing process, spin-wave frequency combs and oscillations of the longitudinal magnetization used in our protocols have already been observed in other magnets, such as permalloy (Py), Fe, and CoFe [18–20, 28]. The increased spin-wave damping in these materials compared to YIG reduces the spin-wave amplitudes, but this is partially compensated by a larger saturation magnetization that increases the stray fields.

The coherent nature of the frequency conversion enables coherent manipulation of solid-state spins via off-resonant drive fields, as demonstrated here for spins in diamond. This coherence allows combining with advanced spin-manipulation protocols such as heterodyne or dressed-state sensing [29–31] to further enhance the detection capabilities, and opens the way for applications in hybrid quantum technologies [32]. Wide-field readout of NV centers in a larger sensing volume would enhance the microwave sensitivity, which is ultimately limited by thermal spin-wave noise. We envision the detection of free-space microwaves using on-chip microwave-to-spin-wave transducers[33] such as stripline resonators, and the characterization of local microwave generators such as spin-torque oscillators by combining with a suitable magnetic material[34] and applying a pump field. Imaging of the spatial magnetization dynamics generated by spin-wave mixing using scanning-NV magnetometry could provide insight into the spin-wave dispersion and interactions with nanoscale sensitivity [2]. The demonstrated hybrid diamond-magnet sensor platform enables broadband microwave characterization without requiring large magnetic bias fields and opens the way for probing high-frequency magnetic spectra of new materials, such as van-der-Waals magnets.

4.4. MATERIALS AND METHODS

4.4.1. EXPERIMENTAL SETUP

The NV photoluminescence is read out using a confocal microscope described in Ref. [11]. The NV-YIG chip and its fabrication were described in Ref. [21]. It consists of a 2x2x0.05-mm^3 diamond membrane with an estimated near-surface NV density of $10^3/\mu m^2$ placed on top of a 235-nm-thick YIG film grown using liquid phase epitaxy on a 500-µm-thick GGG substrate (Matesy GmbH). The diamond-YIG separation distance is ~ 2 µm, limited by small particles (such as dust) between the diamond and the YIG surfaces. The signal and pump microwaves are generated by two Rohde & Schwarz microwave sources (SGS100A), combined by a Mini-Circuits power combiner (ZFRSC-123-S+, total loss: ~ -10 dB) and amplified by an AR amplifier (30S1G6, amplification: ~ 44 dB). All measurements were performed at room temperature.

4.4.2. NV MICROWAVE MAGNETOMETRY

The four NV-center families are sensitive to microwave magnetic fields at their electron spin resonance (ESR) frequencies, which are determined by the magnetic bias field $\mathbf{B}_{\mathrm{NV}}$ via the NV spin Hamiltonian $H = DS_z^2 + \gamma \mathbf{B}_{\mathrm{NV}} \cdot \mathbf{S}$, with $D = 2.87$ GHz the zero-field splitting, $\gamma = 28$ GHz/T the electron gyromagnetic ratio and $S_{i\in\{x,y,z\}}$ the ith spin-1 Pauli matrix. In this work, we align the field along one of the NV orientations, such that this "on-axis" family has $|0\rangle \leftrightarrow |\pm 1\rangle$ ESR frequencies given by $D \pm \gamma B_{\mathrm{NV}}$ (with $B_{\mathrm{NV}} = |\mathbf{B}_{\mathrm{NV}}|$). For the other three "off-axis" families, the bias field is equally misaligned by $\sim 71^\circ$ due to crystal symmetry, leading to the ESR frequency plotted in Fig. 4B (labeled "Off-axis"). The photoluminescence dips were recorded using continuous-wave microwaves and non-resonant optical excitation at 515 nm. For the Rabi oscillations we first initialize the NV spin in the $|0\rangle$-state via a $\sim$ 1-µs green laser pulse, then we drive the spin using an idler pulse and finally we read out the NV photons in the first 300-400 ns of a second laser pulse.

4.4.3. DATA PROCESSING

The data presented in Figs. 4.2F and 4.4D is normalized by the median of each row and column (Fig. 4.5).

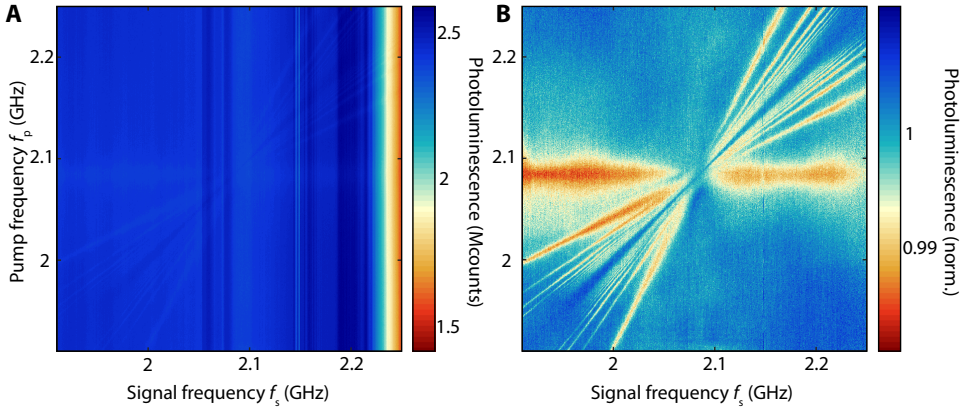

Figure 4.5: Normalization procedure applied for Figs. 4.2F and 4.4D. (**A**) Raw photoluminescence data of the measurement. We attribute the fluctuations between columns to drifts of the objective focus and laser power over the course of the measurement. (**B**) By dividing the data by the median of each column the spin-wave comb is revealed. To remove the horizontal line of photoluminescence contrast caused by resonant driving at the ESR frequency $f_{\mathrm{NV}} = 2.086$ GHz, we divide the data a second time by the median of each row, resulting in Fig. 4.2F. The same normalization procedure was applied for Fig. 4.4D.

ACKNOWLEDGEMENTS

We thank M. N. Ali for reviewing the manuscript.

Funding: This work was supported by the Dutch Research Council (NWO) through the Frontiers of Nanoscience (NanoFront) program, the NWO Projectruimte grant

680.91.115, the Kavli Institute of Nanoscience Delft, and the Japan Society for the Promotion of Science (JSPS) by Kakenhi Grant # 19H00645.
Author contributions: J.J.C. and T.v.d.S. conceived the experiment. I.B. built the setup and fabricated the sample. R.W.M., J.J.C., I.B. and A.T. performed the measurements and analyzed the data. M.E., Y.M.B. and G.E.W.B. developed the theoretical model for the idler amplitude, B.G.S. fabricated the diamond membrane, J.J.C., T.v.d.S., I.B. and A.T. wrote the manuscript with help from all coauthors.
Competing interests: The authors declare that they have no competing interests.
Data availability: The numerical data plotted in the figures in this work are available at Zenodo with identifier https://doi.org/10.5281/zenodo.6543615. The codes used for the numerical calculation of the idler amplitude are available upon request.

4.5. SUPPLEMENTARY INFORMATION

4.5.1. DERIVATION OF THE SPIN-WAVE DISPERSION FOR BIAS FIELDS ALONG THE NV AXIS

Here we derive the spin-wave dispersion for a magnetic film in the xy-plane with perpendicular magnetic anisotropy (PMA) and a magnetic bias field $\mathbf{B}_B$ in an arbitrary direction. The dispersion is given by the poles of the transverse magnetic susceptibility [21, 35] that relates the transverse magnetization to a drive field $\mathbf{B}_{\mathrm{AC}}$. We derive the magnetic susceptibility from the Landau-Lifshitz-Gilbert (LLG) equation that describes the dynamics of the unit magnetization vector $\mathbf{m}$

$$\dot{\mathbf{m}} = -\gamma \mathbf{m} \times \mathbf{B} - \alpha_{\mathrm{G}} \dot{\mathbf{m}} \times \mathbf{m}, \tag{4.2}$$

where α_{G} is the Gilbert damping and the "overdot" denotes the time derivative. We solve this equation in the (x',y',z') magnet frame that is tilted with respect to the (x,y,z) lab frame by an angle θ_0, such that the equilibrium magnetization points in the $\hat{\mathbf{z}}'$ direction and the $\hat{\mathbf{y}}^{(')}$ axes overlap. $\mathbf{B} = \mathbf{B}_{\mathrm{eff}} + \mathbf{B}_{\mathrm{AC}}$, with $\mathbf{B}_{\mathrm{eff}}$ the effective magnetic field as derivative of the magnetic free energy density F

$$B_{\mathrm{eff},\alpha'} = -\frac{1}{M_{\mathrm{s}}} \frac{\partial F}{\partial m_{\alpha'}}, \tag{4.3}$$

where M_{s} is the saturation magnetization and $\alpha' \in \{x', y', z'\}$ indicates the vector components in the magnet frame. The free energy density includes the Zeeman energy, the demagnetizing field $\mathbf{B}_{\mathrm{d}}$, the PMA energy F_{A}, and the exchange interaction

$$F = -M_{\mathrm{s}} \mathbf{m} \cdot (\mathbf{B}_B + \frac{\mathbf{B}_{\mathrm{d}}}{2}) + F_{\mathrm{A}} + \frac{D}{2} \sum_{\alpha,\beta=x,y,z} \left(\frac{\partial m_{\alpha'}}{\partial \beta} \right)^2. \tag{4.4}$$

In the magnet frame

$$F_{\mathrm{A}} = \frac{K}{2} m_z^2 = \frac{K}{2} (\sin\theta_0 m_{x'} + \cos\theta_0 m_{z'})^2, \tag{4.5}$$

such that the x' and z' components of the anisotropy effective field are

$$\begin{aligned} B_{\mathrm{A},x'} &= -\frac{1}{M_\mathrm{s}}\frac{\partial F}{\partial m_{x'}} = -\frac{K}{M_\mathrm{s}}(\sin^2\theta_0 m_{x'} + \cos\theta_0 \sin\theta_0 m_{z'}), \\ B_{\mathrm{A},z'} &= -\frac{1}{M_\mathrm{s}}\frac{\partial F}{\partial m_{z'}} = -\frac{K}{M_\mathrm{s}}(\cos\theta_0 \sin\theta_0 m_{x'} + \cos^2\theta_0 m_{z'}). \end{aligned} \tag{4.6}$$

The contributions of the Zeeman-, demagnetizing- and exchange energy to $\mathbf{B}_\mathrm{eff}$ have been derived in Refs. [21, 35].
In linear response with $m_{z'} \approx 1$, the LLG equation describes the transverse magnetization dynamics. In the frequency domain it reads

$$\begin{aligned} -i\omega m_{x'} &= -\gamma(m_{y'}B_{z'} - B_{y'}) + i\alpha_\mathrm{G}\omega m_{y'}, \\ -i\omega m_{y'} &= \gamma(m_{x'}B_{z'} - B_{x'}) - i\alpha_\mathrm{G}\omega m_{x'}, \end{aligned} \tag{4.7}$$

where ω is the angular frequency. Substituting the components of the effective magnetic field and rewriting the equations in matrix form,

$$\begin{pmatrix} \omega_2 - i\alpha_\mathrm{G}\omega & -\omega_1 + i\omega \\ -\omega_1 - i\omega & \omega_3 - i\alpha_\mathrm{G}\omega \end{pmatrix} \begin{pmatrix} m_{x'} \\ m_{y'} \end{pmatrix} = \gamma \begin{pmatrix} B_{\mathrm{AC},x'} \\ B_{\mathrm{AC},y'} \end{pmatrix}, \tag{4.8}$$

where

$$\begin{aligned} \omega_0 &= -(\omega_M - \omega_K)\cos^2\theta_0 + \omega_B \cos(\theta_B - \theta_0) + \omega_D k^2, \\ \omega_1 &= \omega_M f \sin\phi\cos\phi\cos\theta_0, \\ \omega_2 &= \omega_0 + \omega_M f(\cos^2\phi\cos^2\theta_0 - \sin^2\theta_0) + (\omega_M - \omega_K)\sin^2\theta_0, \\ \omega_3 &= \omega_0 + \omega_M f \sin^2\phi, \end{aligned} \tag{4.9}$$

and $\omega_B = \gamma B_B$, $\omega_M = \gamma\mu_0 M_\mathrm{s}$, $\omega_D = \frac{\gamma D}{M_\mathrm{s}}$ and $\omega_K = \frac{\gamma K}{M_\mathrm{s}}$. μ_0 is the vacuum permeability, $k = |\mathbf{k}|$ is the modulus of the wavevector along an angle ϕ with respect to the in-plane projection of the magnetization, θ_B is the angle of the magnetic bias field with respect to the plane normal (z axis), and $f = 1 - \frac{1-e^{-kt}}{kt}$ depends on the film thickness t. By inverting the matrix in Eq. 4.8, we obtain the transverse magnetic susceptibility, which is singular when

$$(\omega_2 - i\alpha_\mathrm{G}\omega)(\omega_3 - i\alpha_\mathrm{G}\omega) - \omega_1^2 - \omega^2 = 0. \tag{4.10}$$

Assuming $\alpha_\mathrm{G} \ll 1$, the real part of the solutions of this quadratic equation gives the spin-wave dispersion as a function of k

$$\omega^2 = \omega_2\omega_3 - \omega_1^2. \tag{4.11}$$

The theoretical lines in Figs. 4.2 and 4.4 are based on Eq. 4.11. We assume that the field is applied parallel to the NV axis, such that $\theta_B = 54.7°$, with in-plane projection along the stripline. We consider only spin waves with $\phi = \pi/2$, since these are most efficiently excited by our 150-micron-long stripline. θ_0 minimizes the free energy density and is found by numerically solving $\frac{\partial F}{\partial \theta_0} = 0$. The ferromagnetic resonance (FMR) frequency corresponds to $k = 0$. Table 4.1 states the values of the saturation magnetization, exchange and uniaxial anisotropy constants for different magnetic materials used for calculating the spin-wave dispersions in Fig. 4.4E.

Material	M_s (A/m)	D (J/m)	K (J/m^3)	Reference
YIG	$1.42 \cdot 10^5$	$4.15 \cdot 10^{-12}$	0	Ref. [11]
Permalloy (Py)	$8.46 \cdot 10^5$	$2.4 \cdot 10^{-12}$	0	
Cobalt (Co)	$13 \cdot 10^5$	$2.4 \cdot 10^{-12}$	0	
$CrBr_3$	$2.55 \cdot 10^5$	$1.2 \cdot 10^{-12}$	$2.24 \cdot 10^5$	Ref. [36]
CrI_3	$2.15 \cdot 10^5$	$1.35 \cdot 10^{-12}$	$6.30 \cdot 10^5$	Ref. [36]
Fe_3GeTe_2	$3.76 \cdot 10^5$	$9.5 \cdot 10^{-13}$	$1.46 \cdot 10^6$	Ref. [37]

Table 4.1: Values of the saturation magnetization (M_s), exchange constant (D) and uniaxial anisotropy constant (K) used to calculate the spin-wave dispersions in Fig. 4.4F.

4

4.5.2. SPIN-WAVE FREQUENCY COMB VERSUS DRIVE POWER

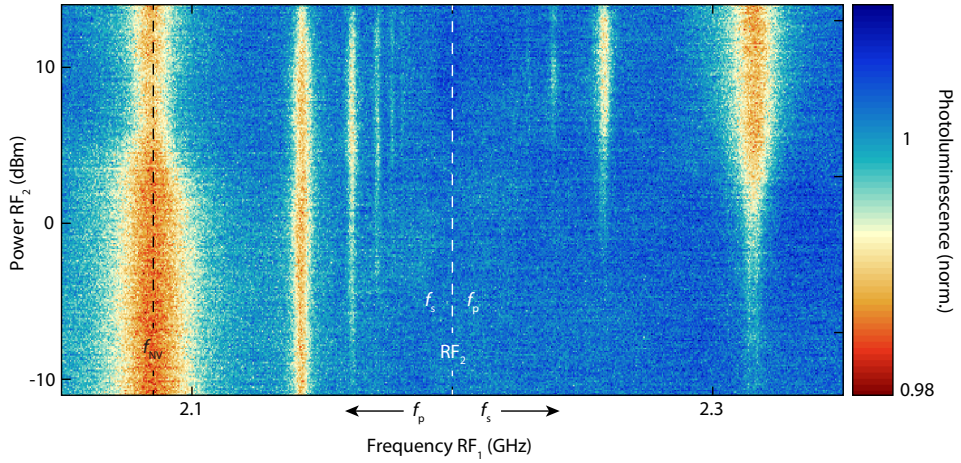

Figure 4.6: Emergence of a spin-wave comb generated by two microwave drives RF$_1$ and RF$_2$. Normalized NV photoluminescence at B_{NV} = 28 mT as a function of RF$_1$ frequency (RF$_2$ is kept at 2.2 GHz, red dashed line), and RF$_2$ power (RF$_1$ is kept at 4 dBm). An increasing number of higher-order idlers appear at increased drive power. RF$_1$ and RF$_2$ function either as pump or signal field depending on which frequency is closer to the ESR frequency f_{NV} = 2.086 GHz, as is indicated by the labels f_s and f_p with matching colors.

4.5.3. DEPENDENCE OF THE DETECTION BANDWIDTH ON THE MICROWAVE DRIVE FIELD

For efficient frequency conversion, the microwaves should excite propagating spin waves with a significant amplitude. The spin-wave excitation efficiency depends on the microwave power and the spatial mode overlap between the drive field and the spin waves [11]. In our experiment, a 5-micron-wide stripline creates an inhomogeneous microwave drive field with a sinc-like amplitude in k-space (Fig. 4.7A). The efficiency drops with decreasing wavelength with nodes at $\lambda = w/n$, where w is the stripline width and n is an integer.

To characterize the dependence on the drive field, we measure the bandwidth induced

by four-wave mixing as a function of the pump power (Fig. 4.7B). As expected, the bandwidth increases with microwave power. The photoluminescence contrast is suppressed at spin-wave frequencies that correspond to the nodes of the drive field in Fig. 4.7A (colored dashed lines). The frequencies of these modes agree with the spin-wave dispersion derived in the previous section [Eq. 4.11]. The spin-wave excitation antenna is therefore an important design parameter for hybrid diamond-magnet microwave sensors.

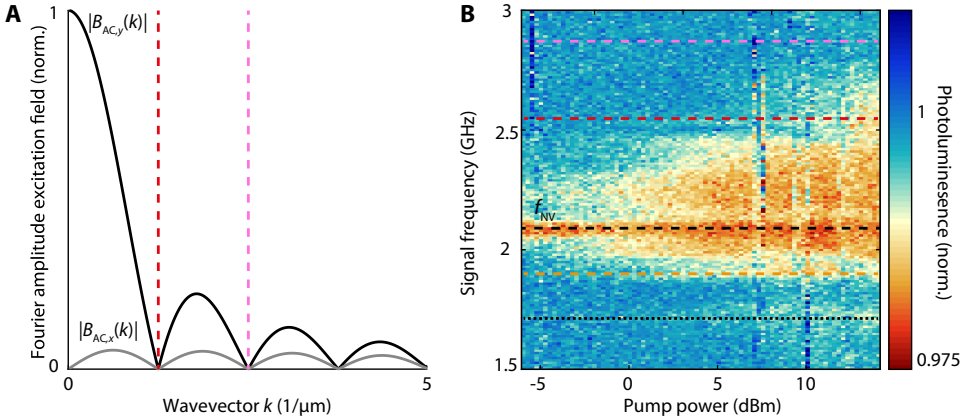

Figure 4.7: The detection bandwidth is determined by the spin-wave excitation efficiency. (**A**) Normalized Fourier amplitude of the out-of-plane (x, gray) and in-plane (y, black) components of the microwave drive field $\mathbf{B}_{\mathrm{AC}}$ generated by a 5-micron-wide stripline. The colored dashed lines indicate the first two nodes in the spectrum. (**B**) Normalized NV photoluminescence induced by four-wave mixing as a function of signal frequency and pump power at a static magnetic field of $B_{\mathrm{NV}} = 28$ mT. The ESR frequency is at $f_{\mathrm{NV}} = 2.08$ GHz (black dashed line, labeled f_{NV}) and the dashed (dotted) orange (black) lines indicate the frequencies at which the signal (pump) spin waves are driving the FMR. The red and pink horizontal dashed lines indicate the frequencies of the spin waves that nominally cannot be excited by the stripline, where colors match the nodes in (A).

4.5.4. COMPARISON BETWEEN THE IDLER-DRIVEN RABI FREQUENCY AND DYNAMICAL STARK SHIFT

A strong microwave field detuned by δf from the NV ESR frequency (f_{NV}), causes the latter to shift, an effect known as the AC (or dynamical) Stark shift [26]. The Stark shift increases with drive power and is inversely proportional to δf, which allows detecting the presence of an off-resonant microwave signal. We show here that the idler-driven Rabi frequency resulting from four-spin-wave mixing is about an order magnitude larger than the Stark shift at the same off-resonant drive power.

We measure the Stark shift via pump-probe microwave spectroscopy. The high-power pump is detuned from f_{NV} by 10-1000 MHz, while a low-power probe measures the ESR frequency. We determine the Stark shift for every detuning by measuring the ESR frequency with and without pump (blue data in Fig. 4.8A).

Next, we measure Rabi oscillations using the four-spin-wave mixing technique. We ex-

tract the Rabi frequency for signal spin waves detuned from 10 to 710 MHz (red data in Fig. 4.8A). We attribute the small oscillations in the Rabi frequency and Stark shift to frequency-dependent (cable) resonances in the microwave transmission of the stripline. Fig. 4.8B shows that the Rabi frequencies are larger than the Stark shift by about an order of magnitude over the measurement range.

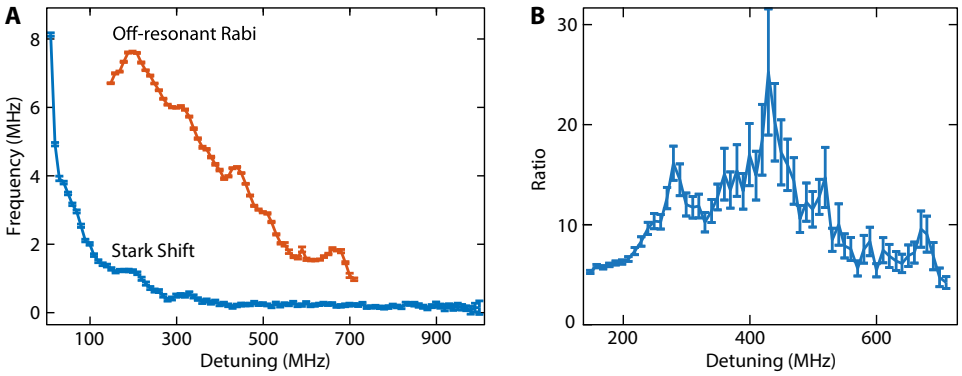

Figure 4.8: Comparison of the four-spin-wave mixing and Stark shift off-resonant detection techniques. (**A**) Blue: Measured shift in NV ESR frequency due to the AC Stark effect as a function of frequency detuning of the applied drive field. Red: Frequency of the Rabi oscillations driven by the first-order idler mode using the four-spin-wave down conversion technique as a function of drive-field detuning. (**B**) Ratio between the Rabi frequency and Stark shift as a function of detuning. The measurements were carried out at a magnetic bias field of $B_{\mathrm{NV}} = 28$ mT.

4.5.5. EIGHT-MODES MODEL

Here we describe the details of the model for the spin-wave dynamics under a two-tone drive used to calculate the idler amplitude as a function of pump and signal power, as plotted in Fig. 4.3E.

Fig. 4.9 shows the spin-wave dispersion of a YIG film for $\theta_{\mathbf{k}} = 0$ (blue line) and $\theta_{\mathbf{k}} = \pi/2$ (black line), where $\theta_{\mathbf{k}}$ is the angle between the in-plane spin-wave wavevector $\mathbf{k}$ and the static magnetization for the parameters in Table S1. Since the out-of-plane component of the applied bias field $\mathbf{B}_{\mathrm{NV}}$ is small compared to the demagnetizing field of ~ 178 mT in YIG, we assume that the static magnetization lies in-plane along $\hat{\mathbf{z}}$ ($\hat{\mathbf{x}}$ is the out-of-plane axis), parallel to $B_{\hat{\mathbf{z}}}$, the in-plane component of $\mathbf{B}_{\mathrm{NV}}$. The long stripline along $\hat{\mathbf{z}}$ excites signal and pump spin waves with $\theta_{\mathbf{k}} = \pi/2$. Conservation of momentum dictates that the two created idler spin waves also lie on the $\theta_{\mathbf{k}} = \pi/2$ branch with wavevectors $\mathbf{k}_{\mathrm{i}} = 2\mathbf{k}_{\mathrm{p}} - \mathbf{k}_{\mathrm{s}}$ and $\mathbf{k}_{\mathrm{i}'} = 2\mathbf{k}_{\mathrm{s}} - \mathbf{k}_{\mathrm{p}}$ (Fig. 4.9).

When the pump mode is strongly driven beyond a certain threshold, the four magnon scattering term in the spin-wave Hamiltonian $c^{\dagger}_{\mathbf{k}_{\mathrm{p}}} c^{\dagger}_{\mathbf{k}_{\mathrm{p}}} c_{\mathbf{k}'} c_{\mathbf{k}''}$ leads to a Suhl instability. Here $c^{(\dagger)}_{\mathbf{k}}$ is the annihilation (creation) operator for a magnon with wavevector $\mathbf{k}$, which is normalized by $\sqrt{S}$, where $S = V s_n / V_n$ is the total number of spins, V is the volume,

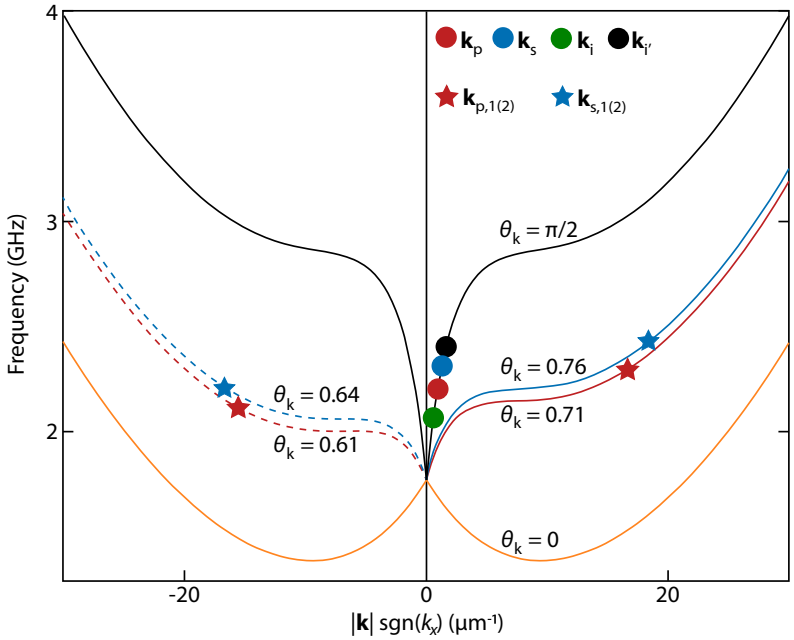

Figure 4.9: Eight-modes model for the calculation of the idler amplitude. In our model we consider the signal (blue dot), pump (red dot), idlers (green and black dots), "efficient signal Suhl instability pair" (blue stars) and "efficient pump Suhl instability pair" (red stars) spin waves. The lines are branches of the spin-wave dispersion corresponding to different angles $\theta_{\mathbf{k}}$ of the wavevector with respect to the static magnetization (see legend). The dispersion is symmetric upon rotations of $\theta_{\mathbf{k}}$ by π. Calculations like those presented in Fig. S6 lead to the wavevectors of the efficient pump and signal pairs. Here $B_{\hat{\mathbf{z}}} = 23$ mT.

s_n is the number of spins per unit cell, and V_n is the unit cell volume. A specific pair of magnons wins the "instability competition", $\mathbf{k}' = \mathbf{k}_{\mathrm{p},1}$ and $\mathbf{k}'' = \mathbf{k}_{\mathrm{p},2} = 2\mathbf{k}_{\mathrm{p}} - \mathbf{k}_{\mathrm{p},1}$, which we call the "efficient Suhl pair" of the pump mode. The efficient Suhl pair for the signal $\mathbf{k}_{\mathrm{s},1}$ and $\mathbf{k}_{\mathrm{s},2}$ should also be considered when its mode amplitude is sufficiently large. We disregard cascades that lead to the weak higher-order idlers in Fig. 4.2F, as well as the Suhl pairs of the idlers that are safely below their instability threshold at the presently applied powers. A minimal model should therefore include the eight modes indicated in Fig. 4.9.

The efficient pump and signal pairs can be identified from the threshold amplitude of the pump (signal) mode $x = |\alpha_{\mathrm{p,s}}|^2$ above which the Suhl instability leads to $\{\mathbf{k}', \mathbf{k}''\}$ pairs, which solve [38]

$$(\mathscr{D}^{\mathrm{Suhl}}_{\mathrm{p(s)};\mathbf{k}';\mathbf{k}''}{}^{2} - \mathscr{D}^{\mathrm{CK}}_{\mathrm{p(s)};\mathbf{k}'}{}^{2})x^2 - 2\Delta\mathscr{D}^{\mathrm{CK}}_{\mathrm{p(s)};\mathbf{k}'}x - \xi^2 - \Delta^2 = 0, \tag{4.12}$$

where $\Delta = \omega_{\mathrm{p(s)}} - (\omega_{\mathbf{k}'} + \omega_{\mathbf{k}''})/2$, with ω an angular frequency, and ξ is a dissipation rate chosen here to be 10 MHz for all modes. $\mathscr{D}^{\mathrm{Suhl}}_{\mathrm{p(s)};\mathbf{k}';\mathbf{k}''}$ ($\mathscr{D}^{\mathrm{CK}}_{\mathrm{p(s)};\mathbf{k}'}$) is the matrix element for the scattering process $c^\dagger_{\mathbf{k}_{\mathrm{p(s)}}} c^\dagger_{\mathbf{k}_{\mathrm{p(s)}}} c_{\mathbf{k}'} c_{\mathbf{k}''}$ ($c^\dagger_{\mathbf{k}_{\mathrm{p(s)}}} c_{\mathbf{k}_{\mathrm{p(s)}}} c^\dagger_{\mathbf{k}'} c_{\mathbf{k}'}$) in the Hamiltonian [17]. First,

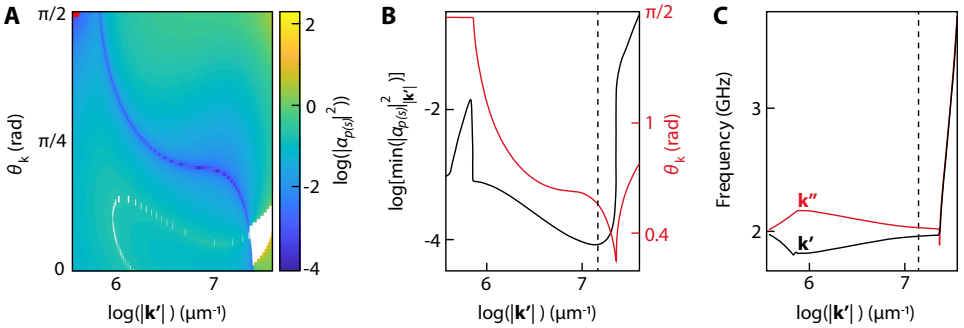

Figure 4.10: Finding the efficient Suhl pair with the lowest excitation threshold. (**A**) Calculated threshold amplitude $|\alpha_{\mathrm{p(s)}}|^2$ that triggers the Suhl instability of a spin-wave pair with wavevectors $\mathbf{k}'$ and $\mathbf{k}'' = 2\mathbf{k}_{\mathrm{p(s)}} - \mathbf{k}'$ as a function of $|\mathbf{k}'|$ and $\theta_{\mathbf{k}'}$. The amplitude is normalized by the total spin S. In the white regions no momentum-conserving scattering processes can take place. Here we adopted $B_{\hat{\mathbf{z}}} = 24$ mT, $\omega_{\mathrm{p(s)}}/2\pi = 2$ GHz and $\theta_{\mathbf{k}_{\mathrm{p(s)}}} = \pi/2$, corresponding to the red dot. (**B**) Minimal threshold amplitude as a function of $|\mathbf{k}'|$ (black line, left axis) and corresponding $\theta_{\mathbf{k}'}$ (red line, right axis). (**C**) Frequencies of the modes corresponding to the pairs in (C). The pair with the lowest threshold is indicated by the vertical dashed line in (B) and (C), and defines the "efficient pump (signal) pair" of the Suhl instability.

we numerically calculate the threshold amplitude $|\alpha_{\mathrm{p,s}}|^2$ as a function of $|\mathbf{k}'|$ and $\theta_{\mathbf{k}'}$ as in Fig. 4.10A. We identify the minimum threshold amplitude in the $(|\mathbf{k}'|,\theta_{\mathbf{k}'})$ plane of Fig. 4.10A as a function of modulus $|\mathbf{k}'|$ in Fig. 4.10B. The corresponding $\theta_{\mathbf{k}'}$ and spin-wave pair frequencies are shown in Figs. 4.10B and 4.10C, respectively. The spin-wave pair with the lowest threshold amplitude – the effective pump (signal) Suhl pair – turns out to be at angles $\theta_{\mathbf{k}'}$ far from $\pi/2$ (as indicated by the vertical dashed lines in Fig. 4.10B-C).

Our model Hamiltonian reads

$$\begin{aligned} H = &\sum_X \omega_X c_X^\dagger c_X + [\mathscr{D}^{\mathrm{Suhl}}_{\mathrm{p;p,1;p,2}} c^\dagger_{\mathbf{k}_\mathrm{p}} c^\dagger_{\mathbf{k}_\mathrm{p}} c_{\mathbf{k}_{\mathrm{p},1}} c_{\mathbf{k}_{\mathrm{p},2}} + \\ &\mathscr{D}^{\mathrm{Suhl}}_{\mathrm{p;s;i}} c^\dagger_{\mathbf{k}_\mathrm{p}} c^\dagger_{\mathbf{k}_\mathrm{p}} c_{\mathbf{k}_\mathrm{s}} c_{\mathbf{k}_\mathrm{i}} + \mathscr{D}^{\mathrm{Suhl}}_{\mathrm{s;s,1;s,2}} c^\dagger_{\mathbf{k}_\mathrm{s}} c^\dagger_{\mathbf{k}_\mathrm{s}} c_{\mathbf{k}_{\mathrm{s},1}} c_{\mathbf{k}_{\mathrm{s},2}} + \\ &\mathscr{D}^{\mathrm{Suhl}}_{\mathrm{s;p;i'}} c^\dagger_{\mathbf{k}_\mathrm{s}} c^\dagger_{\mathbf{k}_\mathrm{s}} c_{\mathbf{k}_\mathrm{p}} c_{\mathbf{k}_{\mathrm{i}'}} + \mathrm{H.c.}] + \\ &\sum_X [\mathscr{D}^{\mathrm{SK}}_X c^\dagger_X c_X c^\dagger_X c_X + \sum_Y \mathscr{D}^{\mathrm{CK}}_{X;Y} c^\dagger_X c_X c^\dagger_Y c_Y] + \\ &E'_\mathrm{p}(e^{-i\omega_\mathrm{p} t} c^\dagger_\mathrm{p} + \mathrm{H.c.}) + E'_\mathrm{s}(e^{-i\omega_\mathrm{s} t} c^\dagger_\mathrm{s} + \mathrm{H.c.}). \end{aligned} \tag{4.13}$$

Here $X, Y \in \{\mathrm{p;s;i;i';p,1(2);s,1(2)}\}$, and "H.c." denotes the Hermitian conjugate. E'_s and E'_p are the drive amplitudes of the signal and pump modes, respectively, which are related to the excitation power of the microstrip by (cf. Fig. 4.7A),

$$P_{\mathrm{p(s)}} = E^2_{\mathrm{p(s)}} Z(\omega_{\mathrm{p(s)}}) \left[\frac{\mu_0 \gamma \left(e^{-|\mathbf{k}_{\mathrm{p(s)}}|d} - 1\right) \sin\left(\frac{|\mathbf{k}_{\mathrm{p(s)}}|W}{2}\right)}{W d |\mathbf{k}_{p(s)}|^2} \right]^{-2}. \tag{4.14}$$

Here, μ_0 is the vacuum permeability, d is the thickness of the stripline and W is its

width, $Z(\omega)$ is the impedance at ω, and we assumed $\theta_{\mathbf{k}_{\mathrm{p(s)}}} = \pi/2$. We adopt $Z(\omega_{\mathrm{p(s)}}) = 50$ Ω, $d = 200$ nm, $W = 5$ µm , $E_{\mathrm{p(s)}} = E'_{\mathrm{p(s)}}\sqrt{L}$, where $L \sim W$ is the length of the excited part of the sample, $\omega_{\mathrm{p}}/2\pi = 2.2$ GHz, $\omega_{\mathrm{s}}/2\pi = 2.32$ GHz and $\mathbf{B}_{\hat{\mathbf{z}}} = 23$ mT, corresponding to $B_{\mathrm{NV}} \sim 28$ mT. From the four-magnon-scattering parameters $\mathscr{D}^{\mathrm{Suhl}}_{\mathrm{p;p,1;p,2}}/\mathscr{D}^{\mathrm{Suhl}}_{\mathrm{p;s;i}} \sim \mathscr{D}^{\mathrm{Suhl}}_{\mathrm{s;s,1;s,2}}/\mathscr{D}^{\mathrm{Suhl}}_{\mathrm{s;p;i'}} \sim 10$, and $\mathscr{D}^{\mathrm{Suhl}}_{\mathrm{s;p;i'}} \sim \mathscr{D}^{\mathrm{Suhl}}_{\mathrm{p;s;i}} = -7.2$ GHz, and $\mathscr{D}^{\mathrm{SK}}_{\mathrm{p(s,i,i')}} \sim \mathscr{D}^{\mathrm{CK}}_{\mathrm{p(s,i,i'),p(s,i,i')}} \sim \mathscr{D}^{\mathrm{Suhl}}_{\mathrm{p;s;i}}$, and $\mathscr{D}^{\mathrm{SK}}_{\mathrm{s,1(s,2;p,1;p,2)}} \sim \mathscr{D}^{\mathrm{CK}}_{\mathrm{p(s),s,1(s,2;p,1;p,2)}} \sim \mathscr{D}^{\mathrm{Suhl}}_{\mathrm{p;p,1;p,2}}$ we calculate the mean field amplitude of the idler mode $\langle c^\dagger_{\mathbf{k}_{\mathrm{i}}} c_{\mathbf{k}_{\mathrm{i}}}\rangle = |\alpha_{\mathrm{i}}|^2$ as a function of P_{s} and P_{p}. In Fig. 4.3E we plot $|\alpha_{\mathrm{i}}|$, since it is linearly proportional to the idler-driven Rabi frequency of the NV center [11].

We find an idler amplitude (and thus a Rabi frequency) that initially grows as a function of pump and signal power. However, above the Suhl instability thresholds, the amplitude of the idler mode decreases due to the newly opened dissipation channels, as observed in the experiments in Fig. 4.3D. Since $\langle c^\dagger_X c_X\rangle \propto E^2_{\mathrm{p(s)}}/\xi^2$, ξ can be scaled by q to achieve the same phase diagram for $P_{\mathrm{p(s)}}$ shifted by $20\cdot\log(q)$ dBm. Our current assumption of $\xi = 10$ MHz for $\omega_X/2\pi \sim 2$ GHz corresponds to a Gilbert damping of $\alpha_{\mathrm{G}} = 5\cdot 10^{-3}$.

4.5.6. DIFFERENCE-FREQUENCY GENERATION BY THE LONGITUDINAL COMPONENT OF THE MAGNETIZATION

In this section we demonstrate that simultaneous transverse magnetization dynamics at the signal and pump frequencies (f_{s} and f_{p}, respectively) causes a beating in the longitudinal component at the difference frequency $|f_{\mathrm{s}} - f_{\mathrm{p}}|$. The normalized transverse magnetization m_{T} of two propagating circularly-polarized spin waves is the superposition

$$m_{\mathrm{T}} = m_{\mathrm{s}} e^{i(k_{\mathrm{s}}x-\omega_{\mathrm{s}}t)} + m_{\mathrm{p}} e^{i(k_{\mathrm{p}}x-\omega_{\mathrm{p}}t)}. \tag{4.15}$$

$k_i = 2\pi/\lambda_i$ is the wavevector of the ith spin wave, with $i \in \{\mathrm{s},\mathrm{p}\}$, in terms of the wavelength λ_i, $\omega_i = 2\pi f_i$ is the angular frequency and $m_i = M_i/M_{\mathrm{s}}$ is the magnetization amplitude normalized by the saturation magnetization. The transverse x and y components are the real and imaginary parts of m_{T} while the normalized longitudinal component of the magnetization reads

$$m_{\mathrm{L}} = \sqrt{1-|m_{\mathrm{T}}|^2}. \tag{4.16}$$

When driving two spin waves at frequencies ω_{s} and ω_{p}, and amplitudes m_{s} and m_{p}, the squared modulus

$$|m_{\mathrm{T}}|^2 = m_{\mathrm{T}} m^*_{\mathrm{T}} = m^2_{\mathrm{s}} + m^2_{\mathrm{p}} + 2m_{\mathrm{s}}m_{\mathrm{p}}\cos((k_{\mathrm{s}}-k_{\mathrm{p}})x - (\omega_{\mathrm{s}}-\omega_{\mathrm{p}})t) \tag{4.17}$$

depends on time. For $m_i \ll 1$ the longitudinal component oscillates at the difference frequency

$$m_{\mathrm{L}} \propto m_{\mathrm{s}}m_{\mathrm{p}}\cos((k_{\mathrm{s}}-k_{\mathrm{p}})x - (\omega_{\mathrm{s}}-\omega_{\mathrm{p}})t), \tag{4.18}$$

as detected in our experiments.

BIBLIOGRAPHY

[1] C. L. Degen, F. Reinhard, and P. Cappellaro, "Quantum sensing", Reviews of Modern Physics **89**, 035002 (2017).

[2] L. Rondin et al., "Magnetometry with nitrogen-vacancy defects in diamond", Reports on Progress in Physics **77**, 056503 (2014).

[3] N. Aslam et al., "Nanoscale nuclear magnetic resonance with chemical resolution", Science **357**, 67 (2017).

[4] I. Lovchinsky et al., "Magnetic resonance spectroscopy of an atomically thin material using a single-spin qubit", Science **355**, 503 (2017).

[5] R. Schirhagl, K. Chang, M. Loretz, and C. L. Degen, "Nitrogen-Vacancy Centers in Diamond: Nanoscale Sensors for Physics and Biology", Annual Review of Physical Chemistry **65**, 83 (2014).

[6] D. R. Glenn et al., "Micrometer-scale magnetic imaging of geological samples using a quantum diamond microscope", Geochemistry, Geophysics, Geosystems **18**, 3254 (2017).

[7] F. Casola, T. van der Sar, and A. Yacoby, "Probing condensed matter physics with magnetometry based on nitrogen-vacancy centres in diamond", Nature Reviews Materials **3**, 17088 (2018).

[8] M. J. H. Ku et al., "Imaging viscous flow of the Dirac fluid in graphene", Nature **583**, 537 (2020).

[9] J. P. Tetienne et al., "Quantum imaging of current flow in graphene", Science Advances **3**, e1602429 (2017).

[10] P. Appel, M. Ganzhorn, E. Neu, and P. Maletinsky, "Nanoscale microwave imaging with a single electron spin in diamond", New Journal of Physics **17** (2015).

[11] I. Bertelli et al., "Magnetic resonance imaging of spin-wave transport and interference in a magnetic insulator", Science Advances **6**, eabd3556 (2020).

[12] L. Thiel et al., "Quantitative nanoscale vortex imaging using a cryogenic quantum magnetometer", Nature Nanotechnology **11**, 677 (2016).

[13] B. Fortman et al., "Electron–electron double resonance detected NMR spectroscopy using ensemble NV centers at 230 GHz and 8.3 T", Journal of Applied Physics **130**, 083901 (2021).

[14] A. V. Chumak, V. I. Vasyuchka, A. A. Serga, and B. Hillebrands, "Magnon spintronics", Nature Physics **11**, 453 (2015).

[15] J. Marsh and R. E. Camley, "Two-wave mixing in nonlinear magnetization dynamics: A perturbation expansion of the Landau-Lifshitz-Gilbert equation", Physical Review B **86**, 224405 (2012).

[16] H. Suhl, "The theory of ferromagnetic resonance at high signal powers", Journal of Physics and Chemistry of Solids **1**, 209 (1957).

[17] P. Krivosik and C. E. Patton, "Hamiltonian formulation of nonlinear spin-wave dynamics: Theory and applications", Physical Review B **82**, 184428 (2010).

[18] H. Schultheiss, K. Vogt, and B. Hillebrands, "Direct observation of nonlinear four-magnon scattering in spin-wave microconduits", Phys. Rev. B **86**, 054414 (2012).

[19] T. Hula et al., "Nonlinear losses in magnon transport due to four-magnon scattering", Applied Physics Letters **117**, 042404 (2020).

[20] Y. Khivintsev et al., "Nonlinear amplification and mixing of spin waves in a microstrip geometry with metallic ferromagnets", Applied Physics Letters **98**, 042505 (2011).

[21] I. Bertelli et al., "Imaging Spin-Wave Damping Underneath Metals Using Electron Spins in Diamond", Advanced Quantum Technologies **4**, 2100094 (2021).

[22] P. Che, K. Baumgaertl, A. Kúkol'ová, C. Dubs, and D. Grundler, "Efficient wavelength conversion of exchange magnons below 100 nm by magnetic coplanar waveguides", Nature Communications **11**, 1445 (2020).

[23] N. Picqué and T. W. Hänsch, "Frequency comb spectroscopy", Nature Photonics **13**, 146 (2019).

[24] Z. Wang et al., "Magnonic Frequency Comb through Nonlinear Magnon-Skyrmion Scattering", Physical Review Letters **127**, 037202 (2021).

[25] C. Koerner et al., "Frequency multiplication by collective nanoscale spin-wave dynamics", Science **375**, 1165 (2022).

[26] C. Wei, A. S. Windsor, and N. B. Manson, "A strongly driven two-level atom revisited: Bloch-Siegert shift versus dynamic Stark splitting", Journal of Physics B: Atomic, Molecular and Optical Physics **30**, 21 (1997).

[27] B. Flebus and Y. Tserkovnyak, "Quantum-Impurity Relaxometry of Magnetization Dynamics", Physical Review Letters **121**, 187204 (2018).

[28] T. Gerrits, P. Krivosik, M. L. Schneider, C. E. Patton, and T. J. Silva, "Direct Detection of Nonlinear Ferromagnetic Resonance in Thin Films by the Magneto-Optical Kerr Effect", Physical Review Letters **98**, 207602 (2007).

[29] J. Meinel et al., "Heterodyne sensing of microwaves with a quantum sensor", Nature Communications **12**, 2737 (2021).

[30] T. Joas, A. M. Waeber, G. Braunbeck, and F. Reinhard, "Quantum sensing of weak radio-frequency signals by pulsed Mollow absorption spectroscopy", Nature Communications **8**, 964 (2017).

[31] A. Stark et al., "Narrow-bandwidth sensing of high-frequency fields with continuous dynamical decoupling", Nature Communications **8**, 1105 (2017).

[32] D. D. Awschalom et al., "Quantum Engineering With Hybrid Magnonic Systems and Materials (Invited Paper)", IEEE Transactions on Quantum Engineering **2**, 1 (2021).

[33] Y. Au et al., "Resonant microwave-to-spin-wave transducer", Applied Physics Letters **100**, 182404 (2012).

[34] H. Fulara et al., “Spin-orbit torque-driven propagating spin waves”, Science Advances **5**, eaax8467 (2019).

[35] A. Rustagi, I. Bertelli, T. van der Sar, and P. Upadhyaya, “Sensing chiral magnetic noise via quantum impurity relaxometry”, Phys. Rev. B **102**, 220403 (2020).

[36] X. Shen et al., “Multi-domain ferromagnetic resonance in magnetic van der Waals crystals CrI_3 and $CrBr_3$”, Journal of Magnetism and Magnetic Materials **528**, 167772 (2021).

[37] N. León-Brito, E. D. Bauer, F. Ronning, J. D. Thompson, and R. Movshovich, “Magnetic microstructure and magnetic properties of uniaxial itinerant ferromagnet Fe_3GeTe_2”, Journal of Applied Physics **120**, 083903 (2016).

[38] M. Elyasi, E. Saitoh, and G. E. W. Bauer, “Stochasticity of the magnon parametron”, Physical Review B **105**, 054403 (2022).

5

ELECTRICAL SPECTROSCOPY OF THE SPIN-WAVE DISPERSION AND BISTABILITY IN GALLIUM-DOPED YTTRIUM IRON GARNET

Yttrium iron garnet (YIG) is a magnetic insulator with record-low damping, allowing spin-wave transport over macroscopic distances. Doping YIG with gallium ions greatly reduces the demagnetizing field and introduces a perpendicular magnetic anisotropy, which leads to an isotropic spin-wave dispersion that facilitates spin-wave optics and spin-wave steering. Here, we characterize the dispersion of a gallium-doped YIG (Ga:YIG) thin film using electrical spectroscopy. We determine the magnetic anisotropy parameters and Gilbert damping from the frequency and linewidth of the ferromagnetic resonance (FMR). Next, we use propagating spin wave spectroscopy in the Damon-Eshbach configuration to detect the small spin-wave magnetic fields of this ultrathin weak magnet over a wide range of wavevectors, enabling the extraction of the exchange constant $\alpha_{ex} = 1.3(2) \cdot 10^{-12}$ *J/m. We observe foldover of the FMR with increasing drive power, leading to frequency shifts of the spin-wave modes and a bistable region in the spin-wave spectra. Our results shed light on isotropic spin-wave transport in Ga:YIG and highlight the potential of electrical spectroscopy to map out the dispersion and bistability of propagating spin waves in magnets with a low saturation magnetization.*

This chapter has been published in *Applied Physics Letters* **119**, 202403 (2021) by **J. J. Carmiggelt**, O. C. Dreijer, C. Dubs, O. Surzhenko, and T. van der Sar.

5.1. INTRODUCTION

Yttrium iron garnet (YIG) is a magnetic insulator that is famous for its low Gilbert damping and long-range spin-wave propagation [1]. At low bias fields the YIG magnetization is typically pushed in the plane by the demagnetizing field [2], leading to an anisotropic spin-wave dispersion at microwave frequencies. For applications that rely on spin-wave optics and spin-wave steering an isotropic spin-wave dispersion is desirable [3, 4], which can be achieved by introducing gallium dopants in the YIG: The presence of the dopants reduces the saturation magnetization and thereby the demagnetizing field [5], and induces a perpendicular magnetic anisotropy (PMA) [6, 7], such that the magnetization points out-of-plane. Isotropic transport of forward-volume spin waves has been observed even at zero bias field [8], opening the door for spin-wave logic devices [9–11].

To harness isotropic spin waves it is essential to know the spin-wave dispersion, which is dominated by the exchange interaction for magnets with a low saturation magnetization [12]. Here, we use all-electrical spectroscopy of propagating spin waves [13–17] to characterize the spin-wave dispersion of a 45-nm-thick film of gallium-doped YIG (Ga:YIG). Rather than looking at the discrete mode numbers of perpendicular standing spin waves [18], this method enables extracting the exchange constant by monitoring the spin-wave transmission for a continuously-tunable range of wavevectors. We show that this technique has sufficient sensitivity to characterize spin waves in nanometer-thick Ga:YIG films, where perpendicular modes may be challenging to detect due to their high frequencies and small mode overlap with the stripline drive field.

We extract the anisotropy parameters from the field dependence of the ferromagnetic resonance (FMR) frequency at different bias field orientations and find that the PMA is strong enough to lift the magnetization out of the plane. Next, we determine the damping of our film from the linewidth of the FMR and characterize the spin-wave dispersion from electrically-detected spin-wave spectra. We measure in the Damon-Eshbach configuration to boost the inductive coupling of the spin waves to the striplines [19], allowing the extraction of the spin-wave group velocity over a wide range of wavevectors from which we determine the exchange constant. When increasing the microwave excitation power, we observe clear frequency shifts of the spin-wave modes. The shifts result from the foldover of the FMR, which we verify by comparing upward and downward frequency sweeps. These results benchmark propagating spin wave spectroscopy as an accessible tool to characterize the exchange constant and spin-wave bistability in technologically attractive thin-film magnetic insulators with low saturation magnetization and PMA.

5.2. RESULTS

We use liquid phase epitaxy to grow a 45-nm-thick film of Ga:YIG on an (111)-oriented gadolinium gallium garnet (GGG) substrate (see Methods). Using vibrating sample magnetometry (VSM) we determine the saturation magnetization $M_s = 1.52(6) \cdot 10^4$ A/m (Fig. 5.1a, the number in parentheses denotes the 95% confidence interval), which is approximately an order of magnitude smaller than undoped YIG films of similar thicknesses [20].

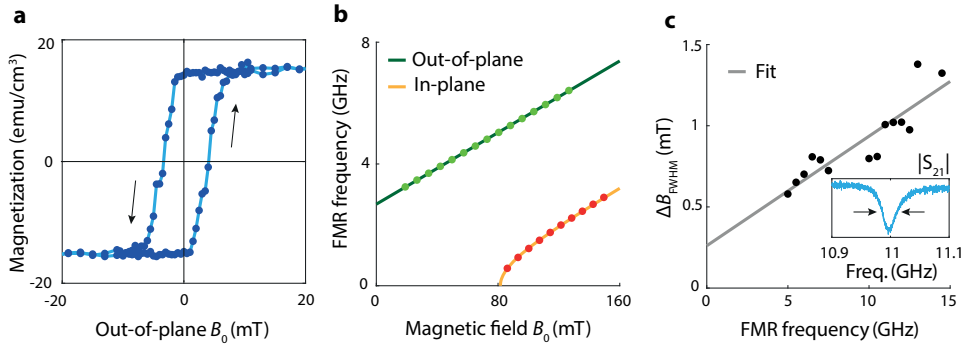

Figure 5.1: The saturation magnetization, magnetic anisotropies and Gilbert damping of Ga:YIG. (**a**) Hysteresis loop of the magnetization of a 45-nm-thick Ga:YIG film as a function of out-of-plane magnetic field B_0 measured using vibrating sample magnetometry and corrected for magnetic background. The arrows denote the sweep direction of the magnetic field. (**b**) FMR measurements using an out-of-plane (green) and in-plane (red) magnetic field B_0. From the fits of the FMR frequencies (solid lines) we determine the perpendicular and cubic anisotropy fields (see text). (**c**) Frequency dependence of the FMR linewidth. The data points are obtained from FMR absorption spectra at different in-plane magnetic fields (see the inset for an example measurement). We convert the absorption spectra to the magnetic field scale using Eq. 5.2 and fit them with a Lorentz function to extract the full-width at half-maximum (FWHM, ΔB_{FWHM}). From the linear fit (solid grey line) we extract the Gilbert damping $\alpha_{\mathrm{G}} = 1.0(3) \cdot 10^{-3}$.

In addition to PMA, Ga:YIG films also have a cubic magnetic anisotropy due to a cubic unit cell. We start by determining the cubic and perpendicular anisotropy fields from the ferromagnetic resonance (FMR) frequencies $\omega_{\mathrm{FMR}}/2\pi$ using an out-of-plane ($\perp$) and in-plane ($||$) magnetic bias field B_0. For (111)-oriented films the out-of-plane and in-plane Kittel relations are given by [20, 21]

$$\omega_{\mathrm{FMR}(\perp)} = \gamma_{\perp}(B_0 - \mu_0 M_{\mathrm{s}} + \frac{2K_{2\perp}}{M_{\mathrm{s}}} - \frac{4}{3}\frac{K_4}{M_{\mathrm{s}}}), \tag{5.1}$$

$$\omega_{\mathrm{FMR}(||)} = \gamma_{||}\sqrt{B_0(B_0 + \mu_0 M_{\mathrm{s}} - \frac{2K_{2\perp}}{M_{\mathrm{s}}} - \frac{K_4}{M_{\mathrm{s}}})}. \tag{5.2}$$

Here $\gamma_{\perp,||} = g_{\perp,||}\mu_{\mathrm{B}}/\hbar$ is the gyromagnetic ratio with $g_{\perp,||}$ the anisotropic g-factor, μ_{B} the Bohr magneton and $\hbar$ the reduced Planck constant, μ_0 is the magnetic permeability of free space, $K_{2\perp}$ is the uniaxial out-of-plane anisotropy (e.g. PMA) constant and K_4 the cubic anisotropy constant. During the in-plane FMR measurement we apply the magnetic field along the $[1\bar{1}0]$ crystallographic axis to minimize the out-of-plane component of the magnetization (section 5.5.1). We neglect any uniaxial in-plane anisotropy as it is known to be small in YIG samples [20].

By substituting the value of M_{s} that we obtained with VSM into Eqns. 5.1 and 5.2, we can determine $K_{2\perp}$ and K_4 from the FMR frequencies (Fig. 5.1b) [22]. From the fits (solid lines) we extract the uniaxial out-of-plane anisotropy field $2K_{2\perp}/M_{\mathrm{s}} = 104.7(8)$ mT and the cubic anisotropy field $2K_4/M_{\mathrm{s}} = -8.2(5)$ mT (section 5.5.2). Undoped YIG films of similar thicknesses have comparable cubic anisotropy fields [20], which agrees with previous work on micrometer-scale films showing that the cubic anisotropy of YIG does not

depend on gallium concentration [23]. We determine the in-plane and out-of-plane g-factors to be $g_{||} = 2.041(4)$ and $g_{\perp} = 2.101(3)$ [24].

We extract the Gilbert damping α_G of our film from the linewidth ΔB_{FWHM} of the FMR [25], which is given by

$$\Delta B_{FWHM} = \Delta B_0 + \frac{2\alpha_G}{\gamma_{||}} \omega_{FMR(||)}. \tag{5.3}$$

Here ΔB_0 is the inhomogeneous broadening and the magnetic field is applied in the plane. By fitting the frequency dependence of the FMR linewidth we find $\alpha_G = 1.0(3) \cdot 10^{-3}$ (Fig. 5.1c), which is about three times larger than for bismuth-doped YIG films of similar thickness [26, 27].

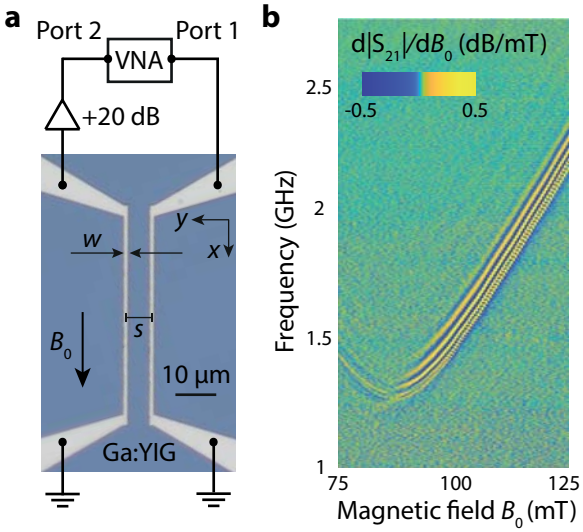

Figure 5.2: All-electrical propagating spin wave spectroscopy. (**a**) Optical micrograph of a Ga:YIG film with two gold striplines that are connected to the ports of a vector network analyser (VNA). Port 1 applies a microwave current (typical excitation power: −35 dBm) that induces a radio-frequency magnetic field B^{RF} at the injector stripline. This field excites propagating spin waves that couple inductively to the detector stripline at a distance s. The generated microwave current is amplified and detected at port 2. A static magnetic field B_0 is applied in the Damon-Eshbach configuration and is oriented such that the chirality of B^{RF} favours the excitation of spin waves propagating towards the detector stripline [28]. (**b**) Field-derivative of the microwave transmission $|S_{21}|$ between two striplines ($w = 1$ µm, $s = 6$ µm) as a function of B_0 and microwave frequency. The colormap is squeezed, such that also fringes corresponding to low-amplitude spin waves are visible. A masked background was subtracted to highlight the signal attributed to spin waves (section 5.5.3).

We now use propagating spin wave spectroscopy to characterize the spin-wave dispersion in Ga:YIG. We measure the microwave transmission $|S_{21}|$ between two microstrips fabricated directly on the Ga:YIG as a function of static magnetic field B_0 and frequency f (Fig. 5.2a). The magnetic field is applied in the Damon-Eshbach geometry to maximize the inductive coupling between the spin waves and the striplines [19]. We measure a clear Damon-Eshbach spin-wave signal in the microwave transmission spectrum when B_0 overcomes the PMA and pushes the spins in the plane (Fig. 5.2b, section 5.5.3). The

signal appears at a finite frequency, because the bias field B_0 is applied along the $[11\bar{2}]$ crystallographic axis with a finite out-of-plane angle of $\sim 1^\circ$ (section 5.5.1).
The fringes in the transmission spectra result from the interference between the spin waves and the microwave excitation field [29, 30]. Each fringe indicates an extra spin-wavelength λ that fits between the striplines. We can thus use the fringes to determine the group velocity v_g of the spin waves via [14]

$$v_g = \frac{\partial \omega_{SW}}{\partial k} \approx \frac{2\pi\Delta f}{2\pi/s} = \Delta f s. \tag{5.4}$$

Here $\omega_{SW} = 2\pi f$ and $k = 2\pi/\lambda$ are the spin wave's angular frequency and wavevector, Δf is the frequency difference between two consecutive maxima or minima of the fringes (Fig. 5.3a) and s is the center-to-center distance between both microstrips.

We extract the exchange constant of our Ga:YIG film by fitting the measured group velocity to an analytical expression derived from the spin-wave dispersion. The Damon-Eshbach spin-wave dispersion for magnetic thin films with cubic and perpendicular anisotropy is given by [21] (section 5.5.4)

$$\omega_{SW}(k) = \sqrt{\omega_B(\omega_B + \omega_M - \omega_K) + \frac{\omega_M t}{2}(\omega_M - \omega_K)k + \gamma_{||} D(2\omega_B + \omega_M - \omega_K)k^2 + \gamma_{||}^2 D^2 k^4}. \tag{5.5}$$

Here we defined for notational convenience $\omega_B = \gamma_{||} B_0$, $\omega_M = \gamma_{||}\mu_0 M_s$, $\omega_D = \frac{\gamma_{||} D}{M_s}$, and $\omega_K = \gamma_{||}(2K_{2\perp}/M_s + K_4/M_s)$, t is the thickness of the film and $D = 2\alpha/M_s$ is the spin stiffness, with α the exchange constant. Differentiating with respect to k gives an analytical expression for the group velocity

$$v_g(k) = \frac{1}{2\sqrt{\omega_{SW}(k)}}\left(\frac{\omega_M t}{2}(\omega_M - \omega_K) + 2\gamma_{||} D(2\omega_B + \omega_M - \omega_K)k + 4\gamma_{||}^2 D^2 k^3\right). \tag{5.6}$$

Since we determined M_s and the anisotropy constants from the VSM and FMR measurements, the exchange constant is the only unknown variable in the dispersion. We determine the exchange constant from spin-wave spectra measured using two sets of striplines with different widths and line-to-line distances (w = 1 µm, s = 6 µm and w = 2.5 µm, s = 12.5 µm) at the same static field (Fig. 5.3a,b). First we extract v_g as a function of frequency from the extrema in the spin-wave spectra using Eq. 5.4 (Fig. 5.3c). By then fitting the measured $v_g(f)$ using Eqns. 5.5 and 5.6 (solid line in Fig. 5.3c), we find $\alpha = 1.3(2) \times 10^{-12}$ J/m and $B_0 = 117.5(3)$ mT (section 5.5.2). The determined exchange constant is about 3 times smaller compared to undoped YIG [18], which is in line with earlier observations of a decreasing exchange constant with increasing gallium concentration in micrometer-thick YIG films [31]. Simultaneously the spin stiffness is increased by about 3 times compared to undoped YIG [18] due to the strong reduction of the saturation magnetization. For large wavelengths the group velocity is negative as a result of the PMA in the sample. Using the extracted exchange constant and Gilbert damping, we calculate a decay length of $\sim$ 30 µm for spin waves with a wavelength of 1 µm (section 5.5.5).
The spin-wave excitation and detection efficiency depends on the absolute value of the Fourier amplitude of the radio-frequency magnetic field B^{RF} generated by a stripline,

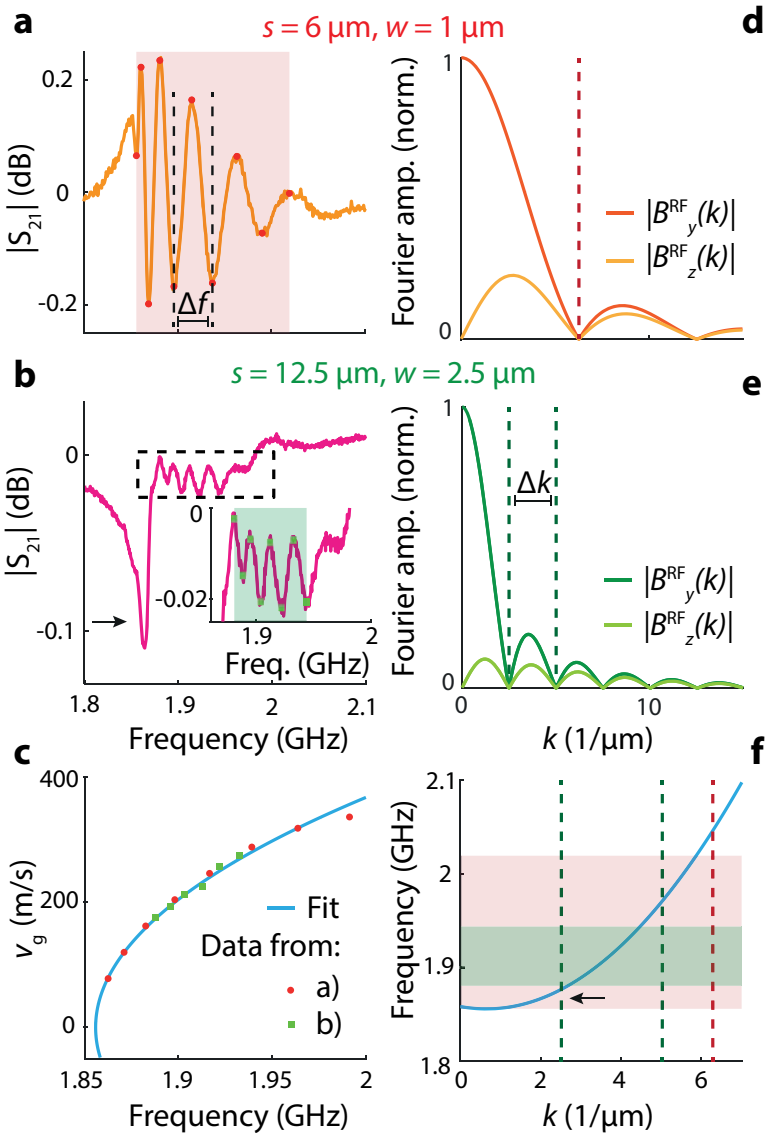

Figure 5.3: Extracting the exchange constant from spin-wave transmission spectra. (**a**,**b**) Background-subtracted linetraces of $|S_{21}|$ for two sets of striplines (a: $w = 1$ µm, $s = 6$ µm, b: $w = 2.5$ µm, $s = 12.5$ µm, excitation power: −35 dBm). The red circles (a) and green squares (inset of b) mark the extrema of the spin-wave fringes. (**c**) From the frequency difference between the extrema Δf we determine the group velocity v_g of the spin waves at the center frequency between the extrema. The blue line fits the data with an analytical expression for v_g, extracting the exchange constant $\alpha = 1.3(2) \times 10^{-12}$ J/m. (**d**,**e**) Normalized Fourier amplitude of the y and z components of the microwave excitation field B^{RF} for striplines with widths $w = 1$ µm (d) and $w = 2.5$ µm (e). (**f**) Reconstructed spin-wave dispersion based on the fit in (c). The shaded areas correspond to the frequencies of the extrema in (a,b). The dashed lines are the same as in (d,e) and indicate the nodes in $|B^{RF}(k)|$ of the striplines. Only spin waves that are efficiently excited and detected by the striplines are observed in (a,b).

which oscillates in k with a period given by $\Delta k = 2\pi/w$ (Fig. 5.3e) [29, 30]. To verify that the spin waves we observe are efficiently excited and detected by our striplines, we substitute the extracted exchange constant into Eq. 5.5 and plot the spin-wave dispersion (Fig. 5.3f). The shaded areas correspond to the frequencies of the spin-wave fringes (Fig. 5.3a,b) and the dashed lines indicate the nodes in $|B^{\mathrm{RF}}(k)|$ of both striplines (Fig. 5.3d,e). We conclude that the fringes in Fig. 5.3a correspond to spin waves excited by the first maximum of $|B^{\mathrm{RF}}(k)|$ and that the fringes in Fig. 5.3b correspond to spin waves excited by the second maximum.

Surprisingly, we do not observe fringes in Fig. 5.3b corresponding to the first maximum of $|B^{\mathrm{RF}}(k)|$, but rather see a dip in this frequency range (arrows in Fig. 5.3b,f). This can be understood by noting that the average frequency difference between the fringes would be smaller than the spin-wave linewidth (section 5.5.6). Low-amplitude fringes corresponding to small-wavelength spin waves excited by the second k-space maximum of the 1-µm-wide stripline are also visible (Fig. 5.2b, section 5.5.7). These results demonstrate that the spin-wave dispersion in weak magnets can be reliably extracted using propagating spin wave spectroscopy by combining measurements on striplines with different widths and spacings.

The spin-wave excitation and detection efficiency depends on the absolute value of the Fourier amplitude of the radio-frequency magnetic field B^{RF} generated by a stripline, which oscillates in k with a period given by $\Delta k = 2\pi/w$ (Fig. 5.3e) [29, 30]. To verify that the spin waves we observe are efficiently excited and detected by our striplines, we substitute the extracted exchange constant into Eq. 5.5 and plot the spin-wave dispersion (Fig. 5.3f). For small wavevectors the dispersion decreases due to the PMA in the sample, until the exchange interaction becomes dominant and the dispersion starts increasing. The shaded areas correspond to the frequencies of the spin-wave fringes (Fig. 5.3a,b) and the dashed lines indicate the nodes in $|B^{\mathrm{RF}}(k)|$ of both striplines (Fig. 5.3d,e). We conclude that the fringes in Fig. 5.3a correspond to spin waves excited by the first maximum of $|B^{\mathrm{RF}}(k)|$ and that the fringes in Fig. 5.3b correspond to spin waves excited by the second maximum.

Surprisingly, we do not observe fringes in Fig. 5.3b corresponding to the first maximum of $|B^{\mathrm{RF}}(k)|$, but rather see a dip in this frequency range (arrows in Fig. 5.3b,f). This can be understood by noting that the average frequency difference between the fringes would be smaller than the spin-wave linewidth (section 5.5.6). Low-amplitude fringes corresponding to small-wavelength spin waves excited by the second k-space maximum of the 1-µm-wide stripline are also visible (Fig. 5.2b, section 5.5.7). These results demonstrate that the spin-wave dispersion in weak magnets can be reliably extracted using propagating spin wave spectroscopy by combining measurements on striplines with different widths and spacings.

When strongly driven to large amplitudes, the FMR behaves like a Duffing oscillator with a bistable response [32]. Such bistability could potentially be harnessed for microwave switching [33]. Foldover of the FMR and standing spin-wave modes has been studied

for several decades [32–34], but bistability of propagating spin waves was only observed before in active feedback rings [35], spin-pumped systems [36] and magnonic ring resonators [37]. We show that we can characterize the bistability of propagating spin waves in Ga:YIG thin films using our spectroscopy technique.

When increasing the drive power we observe frequency shifts of the spin waves (Fig. 5.4a,c). These nonlinear shifts result from the four-magnon self-interaction term in the spin-wave Hamiltonian. For an in-plane magnetized thin film, the shifts are given by [38]

$$\tilde{\omega}_k = \omega_k + W_{kk,kk}|a_k|^2. \tag{5.7}$$

Here $\tilde{\omega}_k$ (ω_k) is the nonlinear (linear) spin-wave angular frequency, $W_{kk,kk}$ is the four-wave frequency-shift parameter and a_k is the spin-wave amplitude. In our case $W_{kk,kk}$ is positive as a result of the PMA in the sample, leading to positive frequency shifts of the spin-wave modes and the FMR (section 5.5.8).

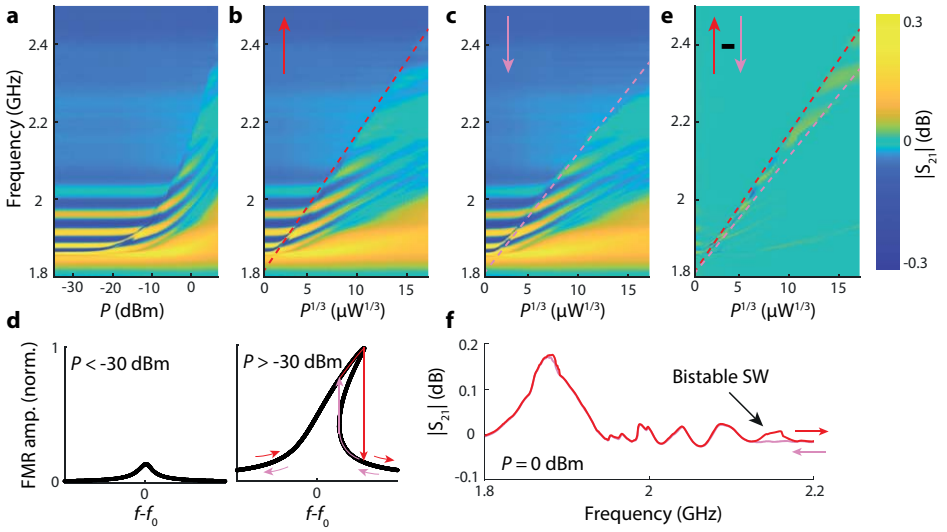

Figure 5.4: Observation of spin-wave frequency shifts and bistability. (**a**) Spin-wave spectra vs excitation power P for an upward frequency sweep ($w = 1$ μm, $s = 6$ μm). Low-frequency spin waves shift to higher frequencies when the microwave excitation power is increased. (**b**,**c**) Spin-wave spectra plotted against $P^{1/3}$ for an upward (b) and downward (c) frequency sweep. The transition frequency, indicated by the dashed lines, scales linearly with $P^{1/3}$. The frequency-sweep direction is indicated by arrows. (**d**) Sketch of the FMR amplitude vs drive frequency at low and high drive power assuming a nonlinear (Duffing) oscillator response. As a result of the foldover at high drive power the amplitude becomes bistable. The amplitude jumps between the two stable branches at higher frequencies for upward frequency sweeps (red arrows) than for downward sweeps (pink arrows). This behaviour and its bistability is also observed in (b) and (c) for $P > -30$ dBm. (**e**) Difference spectra highlighting the bistability region, obtained by subtracting the spectra in (c) from those in (b). (**f**) Linetraces from panels (b) and (c) at $P = 0$ dBm, the black arrow indicates the bistability region. All dashed lines serve as a guide to the eye.

At increased microwave power P, we observe an abrupt transition in the spin-wave spectrum (Fig. 5.4a) at which the spin waves fall back to their unshifted low-power frequencies. We find that the transition frequency scales linearly with $P^{1/3}$ for both upward and downward frequency sweeps (Fig. 5.4b,c, dashed lines) and that it is larger for the upward sweep. Such a $P^{1/3}$ scaling was previously observed for FMR foldover in permalloy, where it was attributed to a significant nonlinear damping term in the Duffing oscillator equation used to model the resonance [32]. This model predicts that the FMR amplitude becomes bistable at large drive power (Fig. 5.4d) and abruptly switches between the high- and low-amplitude states at a transition frequency that scales with $P^{1/3}$ for both up- and downward frequency sweeps.

We extract the bistability region by subtracting the upward and downward frequency sweeps of Fig. 5.4b,c and plotting the result in Fig. 5.4e. We further highlight the bistability by plotting linetraces of the up- and downward frequency sweeps at $P = 0$ dBm (Fig. 5.4f). The foldover starts at a surprisingly low drive power of ~ -30 dBm , potentially caused by reduced spin-wave scattering [34] due to the low density of states associated with the increased spin stiffness and reduced saturation magnetization of our sample.
The observed frequency shifts provide an extra knob for tuning the dispersion of spin waves. They give rise to strong nonlinear microwave transmission between the striplines as a function of excitation power, which may provide opportunities for neuromorphic computing devices that simulate the spiking of artificial neurons above a certain input threshold [37, 39].

5.3. CONCLUSIONS

In summary, we used propagating spin wave spectroscopy to characterize the spin-wave dispersion in a 45-nm-thick film of Ga:YIG. The gallium doping reduces the saturation magnetization of the YIG and introduces a small PMA that lifts the magnetization out of the plane and causes the dispersion to be dominated by the exchange constant. We extract the exchange constant by fitting the group velocity at different frequencies and demonstrate that the detected spin waves are efficiently excited by the excitation fields of the striplines. Finally, we observe pronounced power-dependent frequency shifts and bistability of the spin waves, resulting from the foldover of the FMR. Our results highlight the potential of all-electrical spectroscopy to shed light on the dispersion and nonlinear response of propagating spin waves in weakly-magnetic thin films.

5.4. MATERIALS AND METHODS

A film of gallium-doped yttrium iron garnet (Ga:YIG) was grown using liquid phase epitaxy on an one-inch (111) gadolinium gallium garnet (GGG) substrate and cut into chips of 5x5x0.5 mm^3. Using X-ray reflectometry (XRR) we determined the film thickness to be 45(1) nm [20]. Striplines were fabricated on top of the Ga:YIG by e-beam lithography using PMMA(A8 495)/PMMA(A3 950) bilayer resist with an Elektra92 coating to avoid charging, and subsequent evaporation of Ti/Au (10 nm/190 nm). We wirebond the striplines to a printed circuit board and connect them to our vector network anal-

yser (VNA, Keysight, P9372A) via small, non-magnetic SMPM connectors (Amphenol RF, 925-169J-51PT) to minimize spurious magnetic-field dependent signals and maximize the dynamic range of the bias field. Before reaching the VNA, the signals are amplified by a low noise +20 dB amplifier (Minicircuits, ZX60-83LN-S+) to avoid detection noise on the order of our signals. We place the sample between two large cylindrical permanent magnets (Supermagnete, S35-20-N) to apply a strong and homogeneous bias field. The magnets sit in home-built magnet holders that are mounted on computer-controlled translation stages (Thorlabs, MTS25-Z8, 25 mm range), which allow sweeping the field. We calibrate the magnetic field using a Hall probe (Hirst Magnetic Instruments, GM08). All measurements were performed at room temperature.

ACKNOWLEDGEMENTS

The authors thank A.V. Chumak for reviewing the manuscript, A. Katan, E. Lesne for useful discussions and C.C. Pothoven for fabricating the magnet holders used in the experimental setup. We also thank the staff of the TU Delft electronic support division and the Kavli Nanolab Delft for their support in soldering the printed circuit board and fabricating the microwave striplines.

Funding: This work was supported by the Netherlands Organisation for Scientific Research (NWO/OCW), as part of the Frontiers of Nanoscience program and by the Deutsche Forschungsgemeinschaft (DFG, German Research Foundation) - 271741898.

Author contributions: J.J.C. and T.v.d.S. conceived the experiment. J.J.C. and O.D. built the experimental setup, performed the experiments and analyzed the data. C.D. grew the Ga:YIG film and O.S. performed the VSM and FMR linewidth measurements. J.J.C. fabricated the striplines. J.J.C. and T.v.d.S. wrote the manuscript with contributions from all coauthors. T.v.d.S. supervised the project.

Data and materials availability: All data contained in the figures are available in Zenodo.org at http://doi.org/10.5281/zenodo.5494466, reference number [40]. Additional data related to this paper are available from the corresponding author upon reasonable request.

Competing interests: The authors declare that they have no competing interests.

5.5. SUPPLEMENTARY MATERIAL

5.5.1. EFFECT OF THE MAGNETIC FIELD ALIGNMENT ON THE FMR FREQUENCY

In this section we show that for (111)-oriented lattices with cubic anisotropy the in-plane Kittel relation holds when a strong magnetic field B_0 is applied along the in-plane $[1\bar{1}0]$ crystallographic axis. We also investigate the effect of a $\sim 1^\circ$ out-of-plane angle of B_0 on the FMR frequency and the magnetization direction. Such a small angle may be present due to the manual placement of the sample in our setup (see Methods).
The FMR frequency is calculated according to [41]

$$\omega_{\mathrm{FMR}}^2 = \frac{\gamma^2}{\sin(\theta_M)^2} \cdot \Big(\frac{\partial^2 F}{\partial \theta_M^2} \frac{\partial^2 F}{\partial \phi_M^2} - \big(\frac{\partial^2 F}{\partial \theta_M \partial \phi_M} \big)^2 \Big). \tag{5.8}$$

Here θ_M is the angle of the magnetization with respect to the film's normal, ϕ_M is the in-plane angle of the magnetization with respect to the $[1\bar{1}0]$ crystallographic axis and $F = \frac{F'}{M_s}$, with F' the free energy density and M_s the saturation magnetization (Fig. 5.5). $\gamma = \frac{g\mu_B}{\hbar}$ is the gyromagnetic ratio, with μ_B the Bohr magneton and $\hbar$ the reduced Planck constant. The anisotropic g-factor is given by $g = \sqrt{g_\perp^2 \cos(\theta_M)^2 + g_{||}^2 \sin(\theta_M)^2}$, with $g_{||}$ and $g_\perp$ respectively the in-plane and out-of-plane g-factors [24].
For (111)-oriented films with cubic and uniaxial out-of-plane magnetic anisotropies the normalized free energy density is given by [20, 22]

$$\begin{aligned} F = &-B_0 \Big(\sin(\theta_M)\sin(\theta_B)\cos(\theta_M - \theta_B) + \cos(\theta_M)\cos(\theta_B) \Big) + \frac{1}{2}\big(\mu_0 M_s - \frac{2K_{2\perp}}{M_s}\big)\cos^2(\theta_M) \\ &+ \frac{1}{2} \cdot \frac{2K_4}{M_s} \Big(\frac{1}{3}\cos^4(\theta_M) + \frac{1}{4}\sin^4(\theta_M) - \frac{\sqrt{2}}{3}\sin^3(\theta_M)\cos(\theta_M)\sin(3\phi_M) \Big), \end{aligned} \tag{5.9}$$

with θ_B and ϕ_B the angles of B_0 with respect to respectively the film's normal and the in-plane $[1\bar{1}0]$ crystallographic axis (Fig. 5.5) and μ_0 the vacuum permeability. $\frac{2K_{2\perp}}{M_s}$ and $\frac{2K_4}{M_s}$ are respectively the uniaxial out-of-plane and cubic anisotropy fields, with $K_{2\perp}$ and K_4 the perpendicular and cubic anisotropy constants. Note that to calculate the FMR frequency using Eq. 5.8 at a certain B_0, θ_B and ϕ_B, we first need to find θ_M and ϕ_M that minimize the free energy by numerically solving $\frac{\partial F}{\partial \theta_M}(\theta_M, \phi_M) = 0$ and $\frac{\partial F}{\partial \phi_M}(\theta_M, \phi_M) = 0$. Using Eqns. 5.8 and 5.9 we can calculate the FMR frequency for an out-of-plane magnetic field and magnetization ($\theta_B = \theta_M = 0^\circ$), which gives

$$\omega_{\mathrm{FMR}(\perp)} = \gamma_\perp (B_0 - \mu_0 M_s + \frac{2K_{2\perp}}{M_s} - \frac{4K_4}{3M_s}). \tag{5.10}$$

For an in-plane magnetic field and magnetization ($\theta_B = \theta_M = 90^\circ$), we find

$$\omega_{\mathrm{FMR}(||)} = \gamma_{||} \sqrt{B_0 \cdot \big(B_0 + \mu_0 M_s - \frac{2K_{2\perp}}{M_s} - \frac{K_4}{M_s}\big) - 2\big(\frac{K_4}{M_s}\cos(3\phi_M)\big)^2}. \tag{5.11}$$

The factor 3 in the cosine arises from the triangular in-plane symmetry of a cubic unit cell with its normal along the [111] direction (Fig. 5.5). In our measurements a large in-plane magnetic field is needed to overcome the perpendicular anisotropy and push the magnetization in the plane, such that generally $B_0 \gg |\frac{2K_4}{M_s}| = 8.2$ mT and we can ignore the last term [22]

$$\omega_{\mathrm{FMR}(||)} = \gamma_{||}\sqrt{B_0 \cdot (B_0 + \mu_0 M_s - \frac{2K_{2\perp}}{M_s} - \frac{K_4}{M_s})}. \tag{5.12}$$

Eqns. 5.10 and 5.12 are the same as Eqns. 5.1 and 5.2.

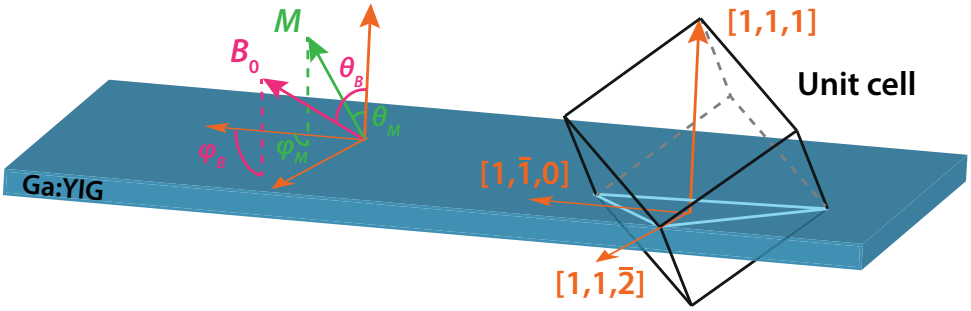

Figure 5.5: Coordinate frame and crystallographic axes in Ga:YIG. The [1$\bar{1}$0] axis is slightly displaced to highlight the triangular symmetry plane (light blue) of the (111)-oriented cubic unit cell. After [22].

FMR FREQUENCY AND MAGNETIZATION DIRECTION AT $\phi_B = 0°$

Fig. 5.6a shows a flipchip FMR measurement with the magnetic field applied along the [1$\bar{1}$0] direction ($\theta_B = 90°$, $\phi_B = 0°$). The solid white line shows a fit to Eq. 5.12 for magnetic fields at which the FMR frequency is increasing. Together with the fitted out-of-plane FMR, we extract $\frac{2K_{2\perp}}{M_s} = 104.7$ mT, $\frac{2K_4}{M_s} = -8.2$ mT and $\frac{\gamma_{||}}{2\pi} = 28.56$ MHz/mT. The same fit and data are presented in Fig. 5.1b.

We can calculate the FMR frequency also for low bias fields by substituting the extracted parameters into Eqns. 5.8 and 5.9. We obtain the black dashed line, which fits reasonably well to the measured FMR, even when the FMR frequency is decreasing with field. The red dashed line shows the calculated FMR frequency when B_0 has an 1° out-of-plane angle ($\theta_B = 89°$), which dramatically increases the minimum FMR frequency. This is because the magnetization turns only asymptotically into the plane when the angle is offset, instead of abruptly (Fig. 5.6b, black line: $\theta_B = 90°$, red line: $\theta_B = 89°$).

We note that in Fig. 5.6a at large bias fields both the black and red dashed lines overlap with the white fit. Therefore, we conclude that the in-plane FMR at $\phi_B = 0°$ is quite robust to any small out-of-plane component of the static field that might be present in our experimental setup, validating the white fit using Eq. 5.12 [22].

FMR FREQUENCY AND MAGNETIZATION DIRECTION AT $\phi_B = 90°$

Fig. 5.6c shows a similar flipchip FMR measurement as in Fig. 5.6a, but now with the field applied along the [11$\bar{2}$] direction ($\theta_B = 90°$, $\phi_B = 90°$, the white line is the same

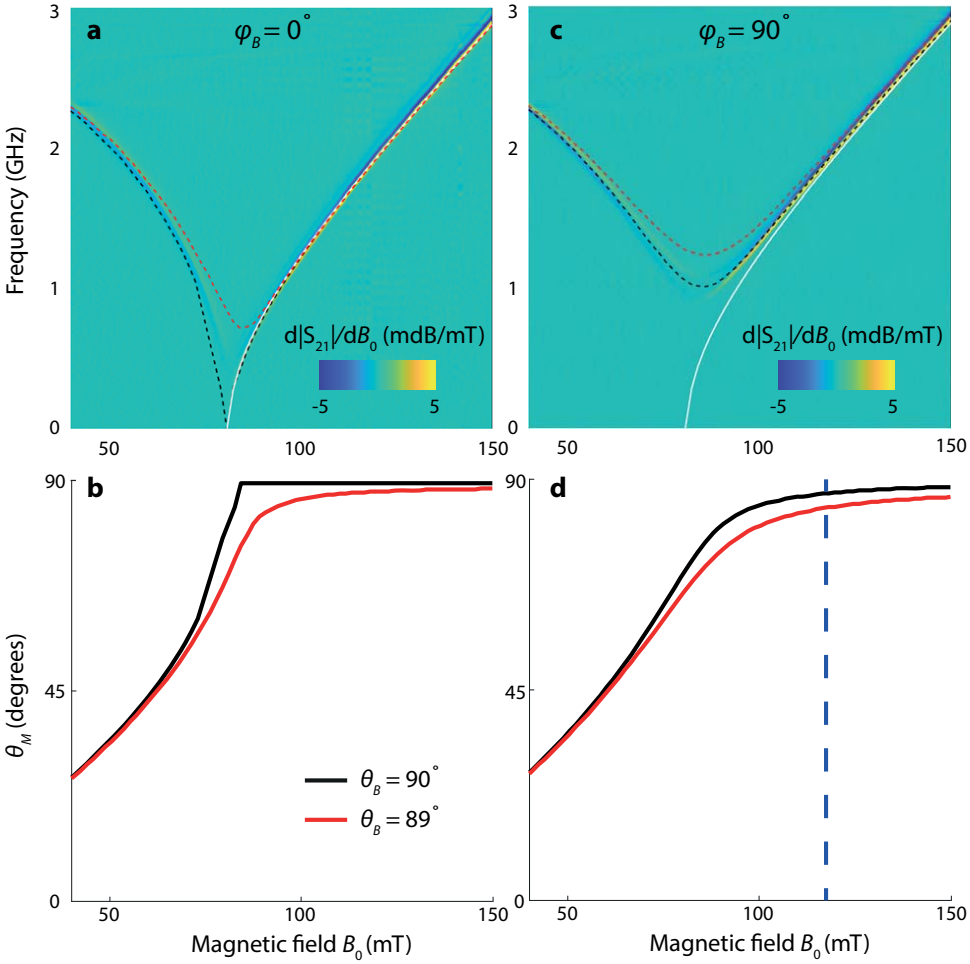

Figure 5.6: Dependence of the FMR frequency on the direction of the external magnetic field B_0. (**a**) Flipchip FMR measurement with B_0 applied parallel to a 180-μm-wide excitation stripline and along the in-plane $[1\bar{1}0]$ crystallographic direction ($\phi_B = 0°$). The FMR is extracted from the field-derivative of the microwave transmission $|S_{21}|$. The solid white line shows a fit to the Kittel relation (Eq. 5.12). Using the extracted anisotropy fields and gyromagnetic ratio, the FMR frequency for the entire B_0-range was numerically calculated assuming $\theta_B = 90°$ (black dashed line) and $\theta_B = 89°$ (red dashed line). (**b**) The minimum FMR frequency is raised at $\theta_B = 89°$ because the magnetization does not abruptly turn into the plane. (**c**) Similar FMR measurement, but with B_0 applied along the $[11\bar{2}]$ direction ($\phi_B = 90°$). The white line is the same as in (a). The black and red dashed lines are the calculated FMR frequencies for $\phi_B = 90°$ at respectively $\theta_B = 90°$ and $\theta_B = 89°$ using the parameters extracted in (a). (**d**) The magnetization maintains a finite out-of-plane component even when $\theta_B = 90°$. The blue dashed line indicates the field at which the exchange constant was determined from the spin-wave spectra. In (a) and (c) a similar background subtraction was performed as in Fig. 5.8.

as in Fig. 5.6a and is added as a reference). The FMR reaches a minimum frequency of about 1 GHz, which is significantly larger than the minimum in the $\phi_B = 0°$ geometry. We reproduce this enhanced frequency minimum by calculating the expected FMR frequency using the parameters extracted in section 5.5.1 (black dashed line, we ignore any potential in-plane anisotropy of the g-factor). The calculated FMR frequency matches the measured FMR remarkably well for all magnetic field values, demonstrating the accuracy of the white fit.

Again we attribute the enhanced FMR minimum to the fact that the magnetization only slowly turns into the plane, even for a perfect in-plane magnetic field $\theta_B = 90°$ (Fig. 5.6d, black line). As a result the FMR frequency asymptotically approaches the in-plane Kittel relation (Eq. 5.12, white line). Similar to before, a change of 1° in θ_B lifts the minimum FMR frequency, explaining the minimum FMR frequency of about 1.25 GHz observed in Fig. 5.2b. Variations on the order of 1° in θ_B are expected in our measurement setup since we manually place the sample between two permanent magnets (see Methods).

Fig. 5.6d shows that the magnetization does not point exactly in the plane during our propagating spin wave spectroscopy measurements, even though this is assumed in the data analysis. We derived the exchange constant from spin-wave spectra taken at approximately $B_0 = 117.5$ mT, at which the magnetization points ~3-6 degrees out of the plane (blue dashed line in Fig. 5.6d). We neglect this small out-of-plane angle, because we expect the induced error to be negligible compared to the ~ 15% error obtained from the fit in Fig. 5.3c.

5.5.2. SYSTEMATIC ERROR IN THE APPLIED BIAS FIELD

In this section we calculate how a systematic error in the applied bias field affects the error of the anisotropy fields, which we extracted from the FMR frequency (Fig. 5.1b). From the fits of the FMR frequency we obtain $\frac{\gamma_\perp}{2\pi} = 29.40(3)$ MHz/mT and $\alpha = -\mu_0 M_s + \frac{2K_{2\perp}}{M_s} - \frac{2}{3}\frac{2K_4}{M_s} = 91.1(2)$ mT (out-of-plane bias field), $\frac{\gamma_\parallel}{2\pi} = 28.56(4)$ MHz/mT and $\beta = \mu_0 M_s - \frac{2K_{2\perp}}{M_s} - \frac{1}{2}\frac{2K_4}{M_s} = -81.5(1)$ mT (in-plane bias field). Since we know from vibrating sample magnetometry (VSM) that $M_s = 1.52(6) \cdot 10^4$ A/m, we can calculate the magnetic anisotropy fields

$$\begin{aligned} \frac{2K_4}{M_s} &= -\frac{6}{7}(\alpha+\beta) = 8.2(2)\ \text{mT}, \\ \frac{2K_{2\perp}}{M_s} &= \mu_0 M_s + \frac{3}{7}\alpha - \frac{4}{7}\beta = 104.7(8)\ \text{mT}. \end{aligned} \tag{5.13}$$

Since we manually place our sample between the magnets (Methods), it may have a small offset of ~ 1 mm with respect to the center position. Such an offset would cause a systematic error in the applied magnetic field B_0, which enhances the error of the anisotropy fields. To obtain a conservative estimate of these errors, we determine the systematic error in the applied magnetic field via

$$\Delta B_0(x) = B_0(x+1) + B_0(x-1) - 2 \cdot B_0(x). \tag{5.14}$$

$B_0(x)$ is the magnetic field of a cylindrical magnet at a distance of x mm along its symmetry axis

$$B_0(x) = \frac{B_r}{2}\left(\frac{x+L}{\sqrt{r^2+(x+L)^2}} - \frac{x}{\sqrt{r^2+x^2}}\right). \tag{5.15}$$

Here $B_r = 1320$ mT is the remanence, $L = 20$ mm and $r = 17.5$ mm are the length and radius of the magnet. Fig. 5.7 shows the calculated error $\Delta B_0(x)$ for a 1-mm-offset against the magnetic field B_0 at the center position between the magnets. Including this error in the fit of Fig. 5.1b gives $\alpha = 91.1(3)$ mT and $\beta = -81.5(5)$ mT, resulting in a slight increase in the error of the cubic anisotropy field $\frac{2K_4}{M_s} = 8.2(5)$ mT. The errors in the gyromagnetic ratios and perpendicular anisotropy field do not change significantly. At the magnetic field $B_0 = 117.5$ mT at which we took the spin-wave spectra the error in the field ΔB_0 is ~ 0.3 mT.

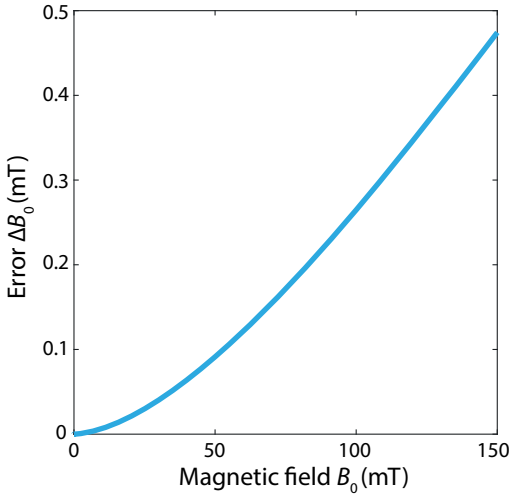

Figure 5.7: Error in the static magnetic field as a result of a 1 mm offset of the sample with respect to the center position between the magnets. For magnetic fields between 100 mT and 150 mT an error of ~ 0.3-0.5 mT is expected.

5.5.3. BACKGROUND-SUBTRACTION PROCEDURES OF THE SPIN-WAVE SPECTRA

For the spin-wave spectra in Fig. 5.3a,b and Fig. 5.4a,b,c,f a background spectrum was subtracted consisting of the mean $|S_{21}|$ transmission at 100 mT and 138 mT, for which there are no spin waves in the frequency range of interest. In Fig. 5.2b a background was subtracted using Gwyddion (Fig. 5.8).

5.5.4. THE SPIN-WAVE DISPERSION OF A MAGNETIC THIN FILM WITH PERPENDICULAR AND CUBIC MAGNETIC ANISOTROPY

The spin-wave dispersion for magnetic thin films with perpendicular magnetic anisotropy (PMA) and cubic anisotropy was derived in reference [21]. Eq. 30 of this work states the

dispersion for an (111)-oriented film with in-plane magnetization, similar as in our experiment

$$\omega_{\mathrm{SW}}(k) = \gamma_{||}\sqrt{\left(B_0 + Dk^2 + \mu_0 M_{\mathrm{s}}(1-f) - \frac{2K_{2\perp}}{M_{\mathrm{s}}} - \frac{K_4}{M_{\mathrm{s}}}\right)\cdot\left(B_0 + Dk^2 + \mu_0 M_{\mathrm{s}} f \sin^2(\phi)\right) - 2\left(\frac{K_4}{M_{\mathrm{s}}}\cos(3\phi_M)\right)^2}. \tag{5.16}$$

Here ω_{SW} is the angular frequency of a spin wave with wavevector k that propagates at an angle ϕ with respect to the magnetization. $D = 2\alpha_{\mathrm{ex}}/M_{\mathrm{s}}$ is the spin stiffness, with α_{ex} the exchange constant, and $f = 1-(1-e^{-kt})/kt$ with t the thickness of the film and ϕ_M is the angle of the magnetization with respect to $[1\bar{1}0]$ crystallographic direction. We note that if we set $k = 0$ in Eq. 5.16, we obtain the in-plane FMR frequency derived before (Eq. 5.11).

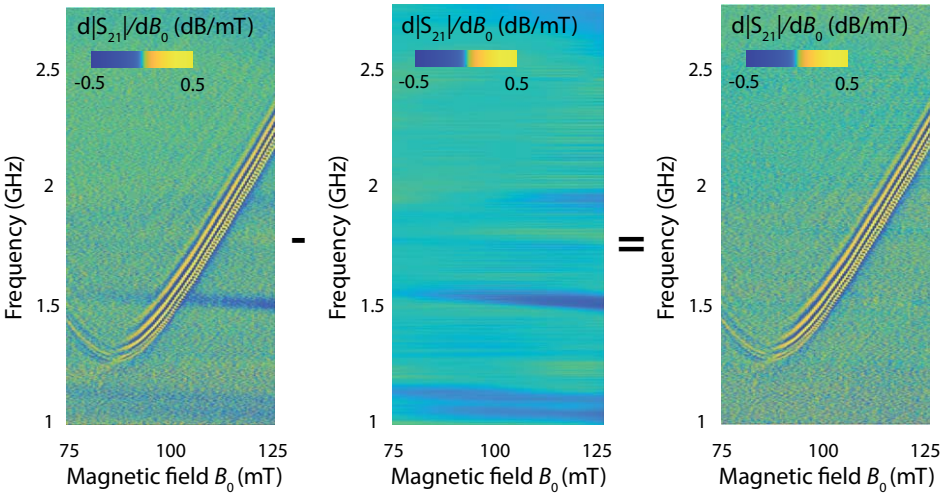

Figure 5.8: Background-subtraction procedure of the microwave spectrum in Fig. 5.2b. The measured data (left figure) contains spurious signals attributed to small changes in the microwave transmission of the cables and connectors that attach the VNA to the striplines as a function of magnetic field. We filter these signals by first masking the high-curvature part of measured data that contains the spin-wave fringes. Then we fit a fifth-order polynomial through each horizontal line, excluding the masked data, and subtract it as a background (middle figure). The resulting spectrum only contains the spin-wave fringes (right figure, same as Fig. 5.2b). The image processing was performed using Gwyddion (version 2.58).

In our experiment we measure spin waves in the Damon-Eshbach configuration ($\phi = \pi/2$), we apply the external field B_0 along $[11\bar{2}]$ ($\phi_M = \pi/2$) and the wavelengths of the detected spin waves are much smaller than the thickness of the film ($kt \ll 1$), such that we can approximate $f \approx kt/2$. This gives

$$\omega_{\mathrm{SW}}(k) = \sqrt{\left(\omega_B + \gamma_{||}Dk^2 - \omega_K + \omega_M(1-kt/2)\right)\left(\omega_B + \gamma_{||}Dk^2 + \omega_M kt/2\right)}, \tag{5.17}$$

where we defined $\omega_B = \gamma_{||} B_0$, $\omega_M = \gamma_{||}\mu_0 M_s$, and $\omega_K = \gamma_{||}(\frac{2K_{2\perp}}{M_s} + \frac{K_4}{M_s})$ for convenience of notation. Working out the brackets and rearranging the terms in orders of k gives

$$\omega_{SW} = \sqrt{\omega_B\big(\omega_B + \omega_M - \omega_K\big) + \frac{\omega_M t}{2}\big(\omega_M - \omega_K\big)k + \gamma_{||}D\big(2\omega_B + \omega_M - \omega_K - (\frac{\omega_M t}{2})^2\big)k^2 + \gamma_{||}^2 D^2 k^4}. \tag{5.18}$$

For the spin-wave spectra taken at $B_0 = 117.5$ mT we find $(\frac{\omega_M t}{2})^2 \ll 2\omega_B + \omega_M - \omega_K$ due to the low saturation magnetization and thickness of our film, such that we can further approximate

$$\omega_{SW} = \sqrt{\omega_B(\omega_B + \omega_M - \omega_K) + \frac{\omega_M t}{2}(\omega_M - \omega_K)k + \gamma_{||}D(2\omega_B + \omega_M - \omega_K)k^2 + \gamma_{||}^2 D^2 k^4}, \tag{5.19}$$

which is Eq. 5.5.

We derive the group velocity v_g by differentiating with respect to k

$$v_g = \frac{\partial \omega_{SW}}{\partial k} = \frac{1}{2\sqrt{\omega_{SW}}}\big(\frac{\omega_M t}{2}(\omega_M - \omega_K) + 2\gamma_{||}D(2\omega_B + \omega_M - \omega_K)k + 4\gamma_{||}^2 D^2 k^3\big), \tag{5.20}$$

which is Eq. 5.6.

5.5.5. CALCULATION OF THE SPIN-WAVE DECAY LENGTH

We consider a magnetic film with perpendicular magnetic anisotropy (PMA) in the yz-plane and a static magnetic field B_0 oriented along z, that pushes the unit magnetization $\mathbf{m}$ into the plane in the z-direction. Spin waves are excited by a stripline oriented along z. The transverse magnetic susceptibility tensor $\overleftrightarrow{\chi}$ relates the transverse magnetization to the drive field of the stripline $\mathbf{B_{AC}}$, according to

$$\begin{pmatrix} m_x \\ m_y \end{pmatrix} = \overleftrightarrow{\chi}\begin{pmatrix} B_{AC,x} \\ B_{AC,y} \end{pmatrix}. \tag{5.21}$$

The decay length y_{decay} is given by the linewidth of $\overleftrightarrow{\chi}$ in k-space [42], which we derive from the Landau-Lifshitz-Gilbert (LLG) equation.

THE LLG EQUATION

The LLG equation describes the dynamics of the magnetization and is given by

$$\dot{\mathbf{m}} = -\gamma \mathbf{m} \times \mathbf{B} - \alpha_G \dot{\mathbf{m}} \times \mathbf{m}, \tag{5.22}$$

where γ is the gyromagnetic ratio, α_G is the Gilbert damping and $\mathbf{B} = \mathbf{B_{eff}} + \mathbf{B_{AC}}$. The effective magnetic field $\mathbf{B_{eff}}$ is derived from the free energy density F of the magnet

$$B_{eff,\alpha} = -\frac{1}{M_s}\frac{\partial F}{\partial m_\alpha}, \tag{5.23}$$

where $\alpha = x, y, z$. The free energy density includes the Zeeman energy, the demagnetizing field $\mathbf{B}_d$, the PMA energy, and the exchange interaction

$$F = -M_s m_z B_0 - M_s \mathbf{m}\cdot\mathbf{B}_d/2 - \frac{K}{2}m_x^2 + \frac{D}{2}\sum_{\alpha,\beta=x,y,z}\left(\frac{\partial m_\alpha}{\partial \beta}\right)^2, \tag{5.24}$$

where D is the spin stifness and K is the uniaxial anisotropy constant perpendicular to the film. We use a positive sign convention such that a positive K favours an out-of-plane magnetization. For convenience of notation we define $\omega_B = \gamma B_0$, $\omega_M = \gamma \mu_0 M_s$, $\omega_D = \frac{\gamma D}{M_s}$, and $\omega_K = \frac{\gamma K}{M_s}$.

THE TOTAL MAGNETIC FIELD

From Eqns. 5.23 and 5.24 we find that the anisotropy contribution to the effective magnetic field is given by

$$B_{\text{eff},x}^{\text{PMA}} = -\frac{1}{M_s}\frac{\partial F^{\text{PMA}}}{\partial m_x} = \frac{\omega_K}{\gamma} m_x. \tag{5.25}$$

The contributions of the Zeeman-, demagnetizing- and exchange energy to $\mathbf{B}_{\text{eff}}$ have been derived elsewhere [42, 43]. For spin waves propagating in the y-direction as in our experiments, this results in

$$\begin{aligned} \gamma B_x &= \omega_M (f-1) m_x - \omega_D k^2 m_x + \omega_K m_x + \gamma B_{\text{AC},x}, \\ \gamma B_y &= -\omega_M f m_y - \omega_D k^2 m_y + \gamma B_{\text{AC},y}, \\ \gamma B_z &= \omega_B. \end{aligned} \tag{5.26}$$

Here $f = 1 - (1 - e^{-kt})/kt$, with t the thickness of the film.

THE MAGNETIC SUSCEPTIBILITY

We derive the magnetic susceptibility by rewriting the LLG equation (Eq. 5.22) in the frequency domain and assuming a small, linear response such that $m_z \approx 1$:

$$\begin{aligned} -i\omega m_x &= -\gamma(B_z m_y - B_y) + i\alpha_G \omega m_y, \\ -i\omega m_y &= -\gamma(B_x - B_z m_x) - i\alpha_G \omega m_x. \end{aligned} \tag{5.27}$$

We can rewrite this in matrix form, according to

$$\begin{pmatrix} \omega_1 - i\alpha_G\omega & i\omega \\ -i\omega & \omega_2 - i\alpha_G\omega \end{pmatrix} \begin{pmatrix} m_x \\ m_y \end{pmatrix} = \gamma \begin{pmatrix} B_{\text{AC},x} \\ B_{\text{AC},y} \end{pmatrix}, \tag{5.28}$$

in which

$$\begin{aligned} \omega_1 &= \omega_B + \omega_D k^2 - \omega_K + \omega_M (1-f), \\ \omega_2 &= \omega_B + \omega_D k^2 + \omega_M f. \end{aligned} \tag{5.29}$$

We obtain the susceptibility by inverting Eq. 5.28

$$\overleftrightarrow{\chi} = \frac{\gamma}{(\omega_1 - i\alpha_G\omega)(\omega_2 - i\alpha_G\omega) - \omega^2} \begin{pmatrix} \omega_2 - i\alpha_G\omega & -i\omega \\ i\omega & \omega_1 - i\alpha_G\omega \end{pmatrix}. \tag{5.30}$$

The susceptibility becomes singular when

$$\Lambda = (\omega_1 - i\alpha_G\omega)(\omega_2 - i\alpha_G\omega) - \omega^2 = 0. \tag{5.31}$$

We find the linewidth in k-space by Taylor expanding $\omega(k) \approx \omega(k_0) + v_g(k - k_0)$, giving

$$\Lambda = 2\omega(k)\big(v_g(k-k_0) - i\alpha_G \frac{\omega_1+\omega_2}{2}\big) = 0. \tag{5.32}$$

Solving this equation gives

$$k = k_0 + i\alpha_G \frac{\omega_1+\omega_2}{2v_g}, \tag{5.33}$$

such that decay length is given by

$$y_{\text{decay}} = \frac{2v_g}{\alpha_G(\omega_1+\omega_2)}. \tag{5.34}$$

Using Eq. 5.34 and the parameters extracted in this study ($B_0 = 117.5$ mT, $\alpha_{ex} = 1.3\cdot10^{-12}$ J/m, $\frac{2K_{2\perp}}{M_s} = 104.7$ mT, $\frac{\gamma_{||}}{2\pi} = 28.56$ MHz/mT, $M_s = 1.52\cdot10^{-4}$ A/m, $t = 45$ nm and $\alpha_G = 1\cdot10^{-3}$), we obtain a decay length ~ 30 µm for spin waves with a wavelength of 1 µm.

5.5.6. COMPARING THE FREQUENCY DIFFERENCE BETWEEN FRINGES TO THE SPIN-WAVE LINEWIDTH

In this section we calculate the expected average frequency difference Δf between spin-wave fringes excited by the first maximum of the microwave driving field Fourier amplitude ($|B^{RF}(k)|$) in Fig. 5.3b. The stripline has a width $w = 2.5$ µm, such that $|B^{RF}(k)|$ has its first node at $k_{min} = \frac{2\pi}{2.5}$ µm^{-1} [29]. Everytime another wavelength fits within the center-to-center distance s between both striplines another fringe is observed in the signal. Therefore the condition $s = n\lambda$ applies for every nth fringe, with λ the spin-wave wavelength. This means that fringes occur every $\Delta k = \frac{2\pi}{s} = \frac{2\pi}{12.5}$ µm^{-1} in k-space. In the first maximum of the excitation spectrum we would thus expect $\frac{k_{min}}{\Delta k} = 5$ fringes. According to the reconstructed dispersion (Fig. 5.3f) the frequency difference between spin waves with wavevector k_{min} and the minimum of the band is about 20 MHz, leading to an average frequency difference of $\frac{20}{5} = 4$ MHz between consecutive fringes. This is on the order of the FMR linewidth of undoped YIG films of similar thicknesses [20]. Assuming that Ga:YIG has a similar or larger linewidth, we argue that we cannot resolve fringes in the first maximum of the excitation field's Fourier amplitude because they are too narrow compared to the intrinsic spin-wave linewidth.

5.5.7. ZOOMED-IN SPIN-WAVE SPECTRA DISPLAYING LOW-AMPLITUDE FRINGES

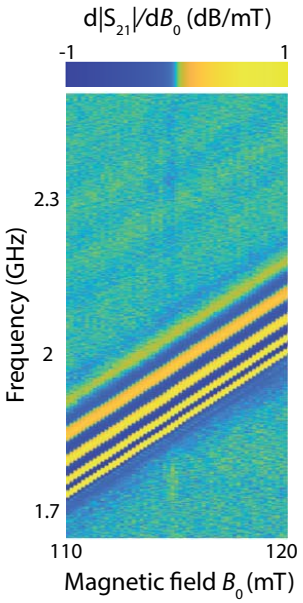

Figure 5.9: Detailed microwave spectrum zoomed-in on the spin-wave fringes. Low-amplitude fringes excited by the second maximum of the excitation field's Fourier amplitude are visible at high frequencies. The actual measured data without any background-subtraction is presented ($w = 1$ µm, $s = 6$ µm, excitation power -35 dBm).

5.5.8. CALCULATION OF THE NONLINEAR FREQUENCY-SHIFT COEFFICIENT

For Damon-Eshbach spin waves with wavevector k and frequency $\omega_k/2\pi$ the nonlinear four-magnon frequency-shift coefficient $W_{kk,kk}$ is given by [38]

$$W_{kk,kk} = \frac{1}{2}\Big(\frac{2\omega_B + \omega_M(N_{xx,k} + N_{yy,k})}{2\omega_k}\Big)^2 \cdot \big(3\omega_B + \omega_M(2N_{zz,0} + N_{zz,2k})\big) - \frac{1}{2}\big(3\omega_B + \omega_M(N_{xx,k} + N_{yy,k} + N_{zz,2k})\big), \tag{5.35}$$

with $N_{ij,k}$ the (i,j)th index of the spin-wave tensor N_k. The three-wave correction term vanishes since the spin waves propagate perpendicular to the magnetization. The precessional xyz-frame is defined such that z points in the plane along the magnetization, x along the film normal and y points in-plane perpendicular to z and parallel to the wavevector of the spin waves.

N_k is the Fourier transform of the tensorial Green's function $N(r,r') = N(r,r')_{\text{dip}} + N(r,r')_{\text{ex}} + N(r,r')_{\text{ani}}$, which has components due to uniaxial anisotropy and the dipolar and ex-

change interactions

$$N_k e^{ikr} = \int N(r,r')e^{ikr'}\,d^3r' = \int \left(N(r,r')_{\text{dip}} + N(r,r')_{\text{ex}}\right)e^{ikr'}\,d^3r' + \int N(r,r')_{\text{ani}}\,e^{ikr'}\,d^3r'. \tag{5.36}$$

The contribution to N_k from the $N(r,r')_{\text{dip}}$ and $N(r,r')_{\text{ex}}$ components in the thin-film limit were derived earlier [38]. Following this work, $N(r,r')_{\text{ani}}$ due to uniaxial anisotropy in the out-of-plane x-direction is given by

$$N(r,r')_{\text{ani}} = -\frac{B_{2\perp}}{\mu_0 M_s}\delta(r-r')\hat{x}\otimes\hat{x}. \tag{5.37}$$

Here $B_{2\perp} = \frac{2K_{2\perp}}{M_s}$ is the uniaxial out-of-plane anisotropy field, $\otimes$ denotes a dyadic unit vector product and $\delta(r-r')$ is the Dirac delta function. As a result of the dyadic product only the (x,x) index of $N(r,r')_{\text{ani}}$ is non-zero, leading to a contribution on $N_{xx,k}$

$$N_{xx,k}e^{ikr} = \int -\frac{B_{2\perp}}{\mu_0 M_s}\delta(r-r')e^{ikr'}\,d^3r' = -\frac{B_{2\perp}}{\mu_0 M_s}e^{ikr}. \tag{5.38}$$

By adding this contribution to the other components, we find that the diagonal elements of N_k in the Damon-Eshbach configuration are given by

$$\begin{aligned} N_{xx,k} &= \frac{D}{\mu_0 M_s}k^2 + 1 - f - \frac{B_{2\perp}}{\mu_0 M_s}, \\ N_{yy,k} &= \frac{D}{\mu_0 M_s}k^2 + f, \\ N_{xx,k} &= \frac{D}{\mu_0 M_s}k^2, \end{aligned} \tag{5.39}$$

with $f = 1-(1-e^{-kt})/kt$ and t the thickness of the film as before. We neglected the cubic anisotropy since it is small relative to the uniaxial anisotropy.

By substituting Eqns. 5.39 into Eq. 5.35 we can calculate $W_{kk,kk}$ for the wavevectors relevant for this work (Fig. 5.10). For all these wavevectors $W_{kk,kk}$ is positive, explaining the positive frequency shifts of the spin waves that we observe when increasing the drive power. This is in contrast to the frequency shift caused by the reduction of the saturation magnetization as a result of strong driving or heating. In this simple picture a downward frequency shift is expected for in-plane magnetization (Fig. 5.11), highlighting the value of the Hamiltonian formalism that was used to calculate the nonlinear frequency-shift coefficient [38].

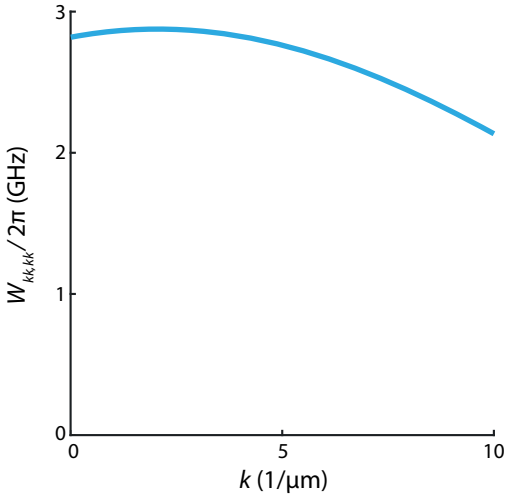

5

Figure 5.10: Nonlinear frequency-shift coefficient $W_{kk,kk}$ for Damon-Eshbach spin waves in Ga:YIG. We used the dispersion in Fig. 5.3f as an input, together with the extracted parameters $B_0 = 117.5$ mT, $\alpha_{ex} = 1.3 \cdot 10^{-12}$ J/m, $\frac{2K_{2\perp}}{M_S} = 104.7$ mT, $\frac{\gamma_{||}}{2\pi} = 28.56$ MHz/mT, $M_S = 1.52 \cdot 10^{-4}$ A/m and $t = 45$ nm. The cubic anisotropy is neglected. The positive sign of the calculated frequency-shift coefficient matches the positive frequency shifts observed in the experiment.

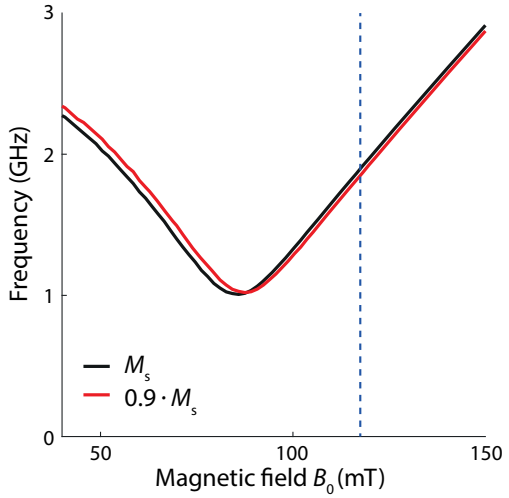

Figure 5.11: Expected downward frequency shift upon reduction of the saturation magnetization. Field dependence of the FMR frequency of Ga:YIG for unreduced saturation magnetization ($M_S = 1.52 \cdot 10^4$ A/m, black line) and for 10%-reduced saturation magnetization ($M_S = 1.37 \cdot 10^4$ A/m, red line). The bias field is applied in the $[11\bar{2}]$ direction and the magnetic anisotropy fields are the same for both curves. The dashed line indicates the field at which we performed our spin-wave spectroscopy measurements. Clearly a negative frequency shift is expected upon decreasing the saturation magnetization, which is in contrast to the positive frequency shifts we observe.

BIBLIOGRAPHY

[1] A. A. Serga, A. Chumak, and B. Hillebrands, "YIG magnonics", Journal of Physics D: Applied Physics **43**, 264002 (2010).

[2] K. Y. Guslienko and A. N. Slavin, "Magnetostatic Green's functions for the description of spin waves in finite rectangular magnetic dots and stripes", Journal of Magnetism and Magnetic Materials **323**, 2418 (2011).

[3] P. Pirro, V. I. Vasyuchka, A. A. Serga, and B. Hillebrands, "Advances in coherent magnonics", Nature Reviews Materials (2021).

[4] A. Barman et al., "The 2021 Magnonics Roadmap", Journal of Physics: Condensed Matter **33**, 413001 (2021).

[5] P. Hansen et al., "Saturation magnetization of gallium-substituted yttrium iron garnet", Journal of Applied Physics **45**, 2728 (1974).

[6] J. E. Mee, G. R. Pulliam, D. M. Heinz, J. M. Owens, and P. J. Besser, "Mobile cylindrical domains in epitaxial Ga:YIG films", Applied Physics Letters **18**, 60 (1971).

[7] D. M. Heinz, P. J. Besser, J. M. Owens, J. E. Mee, and G. R. Pulliam, "Mobile cylindrical magnetic domains in epitaxial garnet films", Journal of Applied Physics **42**, 1243 (1971).

[8] A. Haldar, C. Tian, and A. O. Adeyeye, "Isotropic transmission of magnon spin information without a magnetic field", Science Advances **3**, e1700638 (2017).

[9] A. B. Ustinov, B. A. Kalinikos, and E. Lähderanta, "Nonlinear phase shifters based on forward volume spin waves", Journal of Applied Physics **113**, 113904 (2013).

[10] S. Klingler et al., "Spin-wave logic devices based on isotropic forward volume magnetostatic waves", Applied Physics Letters **106**, 212406 (2015).

[11] N. Kanazawa et al., "Demonstration of a robust magnonic spin wave interferometer", Scientific Reports **6**, 30268 (2016).

[12] B. A. Kalinikos and A. N. Slavin, "Theory of dipole-exchange spin wave spectrum for ferromagnetic films with mixed exchange boundary conditions", Journal of Physics C: Solid State Physics **19**, 7013 (1986).

[13] V. Vlaminck and M. Bailleul, "Current-Induced Spin-Wave Doppler Shift", Science **322**, 410 (2008).

[14] S. Neusser et al., "Anisotropic propagation and damping of spin waves in a nanopatterned antidot lattice", Physical Review Letters **105**, 1 (2010).

[15] J. Chen et al., "Spin wave propagation in ultrathin magnetic insulators with perpendicular magnetic anisotropy", Applied Physics Letters **114**, 212401 (2019).

[16] H. Qin, S. J. Hämäläinen, K. Arjas, J. Witteveen, and S. van Dijken, "Propagating spin waves in nanometer-thick yttrium iron garnet films: Dependence on wave vector, magnetic field strength, and angle", Physical Review B **98**, 224422 (2018).

[17] J. Chen et al., "Excitation of unidirectional exchange spin waves by a nanoscale magnetic grating", Physical Review B **100**, 104427 (2019).

[18] S. Klingler et al., "Measurements of the exchange stiffness of YIG films using broadband ferromagnetic resonance techniques", Journal of Physics D: Applied Physics **48**, 015001 (2015).

[19] U. K. Bhaskar, G. Talmelli, F. Ciubotaru, C. Adelmann, and T. Devolder, "Backward volume vs Damon–Eshbach: A traveling spin wave spectroscopy comparison", Journal of Applied Physics **127**, 33902 (2020).

[20] C. Dubs et al., "Low damping and microstructural perfection of sub-40nm-thin yttrium iron garnet films grown by liquid phase epitaxy", Physical Review Materials **4**, 024416 (2020).

[21] B. A. Kalinikos, M. P. Kostylev, N. V. Kozhus, and A. N. Slavin, "The dipole-exchange spin wave spectrum for anisotropic ferromagnetic films with mixed exchange boundary conditions", Journal of Physics: Condensed Matter **2**, 9861 (1990).

[22] S. A. Manuilov, S. I. Khartsev, and A. M. Grishin, "Pulsed laser deposited $Y_3Fe_5O_{12}$ films: Nature of magnetic anisotropy I", Journal of Applied Physics **106**, 123917 (2009).

[23] V. B. Bobkov, I. Zavislyak, and V. F. Romanyuk, "Microwave spectroscopy of magnetostatic waves in epitaxial ferrite films", Journal of Communications Technology and Electronics **48**, 196 (2003).

[24] M. Farle, "Ferromagnetic resonance of ultrathin metallic layers", Reports on Progress in Physics **61**, 755 (1998).

[25] C. Dubs et al., "Sub-micrometer yttrium iron garnet LPE films with low ferromagnetic resonance losses", Journal of Physics D: Applied Physics **50**, 204005 (2017).

[26] L. Soumah et al., "Ultra-low damping insulating magnetic thin films get perpendicular", Nature Communications **9**, 3355 (2018).

[27] M. Evelt et al., "Emission of Coherent Propagating Magnons by Insulator-Based Spin-Orbit-Torque Oscillators", Physical Review Applied **10**, 041002 (2018).

[28] T. Yu, Y. M. Blanter, and G. E. W. Bauer, "Chiral Pumping of Spin Waves", Physical Review Letters **123**, 247202 (2019).

[29] F. Ciubotaru, T. Devolder, M. Manfrini, C. Adelmann, and I. P. Radu, "All electrical propagating spin wave spectroscopy with broadband wavevector capability", Applied Physics Letters **109**, 012403 (2016).

[30] I. Bertelli et al., "Magnetic resonance imaging of spin-wave transport and interference in a magnetic insulator", Science Advances **6**, eabd3556 (2020).

[31] J. W. Boyle et al., "Investigations of epitaxial Ga : YIG(111) films by Brillouin light scattering and microwave spectroscopy", Le Journal de Physique IV **07**, C1–497–C1 (1997).

[32] Y. S. Gui, A. Wirthmann, and C.-M. Hu, "Foldover ferromagnetic resonance and damping in permalloy microstrips", Physical Review B **80**, 184422 (2009).

[33] Y. Fetisov, C. Patton, and V. Synogach, "Nonlinear ferromagnetic resonance and foldover in yttrium iron garnet thin films-inadequacy of the classical model", IEEE Transactions on Magnetics **35**, 4511 (1999).

[34] Y. Li et al., "Nutation Spectroscopy of a Nanomagnet Driven into Deeply Nonlinear Ferromagnetic Resonance", Physical Review X **9**, 041036 (2019).

[35] P. A. P. Janantha, B. Kalinikos, and M. Wu, "Foldover of nonlinear eigenmodes in magnetic thin film based feedback rings", Physical Review B **95**, 064422 (2017).

[36] K. Ando and E. Saitoh, "Spin Pumping Driven by Bistable Exchange Spin Waves", Phys. Rev. Lett. **109**, 26602 (2012).

[37] Q. Wang et al., "A nonlinear magnonic nano-ring resonator", npj Computational Materials **6**, 192 (2020).

[38] P. Krivosik and C. E. Patton, "Hamiltonian formulation of nonlinear spin-wave dynamics: Theory and applications", Physical Review B **82**, 184428 (2010).

[39] J. Feldmann, N. Youngblood, C. D. Wright, H. Bhaskaran, and W. H. P. Pernice, "All-optical spiking neurosynaptic networks with self-learning capabilities", Nature **569**, 208 (2019).

[40] J. J. Carmiggelt, O. C. Dreijer, C. Dubs, O. Surzhenko, and T. van der Sar, *Electrical spectroscopy of the spin-wave dispersion and bistability in gallium-doped yttrium iron garnet* (Zenodo, 2021).

[41] H. Suhl, "Ferromagnetic Resonance in Nickel Ferrite Between One and Two Kilomegacycles", Physical Review **97**, 555 (1955).

[42] I. Bertelli et al., "Imaging Spin-Wave Damping Underneath Metals Using Electron Spins in Diamond", Advanced Quantum Technologies **4**, 2100094 (2021).

[43] A. Rustagi, I. Bertelli, T. van der Sar, and P. Upadhyaya, "Sensing chiral magnetic noise via quantum impurity relaxometry", Phys. Rev. B **102**, 220403 (2020).

6

EXCITON-TO-TRION CONVERSION AS A CONTROL MECHANISM FOR VALLEY POLARIZATION IN ROOM-TEMPERATURE MONOLAYER WS_2

Transition metal dichalcogenide (TMD) monolayers are two-dimensional semiconductors with two valleys in their band structure that can be selectively addressed using circularly polarized light. Their photoluminescence spectrum is characterized by neutral and charged excitons (trions) that form a chemical equilibrium governed by the net charge density. Here, we use chemical doping to drive the conversion of excitons into trions in WS_2 monolayers at room temperature, and study the resulting valley polarization via photoluminescence measurements under valley-selective optical excitation. We show that the doping causes the emission to become dominated by trions with a strong valley polarization associated with rapid non-radiative recombination. Simultaneously, the doping results in strongly quenched but highly valley-polarized exciton emission due to the enhanced conversion into trions. A rate equation model explains the observed valley polarization in terms of the doping-controlled exciton-trion equilibrium. Our results shed light on the important role of exciton-trion conversion on valley polarization in monolayer TMDs.

This chapter has been published in *Scientific Reports* **10**, 17389 (2020) by **J. J. Carmiggelt***, M. Borst*, and T. van der Sar.
* indicates equal contribution.

6.1. INTRODUCTION

Transition metal dichalcogenide (TMD) monolayers are direct-bandgap semiconductors of which the conduction and valence band extrema consist of two valleys [1, 2]. The broken inversion symmetry of the lattice gives rise to optical selection rules that enable valley-selective, inter-band excitation of electrons using circularly polarized light [3–5]. A strong Coulomb interaction results in the subsequent formation of excitons [6], which maintain a valley polarization that is determined by the ratio between the intervalley scattering time and the exciton lifetime [3, 7]. Such valley-polarized excitons have been proposed as carriers of information and play a central role in the field of valleytronics [8, 9]. As such, understanding the processes that govern the exciton lifetime and associated valley polarization is important for assessing the potential applicability of valley-polarized excitons in devices.

Under optical excitation, a charge-density-controlled chemical equilibrium between neutral and charged excitons (trions) forms in a TMD monolayer [10–12]. The conversion into trions reduces the exciton lifetime [13] and may therefore be expected to lead to a large valley polarization of excitons that are created via valley-selective optical pumping, but demonstrating this effect has thus far remained elusive.

The charge density of TMD monolayers can be controlled via electrostatic gating or chemical doping [10, 11, 14–20]. While electrostatic gating is a flexible technique that allows a continuous change of the charge density [10, 11, 14], chemical doping provides a convenient alternative that requires no microfabrication and is well suited for achieving high doping levels [15–20]. Here, we study the valley polarization of excitons and trions in monolayer WS_2 and show that chemical doping via aromatic anisole (methoxybenzene) quenches the exciton photoluminescence and causes the spectrum to become dominated by trions with a strong valley polarization. A spatial study of the remaining exciton emission shows that also the excitons attain a strong valley polarization, which we attribute to the rapid doping-induced conversion into trions. We extend a rate equation model describing exciton-trion conversion [10] to include the two valleys and use it to explain the observed valley polarization in terms of the doping-controlled chemical equilibrium between excitons and trions.

6.2. RESULTS

When doping a TMD monolayer using aromatic molecules such as anisole, Hard Soft Acid Base (HSAB) theory allows predicting whether the dopant will be n- or p-type [16]. Electrons hop between the adsorbed molecules (A) and the monolayer (B) to compensate for the difference in chemical potential μ between both systems [21]. The chemical hardness η of the materials determines how quickly an equilibrium is reached, leading to an average number of transferred electrons per molecule ΔN:

$$\Delta N = \frac{\mu_A - \mu_B}{\eta_A + \eta_B}. \tag{6.1}$$

For both anisole and monolayer WS_2, the chemical potential and chemical hardness has been calculated using density functional theory [22, 23]. Using these values (sec-

tion 6.5.1) we find $\Delta N = 0.22$, such that we expect the monolayer to be n-doped upon physisorption of anisole molecules (Fig. 6.1a).

To study the effect of chemical doping with anisole on the valley polarization properties of WS_2, we start by characterizing the photoluminescence of exfoliated WS_2 monolayers on 280 nm Si/SiO_2 substrates. The emission spectrum of an as-prepared monolayer shows the characteristic bright exciton resonance at 2.01 eV (Fig. 6.1b, black line) [24]. After chemical doping by a two-hour treatment in liquid anisole at 70 C°, the bright exciton resonance is strongly quenched and only a weak emission peak that is red-shifted by $\Delta E = 23$ meV remains (Fig. 6.1b, red line). Because the increased binding energy of trions compared to excitons should lead to such a red shift [14] and the expected n-type doping by the anisole molecules should favour trion formation, we attribute this peak to emission associated with trions. This conclusion is further supported by spatial studies of emission spectra showing both exciton and trion components that we will describe below. As expected, the trion emission is weak due to its long radiative lifetime and strong non-radiative decay attributed to Auger recombination [10, 25, 26].

Doping by adsorbed carbon-hydrogen groups [27] was previously shown to result in an increase of the longitudinal acoustic LA(M) and LA(K) modes in the Raman spectrum of WS_2 monolayers. Our treatment causes a similar increase of the LA(M) Raman mode (Fig. 6.1c), which we therefore attribute to the adsorption of anisole molecules. We do not observe an associated increase of the LA(K) mode at about 190 cm^{-1}, which may be due to the different nature of the adsorbates resulting in different lattice deformations and/or defects in the monolayer. We note that a similar behaviour was observed in previous work on WS_2 monolayers [7], which showed an increasing intensity of the LA(M) Raman mode without an associated increase in the LA(K) mode as a function of the defect concentration. In addition, we find that the double-resonance 2LA(M) mode remains unaffected by the doping, indicating that our treatment does not significantly change the monolayer's electronic structure [28].

To study the valley polarization of chemically-doped WS_2 monolayers, we use near-resonant excitation with a 594 nm circularly polarized, continuous-wave laser that is focussed to a diffraction-limited spot. The resulting photoluminescence is polarization filtered and collected using a home-built confocal microscope (see Methods). Before detecting the emission with an avalanche photodiode (APD), we apply a spectral bandpass filter with a transmission window centred around the exciton and trion resonances (see the shaded area in Fig. 6.1b).

We quantify the valley polarization ρ via polarization-resolved photoluminescence measurements according to

$$\rho = \frac{I_{\sigma^+} - I_{\sigma^-}}{I_{\sigma^+} + I_{\sigma^-}}. \tag{6.2}$$

Here, I_{σ^+} and I_{σ^-} represent the intensities of the right- and left-handed emission by the sample under σ^+ excitation and the total photoluminescence is given by $I = I_{\sigma^+} + I_{\sigma^-}$. By scanning the sample while detecting its emission using the APD, we make photolu-

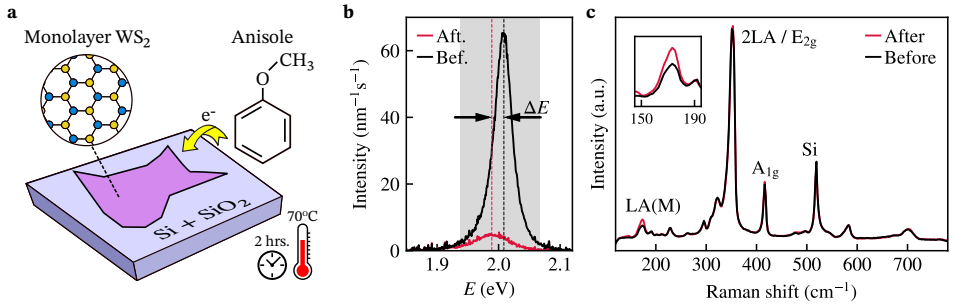

Figure 6.1: Controlling the photoluminescence properties of monolayer WS_2 via chemical doping. (**a**) WS_2 monolayers on Si/SiO_2 substrates become n-doped by treating them with anisole for 2 hours at 70 °C. The insets show the chemical structures of WS_2 and anisole. (**b**) Photoluminescence spectrum of a monolayer WS_2 before and after the anisole treatment. The treatment quenches the neutral exciton resonance, leading to the emergence of the trion resonance. The spectrum before (after) treatment was taken at 4 μW (40 μW) off-resonant laser excitation ($E = 2.331$ eV, $\lambda = 532$ nm). The shaded area indicates the transmission window of the bandpass filter used for the maps in Fig. 6.2. (**c**) Raman spectra before and after the treatment of the same monolayer as in (b), at 514 nm laser excitation. The inset shows the enhanced intensity of the longitudinal acoustic LA(M) phonon mode, attributed to the adsorption of the anisole molecules. Both spectra are averages over multiple positions of the flake, which all show the same mode enhancement.

minescence and valley-polarization maps of our flakes, before and after treating them.

Before the anisole treatment, the photoluminescence is characterized by bright exciton emission (Fig. 6.2a, left panel) with no valley polarization (Fig. 6.2b, left panel). Strikingly, the trion emission that remains after chemical doping (Fig. 6.2a, right panel) has a valley polarization of about 25% (Fig. 6.2b, right panel). We consistently observe the emergence of strong valley polarization after anisole treatment in multiple samples (section 6.5.2).

Next, we demonstrate the substrate independence of the effect of our treatment by repeating the measurements on an yttrium iron garnet (YIG) substrate. YIG is a magnetic insulator that was shown to effectively negatively dope MoS_2 monolayers at low temperatures, possibly due to dangling oxygen bonds at the YIG surface [29]. As such, the total level of doping could be larger for monolayers on YIG due to additional doping from the substrate.

We exfoliated monolayers WS_2 onto polydimethylsiloxane (PDMS) stamps and deposited them onto the YIG substrates [30]. As before, the emission of the monolayers is strongly quenched after chemical doping and a valley polarization of about 20%-40% emerges (Fig. 6.3, section 6.5.2). Compared to the monolayers on Si/SiO_2 substrates we conclude that these data do not indicate significant additional doping from the YIG substrate.

To assess the spatial homogeneity of the doping, we characterize the photoluminescence and valley polarization of a relatively large-area monolayer flake on YIG (Fig. 6.3a,b). In most parts of the flake, we observe a valley polarization of about 40%. In addition, at

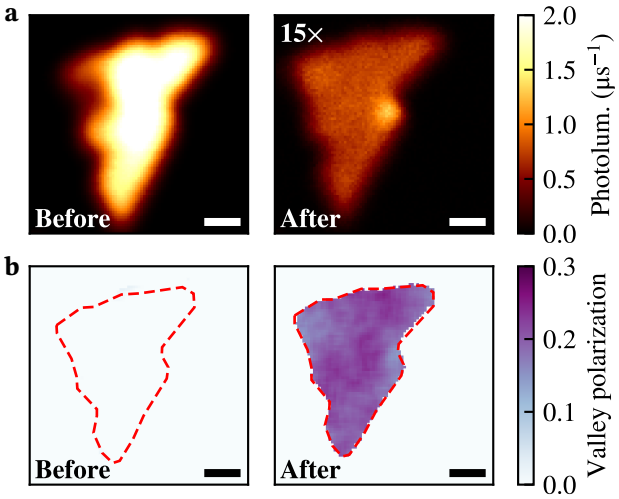

Figure 6.2: Spatial maps of the photoluminescence (a) and valley polarization (b) of a monolayer WS_2 before and after chemical doping with anisole. The treatment quenches the brightness of the flake and gives rise to strongly valley-polarized emission. The flake was exfoliated on a Si/SiO_2 substrate and excited near-resonance ($E = 2.087$ eV, $\lambda = 594$ nm, 4 μW). Scale bar: 2 μm.

multiple spots in the monolayer, we observe an enhanced photoluminescence and reduced valley polarization. A comparison with an atomic force microscope topography image (Fig. 6.3c) shows that these spots are associated with wrinkles in the flake. Spectrally, the spots are characterized by the simultaneous presence of an exciton resonance and a trion resonance, with the exciton resonance rapidly vanishing as we move off the spot and the trion resonance remaining approximately constant (Fig. 6.3d). We extract the valley polarization and brightness of the exciton and trion resonances by fitting similar emission spectra near multiple wrinkles with an exciton and trion component (section 6.5.3). The extracted trion brightness and valley polarization is independent of the local exciton emission (Fig. 6.3e), highlighting their spatial homogeneity. In particular, the trion valley polarization of about 40% is similar to that in the flat areas of the flake (Fig. 6.3b,f). The stronger exciton emission at wrinkles indicates that the doping is less effective, possibly resulting from the restricted physical access to the monolayer at wrinkles or from a decreased substrate-induced doping due to the increased substrate-monolayer distance. In addition, the exciton and trion formation could be altered at the wrinkles as a result of local strain [31].

Strikingly, the excitons at the wrinkles also attained a strong valley polarization, as can be seen from the spectra in Fig. 6.3d. We extend an existing rate equation model [10] to argue that this is the result of the doping-induced conversion of excitons into trions (Fig. 6.4a). This conversion acts as a decay channel for the excitons, enhancing their valley polarization and quenching their photoluminescence. The model predicts that the excitonic valley polarization starts to increase strongly when the conversion rate into trions $\Gamma_{T\leftarrow X}$ becomes comparable to the intervalley scattering rate $\Gamma_{iv,X}$ (Fig. 6.4b,

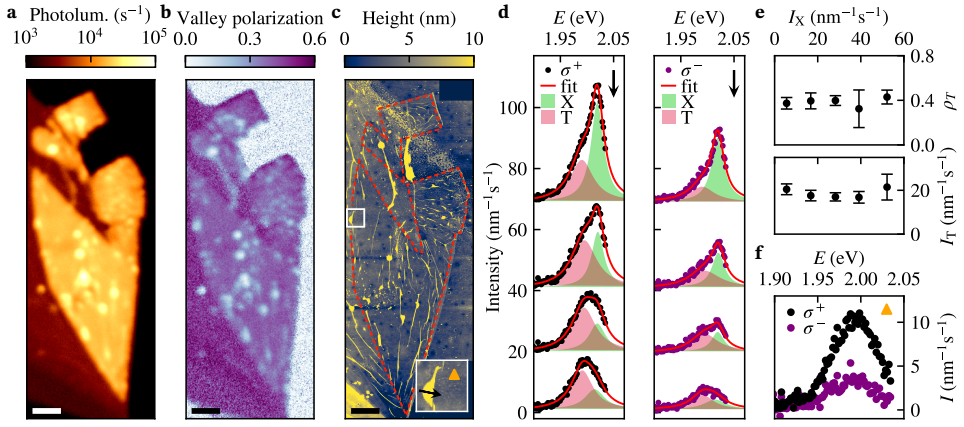

Figure 6.3: Spatial characterization of the exciton and trion emission of a chemically-doped monolayer WS_2 on an yttrium iron garnet (YIG) substrate. (**a-b**) Spatial maps of the photoluminescence and valley polarization under near-resonant excitation (594 nm, 200 µW) after chemical doping. The sample was submerged in liquid anisole for 12 hours at room temperature and vacuum-annealed for 6 hours (400 °C, <1 mTorr) to remove contaminants. Multilayer areas of the flake surrounding the monolayer are identified by their low brightness due to their indirect bandgap [2] and large polarization [32]. A comparison with the atomic force microscope image in (**c**) shows that spots with increased photoluminescence and reduced valley polarization occur at wrinkles of the monolayer. (**d**) Emission spectra at different locations close to a wrinkle indicated by the black arrow in the inset of (c). Lorentzian fits of the trion (red) and exciton (green) resonances reveal the simultaneous presence of trion and exciton emission at wrinkles. (**e**) Average trion brightness and valley polarization plotted against the local exciton photoluminescence at different wrinkles. (**f**) Typical σ^+ and σ^- emission spectra of trions in flat parts of the flake, obtained at the location indicated by the triangle in the inset of (c), corresponding to a valley polarization of about 40%. Scale bar: 5 µm.

green line). Since $\Gamma_{T\leftarrow X}$ is proportional to the electron density as described by a law of mass-action [11, 12], indeed an emergent exciton polarization is expected when doping is strong.

Strongly valley-polarized excitons are expected in the limit of large doping (Fig. 6.4b). For our flakes, doping is strongest in the flat areas away from the wrinkles as reflected by the low photoluminescence in these areas. Because we are unable to spectrally distinguish the weak exciton emission from the dominant trion emission in these areas, we analyse the valley polarization of the integrated photoluminescence spectrum using our APD. When plotting the local valley polarization against the local photoluminescence (Fig. 6.4c), we observe a non-monotonous behaviour with a maximum at low photoluminescence. According to our model, this maximum occurs because the exciton valley polarization (green line in Fig. 6.4b) increases with doping while the exciton photoluminescence vanishes. As a result, the trion contribution (red line) starts to dominate the total signal (black line). These results highlight that the exciton valley polarization becomes large because of the rapid conversion into trions.

On wrinkles, we observe that the excitons have a lower valley polarization than the trions (Fig. 6.3d). In contrast, our model predicts that the local valley polarization of the

trions cannot exceed that of the excitons even at low doping (Fig. 6.4b, section 6.5.4). This indicates that the observed spectra on wrinkles are a result of spatial averaging over less-doped, wrinkled areas with a strong exciton contribution and strongly-doped surrounding areas with a dominant trion emission (section 6.5.5). Such averaging is expected from the diffraction-limited optical spotsize of our confocal microscope (diameter: ~ 500 nm).

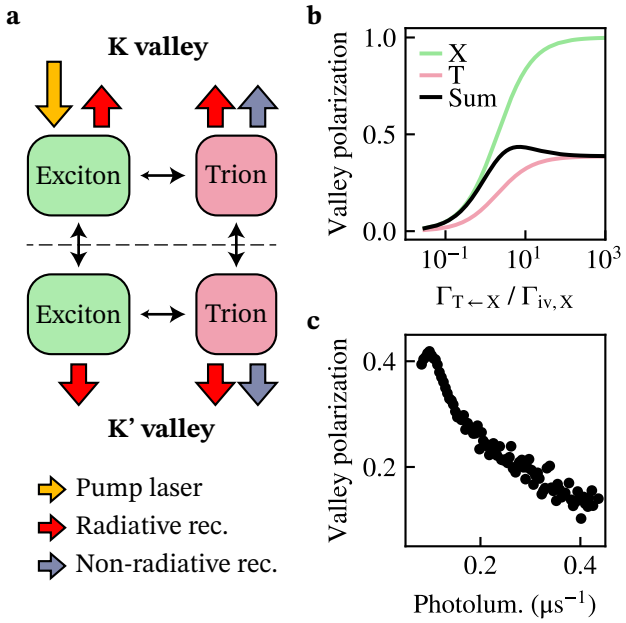

Figure 6.4: Doping-controlled valley polarization of excitons and trions. (**a**) Schematic depiction of the rate equation model used to describe the optically detected valley polarization. Excitons are created by valley-selective optical excitation, after which they can decay radiatively, scatter between the valleys at a rate $\Gamma_{iv,X}$, or change into trions at a doping-controlled rate $\Gamma_{T\leftarrow X}$. The trions can scatter between the valleys, decay radiatively or non-radiatively, and change back into excitons. (**b**) Valley polarization of excitons, trions, and their photoluminescence-weighted average as a function of $\Gamma_{T\leftarrow X}/\Gamma_{iv,X}$ calculated using the rate equation model shown in (a). (**c**) Valley polarization versus photoluminescence extracted by averaging data from individual pixels in the monolayer area of Fig. 6.3a,b.

6.3. CONCLUSIONS

In summary, we have demonstrated that chemical doping with anisole is an effective method to generate highly valley-polarized excitons and trions in monolayer WS_2 at room temperature. The emission spectrum of as-prepared monolayers is characterized by a bright exciton resonance that exhibits no valley polarization. After chemical doping, a trion resonance appears with a polarization up to 40%. The doping is less efficient at wrinkled areas, which are marked by the simultaneous presence of exciton and trion resonances. The excitons have a robust valley polarization, which we attribute to the rapid conversion into trions induced by the doping. A rate equation model captures the

quenching-induced valley polarization, indicating the presence of excitons with a higher polarization than trions in the limit of maximal quenching. Our results shed light on the effect of the doping-controlled conversion between excitons and trions on the valley polarization in single layers of WS_2 and highlight that valley polarization by itself does not necessarily reflect optovalleytronic potential, since a strongly-quenched carrier lifetime and emission may constrain its application in devices.

6.4. MATERIALS AND METHODS

6.4.1. EXPERIMENTAL SETUP

A schematic overview of the setup is presented in Fig. 6.5. Our samples are excited by a lowpass-filtered 594 nm OBIS laser (Coherent) of which we control the polarization using achromatic half- and quarter-wave plates (Thorlabs). A 50X, NA=0.95 (Olympus) objective focuses the laser to a diffraction-limited spot and collects the emission from the sample. The emission is separated from the excitation by a 10:90 beam splitter (R:T, Thorlabs). The handedness of the excitation and detection is controlled by a second quarter-wave plate, which projects both circular polarizations of the photoluminescence onto two orthogonal linear polarizations of which we select one with the polarizer. The emission is longpass filtered (2x Semrock, BLP01-594R-25) to eliminate the laser reflection. We use a mirror on a computer-controlled flipmount to switch between a fiber-coupled spectrometer (Kymera 193 spectrograph with a cooled iVac 324 CCD detector) and an avalanche photodiode (APD, Laser Components) for the detection of the photoluminescence. Before the emission is detected by the APD, it is filtered with a pinhole and bandpass filter (Semrock, FF01-623/32-25). The sample is mounted on an xyz-piezo stage (Mad City Labs, Nano-3D200FT) to allow nanoscale positioning of the sample. An ADwin Gold II was used to control the piezo stage and read out the APD. The grating in the Raman microscope (Renishaw inVia Reflex, 514 nm laser) had 1600 lines per mm, giving a spectral resolution of ~2 cm^{-1} per pixel. All measurements were performed at room temperature.

6.4.2. SAMPLE FABRICATION

The WS_2 monolayers were exfoliated from commercially-purchased bulk crystals (HQ Graphene) on PDMS stamps, and were transferred to Si/SiO_2 and YIG chips. The 245 nm thick YIG films were grown on a gadolinium gallium garnet (GGG) substrate via liquid phase epitaxy and were purchased at Matesy gmbh. YIG samples were sonicated in acetone and cleaned in IPA before stamping.

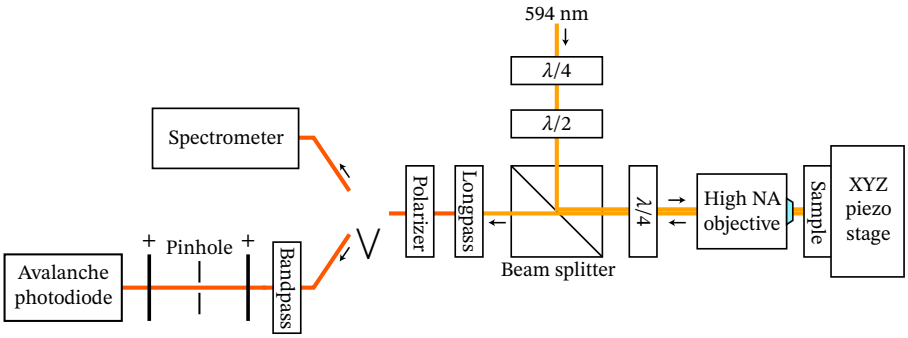

Figure 6.5: Overview of the measurement setup used in our experiments. The first quarter-lambda plate ($\lambda/4$) corrects for imperfections in the laser polarization and makes it perfectly linear, such that the excitation polarization can be controlled by turning the half-lambda plate ($\lambda/2$). A 10:90 beamsplitter (R:T) seperates the excitation from the detection. The polarization of the detection is controlled by the orientation of the second quarter-lambda plate relative to the transmission axis of the polarizer. The objective focusses the laser and collects the photoluminesence of the sample, which is positioned using an XYZ piezo stage. Two longpass filters eliminate the laser reflection. Depending on the orientation of a mirror on a computer-controlled flipmount (indicated by the V) the photoluminesence is detected by an avalange photodiode (APD) or spectrometer. Before the emission is detected by the APD, it is filtered with a pinhole and bandpass filter.

ACKNOWLEDGEMENTS

The authors thank N. Papadopoulos, M. Lee for their advice on fabrication and I. Komen, L. Kuipers for experimental help and discussions.

Funding: This work was supported by the Netherlands Organisation for Scientific Research (NWO/OCW), as part of the Frontiers of Nanoscience program, through the Startup grant 740.018.012, and by the Kavli Institute of Nanoscience Delft.
Author contributions: J.J.C. and T.v.d.S. conceived the experiment. M.B. fabricated the samples. J.J.C. and M.B. conducted the experiment and analysed the results. M.B. created the figures. J.J.C. and T.v.d.S. wrote the manuscript. All authors reviewed the manuscript. T.v.d.S. supervised the project.
Data and materials availability: The numerical data plotted in the figures in this work are available in Zenodo [33].
Competing interests: The authors declare no competing financial interest.

6.5. SUPPLEMENTARY MATERIAL

6.5.1. LITERATURE VALUES OF THE CHEMICAL POTENTIAL AND HARDNESS

	WS_2 monolayer [23]	Anisole [22]
Chemical potential μ (eV)	-4.79	-3.17
Chemical hardness η (eV)	2.64	4.88

Chemical potential and chemical hardness of anisole and monolayer WS_2 calculated using density functional theory.

6.5.2. REPRODUCABLE QUENCHING-INDUCED VALLEY POLARIZATION

We repeat the anisole treatment as specified before on five more WS_2 monolayer flakes, presented in Fig. 6.6, all of which show a strong dimming and emergent room-temperature valley polarization after doping. Of these, three have a Si/SiO_2 substrate and two an yttrium iron garnet (YIG) substrate. Variations in photoluminescence and valley polarization between the flakes are attributed to differences in defect density and unintentional doping prior to the treatment. Furthermore, we confirm the absence of valley polarization before the anisole treatment by presenting spectra of untreated monolayers for different excitation and detection helicities in Fig. 6.7.

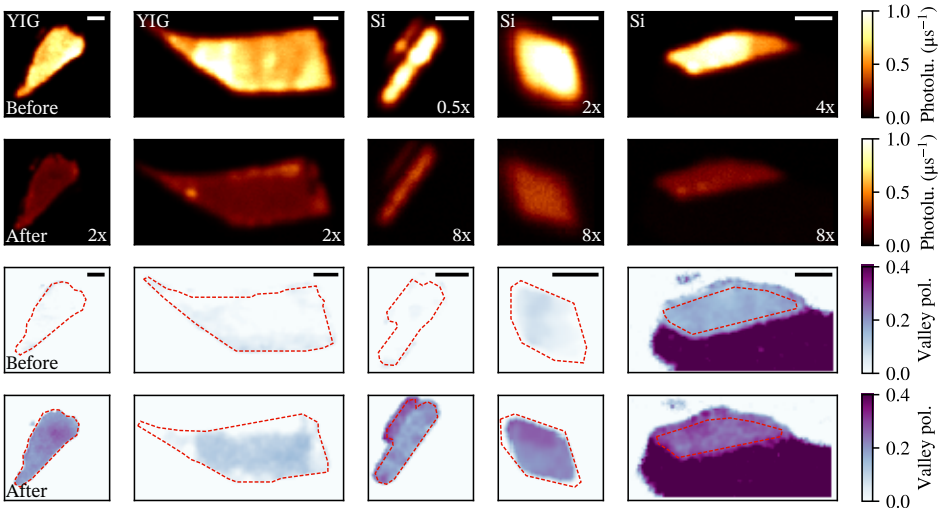

Figure 6.6: Additional photoluminescence and valley polarization maps of WS_2 monolayer flakes before and after anisole treatment. The first two monolayers were stamped on yttrium iron garnet (YIG) and the remaining three on Si/SiO_2. All maps were made using a 594 nm excitation laser at a power of 4 μW before the doping and 40 μW after doping. Scale bar: 2 μm.

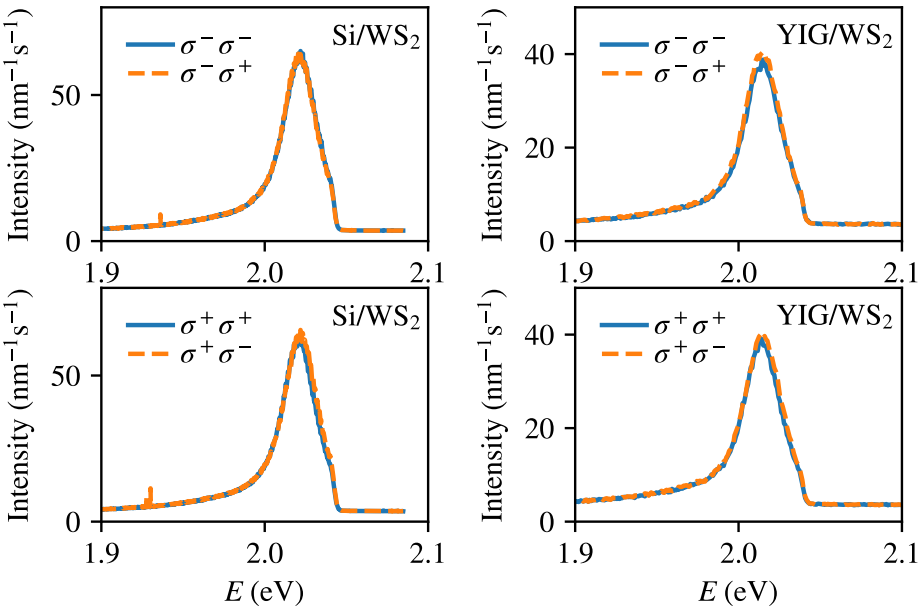

Figure 6.7: σ^+ and σ^- emission spectra under σ^+ and σ^- near-resonance excitation (E =2.087 eV, λ = 594 nm) of untreated WS_2 monolayers on Si/SiO_2 and YIG substrates. In each panel σ^+ and σ^- emission spectra are overlapping, which confirms the absence of valley polarization in these flakes. At about 2.04 eV the spectra are cut by the longpass filters that filter out the excitation laser.

6.5.3. EMERGENCE OF EXCITON EMISSION AT WRINKLES

Here, we plot additional σ^+ emission spectra along spatial traces over wrinkles in the WS_2 flake presented in Fig. 6.3. As demonstrated in Fig. 6.8, each trace is characterized by the emergence of a strong exciton resonance at the center of the wrinkle, highlighted by the asymmetry of the spectra. The central wavelength of both trions and excitons varies slightly over the different wrinkles, which we attribute to local variations in strain [31, 34] and doping [14]. From this, we extract spatially-varying energy splittings between the excitons and trions within the range of 22 meV – 32 meV, in agreement with reported literature values [35]. Additional σ^- emission spectra were taken along the same spatial traces to determine the valley polarization and brightness of the exciton and trion resonances near wrinkles, which were plotted in Fig. 6.3e.

6.5.4. MODELLING DOPING-CONTROLLED VALLEY DYNAMICS

MODEL OVERVIEW

To calculate the expected valley polarization as a function of doping level we extend the rate equation model of Lien *et al.* [10] by incorporating the valleys (Fig. 6.9). The model assumes that excitons are excited in the K valley at a rate Γ_K, scatter to the K' valley at a rate $\Gamma_{iv,X}$, decay radiatively at a rate $\Gamma_{r,X}$, or decay to trions via $\Gamma_{T\leftarrow X}$ while preserving their valley. The trions then scatter between the valleys at a rate $\Gamma_{iv,T}$, decay radiatively

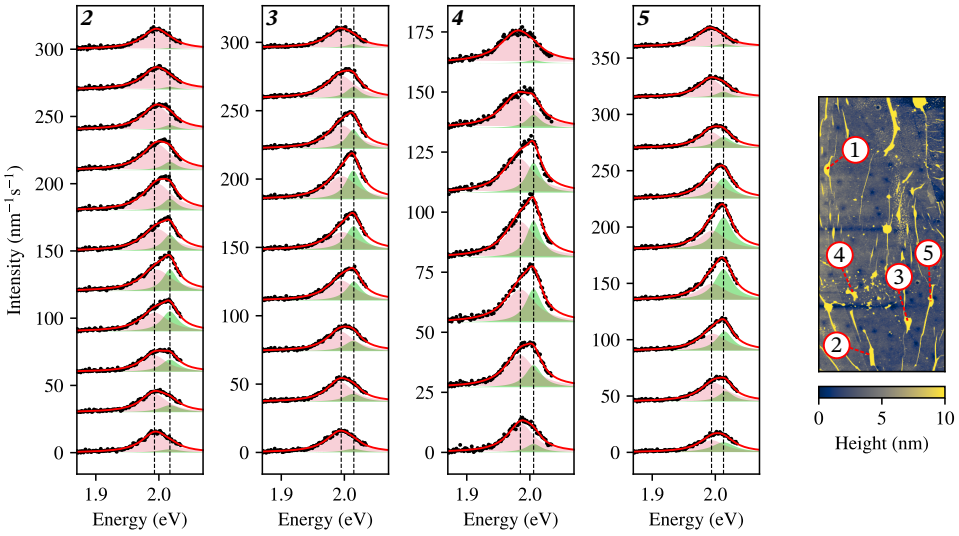

Figure 6.8: Recurrent emergence of exciton emission at wrinkles. σ^+ emission spectra are plotted along spatial traces over multiple wrinkles on the sample of Fig. 6.3. Labels above the spectra correspond to wrinkles in the atomic force microscope map in the right panel. Emission spectra at label 1 are depicted in Fig. 6.3c. All spectra were taken at near-resonance excitation ($E = 2.087$ eV, $\lambda = 594$ nm, 40 μW).

via $\Gamma_{r,T}$, non-radiatively via Γ_{nr}, or back to excitons via $\Gamma_{X\leftarrow T}$ while preserving their valley.

A law of mass-action states that $\Gamma_{T\leftarrow X}$ is linearly proportional to the electron density n_e, while $\Gamma_{X\leftarrow T}$ is fixed [10–12]. As described previously, we expect that $\Gamma_{T\leftarrow X}$ is spatially fluctuating due to local variations in doping level. Since the samples are strongly doped, we assume that $\Gamma_{T\leftarrow X}$ is much larger than any other non-radiative decay rate of the excitons, which we therefore neglect.

We define the probability for the system to be in the ground state as G, the probability to have formed an exciton in the $K^{(\prime)}$ valley as $X_{K^{(\prime)}}$, and the probability to have formed a trion in the $K^{(\prime)}$ valley as $T_{K^{(\prime)}}$. The time evolution of the system is then governed by the following master equations:

$$\frac{dG}{dt} = -\Gamma_K G + \Gamma_{r,X}(X_K + X_{K'}) + (\Gamma_{r,T} + \Gamma_{nr})(T_K + T_{K'}) = 0, \tag{6.3}$$

$$\frac{dX_K}{dt} = \Gamma_K G - (\Gamma_{iv,X} + \Gamma_{T\leftarrow X} + \Gamma_{r,X})X_K + \Gamma_{iv,X}X_{K'} + \Gamma_{X\leftarrow T}T_K = 0, \tag{6.4}$$

$$\frac{dX_{K'}}{dt} = -(\Gamma_{iv,X} + \Gamma_{T\leftarrow X} + \Gamma_{r,X})X_{K'} + \Gamma_{iv,X}X_K + \Gamma_{X\leftarrow T}T_{K'} = 0, \tag{6.5}$$

$$\frac{dT_K}{dt} = -(\Gamma_{iv,T} + \Gamma_{X\leftarrow T} + \Gamma_{nr} + \Gamma_{r,T})T_K + \Gamma_{iv,T}T_{K'} + \Gamma_{T\leftarrow X}X_K = 0, \tag{6.6}$$

$$\frac{dT_{K'}}{dt} = -(\Gamma_{iv,T} + \Gamma_{X\leftarrow T} + \Gamma_{nr} + \Gamma_{r,T})T_{K'} + \Gamma_{iv,T}T_K + \Gamma_{T\leftarrow X}X_{K'} = 0, \tag{6.7}$$

$$G + X_K + X_{K'} + T_K + T_{K'} = 1. \tag{6.8}$$

Here, we set the time derivatives to zero to consider a steady state and finally normalize the probabilities in the last line.

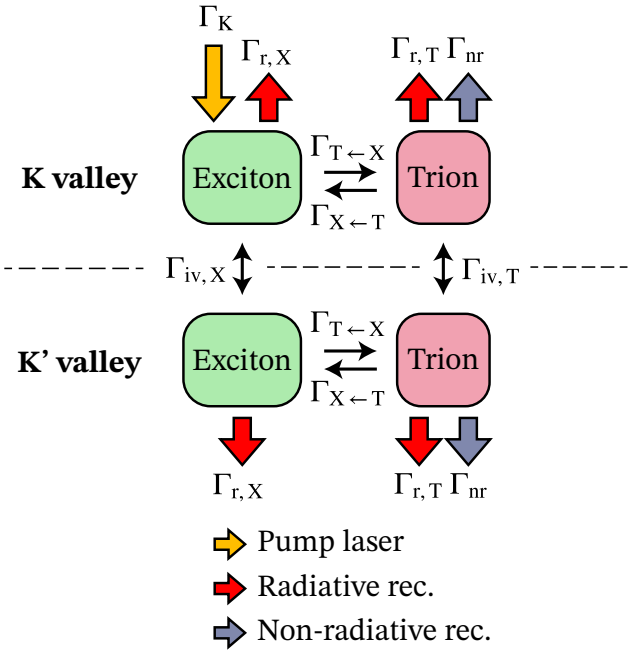

Figure 6.9: Schematic overview of the rate equation model. The closed system can either be in the ground state, or be an exciton or trion in the K or K' valley. By considering its steady state solutions, we model the valley polarization of excitons and trions under continuous-wave illumination.

CALCULATION OF THE TRION AND EXCITON VALLEY POLARIZATION

The valley polarization of the exciton and trion are respectively denoted by ρ_X and ρ_T, and are defined as the normalized asymmetry in valley occupation,

$$\begin{aligned} \rho_X &= \frac{X_K - X_{K'}}{X_K + X_{K'}}, \\ \rho_T &= \frac{T_K - T_{K'}}{T_K + T_{K'}}. \end{aligned} \tag{6.9}$$

By combining Eqns. 6.6-6.7 we derive a relation between ρ_X and ρ_T, demonstrating that the valley polarization of excitons is always larger than that of trions [36]

$$\rho_T = \frac{\Gamma_{X\leftarrow T} + \Gamma_{nr} + \Gamma_{r,T}}{2\Gamma_{iv,T} + \Gamma_{X\leftarrow T} + \Gamma_{nr} + \Gamma_{r,T}}\rho_X. \tag{6.10}$$

We can express ρ_X in terms of the rates by combining Eqns. 6.3-6.7

$$\rho_X = \frac{\frac{\Gamma_{r,X}}{2\Gamma_{iv,X}} + \frac{\Gamma_{r,T}+\Gamma_{nr}}{2(\Gamma_{X\leftarrow T}+\Gamma_{nr}+\Gamma_{r,T})}\frac{\Gamma_{T\leftarrow X}}{\Gamma_{iv,X}}}{1+\frac{\Gamma_{r,X}}{2\Gamma_{iv,X}} + \frac{2\Gamma_{iv,T}+\Gamma_{nr}+\Gamma_{r,T}}{2(2\Gamma_{iv,T}+\Gamma_{X\leftarrow T}+\Gamma_{nr}+\Gamma_{r,T})}\frac{\Gamma_{T\leftarrow X}}{\Gamma_{iv,X}}} \approx \frac{\frac{\Gamma_{nr}}{2(\Gamma_{X\leftarrow T}+\Gamma_{nr})}\frac{\Gamma_{T\leftarrow X}}{\Gamma_{iv,X}}}{1+\frac{2\Gamma_{iv,T}+\Gamma_{nr}}{2(2\Gamma_{iv,T}+\Gamma_{X\leftarrow T}+\Gamma_{nr})}\frac{\Gamma_{T\leftarrow X}}{\Gamma_{iv,X}}}. \tag{6.11}$$

Since the radiative decay rates are known to be low at room temperature [10, 37, 38], we assumed in the last step that $\Gamma_{iv,X} >> \Gamma_{r,X}$ and $\Gamma_{nr} >> \Gamma_{r,T}$. We thus conclude that the valley polarization of the excitons is parametrized by $\frac{\Gamma_{T\leftarrow X}}{\Gamma_{iv,X}}$, and that it reaches a maximum ρ_X^{max} when $\Gamma_{T\leftarrow X} >> \Gamma_{iv,X}$

$$\rho_X^{max} = \frac{\Gamma_{nr}(2\Gamma_{iv,T}+\Gamma_{X\leftarrow T}+\Gamma_{nr})}{(\Gamma_{nr}+2\Gamma_{iv,T})(\Gamma_{nr}+\Gamma_{X\leftarrow T})}. \tag{6.12}$$

ANALYSIS OF THE VALLEY POLARIZATION VERSUS PHOTOLUMINESCENCE

Using Eqns. 6.6, 6.7 and 6.11 we can calculate the valley polarization ρ as it detected by the avalanche photodiode (APD) in the experiment, by summing the exciton and trion emission

$$\begin{aligned}\rho &= \frac{\Gamma_{r,T}(T_K - T_{K'}) + \Gamma_{r,X}(X_K - X_{K'})}{\Gamma_{r,T}(T_K + T_{K'}) + \Gamma_{r,X}(X_K + X_{K'})} \\ &= \frac{\frac{\Gamma_{r,T}}{\Gamma_{r,X}(2\Gamma_{iv,T}+\Gamma_{X\leftarrow T}+\Gamma_{nr})}\Gamma_{T\leftarrow X}+1}{\frac{\Gamma_{r,T}}{\Gamma_{r,X}(\Gamma_{X\leftarrow T}+\Gamma_{nr})}\Gamma_{T\leftarrow X}+1}\,\frac{\frac{\Gamma_{nr}}{2\Gamma_{iv,X}(\Gamma_{X\leftarrow T}+\Gamma_{nr})}\Gamma_{T\leftarrow X}}{\frac{2\Gamma_{iv,T}+\Gamma_{nr}}{2\Gamma_{iv,X}(2\Gamma_{iv,T}+\Gamma_{X\leftarrow T}+\Gamma_{nr})}\Gamma_{T\leftarrow X}+1}.\end{aligned} \tag{6.13}$$

To find a relation between the valley polarization and total photoluminescence $I = I_T + I_X$, we express I in terms of the rates by combining Eqns. 6.3 and 6.6-6.8, and find that it is inversely related to $\Gamma_{T\leftarrow X}$

$$I = \alpha N\big(\Gamma_{r,T}(T_K + T_{K'}) + \Gamma_{r,X}(X_K + X_{K'})\big) \approx \alpha N\Gamma_K\Big(\frac{\Gamma_{r,T}}{\Gamma_{nr}} + \frac{\Gamma_{r,X}(\frac{\Gamma_{X\leftarrow T}}{\Gamma_{nr}}+1)}{\Gamma_{T\leftarrow X}}\Big). \tag{6.14}$$

Here $0 < \alpha < 1$ represents the finite detection efficiency of the confocal microscope and N is the number of electrons in the system. To simplify this expression, we made use of the previous assumptions, and assumed that the system is weakly excited and strongly doped, such that Γ_K is small and $\Gamma_{T\leftarrow X} >> \Gamma_{r,X}$. By inverting this equation and substituting it into Eq. 6.13, we find ρ as a function of I for a sample with a varying doping level

$$\rho = \frac{a_0 I + 1}{b_0 I^2 + c_0 I}. \tag{6.15}$$

Here the constants are given by

$$\begin{aligned} a_0 &= -\frac{\Gamma_{nr}}{2\alpha N\Gamma_K\Gamma_{iv,T}\Gamma_{r,T}}(2\Gamma_{iv,T}+\Gamma_{X\leftarrow T}+\Gamma_{nr}), \\ b_0 &= -\frac{\Gamma_{nr}\Gamma_{iv,X}}{\alpha^2 N^2\Gamma_K^2\Gamma_{r,X}\Gamma_{r,T}\Gamma_{iv,T}}(2\Gamma_{iv,T}+\Gamma_{X\leftarrow T}+\Gamma_{nr}), \\ c_0 &= -\frac{1}{2\alpha N\Gamma_K\Gamma_{iv,T}\Gamma_{r,T}}(\Gamma_{X\leftarrow T}+\Gamma_{nr})(2\Gamma_{iv,T}+\Gamma_{nr}) - \frac{2\Gamma_{iv,X}\Gamma_{r,T}}{\Gamma_{r,X}\Gamma_{nr}}a_0. \end{aligned} \tag{6.16}$$

In agreement to our data, the valley polarization should thus be inversely related to the photoluminescence at high I

$$\rho \approx \frac{a_0}{b_0 I + c_0}. \tag{6.17}$$

This inverse relation is reinforced by the spatial averaging of our diffraction-limited optical spot (see section 6.5.5). At low I, a local maximum in the valley polarization is experimentally observed, only if

$$\frac{\Gamma_{nr}}{2\Gamma_{r,T}}\left(\frac{\Gamma_{r,X}}{\Gamma_{iv,X}} - \frac{\Gamma_{r,T}}{\Gamma_{iv,T}}\right) + \frac{\Gamma_{r,X}\Gamma_{iv,T}}{\Gamma_{iv,X}\Gamma_{r,T}} - \frac{\Gamma_{X\leftarrow T}}{2\Gamma_{iv,T}} > 1. \tag{6.18}$$

This is only true, if $\frac{\Gamma_{r,X}}{\Gamma_{iv,X}} > \frac{\Gamma_{r,T}}{\Gamma_{iv,T}}$, provided that $\Gamma_{iv,T} >> \Gamma_{X\leftarrow T}$. We thus conclude that relatively bright excitons with a significantly higher polarization than trions are required for the observation of a local maximum in the total valley polarization versus photoluminescence.

COMPARISON BETWEEN MODEL AND EXPERIMENT

To better assess the correspondence between the model and the experimental data in Fig. 6.4c, we make a basic estimate of the valley polarization using MoS_2 literature values for the radiative and non-radiative rates [10] ($1/\Gamma_{r,X} = 8$ ns, $1/\Gamma_{r,T} = 110$ ns and $1/\Gamma_{nr} = 50$ ps). For a rough approximation, we assume that $\Gamma_{X\leftarrow T}$ is much smaller than the other rates. As a result, the exciton valley polarization approaches unity at strong doping via Eq. 6.12, while the trion polarization is parametrized by $\Gamma_{iv,T}$ via Eq. 6.10. Following the experimental results in Fig. 6.4c, we tune the trion polarization at maximal doping to about 40%, which gives $1/\Gamma_{iv,T} = 60$ ps. At this stage only $\Gamma_{iv,X}$ remains as a free parameter and it determines whether the valley polarization has a local maximum as a function of photoluminescence via Eq. 6.18.

In Fig. 6.4b we demonstrate that for $1/\Gamma_{iv,X} = 10$ ps a small local maximum in valley polarization can be observed. In contrast, at an enhanced intervalley scattering of $1/\Gamma_{iv,X} = 2$ ps the local maximum disappears (Fig. 6.10, left panel), because $\frac{\Gamma_{r,X}}{\Gamma_{iv,X}} < \frac{\Gamma_{r,T}}{\Gamma_{iv,T}}$.

To compare the model and experiment, we plot the valley polarization versus photoluminescence using Eq. 6.15 for different values of $\Gamma_{iv,X}$ (Fig. 6.10, right panel). We note that we obtain similar plots when increasing $\Gamma_{X\leftarrow T}$, which merely lowers the exciton valley polarization below unity at strong doping and decreases the difference between the trion and exciton polarization, making the presence of a local maximum less likely.

6.5.5. CALCULATION OF THE SPATIALLY-AVERAGED VALLEY POLARIZATION OF ADJACENT REGIONS WITH DIFFERENT DOPING LEVELS

In this section we calculate the valley polarization versus photoluminescence when averaging the emission of two regions with different doping levels. In particular, we consider a strongly-doped region with weak and highly polarized trion emission and a weakly-doped region with strong and weakly polarized exciton emission, similar to the emission detected on wrinkles in Fig. 6.3. The emission from both regions is collected by our

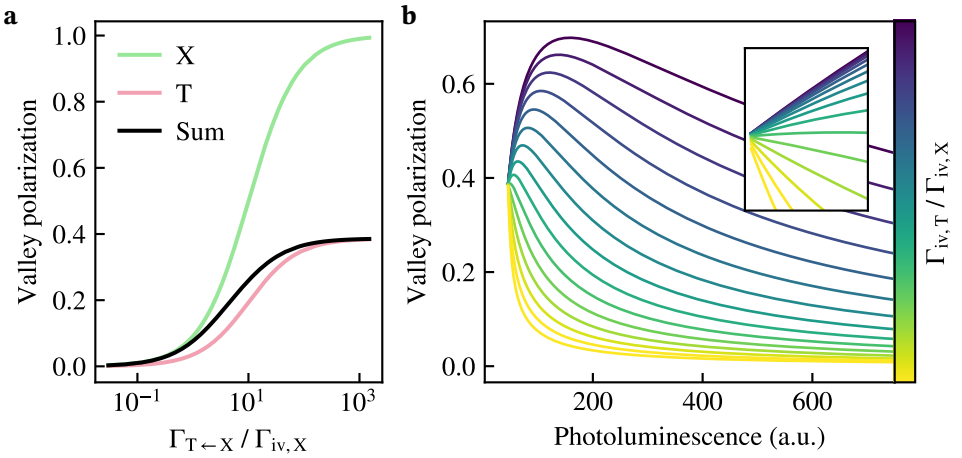

Figure 6.10: Modelling valley polarization as a function of trion-to-exciton conversion and total luminescence. (**a**) Modelled valley polarization versus $\Gamma_{T\leftarrow X}/\Gamma_{iv,X}$ using the same rates as in Fig. 6.4b, demonstrating that a different choice of $\Gamma_{iv,X}$ can yield absence of a local maximum. (**b**) Simulated valley polarization versus photoluminescence using the same rates as in (a), but with logarithmically spaced values for $1/\Gamma_{iv,X}$ ranging between 1 and 100 ps. The inset highlights the presence (absence) of a local maximum at low brightness for low (high) $\Gamma_{iv,X}$.

6

diffraction-limited optical spot, leading to a spatially-averaged valley polarization of

$$\rho = \frac{\Gamma_{r,T}(T_K - T_{K'}) + \Gamma_{r,X}(X_K - X_{K'})}{\Gamma_{r,T}(T_K + T_{K'}) + \Gamma_{r,X}(X_K + X_{K'})} = \frac{\rho_T I_T + \rho_X I_X}{I_T + I_X}. \tag{6.19}$$

Here the valley polarization of the trions ρ_T and excitons ρ_X are constant and their intensities I_T and I_X vary with the area of the weakly-doped region compared to the optical spotsize ($0 \leq A \leq 1$), according to

$$\begin{aligned} I_X &= A \cdot I_{0,X}, \\ I_T &= (1 - A) \cdot I_{0,T}. \end{aligned} \tag{6.20}$$

Here $I_{0,T}$ and $I_{0,X}$ are constants that indicate the trion and exciton photoluminescence when their associated regions would fill an entire optical spot. The total photoluminescence is given by

$$I = I_T + I_X = I_{0,T} + A(I_{0,X} - I_{0,T}). \tag{6.21}$$

By substituting this expression into Eq. 6.19, we find that the ρ is inversely related to I for varying

$$\rho = \frac{\rho_X I_{0,X} - \rho_T I_{0,T}}{I_{0,X} - I_{0,T}} + \frac{I_{0,X} I_{0,T}(\rho_T - \rho_X)}{I_{0,X} - I_{0,T}} \cdot \frac{1}{I}. \tag{6.22}$$

This is a similar inverse relation as the one in Eq. 6.17 for a varying doping level. Note that this relation is exclusively inverse, and cannot explain any local maximum. However, it is likely that the inverse decay of valley polarization in Fig. 6.4c is a combination of 1) spatial averaging due to a diffraction limited optical spot and 2) local variations in doping.

BIBLIOGRAPHY

[1] K. F. Mak, C. Lee, J. Hone, J. Shan, and T. F. Heinz, "Atomically Thin MoS_2: A New Direct-Gap Semiconductor", Phys. Rev. Lett. **105**, 136805 (2010).

[2] A. Splendiani et al., "Emerging Photoluminescence in Monolayer MoS_2", Nano Letters **10**, 1271 (2010).

[3] K. F. Mak, K. He, J. Shan, and T. F. Heinz, "Control of valley polarization in monolayer MoS_2 by optical helicity", Nature Nanotechnology **7**, 494 (2012).

[4] T. Cao et al., "Valley-selective circular dichroism of monolayer molybdenum disulphide", Nature Communications **3**, 887 (2012).

[5] H. Zeng, J. Dai, W. Yao, D. Xiao, and X. Cui, "Valley polarization in MoS_2 monolayers by optical pumping", Nature Nanotechnology **7**, 490 (2012).

[6] T. Mueller and E. Malic, "Exciton physics and device application of two-dimensional transition metal dichalcogenide semiconductors", npj 2D Materials and Applications **2**, 29 (2018).

[7] K. M. McCreary, M. Currie, A. T. Hanbicki, H.-J. Chuang, and B. T. Jonker, "Understanding Variations in Circularly Polarized Photoluminescence in Monolayer Transition Metal Dichalcogenides", ACS Nano **11**, 7988 (2017).

[8] K. F. Mak, D. Xiao, and J. Shan, "Light–valley interactions in 2D semiconductors", Nature Photonics **12**, 451 (2018).

[9] J. R. Schaibley et al., "Valleytronics in 2D materials", Nature Reviews Materials **1**, 16055 (2016).

[10] D.-H. Lien et al., "Electrical suppression of all nonradiative recombination pathways in monolayer semiconductors", Science **364**, 468 (2019).

[11] J. S. Ross et al., "Electrical control of neutral and charged excitons in a monolayer semiconductor", Nature Communications **4**, 1474 (2013).

[12] J. Siviniant, D. Scalbert, A. V. Kavokin, D. Coquillat, and J.-P. Lascaray, "Chemical equilibrium between excitons, electrons, and negatively charged excitons in semiconductor quantum wells", Phys. Rev. B **59**, 1602 (1999).

[13] P. H L, P. Mondal, A. Bid, and J. K. Basu, "Electrical and Chemical Tuning of Exciton Lifetime in Monolayer MoS_2 for Field-Effect Transistors", ACS Applied Nano Materials **3**, 641 (2020).

[14] K. F. Mak et al., "Tightly bound trions in monolayer MoS_2", Nature Materials **12**, 207 (2013).

[15] A. O. A. Tanoh et al., "Enhancing Photoluminescence and Mobilities in WS_2 Monolayers with Oleic Acid Ligands", Nano Letters **19**, 6299 (2019).

[16] Y. Wang et al., "Doping of Monolayer Transition-Metal Dichalcogenides via Physisorption of Aromatic Solvent Molecules", The Journal of Physical Chemistry Letters **10**, 540 (2019).

[17] M. Amani et al., "Near-unity photoluminescence quantum yield in MoS_2", Science **350**, 1065 (2015).

[18] N. Peimyoo et al., "Chemically Driven Tunable Light Emission of Charged and Neutral Excitons in Monolayer WS_2", ACS Nano **8**, 11320 (2014).

[19] S. Mouri, Y. Miyauchi, and K. Matsuda, "Tunable Photoluminescence of Monolayer MoS_2 via Chemical Doping", Nano Letters **13**, 5944 (2013).

[20] S. Tongay et al., "Broad-Range Modulation of Light Emission in Two-Dimensional Semiconductors by Molecular Physisorption Gating", Nano Letters **13**, 2831 (2013).

[21] R. G. Pearson, "The electronic chemical potential and chemical hardness", Journal of Molecular Structure: THEOCHEM **255**, 261 (1992).

[22] R. L. Camacho-mendoza et al., "On the interaction of anisole and thioanisole derivatives with gold clusters studied by DFT", Computational and Theoretical Chemistry **1126**, 54 (2018).

[23] H. L. Zhuang and R. G. Hennig, "Computational Search for Single-Layer Transition-Metal Dichalcogenide Photocatalysts", The Journal of Physical Chemistry C **117**, 20440 (2013).

[24] K. M. McCreary et al., "The Effect of Preparation Conditions on Raman and Photoluminescence of Monolayer WS_2", Scientific Reports **6**, 35154 (2016).

[25] A. T. Hanbicki et al., "Anomalous temperature-dependent spin-valley polarization in monolayer WS_2", Scientific Reports **6**, 18885 (2016).

[26] A. Kurzmann, A. Ludwig, A. D. Wieck, A. Lorke, and M. Geller, "Auger Recombination in Self-Assembled Quantum Dots: Quenching and Broadening of the Charged Exciton Transition", Nano Letters **16**, 3367 (2016).

[27] F. Zhang et al., "Carbon doping of WS_2 monolayers: Bandgap reduction and p-type doping transport", Science Advances **5**, 10.1126/sciadv.aav5003 (2019).

[28] A. Berkdemir et al., "Identification of individual and few layers of WS_2 using Raman Spectroscopy", Scientific Reports **3**, 1755 (2013).

[29] B. Peng et al., "Valley Polarization of Trions and Magnetoresistance in Heterostructures of MoS_2 and Yttrium Iron Garnet", ACS Nano **11**, 12257 (2017).

[30] A. Castellanos-Gomez et al., "Deterministic transfer of two-dimensional materials by all-dry viscoelastic stamping", 2D Materials **1**, 011002 (2014).

[31] M. G. Harats, J. N. Kirchhof, M. Qiao, K. Greben, and K. I. Bolotin, "Dynamics and efficient conversion of excitons to trions in non-uniformly strained monolayer WS_2", Nature Photonics **14**, 324 (2020).

[32] H. Su et al., "Anomalous enhancement of valley polarization in multilayer WS_2 at room temperature", Nanoscale **9**, 5148 (2017).

[33] J. J. Carmiggelt, M. Borst, and T. van der Sar, *Exciton-to-trion conversion as a control mechanism for valley polarization in room-temperature monolayer WS_2* (Zenodo, July 2020).

[34] A. Castellanos-Gomez et al., "Local Strain Engineering in Atomically Thin MoS_2", Nano Letters **13**, 5361 (2013).

[35] A. A. Mitioglu et al., "Optical manipulation of the exciton charge state in single-layer tungsten disulfide", Phys. Rev. B **88**, 245403 (2013).

[36] W. Zhang et al., "Bright and highly valley polarized trions in chemically doped monolayer MoS_2", Applied Physics Express **13**, 35002 (2020).

[37] C. Robert et al., "Exciton radiative lifetime in transition metal dichalcogenide monolayers", Phys. Rev. B **93**, 205423 (2016).

[38] C. R. Zhu et al., "Exciton valley dynamics probed by Kerr rotation in WSe_2 monolayers", Phys. Rev. B **90**, 161302 (2014).

7

CONCLUSION AND OUTLOOK

In this chapter we provide an overview of the main results described in this dissertation. At the end we look ahead and identify opportunities for future research.

Spin-wave microscopy techniques are crucial for the development of magnonic devices and improving our fundamental understanding of magnetism. Nitrogen-vacancy (NV) centers in diamond enable magnetic imaging of microscopic spin waves, which can provide important insights in spin-wave transport and dynamics. In chapter 3 we use NV centers to image coherent spin waves in a thin film of yttrium iron garnet (YIG). The microwave magnetic fields of these spin waves drive coherent rotations of the NV spins ("Rabi oscillations") when their frequency matches the NV electron spin resonance (ESR) frequency. We quantitatively determine the amplitude of the spin-wave stray field from the measured Rabi frequency, allowing spatial imaging of spin-wave wavefronts.

The measured spin-wave images give insight in the magnetic dispersion, which is an important material property that relates the spin-wave wavelength to its frequency. We reconstruct the spin-wave dispersion resonant with the NV sensors by extracting the spin-wave wavelength while tuning the bias field. In addition, we observe autofocussing of spin waves due to enhanced spin-wave transport along caustic directions. This behaviour results from the anisotropy of the spin-wave dispersion and is reproduced by analytical calculations of the expected real-space spin-wave profile.

Furthermore, our results suggest that:

1. NV magnetometry is sensitive enough to detect spin waves in monolayer van-der-Waals magnets.

2. Scanning NV microscopes could image spin waves with wavelengths smaller than the optical diffraction limit. Recently, our group imaged spin waves in YIG using a scanning single-NV microscope with wavelengths down to 360 nm [1]. Previous

scanning NV experiments imaged spin waves with wavelengths of 660 nm [2] and 500 nm [3].

3. NV magnetometry could detect spin waves, even when the magnet is buried underneath optically opaque materials. Our group harnessed this property to image the enhanced damping of spin waves underneath metal electrodes as a result of additional dissipation due to inductively-driven Eddy currents [4].

A key limitation of NV-based microwave sensors is that they are only sensitive to a narrow frequency range around the NV ESR frequency. Circumventing the resonance condition of NV quantum sensing is desirable, since the spin-wave band of many interesting magnets does not overlap with the ESR frequencies as a result of strong magnetic anisotropies. In chapter 4 we demonstrate NV-based detection of spin waves that are detuned from the ESR detection frequency.

Importantly, the demonstrated hybrid sensing platform enhances the versatility of NV centers as microwave detectors by increasing their functional bandwidth. We present two detection schemes that convert the frequencies of two spin waves (called "pump" and "signal") to the NV ESR frequency using the nonlinear magnetization dynamics in YIG. The first scheme relies on four-spin-wave mixing, where the pump and signal create an "idler" spin wave resonant with the NV. Excitingly, this scheme allows high-fidelity Rabi driving of the NV spin with off-resonant microwaves. The second scheme relies on difference frequency generation by the longitudinal component of the magnetization. It enables characterizing the spin-wave bandstructure at multiple gigahertz detuning, even when the ESR frequency lies within the spin-wave gap. As such, this detection protocol offers promising opportunities for detecting high-frequency spin waves in van-der-Waals magnets with NV centers.

In addition to its ultralow spin-wave damping, YIG is an attractive magnonic material due to the tunability of its magnetic properties via doping. In chapter 5 we study a gallium-doped YIG (Ga:YIG) thin film of which the saturation magnetization is about 10 times reduced compared to undoped YIG, making it a promising material for spin-wave optics. We determine the frequency dependence of the spin-wave group velocity by measuring the spin-wave-mediated microwave transmission between two striplines fabricated on top of the film. By fitting the data with an analytical expression, we obtain a quantitative estimate for the exchange constant of Ga:YIG. This constant determines the spin-wave dispersion together with the saturation magnetization and magnetic anisotropy constants, which we retrieve from vibrating sample magnetometry and broadband ferromagnetic resonance (FMR) measurements, respectively. Finally, we observe foldover of the FMR at increased drive powers, resulting in bistability of the detected spin-wave modes.

Chapter 6 focuses on excitons in transition metal dichalogenide (TMD) monolayers, which have been proposed as data carriers in valleytronic devices. Excitons can be selectively excited in one of the two TMD bandstructure valleys using circularly polarized light, but are rapidly redistributed among both valleys due to strong intervalley scatter-

ing. We use chemical doping to drive the conversion of excitons into trions (negatively-charged excitons), which reduces the exciton lifetime compared to the intervalley scattering time and thus induces a finite valley polarization. Since a magnetic moment is associated to each exciton with a sign depending on its valley index, an imbalance in the valley occupation yields a finite steady-state exciton magnetization. In future experiments the magnetic field generated by this light-induced magnetization could potentially be detected using NV centers.

In the following sections we suggest directions for future research based on the results obtained in this thesis.

7.1. NV MAGNETOMETRY OF HIGH-FREQUENCY SPIN WAVES

One of the most exciting opportunities of NV magnetometry is the possibility of exploiting its sensitivity to detect nanoscale spin waves in atomically-thin van-der-Waals magnets. These magnets typically have strong magnetic anisotropies, such that they have a large spin-wave gap in the 100-GHz range at zero bias field (c.f. Fig. 4.4E). To detect the high-frequency spin waves in these materials with NV centers, a Tesla-scale bias field could be applied that tunes the NV ESR frequencies into the spin-wave band. Alternatively, the difference frequency generation detection scheme developed in chapter 4 could enable detection at small bias fields.

The difference-frequency scheme could also provide insight in the group velocity of off-resonant spin waves. As derived in section 4.5.6, the longitudinal component of the magnetization is a traveling wave in the presence of pump and signal spin waves, with a frequency and wavevector given by

$$\begin{aligned} f_\mathrm{L} &= \Delta f = |f_\mathrm{p} - f_\mathrm{s}|, \\ k_\mathrm{L} &= \frac{2\pi}{\lambda_\mathrm{L}} = \Delta k = |k_\mathrm{p} - k_\mathrm{s}|. \end{aligned} \tag{7.1}$$

Here $f_{\mathrm{p(s)}}$ and $k_{\mathrm{p(s)}}$ correspond to the frequency and wavevector of the pump (signal) spin wave. Clearly, the longitudinal magnetization does not only down-convert the temporal frequencies of the pump and signal spin waves, but also the spatial frequencies (i.e. k_L can be small while k_p and k_s are large).

We envision that the longitudinal wavelength λ_L could be measured by applying a phase-locked, spatially homogeneous reference field at the frequency difference f_L (e.g., by mixing the signal and pump microwaves before sending them through the excitation stripline). Similar as in chapter 3, this should create a standing-wave magnetic-field pattern with a frequency and wavelength equal to f_L and λ_L, which could be imaged using NV magnetometry. We note that the evanescent field of the longitudinal magnetization could extend far above the film as it decays on the scale of λ_L.

The spin-wave group velocity v_g at frequency $f = \frac{f_\mathrm{p}+f_\mathrm{s}}{2}$ can be extracted from the mea-

sured longitudinal wavelength, according to

$$v_g = \frac{\partial \omega}{\partial k} \approx 2\pi \frac{\Delta f}{\Delta k} = f_L \lambda_L. \tag{7.2}$$

The frequency dependence of the group velocity could be measured by sweeping f_p and f_s, from which the dispersion of the spin waves could be reconstructed (as is demonstrated in chapter 5).

When the longitudinal wavelength is larger than the optical diffraction limit, it can be imaged with an NV ensemble as the one used in chapters 3 and 4, even while the pump and signal spin waves themselves have nanoscale wavelengths. As such, the difference-frequency scheme could allow characterizing the dispersion of nanoscale spin waves using diffraction-limited NV microscopy.

The sensitivity of the difference-frequency protocol could be greatly enhanced by detecting megahertz frequency differences using AC magnetometry techniques. Since the generated field at the difference frequency scales with spin-wave amplitude, it could potentially be enhanced by nanopatterning the magnet. The spatial confinement modulates the magnon density of states, which may suppress the decay into unwanted spin-wave modes and thereby allow larger pump and signal amplitudes [5].

The dispersion of off-resonant spin waves could also be measured via the Stark shift by relying on the pump-probe detection scheme described in section 4.5.4. A reference field at the spin-wave frequency should create a standing-wave magnetic-field pattern above the film, such that the measured Stark shift should oscillate over space with the wavelength of the spin wave. This approach is particularly promising for imaging spin waves with frequencies close to the ESR, since the Stark shift is inversely proportional to the spin-wave frequency detuning from the ESR (see section 2.1.3).

7.2. NV MAGNETOMETRY OF GLOBAL MICROWAVES

The detection of global microwaves is essential for a wide range of wireless communication technologies (e.g., WiFi operates at 2.4 and 5 GHz). We expect that global microwaves can be detected with high sensitivity by measuring spin waves in a widefield NV microscopy setup. Instead of scanning a focused, diffraction-limited laser spot pixel-by-pixel over a diamond, such a setup detects $\sim 10^6$ pixels at once by combining widefield illumination and camera readout of the NV centers [6].

Target microwaves at the ESR frequency can be measured by converting them first into spin waves (e.g., using a long stripline on top of a magnet), after which the spin-wave fields can be detected with enhanced sensitivity by reading out NV centers in a large sensing area. For example, widefield readout of an NV ensemble in an 1x1 mm^2 area should increase the collected NV photoluminescence by as much as 60 dB compared to readout of a diffraction-limited spot. We expect that spin-wave excitation assists the detection of small-amplitude microwaves, as the spin waves (1) *confine* the microwave radiation (the spin-wave wavelength is much smaller than free-space microwaves) and

(2) *store* microwave energy by acting as a cavity.

Global microwaves detuned from the ESR could be detected using the off-resonant measurement schemes presented in chapter 4. Since the sensitivity of these schemes depends on the spin-wave excitation efficiency at a target frequency, we envision a wideband spectrum analyzer covering the 0-100 GHz range could be realized by reading out pixel-like patches of different magnetic materials that are sensitive to complementary frequency bands (c.f. Fig. 4.4E). We expect that the sensitivity is ultimately limited by thermal spin-wave noise, which could be reduced by cooling down the detector.

7.3. NV MAGNETOMETRY OF VALLEY EXCITONS

NV magnetometry could provide a new window on valley-polarized excitons in TMD monolayers by giving insight in exciton distributions and valley dynamics at the nanoscale. Room-temperature NV experiments aiming for detecting the magnetic moment of TMD excitons could achieve a large valley polarization by driving the conversion of excitons to trions via gating. Alternatively, measurements could be done at cryogenic temperatures, which generally results in a finite valley polarization even without gating.

The highest sensitivity could be obtained by harnessing AC magnetometry protocols where the polarization handedness of an excitation laser is switched in sinc with a train of NV π-pulses [7]. The NV emission should be separated from the exciton emission using bandpass filters that maximize the signal-to-noise ratio [8]. Since a uniform magnetization generates the largest magnetic fields at sharp boundaries, the largest signals are expected at the edges of the flake.

7.4. ALTERNATIVES TO NV CENTERS

Apart from NV centers in diamond, also other solid-state spin defects could act as magnetic-field sensors for detecting spin waves and excitons. For example, very recently it was demonstrated that spin defects in silicon carbide (SiC) can detect magnon scattering processes in a permalloy disk [9]. SiC is technologically a more appealing material than diamond, as established wafer scale fabrication protocols allow its integration in scalable magnon-quantum systems [10].

Recently, sensor spins in two-dimensional hexagonal boron nitride (hBN) are also gaining increasing attention [11–13]. Van-der-Waals heterostructures consisting of an hBN sensor-flake and e.g. a TMD/magnetic monolayer can be assembled using accessible and routine fabrication techniques. They could serve as a natural sensing platform, in which the sensor spins have a minimal stand-off distance to the target material. It is challenging to achieve such a small stand-off distance in our measurement geometry as a result of dust between the sample and the millimeter-sized diamond platelet. The NV stand-off distance could be decreased by etching micron-scale sensor membranes from a diamond platelet or by integrating an NV scanning probe in an atomic force micro-

scope. Even in these geometries the stand-off distance will likely be larger than what could be achieved using hBN-heterostructures, although it should first be demonstrated that spin defects can stably exist in monolayer hBN before the ultimate defect proximity can be reached.

BIBLIOGRAPHY

[1] B. G. Simon et al., "Filtering and Imaging of Frequency-Degenerate Spin Waves Using Nanopositioning of a Single-Spin Sensor", Nano Letters **22**, 9198 (2022).

[2] T. X. Zhou et al., "A magnon scattering platform", Proceedings of the National Academy of Sciences of the United States of America **118**, 2019473118 (2021).

[3] B. G. Simon et al., "Directional Excitation of a High-Density Magnon Gas Using Coherently Driven Spin Waves", Nano Letters **21**, 8213 (2021).

[4] I. Bertelli et al., "Imaging Spin-Wave Damping Underneath Metals Using Electron Spins in Diamond", Advanced Quantum Technologies **4**, 2100094 (2021).

[5] Y. Li et al., "Nutation Spectroscopy of a Nanomagnet Driven into Deeply Nonlinear Ferromagnetic Resonance", Physical Review X **9**, 041036 (2019).

[6] S. C. Scholten et al., "Widefield quantum microscopy with nitrogen-vacancy centers in diamond: Strengths, limitations, and prospects", Journal of Applied Physics **130**, 150902 (2021).

[7] C. L. Degen, F. Reinhard, and P. Cappellaro, "Quantum sensing", Reviews of Modern Physics **89**, 035002 (2017).

[8] B. B. Zhou et al., "Spatiotemporal mapping of a photocurrent vortex in monolayer MoS_2 using diamond quantum sensors", Phys. Rev. X **10**, 011003 (2020).

[9] M. Bejarano et al., "Nonlinear magnon control of atomic spin defects in scalable quantum devices", (2022).

[10] S. Castelletto and A. Boretti, "Silicon carbide color centers for quantum applications", Journal of Physics: Photonics **2**, 22001 (2020).

[11] P. Kumar et al., "Magnetic imaging with spin defects in hexagonal boron nitride", (2022).

[12] M. Huang et al., "Wide field imaging of van der Waals ferromagnet Fe_3GeTe_2 by spin defects in hexagonal boron nitride", Nature Communications **13**, 5369 (2022).

[13] A. J. Healey et al., "Quantum microscopy with van der Waals heterostructures", Nature Physics (2022).

ACKNOWLEDGEMENTS

Often, pursuing a PhD is said to be a personal endeavour that you mainly do by yourself. However, when looking back on the last four years, I realize that the support of many people has been critical during my PhD journey. They not only helped me with technical issues, but also encouraged me to maintain a positive mindset, even during challenging moments. In this paragraph I would like to thank these people.

First of all, thank you, **Toeno**, for teaching me so many things. Five years ago we started brainstorming about ideas for measurements that I could do in my PhD. I remember this as an exciting time in which I felt everything was possible. It was only when you showed me the small size of a diamond (George, 2x2 mm^2) that I realized there is a great difference between developing theoretical ideas and performing actual experiments. During my PhD you constantly supported and encouraged me when facing challenges (there are no problems) and I truly enjoyed our discussions on how to interpret data or theory. I think you are a great physicist and I admire your eye for detail, creativity and writing skills. Finally, I am grateful about how you have stimulated a positive social atmosphere within the lab. I am a great fan of your work-hard-play-hard mentality and your amazing karaoke skills. PoP Goes My Heart, every time I hear you sing!

Next I would like to thank my second promotor. **Gary**, thank you for keeping track of my PhD progress and always showing such interest in my research. You are always asking great questions and your contributions to the social activities within the Quantum Nanoscience (QN) department are fantastic!

I would also like to thank the other members of my PhD committee, **Patrick Maletinsky**, **Helmut Schultheiß**, **Rembert Duine**, **Herre van der Zant** and **Sander Otte**, for reading and assessing my thesis. Sander, thanks for letting me borrow your spin-wave model so many times. I really enjoyed the discussions during the magnetism book club, and say hello to Cees!

I would like to thank the collaborators outside the lab that were involved in my research projects, **Tao**, **Gerrit**, **Yaroslav**, **Carsten**, **Oleksii**, **Angela** and **Mehrdad**. Yaroslav, many thanks for your clear explanations of spin-wave theory and for always taking the time to answer my questions.

My PhD would not have been possible without the endless support, coffees and joyful moments with the van der Sar lab.

Dr. Bertelli, **Iacopo**, you and I go waaay back. You were there during my Master and almost my entire PhD. In that time you taught me countless things in the lab, includ-

ing how to use a screwdriver for which I am particularly grateful. I have always been impressed by your perseverance, Italian cooking and scientific results, and I truly enjoyed working together on joint projects and have a beer at the Teepee Kafee on Friday afternoons. Also thank you for all the fun moments during conferences (Montpellier, Courchevel, Castelldefels, to name a few), where we had interesting discussions during the day and amazing parties in the evenings. I wish you all the best in the next steps of your career!

Brecht(o)! I was superhappy when you told me you would join our lab in Delft after having studied together in Leiden for our Bachelor and Master. In the first few months of our PhDs you managed to successfully train me in the cleanroom, despite my slightly chaotic workstyle and poor compliance to the gowning procedures. Although the cleanroom never became my favourite place to be, you have always inspired me with the diamond cantilevers you managed to fabricate there. What an achievement! Thank you for the supportive talks when cycling home after work, your help in the lab, taking the lead in fabricating and naming all the diamonds, and your enthusiasm to go for drinks after work. You are a great friend and I feel honoured to be your paranymph!

Next comes my labbuddy, **Micha(el)**, JJC thanks you for the amazing time during our MVP (mostly valley physics) project! Like a true Michaelangelo, you constructed amazing measurement setups in the lab, fabricated wonderful devices and did fantastic measurements. I am always blown away by your high level of organization and precise way of working, which somehow combined very well with my tendency to improvise and sometimes cut a corner. I enjoyed our lab cleaning sessions, the beers together and all the posters you used to decorate the lab. Your spin-wave/superconductor experiment is amazing and I wish you all the best with finalizing your PhD!

Samer, thanks for your endless positivity over the last few years! I enjoyed laughing together during a coffee or a beer, and discussing spin-wave physics with you. I think you are a wonderful postdoc - motivating and helping people whenever you can – and I find your discipline, your eagerness to learn new things and your beautiful photography inspiring. I look forward to hear about the results from the low-temperature scanning experiment (yes, finally we cooled down!) and your plans for the future!

Yufan, thank you for your joyful participation during van-der-Sar-lab activities and for being such a steady force in our lab! I find it always nice to hear about your holiday travels in Europe and I think your diamond nanobeams are fantastic! Sorry for sometimes bothering you with showing off my poor Chinese language skills. Wǒ ài píjiǔ, but by now I am sure you know that ;)

Thank you for helping me out so many times in the lab, **Allard**. Especially since I am not particularly a handyman myself, I am grateful that you were around so often for support. I value your expertise and your contributions during (group) discussions. In addition, thanks for your party spirit and for teaching me the basics of mountain biking and darts!

Thank you, **Kaveh**, for all your useful suggestions during group meetings. I wish you and your new group all the best in the future!

Edouard, thanks for our fun discussions about spin- and surface acoustic waves. Also many thanks for helping me out during a couple of crucial moments in the cleanroom!

I am happy and proud that the lab's research efforts will be continued by an energetic and enthusiastic group of NEW KIDS (turbooo!!!).

Roland, I wish you all the best in your future with Andrea and Alessia! I am impressed by how you approach changes in life, by which you have set an example for me. I think the measurements you did in your Master are amazing and I look forward to the results of your experiments the next few years!

Keep up that enthusiasm for climbing, **Pim**! Whether it is a table, chair, tree or the mast of sailboat, I have seen you climb it. I see you as a valuable all-rounder in the lab, knowing stuff about TMDs and spin waves, and I enjoyed hearing about your travel stories. Good luck the coming years!

Annick, I enjoyed working with you on the spin-wave mixing project last year! Your energetic drive is both amazing and inspiring, and I hope you will continue your adventures during climbing trips abroad. I admire your discipline, high level of organization, and willingsness to party!

In addition to the lab, there is a whole lot of people within QN that I had fun with over the past few years or supported me in some way (often both). Below I briefly thank these people, and I apologies in case I forget someone.

First of all, I thank the QN support staff for their help the last few years to let my PhD run smoothly, in particular **Etty**, **Heleen**, **Marijke** and **Lizzy**. **Tino**, thanks for the coffee-corner chats and our fun journey through Delft in search of the right aquarium pump for in the lab. In addition I thank the Kavli cleanroom and DEMO staff for their continuous help in fabricating devices and PCBs. **Kobus**, thanks for leading the department so well and our fun interview.

Next, my office friends. Being the office with six PhDs, F190 was a fun place to work, with the door always open and people walking in regularly. Thanks **Brecht**, **Jorrit**, **Dima**, **Ulderico**, **Luigi** and **Maarten** for all the fun moments and our discussions about academia, job opportunities and the housing market! Jorrit, thanks for always helping me when I had practical questions, even after you were done with your PhD. I hope I will ever run the 10K as fast as you. Maarten, thanks for the beers and your advice on one of life's most joyful moments. Good luck with your postdoc, Luigi!

I also thank the students that I supervised for their enthusiasm, dedication and contributions to the research, **Sibren**, **Olaf**, **Esther**, **Jeroen**, **Roland**, and **Nikolaj**.

Thank you, **Sonia**, for being always cheerful and practising my Spanish. **Jos**, thanks for helping me out whenever I did not understand an exercise when TA-ing Advanced Statistical Mechanics. A big shout-out to **Martin**, **Thierry**, **Allard**, **Edouard** and **Ulderico** for saving me so many times at the wirebonder when the needle had to be threaded (despite countless attempts, I think I managed thread it by myself only once...). Thanks **Irina** for letting Michael and me borrow your orange laser and our discussions about valley polarization in TMDs. Thank you, **Sarwan** and **Jean-Paul** for lending me RF components whenever I needed. Thanks, **Nikos**, for showing me how to exfoliate TMDs at the very beginning of my PhD.

Finally thanks to everyone that I had fun moments with, e.g. during coffees or beers in the TeePee Kafee or during PhD parties, **Thierry**, **Edouard**, **Sona**, **Lukas**, **Laëtitia**, **Rasa**, **Coosje**, **Marc**, **Sabrya**, **Helena**, **Martin**, **Nikos**, **Holger**, **Nina**, **Mattias**, **Patrick**, **David**, **Guido**, **Alexandre**, **Robbie**... and many others!

In addition to the QN community, there are other important people that have encouraged and supported me throughout my PhD.

Ik bedank mijn oud-huisgenoten van **de Molen** en **de Burgwal** voor mijn mooie tijd in Delft. **Eduard**, dank voor de vriendschap en de (0.0)biertjes afgelopen jaren, moge er nog vele volgen! **Neeffie**, bedankt voor al het lachen op de vrijdagavond! Dat helpt om positief, luchtig en met veel plezier door het leven te gaan, iets wat niet altijd vanzelfsprekend is tijdens een PhD. **Erik**, bedankt voor de mooie tijden in het buitenland, waarbij mijn interesse voor het doen van een PhD gewekt is.

Pa, **ma** en **Roen**, bedankt dat jullie me altijd gestimuleerd hebben om nieuwsgierig te zijn en open te staan voor nieuwe dingen. Jullie hebben me altijd alle mogelijkheden geboden om mijzelf vrij en zelfstandig te ontwikkelen, waarvoor ik jullie erg dankbaar ben. Jullie continue steun en betrokkenheid is altijd van groot belang voor mij!

Lieve **Laar**, jouw bijdrage aan mijn PhD is enorm. Van gedetailleerde planningen maken (en mij er aan houden) tot feedback geven op de Nederlandse vertaling van mijn samenvatting, overal hielp jij mij. Ik ben het meest dankbaar voor de momenten dat het tegenzat en jij mij onophoudelijk aanmoedigde om door te zetten (*Frappez toujours!*), in mij bleef geloven en zorgde voor ontspanningsmomenten samen. Ik kijk ontzettend uit naar onze nieuwe tijd in München, dat ongetwijfeld een mooie en spannende periode in ons leven samen wordt!

Joris Jip Carmiggelt
December 2022, The Hague

CURRICULUM VITÆ

Joris Jip CARMIGGELT

24-09-1995 Born in The Hague, The Netherlands.

EDUCATION

2007–2013 **High School** (*cum laude*)
Gymnasium Sorghvliet, The Hague, The Netherlands

2013–2016 **Bachelor of Science in Physics**
Leiden University, The Netherlands
Thesis: Creating spatially entangled 4-photon states by parametric down conversion
Supervisor: Dr. M. J. A. de Dood

2013 Propaedeutic diploma in Astronomy
Leiden University, The Netherlands

2013–2016 Bèta and Life Science Honours Program
Leiden University, The Netherlands

2015–2016 Erasmus+ Exchange Program
Ludwig-Maximilians-Universität (LMU) München, Germany

2016–2018 **Master of Science in Physics** (*cum laude*)
Casimir Pre-PhD track
Leiden University, The Netherlands
Thesis: Spectroscopy and imaging of spin waves using scanning NV center magnetometry
Supervisor: Dr. T. van der Sar (Delft University of Technology)

2017 Visiting student
Eidgenössische Technische Hochschule (ETH) Zürich, Switzerland

2017 Summer research student
CERN, ATLAS detector, Geneva, Switzerland

2018 Visiting research fellow at Yacoby lab
Harvard University, Boston, USA

2018–2022 **Ph.D. in Applied Physics**
Delft University of Technology, The Netherlands
Thesis: Spectroscopy and imaging of spin waves and valley excitons in two dimensions
Promotors: Dr. T. van der Sar
Prof. dr. G. A. Steele

SCHOLARSHIPS

2015 Erasmus+ grant
2017 Leiden university International Study Fund (LISF)
2018 Leiden university International Study Fund (LISF)
2018 Minerva Scholarship Fund (MSF)
2018 Hendrik Muller Fonds
2018 LUSTRA+ Scholarship
2018 Janneke Fruin-Helb Beurs (*honorable mention*)
2018–2022 Casimir PhD scholarship

LIST OF PUBLICATIONS

* indicates equal contribution

9. **J. J. Carmiggelt**, I. Bertelli, R. W. Mulder, A. Teepe, M. Elyasi, B. G. Simon, G. E. W. Bauer, Y. M. Blanter, and T. van der Sar, *Broadband microwave detection using electron spins in a hybrid diamond-magnet sensor chip*, (submitted).

8. B. G. Simon*, S. Kurdi*, **J. J. Carmiggelt**, M. Borst, A. J. Katan, and T. van der Sar, *Filtering and Imaging of Frequency-Degenerate Spin Waves Using Nanopositioning of a Single-Spin Sensor*, Nano Letters **22**, 9198 (2022).

7. A. V. Chumak, P. Kabos, M. Wu, C. Abert, C. Adelmann, A. O. Adeyeye, J. Åkerman, F. G. Aliev, A. Anane, A. Awad, C. H. Back, A. Barman, G. E. W. Bauer, M. Becherer, E. N. Beginin, V. A. S. V. Bittencourt, Y. M. Blanter, P. Bortolotti, I. Boventer, D. A. Bozhko, S. A. Bunyaev, **J. J. Carmiggelt**, R. R. Cheenikundil, F. Ciubotaru, S. Cotofana, G. Csaba, O. V. Dobrovolskiy, C. Dubs, M. Elyasi, K. G. Fripp, H. Fulara, I. A. Golovchanskiy, C. Gonzalez-Ballestero, P. Graczyk, D. Grundler, P. Gruszecki, G. Gubbiotti, K. Guslienko, A. Haldar, S. Hamdioui, R. Hertel, B. Hillebrands, T. Hioki, A. Houshang, C. . -M. Hu, H. Huebl, M. Huth, E. Iacocca, M. B. Jungfleisch, G. N. Kakazei, A. Khitun, R. Khymyn, T. Kikkawa, M. Kläui, O. Klein, J. W. Kłos, S. Knauer, S. Koraltan, M. Kostylev, M. Krawczyk, I. N. Krivorotov, V. V. Kruglyak, D. Lachance-Quirion, S. Ladak, R. Lebrun, Y. Li, M. Lindner, R. Macêdo, S. Mayr, G. A. Melkov, S. Mieszczak, Y. Nakamura, H. T. Nembach, A. A. Nikitin, S. A. Nikitov, V. Novosad, J. A. Otálora, Y. Otani, A. Papp, B. Pigeau, P. Pirro, W. Porod, F. Porrati, H. Qin, B. Rana, T. Reimann, F. Riente, O. Romero-Isart, A. Ross, A. V. Sadovnikov, A. R. Safin, E. Saitoh, G. Schmidt, H. Schultheiss, K. Schultheiss, A. A. Serga, S. Sharma, J. M. Shaw, D. Suess, O. Surzhenko, K. Szulc, T. Taniguchi, M. Urbánek, K. Usami, A. B. Ustinov, T. van der Sar, S. van Dijken, V. I. Vasyuchka, R. Verba, S. V. Kusminskiy, Q. Wang, M. Weides, M. Weiler, S. Wintz, S. P. Wolski, and X. Zhang, *Advances in Magnetics Roadmap on Spin-Wave Computing*, IEEE Transactions on Magnetics **58**, 6 (2022).

6. **J. J. Carmiggelt**, O. C. Dreijer, C. Dubs, O. Surzhenko, and T. van der Sar, *Electrical spectroscopy of the spin-wave dispersion and bistability in gallium-doped yttrium iron garnet*, Applied Physics Letters **119**, 202403 (2021).

5. B. G. Simon*, S. Kurdi*, H. La, I. Bertelli, **J. J. Carmiggelt**, M. T. Ruf, N. de Jong, H. van den Berg, A. J. Katan, and T. van der Sar, *Directional Excitation of a High-Density Magnon Gas Using Coherently Driven Spin Waves*, Nano Letters **21**, 8213 (2021).

4. **J. J. Carmiggelt**, B. G. Simon, I. Bertelli, and T. van der Sar, *Spinsensoren in diamant onthullen golvende spinzee*, Nederlands Tijdschrift voor Natuurkunde **6** (2021).

3. T. X. Zhou*, **J. J. Carmiggelt***, L. M. Gächter*, I. Esterlis, D. Sels, R. J. Stöhr, C. Du, D. Fernandez, J. F. Rodriguez-Nieva, F. Büttner, E. Demler, and A. Yacoby, *A magnon scattering platform*, Proceedings of the National Academy of Sciences **118**, e2019473118 (2021)

2. I. Bertelli, **J. J. Carmiggelt**, T. Yu, B. G. Simon, C. C. Pothoven, G. E. W. Bauer, Y. M. Blanter, J. Aarts, and T. van der Sar, *Magnetic resonance imaging of spin-wave transport and interference in a magnetic insulator*, Science Advances **6**, eabd3556 (2020).

1. **J. J. Carmiggelt***, M. Borst*, and T. van der Sar, *Exciton-to-trion conversion as a control mechanism for valley polarization in room-temperature monolayer WS_2*, Scientific Reports **10**, 17389 (2020).